EFFECT OF TRANSITION METAL SUBSTITUTION ON HIGH-TEMPERATURE PROPERTIES OF THERMOELECTRIC MATERIALS

A THESIS SUBMITTED TO
THE GRADUATE SCHOOL OF NATURAL AND APPLIED SCIENCES
OF
MIDDLE EAST TECHNICAL UNIVERSITY

BY

MURAT GÜNEŞ

IN PARTIAL FULFILLMENT OF THE REQUIREMENTS
FOR
THE DEGREE OF DOCTOR OF PHILOSOPHY
IN
MICRO AND NANOTECHNOLOGY

AUGUST 2014

Approval of the thesis:

EFFECT OF TRANSITION METAL SUBSTITUTION ON HIGH-TEMPERATURE PROPERTIES OF THERMOELECTRIC MATERIALS

submitted by **MURAT GÜNEŞ** in partial fulfillment of the requirements for the degree of **Doctor of Philosophy in Micro and Nanotechnology Department, Middle East Technical University** by,

Prof. Dr. Canan Özgen ___________
Dean, Graduate School of **Natural and Applied Sciences**

Prof. Dr. Tayfun Akın ___________
Head of Department, **Micro and Nanotechnology**

Prof. Dr. A. Macit Özenbaş ___________
Supervisor, **Metallurgical and Materials Engineering Dept., METU**

Prof. Dr. Mehmet Parlak ___________
Co-Supervisor, **Physics Dept., METU**

Examining Committee Members:

Prof. Dr. Mustafa Göktepe, ___________
Physics Dept., Balıkesir University

Prof. Dr. A. Macit Özenbaş ___________
Metallurgical and Materials Engineering Dept., METU

Assoc. Prof. Dr. Haluk Külah, ___________
Electrical & Electronics Eng. Dept., METU

Assoc. Prof. Dr. Burcu Akata Kurç, ___________
Micro and Nanotechnology Dept., METU

Assist. Prof. Dr. Y. Eren Kalay, ___________
Metallurgical and Materials Engineering Dept., METU

Date: ________________

I hereby declare that all information in this document has been obtained and presented in accordance with academic rules and ethical conduct. I also declare that, as required by these rules and conduct, I have fully cited and referenced all material and results that are not original to this work.

Name, Last name : Murat Güneş

Signature :

ABSTRACT

EFFECT OF TRANSITION METAL SUBSTITUTION ON HIGH-TEMPERATURE PROPERTIES OF THERMOELECTRIC MATERIALS

Güneş, Murat
Ph.D., Micro and Nanotechnology
Supervisor : Prof. Dr. A. Macit Özenbaş
Co-Supervisor : Prof. Dr. Mehmet Parlak

August 2014, 178 pages

The objective of the present dissertation is to improve the thermoelectric efficiency (*ZT*) of $Ca_3Co_4O_9$ metal oxide with a focus on nanostructuring, porosity and elemental substitution altering the electrical and thermal transport properties at high temperature and to establish a unique high temperature Seebeck coefficient and electrical resistivity measurement system.

An instrument for the high temperature measurement of Seebeck coefficient and electrical resistivity of one and/or two bulk samples over a temperature range of 300 – 1100 K is designed and implemented in our laboratory. During the installation of the system, five inventions have been made. These are; 1) cold-finger effect eliminated triple beadless thermocouples, 2) magnetic field and furnace eliminated micro-heaters, 3) differential temperature measurement specialty, 4) two-sample simultaneous measurement feature 5) non-destructive axial four-point probe electrical resistivity measurement conduction. Due to the above mentioned major accomplishments, while cost and size is reduced, measurement accuracy and sensitivity is further enhanced. The total estimated data error for the Seebeck coefficient and resistivity measurements is less than 2.6 % and 1 %, respectively.

In order to investigate the effect of nanostructuring and porosity on thermoelectric properties of $Ca_3Co_4O_9$ oxide, samples of the material are synthesized via citrate sol-gel method with different average grain sizes ranging from 18, 30, 68 nm and 2 μm. A considerable increase in electrical resistivity is observed, however, Seebeck coefficient is not much suppressed. It is investigated that thermal conductivity is substantially lower for nano-sized samples due to grain boundary scattering. Porosity further contributes to reducing this value leading to increase in the density of scattering regions. Thermal conductivity is decreased by 23 % with the help of nanostructuring and porosity. The enhancement of *ZT* value is 61 % and it reaches 0.29 at 1000 K for 18 nm sample.

Polycrystalline $Ca_{3-x}Cr_xCo_4O_9$ (x = 0.0, 0.01, 0.03, 0.05 and 0.07) thermoelectric samples are prepared. Cr substitution to Ca-site leads to the spin-entropy enhancement and this caused increase in the Seebeck coefficient with up to x = 0.03 Cr substitution. Power factor is enhanced by 30 %. The thermoelectric performance is the most significant in x = 0.03 sample with *ZT* value of 0.26 at 1100 K. The enhancement in *ZT* value is 33 %.

Keywords: Thermoelectrics, $Ca_3Co_4O_9$, Nanostructuring and Porosity, Cr-substitution, Thermoelectric Properties Measurement System.

ÖZ

TERMOELEKTRİK MALZEMELERİN YÜKSEK SICAKLIK ÖZELLİKLERİ ÜZERİNE GEÇİŞ METALİ KATKILAMANIN ETKİSİ

Güneş, Murat
Doktora, Mikro ve Nanoteknoloji
Tez Yöneticisi : Prof. Dr. A. Macit Özenbaş
Ortak Tez Yöneticisi : Prof. Dr. Mehmet Parlak

Ağustos 2014, 178 sayfa

Bu çalışmanın amacı, yüksek sıcaklıkta $Ca_3Co_4O_9$ termoelektrik metal oksit malzemelerin *ZT* olarak bilinen termoelektrik verimini, nano yapı, gözenekli yapı ve elemental katkılamaya odaklanarak elektrik ve ısı transfer özelliklerini değiştirerek iyileştirmek ve özgün bir yüksek sıcaklık Seebeck katsayısı ve elektriksel direnç ölçüm sistemi kurmaktır.

Bir ve/veya iki örneğin Seebeck katsayısını ve elektriksel direncini 300 - 1100 K sıcaklık aralığında aynı anda ölçebilen bir cihazın tasarımı ve kurulumu laboratuvarımızda yapılmıştır. Sistemi kurulumu sırasında beş buluş gerçekleştirilmiştir. Bunlar: 1) soğuk-parmak etkisini ortadan kaldıran üçlü boncuksuz ısıl çiftler, 2) manyetik alan ve fırını ortadan kaldıran mikro-ısıtıcılar, 3) diferansiyel sıcaklık ölçümü özelliği, 4) aynı anda iki örnek ölçüm özelliği ve 5) tahribatsız eksenel dört nokta elektriksel direnç ölçüm özelliğidir. Yukarıda belirtilen önemli başarılardan dolayı maliyet ve ebat küçülürken, ölçüm doğruluğu ve hassasiyeti oldukça yükseltilmiştir. Seebeck katsayısı ve direnç ölçümleri için toplam veri hatası sırasıyla % 2.6 ve % 1 ‘den daha azdır.

Nano ve gözenekli yapıların $Ca_3Co_4O_9$ oksit malzemelerin termoelektrik özellikleri üzerine etkilerini incelemek üzere, örnekler 18, 30, 68 nm ve 2 μm boyutlarında sitrat sol-jel metodu kullanılarak sentezlendi. Nano-boyutlu örneklerde, elektriksel direnç önemli ölçüde artmıştır, ancak Seebeck katsayısında gözle görünür bir değişiklik olmamıştır. Bu örneklerde, ara yüzeylerdeki tane sınır saçılmasından kaynaklanan oldukça düşük ısıl iletkenlik değeri ölçülmüştür. Gözenekli yapı, saçılma bölgelerin yoğunluğu artırmak suretiyle ısıl iletkenliğin azaltılmasına ayrıca katkıda bulunduğu da gözlenmiştir. Isıl iletkenlik nano ve gözenekli yapıların katkısı ile % 23 oranında azalmıştır. *ZT* değeri 18 nm boyutlu örnek için 1000 K ‘de % 61 ‘lik bir artışla 0.29 değerine ulaşmıştır.

Katkılamanın etkisini incelemek üzere, $Ca_{3-x}Cr_xCo_4O_9$ (x = 0.0, 0.01, 0.03, 0.05 ve 0.07) termoelektrik katlıkristal örnekler hazırlanmıştır. Cr ‘un Ca tarafına katkılanması, x = 0.03 Cr katkılama oranına kadar spin-entropinin artmasına ve dolayısıyla Seebeck katsayısının artmasına neden olmuştur. Termoelektrik performansta en önemli gelişme 1000 K ‘de 0.26 *ZT* değeri ile x = 0.03 Cr örneğinde gözlenmiştir. *ZT* değerindeki artış % 33 ‘dür.

Anahtar Kelimeler: Termoelektrikler, $Ca_3Co_4O_9$, Nano Yapı ve Gözeneklilik,
Cr-Katkılama, Termoelektrik Özellik Ölçüm Sistemi

To my father

my family

and

to my dearest, Anna

ACKNOWLEDGEMENTS

I would like to express my deepest gratitude to my supervisor, Prof. Dr. Macit Özenbaş, for his excellent guidance, caring, patience, and providing me with an excellent atmosphere for doing research.

It is great pleasure to thank my co-supervisor Prof. Dr. Mehmet Parlak for his excellent guidance, and comments.

I would like to thank the thesis monitoring committee members Prof. Dr. Mustafa Göktepe from Physics Dept. of Balıkesir University and Prof. Dr. Haluk Külah from Electrical & Electronics Eng. Dept. of METU for their excellent suggestions and comments during this study.

I would like to express my special thanks to Prof. Dr. Selçuk Atalay for his advices, support and encouragement. I always felt his support in all issues about life.

I am indebted to Prof. Dr. Nita Dragoe from University of Paris Sud 11 for his great guidance, help and suggestions.

I would also like to acknowledge the Prof. Dr. Mustafa Ürgen and Assist. Prof. Dr. Nuri Solak from ITU for providing thermal conductivity measurements.

I would like to thank to all specialists of FE-SEM, XRD, XRF and other facilities in Dept. of Metallurgical and Materials Engineering and in METU Central Laboratory for their great technical support and assistances.

My deepest gratitude goes to my whole family. They are always supporting me and encouraging me with their best wishes.

Finally, I owe my deepest gratitude to my wife, Anna. She is always there cheering me up and stood by me through the good and bad times.

This thesis has been supported by Scientific HR Development Program (ÖYP) at Middle East Technical University through the project BAP-08-11-DPT2002K120510.

TABLE OF CONTENTS

CHAPTERS

LIST OF TABLES

TABLES

LIST OF FIGURES

FIGURES

LIST OF ABBREVIATIONS

TAGS	Te/Ag/Ge/Sb thermoelectric material
TG / DTA	thermal gravimetric analysis / differential thermal analysis
BET	Brunauer–Emmett–Teller
XRD	X-ray diffraction
XRF	X-ray fluorescent spectroscopy
XPS	X-ray photoemission spectroscopy
FE-SEM	field emission scanning electron microscopy
EDS	energy-dispersive X-ray spectrometer
VC	vacuum chamber
SP	sample probe
Mhs	micro heaters
AI	alumina isolator
4AI	4-bore alumina isolator
7AI	7-bore alumina isolator
SHs	sample holders
SPBs	sample probe blocks
SST	stainless steel tube
C-349	$Ca_3Co_4O_9$
SSC	single sample configuration option
DSC	double sample configuration option
PID	proportional-integral-derivative
EMT	effective medium theory

STO-3D	$SrTiO_3$ 3D superlattice ceramics
PGEC	phonon glass-electronic crystals
CWJ	crossed wire junction
SD	standard deviation
Std_dev	standard deviation
RT	room temperature
dc	steady-state condition
qdc	quasi-steady-state condition
ac	Transient condition

LIST OF SYMBOLS

S, α[1]	Seebeck coefficient
S_A	Seebeck coefficients of the metal-A as a function of temperature
S_B	Seebeck coefficients of the metal-B as a function of temperature
κ	total thermal conductivity
κ_{ph}	phonon / lattice thermal conductivity
κ_c	carrier / electronic thermal conductivity
k_{solid}	thermal conductivity of constituent solid
k_{pore}	thermal conductivity of constituent pore
V_{solid}	volume fraction of constituent solid
V_{pore}	volume fraction of constituent pore
κ_{eff}	effective bulk thermal conductivity of the composite
κ_0	bulk thermal conductivity
β	pore shape factor
σ	electrical conductivity
ρ	electrical resistivity
$S^2\sigma$	thermoelectric power factor / power factor
ZT	thermoelectric figure-of-merit of material
T	absolute temperature
T_h	hot site temperature

---

[1] This symbol “α” is used as Seebeck coefficient symbol only in figure 1.3.

T_c	cold side temperature
ΔV	voltage difference
ΔT	temperature difference / gradient
e	electrical charge of an electron
c_{el}	electronic heat capacity for one electron
C_{el}	electronic heat capacity for the whole system
N	the number of electrons in the system
k_B	Boltzmann constant
T_F	Fermi temperature
E_F	Fermi energy
m^*	effective mass
E_g	Energy band gap
L	Lorentz factor
η	energy conversion efficiency
$\Delta T/T_h$	Carnot efficiency
d_{GB}	grain boundary thickness
d_{GI}	grain size
E_{GB}	potential barrier height
τ_e	carrier relaxation time
p	probability of an electron being scattered by the grain boundary
E	electronic energy
I	electronic mean free path
R	interfacial thermal resistance
α	thermal diffusivity
C_p	specific heat capacity
d	density

$\overrightarrow{I_1},\ \overrightarrow{I_2}$	directions of electrical current applied to micro heaters
$\overrightarrow{B_1},\ \overrightarrow{B_2}$	directions of magnetic field created in micro heaters
$\left\lvert\overrightarrow{I_1}\right\rvert,\ \left\lvert\overrightarrow{I_2}\right\rvert$	the magnitude of the current
$\left\lvert\overrightarrow{B_1}\right\rvert,\ \left\lvert\overrightarrow{B_2}\right\rvert$	the magnitude of the magnetic field
V_{IR}	voltage for resistivity calculations
I_{src}	applied electrical current for resistivity measurement
σ [2]	standard deviation
M	molarity

---

[2] This symbol is used as standard deviation symbol only in section 4.4.2.

CHAPTER 1

INTRODUCTION TO THERMOELECTRIC RESEARCH

Thermoelectricity is defined as the science and technology associated with thermoelectric power generation and refrigeration. During the last decade the number of significant advances in thermoelectric area has increased drastically. In recent years, there have been significant developments in the field thermoelectricity.

The main reasons can be the demand of renewable energy sources for long-life electrical power sources because of the increasing detrimental effect of CO_2 emission on global warming that is approaching critical levels. Indeed, the minimizing of the electronics and moving parts in the energy systems are other important factors. As the issue is meeting these requirements mentioned above, the thermoelectric materials as an environmentally friendly method can be key solution [1].

Thermoelectric power generation technology is now expected to help overcome global warming and climate change issues by recovering and converting waste heat directly into electricity irrespective of source size and without the use of moving parts or production of environmentally deleterious wastes, thus improving the total efficiency of energy utilization and suppressing the consumption of fossil fuels that are supposedly the major sources of CO_2 emission [2].

In the last decade, substantial progress has been made in establishing thermoelectric materials for waste heat recovery from automobile industry as energy sources. Indeed, different kind of segmented thermoelectric modules/devices such as thin-film generating, cooling, and sensing devices are also employed for power source applications [1]. However, the materials for above mentioned applications, which satisfy the requirements, have still not been found. The main reasons are that the material should have high conversion efficiency, made up of non-toxic and abundantly available elements with high chemical and thermal stability in air at temperatures of 800 – 1000 K. Environmentally friendly thermoelectric materials are believed to be a promising technology with respect to waste heat energy conversion. A good thermoelectric material needs to demonstrate a low electrical resistivity and thermal conductivity and have a high thermoelectric power. $Ca_3Co_4O_9$ (C-349) is one of the promising materials among all other oxides with its high thermo-power, low thermal conductivity and resistivity values at high temperatures. Moreover, C-349 also shows featured thermoelectric properties as metal oxide has been found thermodynamically stable at elevated temperatures, nontoxic, well-supplied, easy to fabricate and cheap [1]. Thus, it is necessary to improve their efficiency for energy conversion from waste heat in the air.

For any real practical use in power generator, *ZT* needs to be higher than 1. Choosing C-349 based oxide materials as a model system, the present dissertation is aims to investigate and understand how the thermoelectric properties such as electrical and thermal transport ones are affected and tuned by the structural engineering which are carried out through material synthesis and processing.

C-349 oxide material is a base material the electrical and thermal properties of which could be enhanced via nanostructuring. It would be an effective way to reduce the lattice thermal conductivity through phonon scattering at interfaces. Besides, lattice thermal conductivity could further be reduced with the contribution of porosity, which will help to increase the scattering area. Another way for enhancing *ZT* is elemental substitution. Elemental substitutions could be used to increase the Seebeck coefficient and electrical conductivity of C-349 oxide material by spin-entropy mobility enhancement, respectively. In the main body of this dissertation, the structure and thermoelectric properties of nanostructured C-349 oxide system are examined and evaluated via experimental works and the obtained results are evaluated based on physical and mathematical modeling in the literature.

As for other scientific areas, the area of thermoelectrics can also be divided in two sections that are "the development of thermoelectric properties measurement systems" and "the thermoelectric material developments". Every day a new type of materials with different electrical and thermal properties is discovered. Since these both areas should progress synchronously, innovation in metrology science is inevitable. Therefore, the thermoelectric parameters measurement systems should satisfy the necessary conditions for evaluation of the thermoelectric properties of the materials. For this reason, the aim of developing these systems is to present better measurement conditions in order to contribute to the measurement science and to enhance the measurement accuracy for the highest quality results.

The next section, past and recent developments in the area of thermoelectric will be summarized for better understanding. And then, the fundamentals of thermoelectric effect are explained. The basics and applications of thermoelectrics that are known as the Seebeck effect and figure of merit are also provided in the aspect of physical parameters. Additionally, high temperature thermoelectric materials and their thermoelectric properties are presented for better understanding. The requirements placed on such oxides as thermoelectric materials are demonstrated in the aspect of an increasing emphasis on the development of advanced thermoelectric materials for the high temperature energy conversion. C-349 based thermoelectric materials with the advantages of high conversion efficiency, earth abundance and affordability; being non-toxic, high chemical and temperature stability in air at temperatures of 1000 K are highlighted. An example of C-349 oxide system is briefly reviewed with its structural and thermoelectric properties. The established measurement device sensitive at high temperature and doing accurate measurements of Seebeck coefficient and electrical resistivity is introduced. Highly new innovative measurement configurations are applied and true solutions for several challenging source of errors are presented in detail.

As it has been introduced, the significant number of research in thermoelectric area focuses on enhancing the ZT reducing the phonon thermal conductivity. Accordingly, a detailed description of the key structural engineering processes is essential to manipulate thermal transport properties, including nanostructuring and porosity. Chapter 2 is be devoted to the description of these techniques that are employed in the experimental research.

Chapter 3 is be devoted to the description of the methods and techniques that are employed through the experimental work. These are; the synthesis of oxide powders, calcination and sintering processes, various structural characterizations, including XRD, TG / DTA, BET, density and particle size analysis, FE-SEM and the measurements of thermoelectric properties, including Seebeck coefficient, electrical resistivity and thermal conductivity.

Thermoelectric materials with high ZT are necessary for practical applications of thermoelectric modulus not only for power generation, but also for cooling applications. Two of the most significant thermoelectric properties such as Seebeck coefficient, electrical resistivity measurements are unavoidable for evaluation of ZT. For this reason, reliable, accurate, and consistent thermoelectric measurements are significant characterization techniques. Chapter 4 presents the simultaneous measurements of Seebeck coefficient and electrical resistivity system which is developed in our laboratory. The system has unique properties with elimination of possible source of errors such as cold-finger effect, external magnetic field and new measurement features such as beadless thermocouples, micro heaters and reference sample measurement option 1100 K under any desired atmospheric condition.

Chapter 5 mainly focuses on the nanostructuring processes of C-349 thermoelectric material. Basically, this chapter explains the applied synthesis methods in order to produce nanostructured materials in different particle size and their structural characterizations and thermoelectric analyses. Results of experimental work are compared with the theoretical models. The effect of porosity is also discussed and achievements are compared with the ones in the literature.

The elemental substitution effect is detailed and discussed in Chapter 6. In this work, Cr element is substituted for Ca-site of C-349 thermoelectric material in different amount and their structural and thermoelectric properties are discussed. Several structural characterizations including XRF, XPS and FE-SEM have been done in order to understand the substitution level and its mechanisms. The results are confirmed with Rietveld refinements.

The overall studies are discussed and summarized as a final step in Chapter 7. All the achievements are listed and future plans are presented in this chapter.

1.1. Thermoelectric Applications and Theoretical Background

A well-established application is the radioactive thermoelectric generators for deep-space probes (NASA’s Voyager and Cassini missions) [3] and Curiosity as well [4]. Nowadays, thermoelectric energy conversion devices can be installed on vehicles to recover the automobile exhaust heat into useful electrical energy and thereby increase the fuel efficiency [5]. Most of the applications of thermoelectrics are represented in figure 1.1. K. Holmberg [6] claims that almost 30 % of the fuel energy is used to overcome friction in the engine, transmission, tires, and breaks in typical passenger cars. The result shows that only 21.5% of the fuel energy is used to move the car. On the other hand, solid state refrigerating devices, which utilize the thermoelectric or Peltier cooling function, have been widely applied in small-scale cooling in computers, infrared detectors and optoelectronic devices [5]. Thermoelectric car seat climate control system has also been commercialized [7]. There are also some recent applications including the thermoelectric-solar hybrid systems for energy conversion and power generation [8].

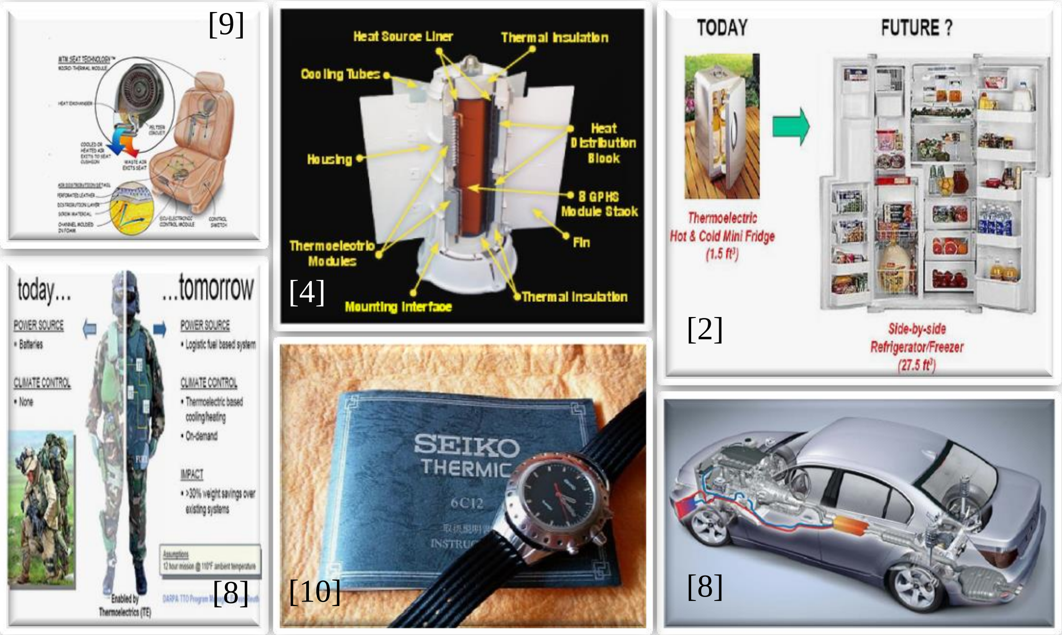

Figure 1.1 Some currently used and future planned thermoelectric applications.

Similarly, as an environmentally friendly method, thermoelectrics could be useful tool for the electricity generation from emitted waste heat such as automobiles, factories and similar sources. Although waste heat could be considered as high quality energy, its source amounts are being small and widely dispersed [2].

1.2 Literature Survey

The current state of the art bulk thermoelectric materials is demonstrated in figure 1.2 [11]. *ZT* is illustrated as a function of temperature and year for n- and p-type materials in this figure. Thermoelectrics is classified in three stages according to their thermoelectric efficiency values. In this figure, first generation thermoelectrics have their *ZT* of about 1.0. Besides, *ZT* from 1.0 to 1.7 is named as the second generation thermoelectrics and the third generation thermoelectrics with *ZT* from 1.8 to 2.2 is titled as [11].

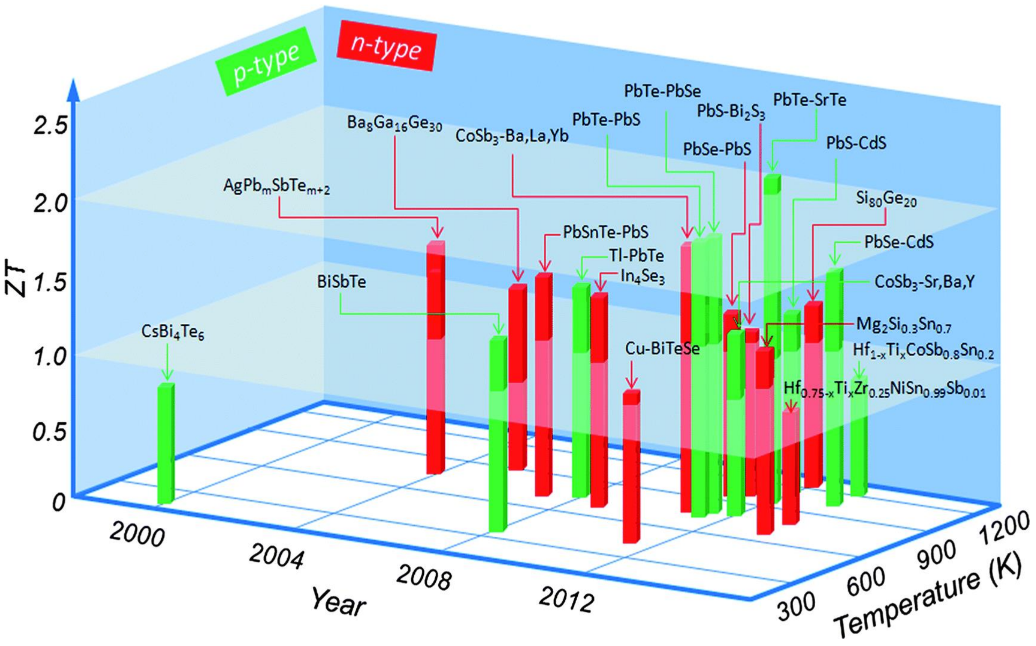

Figure 1.2 Current state of the art bulk thermoelectric materials [11].

Commercial thermoelectric materials, which are used in real life applications, could be classified into three groupings according to their operation temperature. Table 1.1 shows these commercial thermoelectric materials and their well-known properties. Bismuth based alloys in combination with antimony, tellurium, and selenium takes the first place as low-temperature materials, e.g. Bi_2Te_3. The application temperature of these alloys is around 450 K. These universal materials are best known and commercially employed in thermoelectric refrigeration systems. The intermediate temperature range up to around 850 K is filled with lead telluride such as PbTe and Te/Ag/Ge/Sb (TAGS) thermoelectric materials. The last group of thermoelectrics employed at the highest temperatures is silicon germanium alloys (SiGe) 1300 K operation temperature. Although these three groups of materials are commercially available, they unfortunately could not be commercialized widely due to their shortage, such as poor continuity at high temperature in air, high cost and low abundance of the containing elements with high toxicity as shown in figure 1.3 [12]. Therefore, oxide thermoelectric could take the place of these materials due to their properties compared in table 1.1.

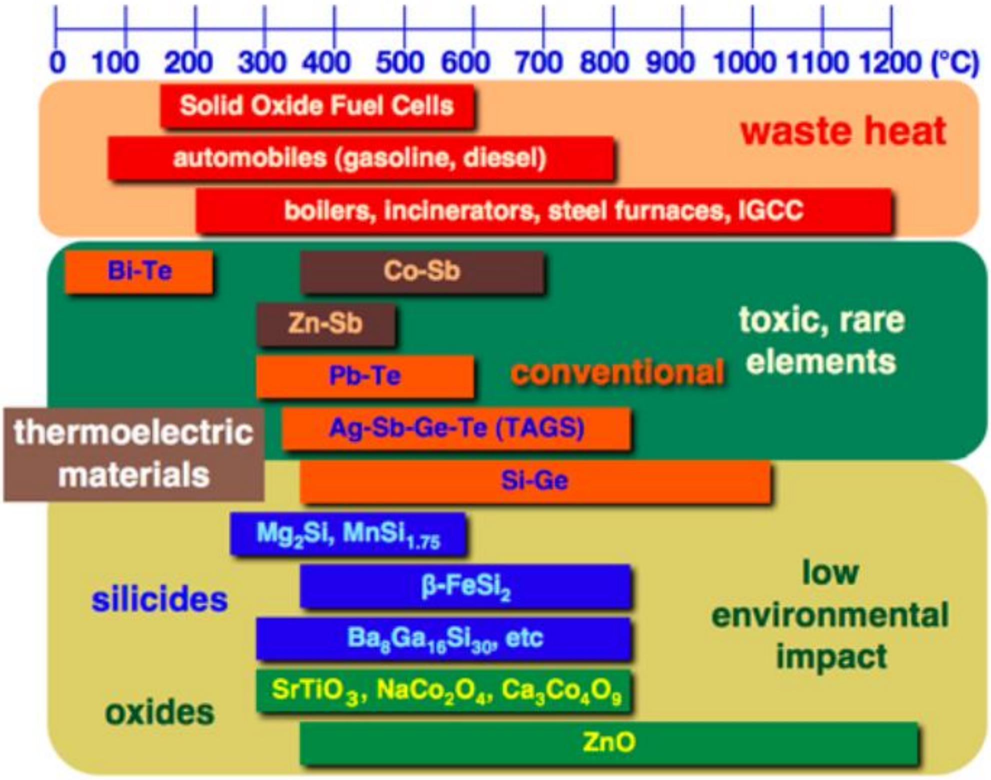

Figure 1.3 Typical waste heat and operating temperature ranges of various thermoelectric materials [12].

Table 1.1 General comparison of conventional thermoelectric materials including oxides.

	Bismuth Based (Bi_2Te_3)	**Lead Telluride Based (PbTe)**	**SiGe Alloys**	**Oxides**
Temperature Range	≈ 450 K	≈ 850 K	≈ 1300 K	**≈ 1300 K**
Durability	Poor	Poor	Poor	**Rich**
Toxicity	Toxic	Toxic	Toxic	**Non-Toxic**
Oxidation	High	High	High	**-**
Abundance	Low	Low	Low	**High**
Cost	High	High	High	**Low**

1.3 Oxides as Thermoelectric Materials

Terasaki *et al*. [13] reported that the sodium cobalt oxide $Na_xCo_2O_4$ has shown large thermoelectric power (0.1 mV/K) coexisting with low electrical resistivity (0.2 Ω.cm) at 300 K. The layered cobaltites, $Na_xCo_2O_4$ and C-349 have been intensively studied as a potential application for clean heat conversion at high temperatures. These cobaltite thermoelectric materials exhibit good thermal and chemical stability at high temperatures in air whereas intermetallic compounds do not. The thermoelectric conversion at high temperature will allow the re-use of exhaust heat from automobiles and plants. The thermoelectric oxides are chemically stable high temperature with low toxicity compared to the intermetallic alloys. Cobalt-based oxides with layered structures have been reported to show good not only p-type thermoelectric properties, but also n-type thermoelectric properties at high temperature in the air. Comparison of established thermoelectric materials which are employed in commercial applications and thermoelectric metal oxides can be plotted dependent upon the temperature range of operation as shown in figure 1.4.

In order to understand why metal oxides show excellent thermoelectric properties we need to look at their basic concept. Metal oxides are ionic compounds consisting of metal cations and oxygen anions alternately placing with the Coulomb attracting interaction between them. Metal-oxygen bonds are highly polarized. Therefore, conducting electrons tend to localize on the positively charged metal cations. Additionally, atomic orbitals’ overlapping between two atoms is smaller than that in compounds with covalent bonds. This is the reason why the carrier mobility of oxides is typically 2 - 3 folds lower than other covalent compounds. To give more details, large bonding energies of the ionic bonds and the small atomic mass of oxygen give a high velocity of the elastic waves propagating the crystal lattice of oxides, which results in a high lattice thermal conductivity, κ_{ph}. Because of this innate characteristic electronic structure of metal oxides which is clearly against the conventional guiding principles for higher *ZT*, metal oxides have been disregarded in the history of thermoelectric materials until 1990s. During this time, establishing featured guiding principles stimulated the scientist to investigate novel materials including oxides due to the global environment issues. Because of several significant properties that are mentioned above, oxide materials became one of the most significant candidates for practical applications of thermoelectric materials [14].

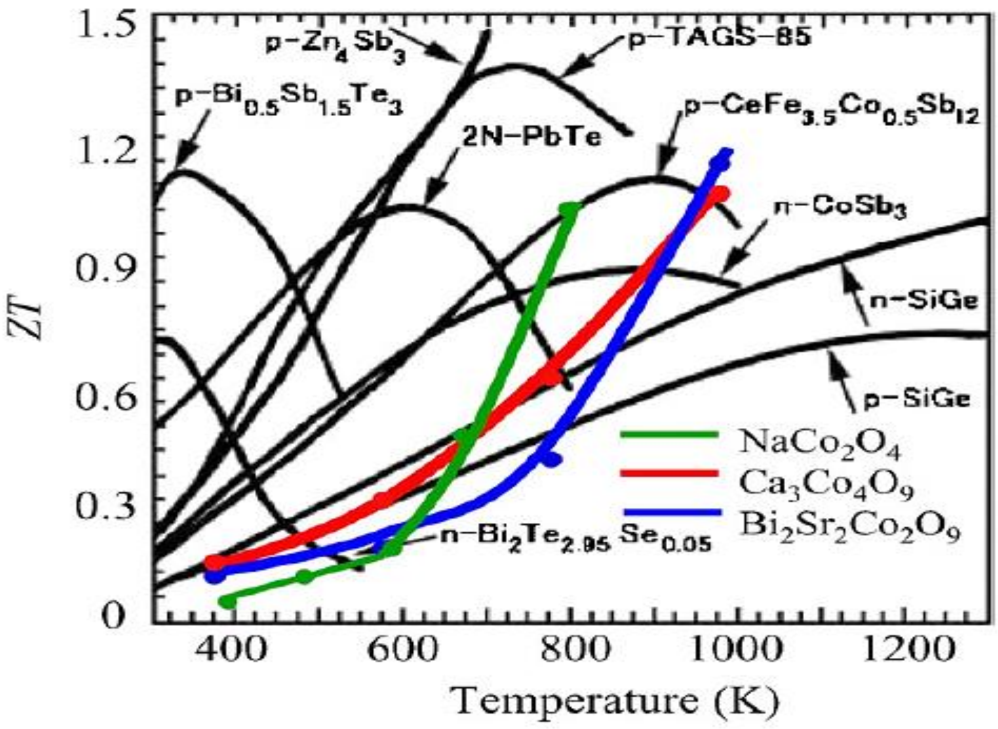

Figure 1.4 Figure of merit (*ZT*) as a function of temperature for several high-efficiency bulk thermoelectric materials [15].

Figure 1.5 demonstrates the history of oxide thermoelectric materials. Due to significant effort which has been made on oxide thermoelectrics, there is significant enhancement in *ZT* that is almost 1. The present-day thermoelectric modules are based on the work that is carried out during the late 1950s and the early 1960s on bismuth telluride and its alloys. Since that time, there have been significant advances in materials for thermoelectric generation, but at all temperatures the efficiency of energy conversion using thermocouples has fallen far short of that expected for an ideal thermodynamic machine. At last, with the advent of nanostructured thermoelements, there is the promise that substantial advances will be made. The basic principles of thermoelectric devices have not been changed over the years [15].

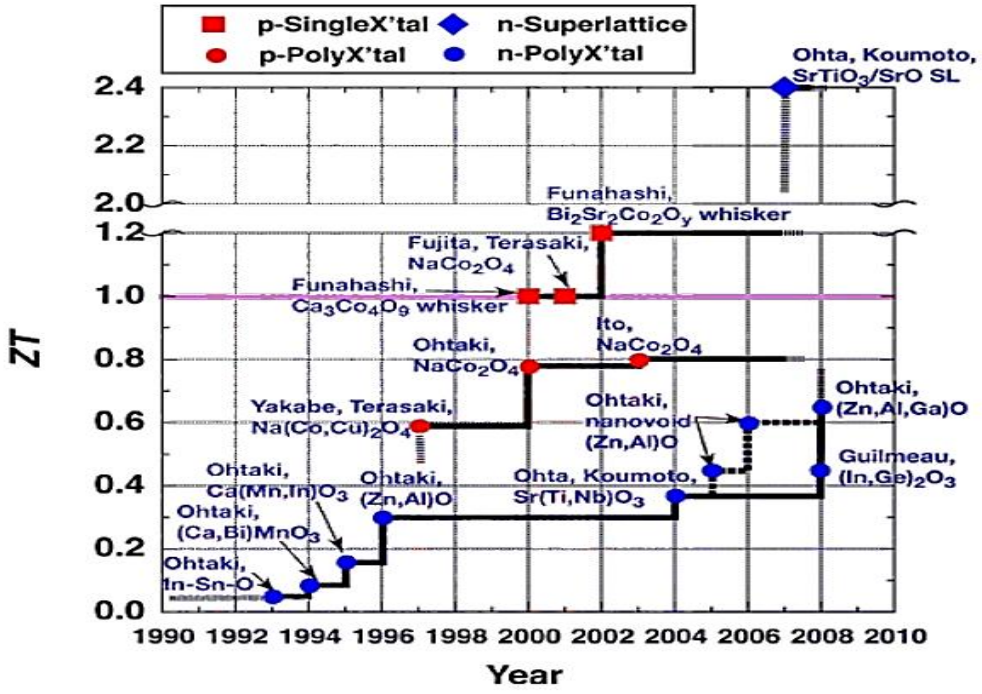

Figure 1.5 Time line of oxide thermoelectric materials with the highest *ZT* [14].

To illustrate the thermoelectric behavior of C-349 materials, crystallographic and structural concepts of it are presented more in detail in the next section.

1.4 $Ca_3Co_4O_9$ Oxide Thermoelectrics

Conventional thermoelectric materials are not stable at high temperatures. However, C-349 shows promising thermoelectric properties, such as thermodynamically stable at elevated temperatures, nontoxic, well-supplied, easy and cheap to fabricate. Therefore, it is necessary to improve their efficiency for energy conversion from waste heat in the air. In order to reach this aim, an attempt to introduce nano-grained bulk materials to achieve phonon-scattering at grain boundaries and as a result, reducing thermal conductivity without degrading electrical conductivity or suppressing thermopower ($S^2\sigma$) to increase ZT is necessary.

Sodium cobalt oxide ($Na_xCo_2O_4$) showed extraordinary thermoelectric properties as a metal oxide when it was discovered by Terasaki *et al.*[13], it [16, 17]. C-349 is one of the promising materials among all other oxides with its high Seebeck coefficient, low thermal conductivity and low electrical resistivity values at high temperatures. This compound belongs to the family of misfit cobalt oxides (see figure 1.6), and the structure of the crystal can be described as an alternate stacking along [001] of distorted rock-salt-type slabs [Ca_2CoO_3] and of [CoO_2] layers displaying a distorted CdI_2-type structure [18]. In these layers, CoO_2 nanosheets that possess a strongly correlated electron system and Ca_2CoO_3 misfit layers which serve as electronic transport layers act as potential phonon scattering regions [19-22].

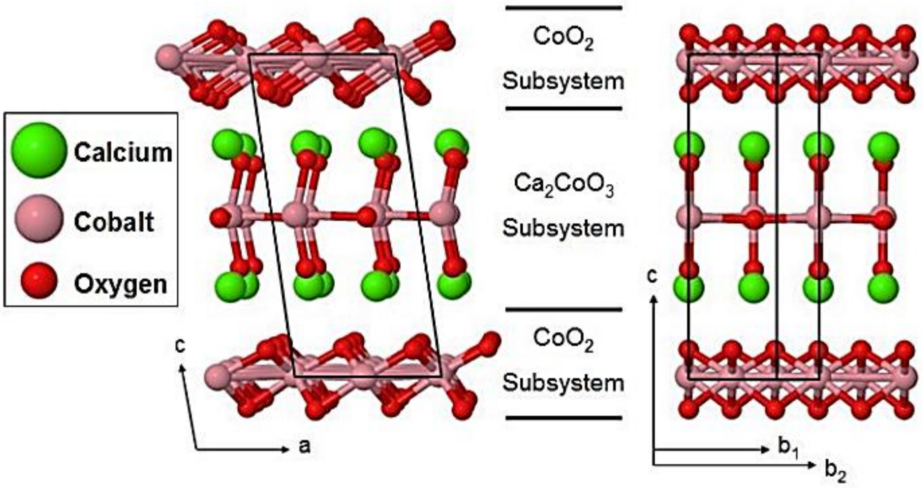

Figure 1.6 Schematic illustration of the crystal structure of C-349 oxide [16].

Table 1.2 introduces the literature survey of the developments on C-349 thermoelectric metal oxide. The table shows material, synthesis method and sintering treatments, Seebeck coefficient, thermal conductivity, electrical resistivity, power factor, figure of merit and the temperature at which these parameters are obtained.

Table 1.2 Thermoelectric properties of C-349 samples from the literature.

Author	**Material**	**Synthesis Method**	T (K)	S (μV/K)	κ (W/mK)	R (mΩ.cm)	PF (mW/mK^2)	ZT
Lu *et. al* **[23]**	$Ca_{3-x}Ba_xCo_4O_9$ (x=0~0.4)	Sol-gel SPS 1073 K, 10 min, 50 MPa 1073 K, 2 h	700	183	1.9	4.28	-	0.4
Wang *et. al* **[24]**	$Ca_{3-x}Eu_xCo_4O_{9+\delta}$ (x=0.3)	Wet chemical SPS 973 K, 10 min, 50 MPa 1173 K in O_2, 36 h	1000	194	1.7	6.5	-	0.3
Wang *et. al* **[25]**	$Ca_{3-x}Dy_xCo_4O_{9+\delta}$ (x=0.3)	Wet chemical SPS 973 K, 10 min, 50 MPa 1173 K in O_2, 36 h	1000	190	1.64	8	-	0.27
Nong *et. al* **[26]**	$Ca_3Co_{4-x}Ga_xO_{9+\delta}$ (x = 0.05)	Solid state Cold Press 1223 K in O_2, 24 h	1200	205	1.5	7.5	5.5	3.8

Table 1.2 (cont'd) Thermoelectric properties of C-349 samples from the literature.

Author	**Material**	**Synthesis Method**	T (K)	S (μV/K)	κ (W/mK)	R (mΩ.cm)	PF (mW/mK^2)	ZT
Nong *et. al* [27]	$Ca_{3-x-y}Ag_xLu_yCo_4O_{9+\delta}$ (x = 0.05, y=0.15)	Solid state Cold Press 1223 K in O_2, 24 h	1118	235	1.42	7.2	-	0.61
Nong *et. al* [28]	$Ca_{2.8}Lu_{0.2}Co_4O_{9+\delta}$	Solid state Hot press 1123 K, 2 h, 60 MPa	1073	190	1.2	9.5	3.8	0.36
Zhang *et. al* [29]	$Ba_xAg_yCa_{3-x-y}Co_4O_9$ $x = y = 0.1$	Citrate sol–gel SPS 1073 K, 5 min, 60 MPa	973	172	1.41	7.2	-	0.29
Liu *et. al* [30]	$Ca_{0.95}$ $Bi_{0.05})_3Co_4O_9$	Citrate sol–gel SPS 1073 K, 5 min, 60 MPa	973	179	1.81	6.8	-	0.25
Pei *et. al* [31]	$Ca_{2.7}Er_{0.3}Co_4O_{9+\delta}$	Sol–gel Hot press 1173 K, 10 h, 35 MPa	1073	191	1.5	10	3.6	0.28

Table 1.2 (cont'd) Thermoelectric properties of C-349 samples from the literature.

Author	Material	Synthesis Method	***T*** (K)	***S*** (µV/K)	***κ*** (W/mK)	***R*** (mΩ.cm)	***PF*** (mW/mK^2)	***ZT***
Lim *et. al* [32]	$Ca_{2.9}K_{0.1}Co_4O_9$	Sol–gel CIP 1173 K , 12 h	1050	174	1.1	8	-	0.19
Su *et. al* [33]	$Ca_{2.7}Bi_{0.3}Co_4O_9$	Solid state Self-ignition 1193 K, 20 h	973	189	19.5	0.64	-	0.27
Wang *et. al* [34]	$Ca_3Co_{3.9}Fe_{0.1}O_{9+\delta}$	Solid state Cold-high pressure 1173 K, 12 h	1000	257.3	9.7	1.77		0.39
Wang *et. al* [34]	$Ca_3Co_{3.9}Mn_{0.1}O_{9+\delta}$	Solid state Cold-high pressure 1173 K, 12 h	1000	240.5	1.79	14.8	-	0.22
Wang *et. al* [34]	$Ca_3Co_{3.9}Cu_{0.1}O_{9+\delta}$	Solid state Cold-high pressure 1173 K, 12 h	1000	174.9	1.68	7.76	-	0.24

Table 1.2 (cont'd) Thermoelectric properties of C-349 samples from the literature.

Author	Material	Synthesis Method	T (K)	S (μV/K)	κ (W/mK)	R (mΩ.cm)	PF (mW/mK^2)	ZT
Xu *et. al* [35]	$Ca_3Co_{3.7}Ti_{0.3}O_9$	Solid state Cold press 1173 K, O_2, 48 h	1000	280	1.8	16.7	-	0.3
Delorme *et. al* [36]	$(Ca_{0.995}Sr_{0.005})_3Co_4O_9$	Ball milling SPS 1123 K, 5 min, 70 MPa	1000	173	1.77	7.9	3.95	0.22
Liu *et. al* [37]	$Ca_{2.7}Y_{0.3}Co_4O_{9+\delta}$	Wet chemical SPS 973 K, 8 h	1073	172	1.5	8	3.75	0.22
Li *et. al* [38]	$Ca_{2.5}Bi_{0.5}Co_4O_{9+\delta}$	Solid state Cold press 1233 K , 12 h	973	160	1.14	9.5	-	0.2
Song *et. al* [39]	$(Ca_{0.95}Bi_{0.05})_3Co_4O_9$ / 0.1Ag	Solid state SPS 1023 K, 5 min, 50 MPa	1023	197	-	7	5.5	-

1.5 Thermoelectric Effect

The thermoelectric effect takes place when a temperature difference arises between the two ends of the material. Under condition that different temperature is applied to each side, a potential difference is created. This is known as the Seebeck effect. On the other hand, if voltage is applied to the ends of the sample, it creates the temperature gradient that is known as the Peltier effect. For the macroscopic point of view, for Seebeck coefficient, temperature gradient causes the charge carriers to diffuse from hot side to the cold side, the condition, which is similar to the classical expansion of the heated gas; hence, the thermally induced current.

There are numerous applications of Seebeck effect: electricity generation, temperature measurement, cooling or heating. Additional significant feature of thermoelectric mechanisms is their effective temperature control, with the voltage polarity as a defining factor of temperature heating or cooling. Therefore, thermoelectric mechanisms are successfully used as temperature controllers.

In general, the Seebeck effect can be understood as the means of converting temperature differences directly into electricity. As for the definition of the term, it is the development of an electromotive force (EMF) across a material, which takes place as a result of a temperature difference.

The equation below represents the Seebeck effect as the proportion of a voltage difference (ΔV) to the temperature difference between two ends of a material (ΔT).

$$S = \frac{\Delta V}{\Delta T} \tag{1.1}$$

The Seebeck coefficient S is known as “ α “ in other official sources, as well as thermopower in the physics context.

For the physical point of view, Seebeck effect can be explained as follow. In any thermoelectric material there exist free electrons or holes containing certain charge and heat, with gas-similar behavior in a thermoelectric semiconductor. To illustrate, molecule behavior under the above mentioned conditions, when uncharged gas placed in a box within a temperature gradient with two sides of opposite temperature (hot and cold) gas molecule behavior at both ends will differ crucially. Molecules at the hot end will move faster, thus diffusing further than the ones at the cold end resulting in a higher density of molecules here. The molecule distribution is shown in figure 1.7. The molecules will be attracted to diffuse back to the hot end. There will not be any homogeneous molecule buildup because of two effects, the effect of the density gradient and the effect of the temperature gradient, will work in opposition to each other. Under the condition that the molecules are charged, a repulsive electrostatic force (electric potential) will be created at the cold end in order for charges to migrate to the hot end. In this case temperature difference produces voltage, known as the Seebeck effect, while proportionality constant is defined as the Seebeck coefficient.

Depending on the type of the material (p-type or n-type) and whether the charge is positive or negative, the excess charge distribution will produce positive or negative potential on the cold side, respectively [5].

$$V = \int_{T_C}^{T_H} \left(S_B(T) - S_A(T)\right) dT \tag{1.2}$$

S_A is the Seebeck coefficient of the metal A, while S_B is the Seebeck coefficient of the metal B as functions of temperature. Also, T_H denotes the temperature of the hot side, while T_C denotes the temperature of the cold one. The primary conditions which the Seebeck coefficient is non-linear depend on are as follows: molecular structure, the conductors' absolute temperature and the material. Provided that Seebeck coefficients are constant for the measured temperature range, the following formula is derived.

$$V = (S_B - S_A).(T_H - T_C) \tag{1.3}$$

formula can be approximated.

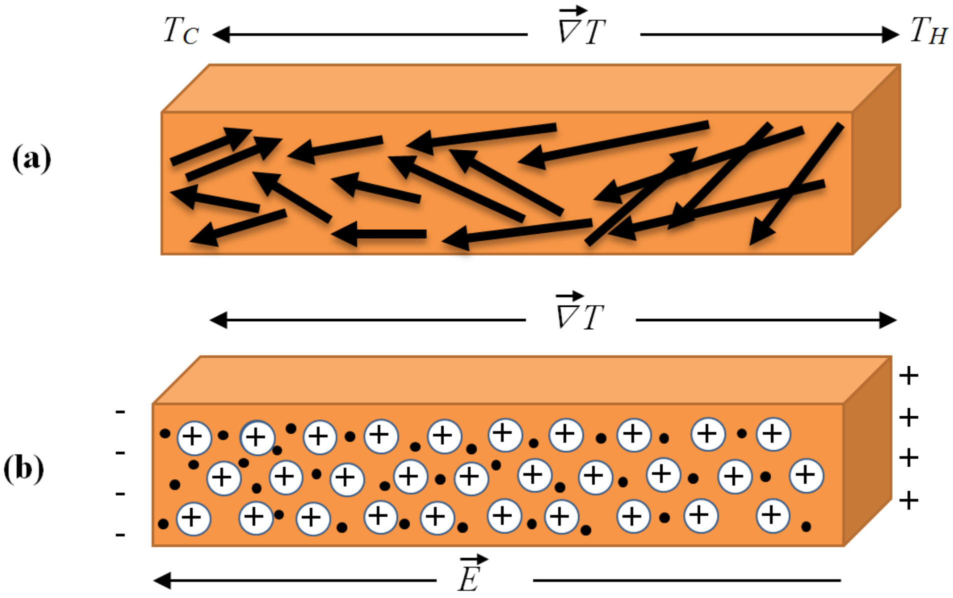

Figure 1.7 The Seebeck effect illustration [5]. (a) Electrons at hot side with higher energy move to the direction of the cold side; (b) Balance due to the creation of internal electric field, as a result of electrons moving from hot to cold side preventing further diffusion.

From physical perspective, the Seebeck coefficient is the heat carried by carriers per charge per temperature, or simply the entropy per carrier. In the present work, several expressions, which derived from some Seebeck coefficient units and parameters, will be introduced in more detail in the way they are introduced in literature.

The first important unit of the Seebeck coefficient is $\mu V/K$,

$$S \sim \frac{V}{K} \sim \frac{eV}{eK} \sim \frac{\text{Specific heat } (eV/K)}{\text{Carrier charge } (e)} \tag{1.4}$$

which corresponds to its physics expression, (1.4)

$$S \approx \frac{c_{el}}{e} = \frac{1}{e}\frac{C_{el}}{N} \tag{1.5}$$

where e is the electronic charge, c_{el} and C_{el} are the electronic heat capacity for one electron and the whole system, respectively, and N is the number of electrons in the system. The following is the electronic heat capacity [10], using the free electron model for metals and degenerated semiconductors;

$$C_{el} = \frac{\partial U_{el}}{\partial T} \tag{1.6}$$

with U_{el} as the total electronic thermal kinetic energy. In the classical electron gas model the Seebeck coefficient is about $\frac{k_B}{e} \approx$ 87 μV/K with $\frac{3}{2}k_B T$; as energy of each electron. In case of metals or degenerated semiconductors, $(N\frac{T}{T_F})$ (T_F is the Fermi temperature) [10] electrons are affected by the temperature and are conductive at temperature T because the only electrons that can be thermally excited and participate to the conduction are those with an energy $k_B T$ of the Fermi level. Consequently, the total electronic thermal kinetic energy equals

$$U_{el} \approx \left(N\frac{T}{T_F}\right) k_B T \tag{1.7}$$

If the equation above is substituted back to equation 1.6, the following is obtained;

$$C_{el} \approx N k_B \frac{T}{T_F} \tag{1.8}$$

It should be taken into account that the Fermi temperature and Fermi energy are related by equation (1.8)

$$E_F = k_B T_F \tag{1.9}$$

If the equations (1.8) and (1.9) above are united and substituted back to (1.5), the result is

$$S \approx \frac{1}{e}\frac{k_B^2}{E_F} = \frac{k_B}{e}\left(\frac{k_B T}{E_F}\right) \tag{1.10}$$

In the literature, the equation is usually recognized as the expression of Seebeck coefficient for metals [5]. According to equation 1.10, only the fraction of conductive electrons, which makes the Seebeck coefficient possible, is ($\frac{k_B T}{E_F}$).

It is also significant that Fermi energy and the effective mass m^* concentration n are interconnected as,

$$E_F = \frac{\hbar^2}{2m^*}(3\pi^2 n)^{\frac{2}{3}} \tag{1.11}$$

Additional important expression which is commonly used to degenerate semiconductors for Seebeck coefficient [40] can presented, (1.11)

$$S \approx \frac{2}{e}\frac{k_B^2}{\hbar} m^* T (3\pi^2 n)^{-\frac{2}{3}} \tag{1.12}$$

where n is the carrier density, $\hbar$ is the Planck constant, m^* is the effective mass and e is the electron charge. It can be derived from the equation 1.2 that the higher the Seebeck coefficient is the higher effective mass it requires together with the small carrier concentration. Seebeck coefficient and temperature interdependence may not be quite easy to define because other parameters are also related to temperature and depend on it. If non-degenerate semiconductors are dealt with, the primary condition upon which charged carriers become a part of the conduction process is then being excited across the band gap, E_g.

Accordingly, below is the expression, which represents the Seebeck coefficient for semiconducting material: [5],

$$S \approx \left(\frac{k_B}{e}\right)\frac{E_g}{k_B T} = \frac{E_g}{eT} \tag{1.13}$$

with ($\frac{k_B}{e}$) representing the Seebeck coefficient for a classical electron gas. The central parameter denoting the thermoelectric property of a material is the figure-of-merit *ZT*; it is also the characteristics of electrical and thermal transport properties of the material. It is described as

$$ZT = \frac{S^2\sigma}{\kappa} T \tag{1.14}$$

where S denotes the Seebeck efficient introduced before, σ is the electrical conductivity, κ represent thermal conductivity as the sum of lattice κ_L and electrical κ_L thermal conductivities, respectively. T is defined as absolute temperature. σ depends on both carrier concentration n and mobility μ as,

$$\sigma = ne\mu \tag{1.15}$$

The result of $S^2\sigma$ multiplication is commonly known as "thermoelectric power factor" or simply "power factor". It can be quite frequently seen in the literature and is the characteristics for the electrical transport properties. The equation 1.14 demonstrates that high figure of merit requires large power factor $S^2\sigma$. Nevertheless, as equations 1.15 and 1.12 further illustrate, while electrical conductivity rises, Seebeck coefficient decreases with carrier concentration. Also, as it is shown in figure 1.8, power factor gets to its maximum under the condition that the carrier concentration reaches its optimized value.

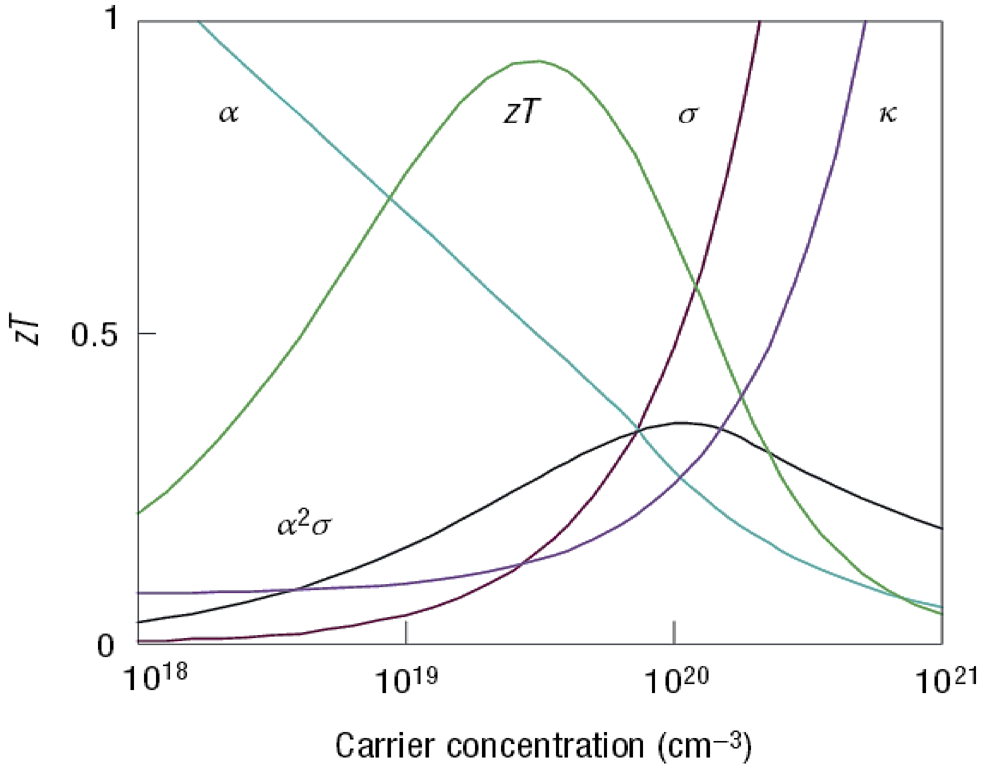

Figure 1.8 Illustration of the carrier concentration dependence of electrical conductivity, Seebeck coefficient α, thermal conductivity κ, power factor $\alpha^2\sigma$ and ZT [40].

The balance between Seebeck coefficient and electrical resistivity is understood is explained in the electronic density of states studies [8]. This study shows that, higher the Seebeck coefficient means higher the asymmetry of density of states (or differential electrical resistivity) is in respect of the Fermi level. Nevertheless, such asymmetry is reduced with increased amount of doping in the material because doping moves the Fermi level deeper into the band of 3D-crystal. In order to make the balance between Seebeck coefficient and electrical resistivity to find good thermoelectric materials, the semiconductor must have one dominant type of charge carriers (electrons or holes). Other than that, if the contribution to electrical conduction is coming from electrons (above the Fermi level) and holes (below the Fermi level) the asymmetry of differential conductivity is reduced and so is Seebeck coefficient.

The third most significant parameter for thermoelectric materials is thermal conductivity. The thermal conductivity is desired as low as necessary to enhance thermoelectric performance. It is well known fact that fundamentally, not only charge carriers (electrons or holes), but also phonons are responsible for thermal transport. The phonon contributions are lattice or phonon thermal conductivity κ_{ph} and carrier thermal conductivity carrier κ_c , respectively, which is written in the expression below,

$$\kappa = \kappa_{ph} + \kappa_c \tag{1.16}$$

where the electronic contribution κ_c is related to electrical conductivity via Lorentz factor L,

$$\kappa_c = L\sigma T = ne\mu LT \tag{1.17}$$

where L is basically taken as 2.48 x 10^{-8} J^2/K^2C^2 for metals and 2.0 x 10^{-8} J^2/K^2C^2 for degenerate semiconductors [5]. With equations 1.16 and 1.17, the thermal conductivity κ increases with carrier concentration n. According to equation 1.14, the possible highest thermoelectric figure of merit ZT is obtained as shown in figure 1.8. The result is achieved as the ratio of $S^2\sigma$ power factor over thermal conductivity κ is reduced with respect to the carrier concentration n. The carrier concentration is typically taken in the range of 10^{19} to 10^{21} carriers per cm^3 [40].

One of the most efficient approaches for high ZT value is the phonon thermal conductivity reduction because low electrical resistivity requires large carrier concentration, whereas low thermal conductivity requires reduced carrier concentration. The reduction in phonon thermal conductivity κ_{ph} (κ_l in figure 1.9) leads to the doubling of ZT. As illustrated in figure 1.9, the ZT optimized with a κ_{ph}

of 0.8 W/mK, shown as the point (1), increases up to point (2) as κ_{ph} decreases down to 0.2 W/mK. Moreover, minimizing the lattice thermal conductivity reoptimizes the carrier concentration n (reduced), results in smaller electronic thermal conductivity κ_c (κ_e in figure 1.9) and high Seebeck coefficient S. The figure of merit ZT is optimized to a higher value that is shown at point (3).

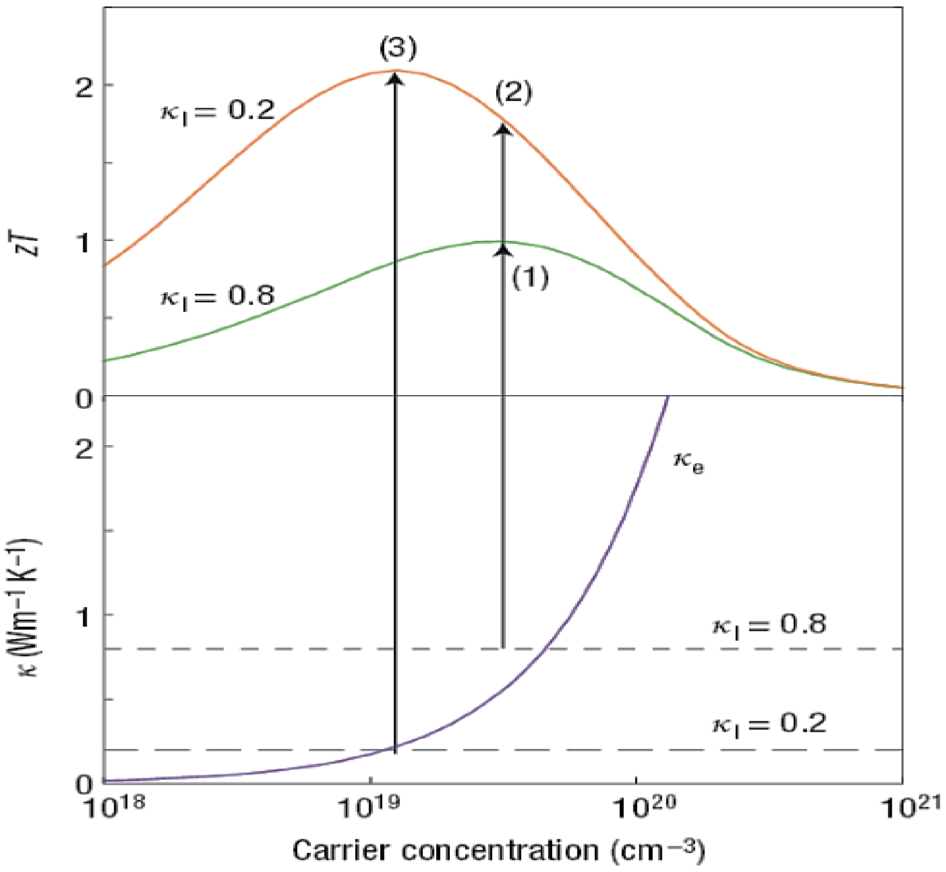

Figure 1.9 The thermoelectric figure of merit by reducing lattice thermal conductivity vs. carrier concentration [40].

Typically, thermoelectric module is basically composed of a pair of n- and p-type thermoelectric materials usually called thermoelectric couple as illustrated in figure 1.10. Thermoelectric applications are achieved by making these single or multiple modules. In the cooling mode, electrical field forces a current flowing through the thermoelectric couples. Because holes drift along the current flow direction, whereas electrons drift in the opposite direction, both holes and electrons are moving away from top side towards the base side, as shown in figure 1.11 (A). Recalling these charge carriers carry heat, electrons and holes are moving from the top size under cooling, the place where the heat sink is developed. Figure 1.11 (B) demonstrates the power generation mode of a thermoelectric module. In this mode, electrons and holes gain more energy at heat input side and therefore diffuse to the base side. Therefore, a flow of current is going through the thermoelectric couple to the base side where power output occurs. For vide range of applications and increasing the overall efficiency of thermoelectric systems a thermoelectric module is made in different geometric configuration, structure and the number of thermoelectric couples. Nevertheless, since this subject is not a part of this present dissertation, detailed information can be found in the literature [9, 41].

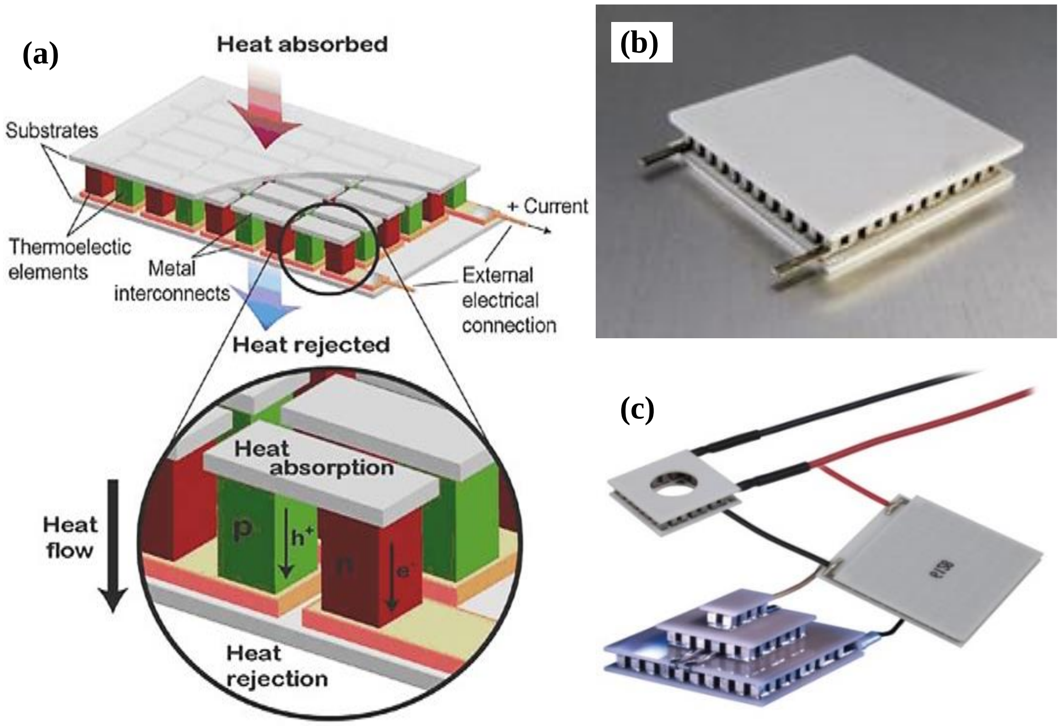

Figure 1.10 (a) The direction of charge flow for both cooling and power generation [40] of **(b)** a commercial thermoelectric module [42] and **(c)** specialized modules developed for various power generations and cooling applications [43].

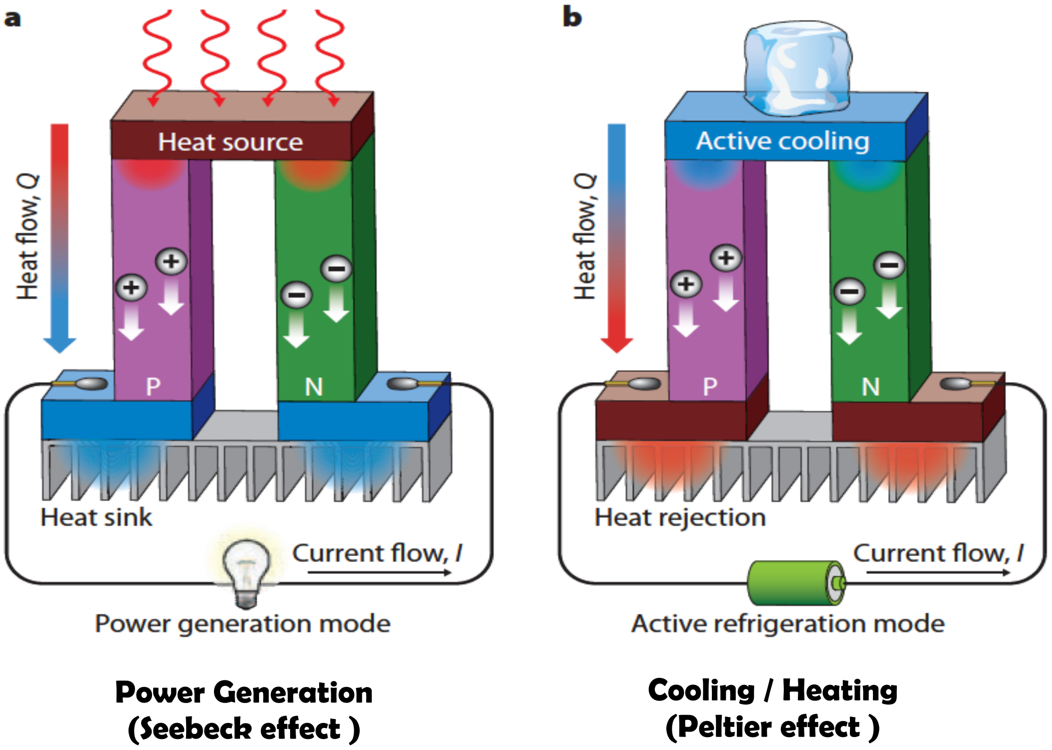

Power Generation (Seebeck effect)

Cooling / Heating (Peltier effect)

Figure 1.11 Schematic representation of power generation (A) and cooling (B) modes in a traditional thermoelectric module [41].

The idealized maximum energy conversion efficiency for power generation mode of a thermoelectric system is given by [44],

$$\eta = \frac{\Delta T}{T_h} \frac{\sqrt{1+ZT_h}-1}{\sqrt{1+ZT_h}+T_C/T_H} \qquad (1.18)$$

T_H is the temperature at which ZT is maximized. Therefore, $\Delta T/T_H$ basically corresponds to the Carnot efficiency which is the maximum efficiency of a heat engine operating between two temperatures. As it is shown in figure 1.12, with the input values of T_H = 1273 K and T_C = 500 K, equation 1.18 is calculated and plotted as a function of ZT. Materials with the energy conversion efficiency are about 12.3 %, where the corresponding ZT of around 1.0 is thought of possessing excellent thermoelectric properties. Important information coming from that equation 1.18 and figure 1.12 is that energy conversion efficiency monotonically increases with ZT.

This is the main point of thermoelectric research from the material science perspective. To conclude, maximizing of values is required for the higher performance of energy conversion.

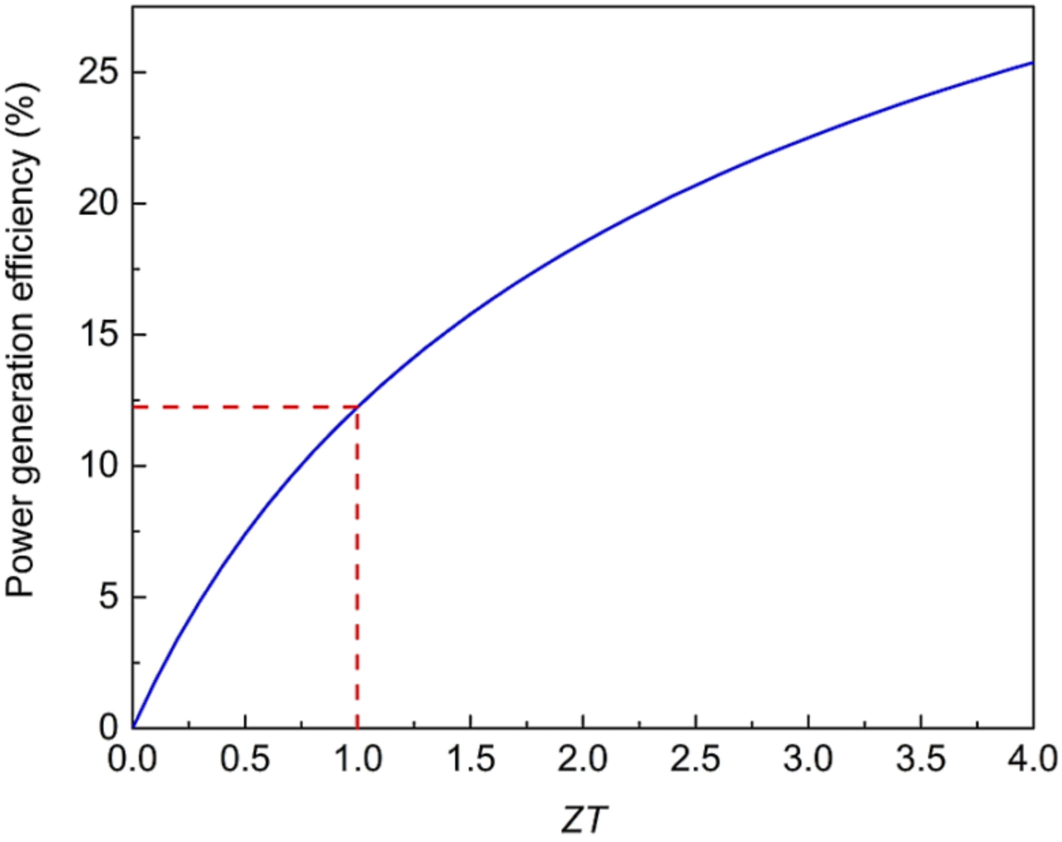

Figure 1.12 Plot of power generation efficiency as a function of *ZT*. (The energy conversion efficiency corresponding to *ZT* of 1.0 is indicated on the plot) [45].

REFERENCES

[1] D.M. Rowe, CRC Handbook of Thermoelectrics, ISBN: 0849322642 (2005) pp 1-2

[2] R. Funahashi, M. Mikami, S. Urata, M. Kitawaki, T. Kouuchi and K. Mizuno, High-throughput screening of thermoelectric oxides and power generation modules consisting of oxide unicouples, Meas. Sci. Technol. 16 (2005) pp 70-80

[3] J.H. Yang, T. Caillat, Thermoelectric materials for space and automotive power generation, MRS Bull. 3 (2006) pp 224-229

[4] N. A. S. A. , John H. Glenn Research Center, (2010), https://solarsystem.nasa.gov/rps/docs/MMRTGfactsFeb_2010.pdf [11.06.2014]

[5] T.M. Tritt, Thermoelectric Phenomena, Materials, and Applications, Annual Review of Materials Research, Editors: D.R. Clarke and P. Fratzl. 41 (2011) pp 433-448

[6] K. Holmberg, P. Andersson, A. Erdemir, Global energy consumption due to friction in passenger cars, Tribology International 47 (2012) pp 221-234

[7] A. Shakouri, Recent Developments in Semiconductor Thermoelectric Physics and Materials, Annual Review of Materials Research, Editors: D.R. Clarke and P. Fratzl. 41(2011) pp 399-431

[8] T.M. Tritt, H. Boettner, and L. Chen, Thermoelectrics: Direct solar thermal energy conversion. MRS Bull. 4 (2008) pp 366-368

[9] F. J. Di Salvo, *et al.* Thermoelectric Cooling and Power Generation, Science 285 (1999) pp 703

[10] C. Kittel, Introduction to Solid State Physics Wiley 8th ed. (2005)

[11] L. D. Zhao, V. P. Dravid and M. G. Kanatzidis, The panoscopic approach to high performance thermoelectrics, Energy Environ. Sci. 7 (2014) pp 251-268

[12] M. Ohtaki, Oxide thermoelectric materials for heat-to-electricity direct energy conversion, Micro Review, Faculty of Engineering Sciences, Kyushu University

[13] I. Terasaki, Y. Sasago, K. Uchinokura, Large thermoelectric power in $NaCo_2O_4$ single crystals Phys. Rev. B 56 (1997) pp 12685–12687

[14] H. Julian, Introduction to Thermoelectricity, Springer Series in Materials Science 121 (2009) pp 2

[15] K. Koumoto, Y. Wang, R. Zhang, A.o Kosuga, R. Funahashi, Oxide thermoelectric materials: A nanostructuring approach, Annu. Rev. Mater. Res. 40 (2010) pp 363–94

[16] K. Koumoto, I. Terasaki, R. Funahashi. Complex oxide materials for potential thermoelectric applications, MRS Bull. 31 (2006) pp 206-210

[17] L. Zhang, X. F. Tang, W. B. Gao, Formation and Growth Mechanism of Highly Tiled γ-$Na_xCo_2O_4$ Crystals by a Novel Sodium Alginate Gel Template Method, J. Phys. Chem. C 113 (2009) pp 7930-7934

[18] S. Lambert, H. Leligny, D. Grebille, Three Forms of the Misfit Layered Cobaltite $[Ca_2CoO_3]$ $[CoO_2]_{1.62}$·A 4D Structural Investigation, J. Solid State Chem. 160 (2001) pp 322–331

[19] R. Funahashi, I. Matsubara, H. Ikuta, T. Takeuchi, U. Mizutani, S. Sodeoka, Oxide single crystal with high thermoelectric performance in air, Jpn. J. Appl. Phys. Part 2 39 (2000) pp 1127-1129

[20] A. C. Masset, C. Michel, A. Maignan, M. Hervieu, O. Toulemonde, F. Studer, B. Raveau, J. Hejtmanek, Misfit-layered cobaltite with an anisotropic giant magnetoresistance: $Ca_3Co_4O_9$, J. Phys. Rev. B 62 (2000) pp 166-175

[21] T. Takeuchi, T. Kondo, K. Soda, U. Mizutani, R. Funahashi, M. Shikano, S. Tsuda, T. Yokoya, S. Shin, T. Muro, Electronic structure and large thermoelectric power in $Ca_3Co_4O_9$, J. Electron Spectrosc. Relat. Phenom. 137 (2004) pp 595-599

[22] S. Bhattacharya, S. Rayaprol, A. Singh, A. Dogra, C. Thinaharan, D. K. Aswa, S. K. Gupta, J. V. Yakhmi, R. N. Kulkarni, S. M. Yusuf, S. N. Bhatia, 085414, Low temperature thermopower and electrical transport in misfit $Ca_3Co_4O_9$ with elongated c-axis, J. Phys. D: Appl. Phys. 41 (2008) pp 085414-5

[23] Q. M. Lu, J. X. Zhang, Q.Y. Zhang, Y. Q. Liu and D. M. Liu, Improved Thermoelectric Properties of $Ca_{3-x}Ba_xCo_4O_9$ (x=0~0.4) Bulks by Sol-Gel and SPS Method, Thermoelectrics, ICT '06 25th International Conference, 66 (2006) pp 66-69

[24] D. Wang, L. Chen, Q. Yao, J. Li, High-temperature thermoelectric properties of $Ca_3Co_4O_{9+\delta}$ with Eu substitution, Solid State Commun. 129 (2004) pp 615–618

[25] D. Wang, L. Chen, Q. Yao, J. Li, Fabrication and thermoelectric properties of $Ca_{3-x}Dy_xCo_4O_{9+\delta}$ system, J. Alloy. Comp. 376 (2004) pp 58–61

[26] N.V. Nong, C. J. Liu, M. Ohtaki, Improvement on the high temperature thermoelectric performance of Ga-doped misfit-layered $Ca_3Co_{4-x}Ga_xO_{9+\delta}$ ($x = 0$, 0.05, 0.1, and 0.2), J. Alloy. Comp. 491 (2010) pp 53–56

[27] N. V. Nong, N. Pryds, S. Linderoth, M. Ohtaki, Enhancement of the Thermoelectric Performance of p-Type Layered Oxide $Ca_3Co_4O_{9+\delta}$ Through Heavy Doping and Metallic Nanoinclusions, Adv. Mater. 23 (2011) pp 2484–2490

[28] N. V. Nong, C. J. Liu, M. Ohtaki, High-temperature thermoelectric properties of late rare earth-doped $Ca_3Co_4O_{9+\delta}$, J. Alloy. Comp. 509 (2011) pp 977-981

[29] F. P. Zhang, Q. M. Lu, J. X. Zhang, Synthesis and high temperature thermoelectric properties of $Ba_xAg_yCa_{3-x-y}Co_4O_9$ compounds, J. Alloy. Comp. 484 (2009) pp 550–554

[30] Y. Liu, Y. Lin, L. Jiang, C. W. Nan, Z. Shen, Thermoelectric properties of Bi^{3+} substituted Co-based misfit-layered oxides, J. Electroceram. 21 (2008) pp 748-751.

[31] J. Pei, G. Chen, N. Zhou, D. Q. Lu, F. Xiao, High temperature transport and thermoelectric properties of $Ca_{3-x}Er_xCo_4O_{9+\delta}$, Physica B 406 (2011) pp 571–4

[32] C. H. Lim, S. M. Choi, W. S. Seo, High-temperature thermoelectric properties of the $Ca_{3-x}K_xCo_4O_9$ ($0 \leq x \leq 0.3$) system, J. Korean Phys. Soc. 57 (2010) pp 1054–8

[33] H. Su, Y. Jiang, X. Lan, X. Liu, H. Zhong, D. Yu, $Ca_{3-x}Bi_xCo_4O_9$ and $Ca_{1-y}Sm_yMnO_3$ thermoelectric materials and their power-generation devices, Phys. Status Solidi A 208 (2011) pp 147–55

[34] Y. Wang, Y. Sui, X. Wang, W. Su, X. Liu, Enhanced high temperature thermoelectric characteristics of transition metals doped $Ca_3Co_4O_{9+\delta}$ by cold high-pressure fabrication, J. Appl. Phys. 107 (2010) pp 033708-9

[35] L. Xu, F. Li, Y. Wang, High-temperature transport and thermoelectric properties of $Ca_3Co_{4-x}Ti_xO_9$, J. Alloys. Compd. 501 (2010) pp 115–9

[36] F. Delorme, C. F. Martin, P. Marudhachalam, D. O. Ovono, G. Guzman, Effect of Ca substitution by Sr on the thermoelectric properties of $Ca_3Co_4O_9$ ceramics, J. Alloys. Compd. 509 (2011) pp 2311–5

[37] H. Q. Liu, Y. Song, S. N. Zhang, X. B. Zhao, F.P. Wang, Thermoelectric properties of $Ca_{3-x}Y_xCo_4O_{9+\delta}$ ceramics, J. Phys. Chem. Solids 70 (2009) pp 600–3

[38] S. Li, R. Funahashi, I. Matsubara, K. Ueno, S. Sodeoka, H. Yamada, Synthesis and thermoelectric properties of the new oxide materials $Ca_{3-x}Bi_xCo_4O_{9+\delta}$ ($0.0<x<0.75$), Chem. Mater. 12 (2000) pp 2424–7

[39] Y. Song, Q. Sun, L. Zhao, F. Wang, Z. Jiang, Synthesis and thermoelectric power factor of $(Ca_{0.95}Bi_{0.05})_3Co_4O_9$/Ag composites, Mater. Chem. Phys. 113 (2009) pp 645–9

[40] G. J. Snyder, E. S. Toberer, Complex thermoelectric materials, Nature Materials 2 (2008) pp 105-114

[41] J. F. Li, W. S. Liu, L. D. Zhao, M. Zhou, High-performance nanostructured thermoelectric materials. NPG Asia Materials 2 (2010) pp152-158

[42] Development, production of TE modules, http://www.kryotherm.com/ [12.06.2014]

[43] Laird Technologies, http://www.lairdtech.com/ [12.06.2014]

[44] G. Homm, P. J. Klar, Thermoelectric materials - Compromising between high efficiency and materials abundance, Physica Status Solidi-Rapid Research Letters 5 (2011) pp 324-331

[45] X. Liang, Structure and Thermoelectric Properties of ZnO Based Materials, PhD Thesis, Harvard University, Massachusetts / USA, (2013) pp 8

CHAPTER 2

THE METHODS FOR ENHANCEMENT OF FIGURE OF MERIT (ZT)

This part focuses on the enhancement of thermoelectric oxides through nanostructure engineering, porosity and elemental substitution approach. Nanostructuring as an effective approach to break the link among Seebeck coefficient, resistivity and thermal conductivity is introduced. The degree of lowering the lattice thermal conductivity via nanostructuring is presented. Porosity contribution for further lowering the lattice thermal conductivity and thereby enhance the overall thermoelectric properties, is shown. Another way to improve the thermoelectric properties is elemental doping or substitution. C-349 based oxide thermoelectrics have a wide range of substitution choices in order for tuning the electrical and thermal transport properties as well as altering the structure. The effect of substitution to thermoelectric materials is also presented.

2.1 Nanostructuring Approach

During the last decade, the nanostructured materials have been attracted by scientists due to their novel mechanical, electrical, magnetic, catalysis and optical properties. These properties are highly distinct from that of the conventional bulk counterparts because of the quantum-size effects, small-size effects and large fraction of grain boundaries [1, 2].

The efficiency of thermoelectric materials is investigated by measuring three parameters; Seebeck coefficient, electrical resistivity as well as thermal conductivity. Good thermoelectric materials are considered as materials which have low electrical resistivity and low thermal conductivity. However, these two parameters; resistivity and thermal conductivity, are interconnected. That is, when the resistivity decreases, the thermal conductivity increases drastically due to the change in microstructure of the material. Therefore, it is highly attractive research to differentiate those parameters individually in order to enhance the efficiency of the thermoelectric materials for a crystalline system [2-5]. Nanostructuring could be a promising solution to break the bond between resistivity and thermal conductivity. Therefore, thermal conductivity could be lowered providing some new scattering mechanisms such as grain boundaries, superlattice structures and porosity to enhance the scattering of medium- and long-wavelength phonons while remaining electrical resistivity in the acceptable range [3-11]. Figure 2.1: (a–d) shows minimizing dimension: (a) bulk, (b) thin film, (c) nanowire, (d) atomic cluster. (e–h) show pure and mixture structures from micro to nano scale: (e) micro-grained bulks, (f) fine and coarse grains, (g) nano-grained bulks, (h) amorphous. (i–l) show composites: (i) normal composites, (j) nano-dispersions located inside grains / at grain boundaries, (k) nano-inclusions / nanodots, modification of boundary, (l) alloying / atomic doping, and vacancies. As it is demonstrated in the figure 2.1 (a - d), reduction in dimension could be a more attractive point to tune these thermoelectric variables individually [12]. As the size decreases and reaches to the nano-scale, more phonons could be scattered. In figure 2.1 (e-h), the structure of micro and nano-scale phases and their illustration is presented. Figure 2.1 (i-l) illustrates the composite structures including elemental doping and alloying. Elemental doping would contribute to creation of some defects to increase the phonon scattering regions.

In order to decrease thermal conductivity without causing increased electrical resistivity, the size of the particles should be smaller than the mean-free path of phonons and larger than the mean-free path of electrons or holes. This way thermal conductivity would be reduced by boundary scattering without affecting electrical transport properties [3, 13]. This idea has been applied to many materials such as bismuth antimony telluride [11], silicon germanium alloy [14] and yttria-stabilized zirconia [15] in order to reduce the thermal conductivity. Among other experimental studies, $SrTiO_3$ system could be given as an example for bulk oxides with nanometer-sized grains [16, 17]. Figure 2.2 demonstrates the grain size dependent phonon mean free path for micro and nano scale $SrTiO_3$ polycrystalline ceramics including bulk single crystal. It is clearly seen that as the grain size of the material decreases, the mean free path of phonons decreases drastically.

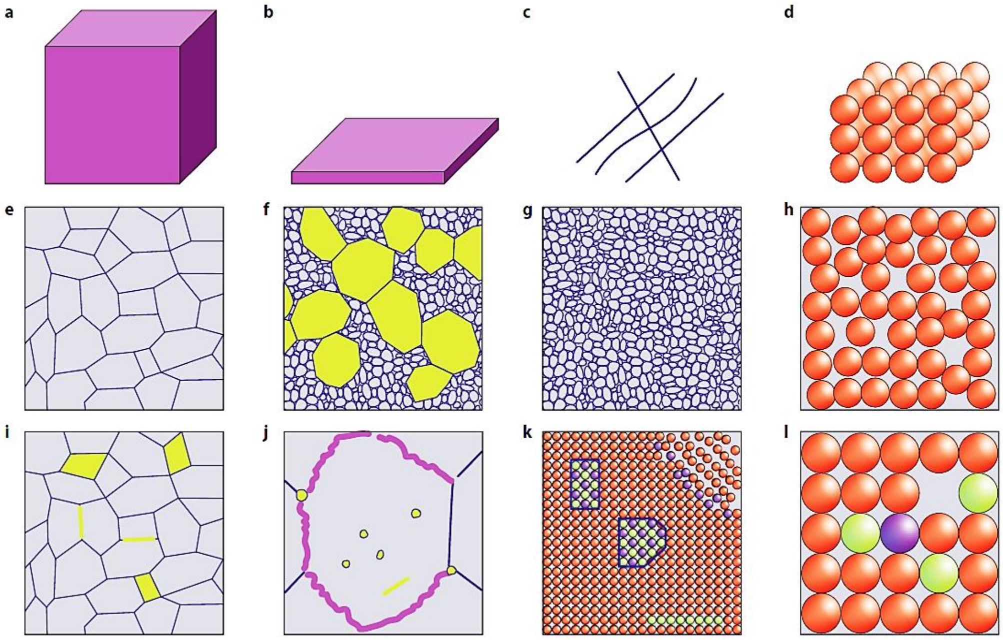

Figure 2.1 A list of thermoelectrics structures from macro- to nanoscale. [12].

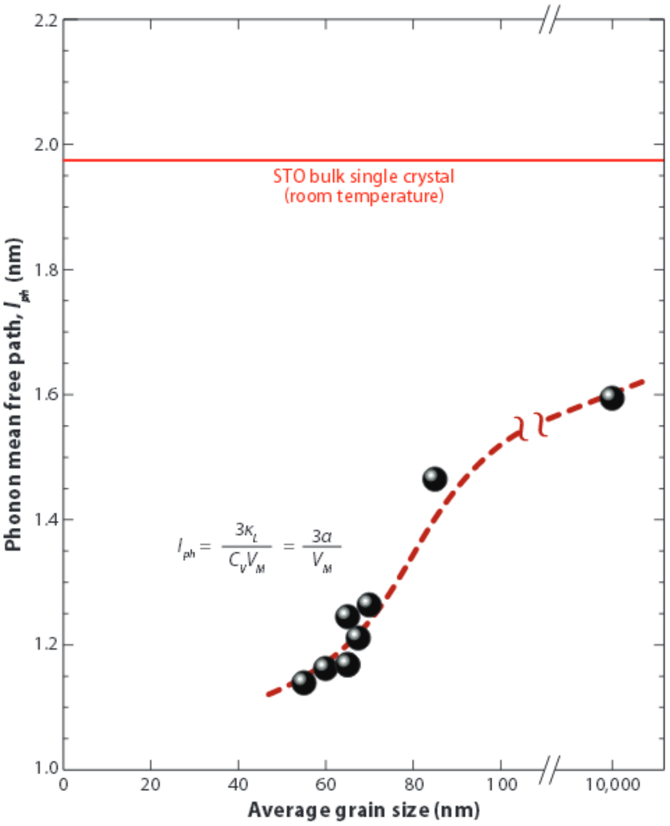

Figure 2.2 Phonon mean free path vs. grain size for micro and nano scale $SrTiO_3$ polycrystalline ceramics and bulk single crystal [10].

As it is also seen from the figure 2.3, significant reduction in thermal conductivity is observed when the grain size decreases from the micrometer to nanometer size. However, the grain size of 50 nm could not go down to the alloy limit due to the fact that length scale is larger than the mean free path of phonon [10]. Indeed, one of the major issues is grain growth that occurs generally during the application at high temperature. Therefore, the reduction of thermal conductivity by grain boundary scattering is compromised or even lost with time. To conclude, it is highly important to synthesize nano-sized particles the length scales of which are close to the unit cell to have coarsening-resistant nanostructures.

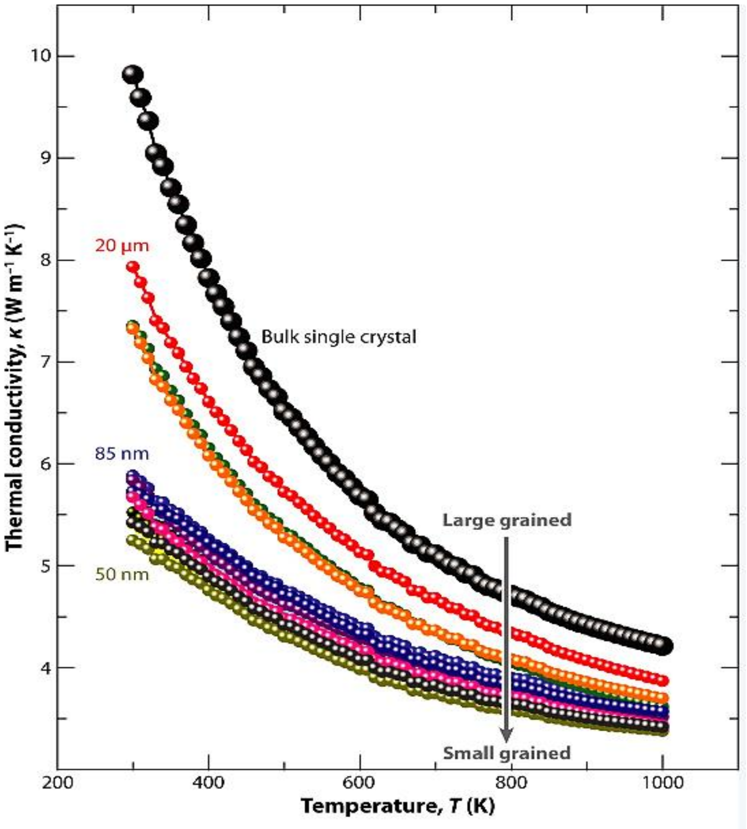

Figure 2.3 The temperature dependence of the thermal conductivity of micro and nano-scale $SrTiO_3$ polycrystalline ceramics and bulk single crystal [10].

2.2 Porosity Approach

There are a number of factors that must be taken into account regarding thermal transport properties. First of all, thermal contact among grains is affected by the quality of grain boundaries and the contact area throughout the bulk. This means that it might be due to the porosity within the bulk. Accordingly, porosity could reduce the thermal conductivity due to the presence of air in the pores that work as an insulator layer among the grains in the bulk sample. Generally, the presence of porosity is expected to decrease the conductivity of the system. The measure actually depends on the fraction of porosity. Various models have been proposed to calculate the effect such as mixture approaches.

Due to the porosity, there are more insulating interfaces. It is expected that in nanocrystalline C-349 porosity would additionally limit the mean free path of some of the phonon modes and thus, contribute to a further decrease in thermal conductivity [18]. The offered model by Litovsky *et. al*. [19] is valid in the whole range of porosity for a two-phase structure with a continuous solid phase and porosity. In this model, structure is considered to be a composite which consists of two phases. These phases are nanocrystalline grains and porosity. The lattice thermal conductivity can be determined by using the following derived model [19];

$$k = k_{solid}\ V_{solid}^{3/2} + k_{pore}\ V_{pore}^{1/4} \tag{2.1}$$

This equation, which is an interpolation formula, relates the effective thermal conductivity of the composite, k, to the thermal conductivities of its constituent solid k_{solid} and pore k_{pore} phases and their volume fractions, V_{solid} and V_{pore}.

Figure 2.4 shows a heterogeneous material in which the two components are distributed randomly, with neither phase being necessarily continuous or dispersed. These components can be considered as nanocrystalline and pore in our case. Either component may form continuous heat conduction pathways, depending on the relative amounts of the components, or therefore this structure is unbiased towards its components. The effective conductivity of this type of structure can therefore be calculated well by the Effective Medium Theory (EMT) equation given above (Eq. 2.1) [18].

Figure 2.5 shows the lattice thermal conductivity as a function of volume fraction of nanocrystalline zirconia is calculated based on a model [19]. In the figure, each sample is indicated with volume fraction and grain size. As it is clearly seen from the figure, lattice thermal conductivity decreases with increasing porosity because higher volume fraction means higher insulation area and greater phonon interface scattering at grain boundaries.

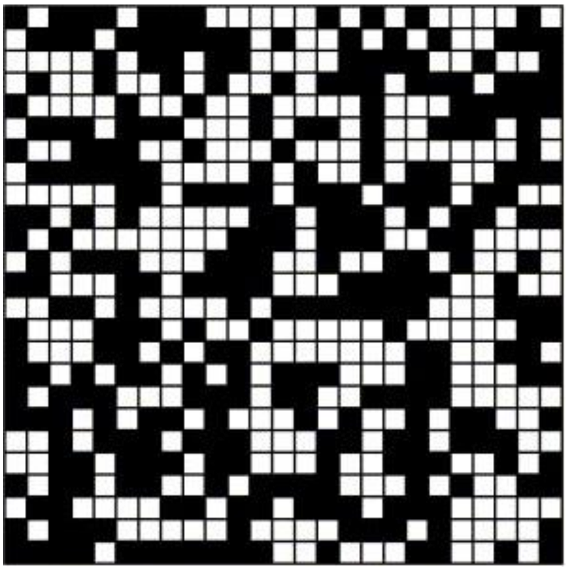

Figure 2.4 Schematic diagram of a material made up of a random dispersion of nanocrystalline and pore [18].

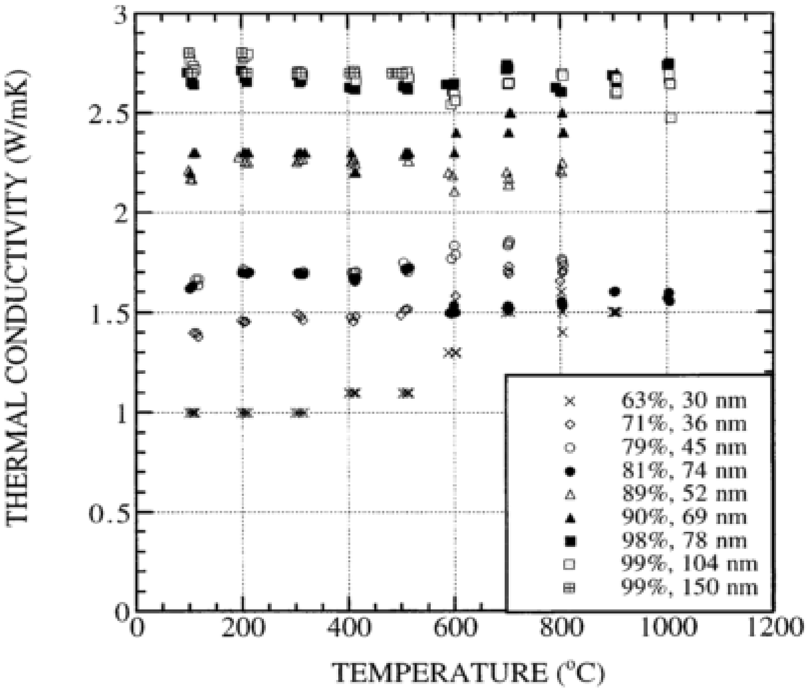

Figure 2.5 Lattice thermal conductivity vs volume fraction of nanocrystalline zirconia [19].

2.3 Grain-Size-Dependent Thermoelectric Properties Based on Theoretical Models

In this part, the grain size and porosity dependence of the power factor, lattice thermal conductivity, and ZT value of C-349 samples are explained based on the offered models. Basically, most simulations of these properties are obtained by deriving the Boltzmann transport equations to their compositions. The objective of this part is to explain our experimental results that are Seebeck coefficient, electrical resistivity and total thermal conductivity based on theoretical models with respect to the nanostructuring and porosity.

Recently, a theoretical study on phonons boundary scattering for amorphous materials indicates that micron and submicron grains could be highly beneficial in order to decrease the lattice thermal conductivity without much lowering the electron mobility [20]. Moreover, Zheng *et al.* [21] have developed another model showing that the bulk thermal conductivity is significantly reduced by decreasing the grain sizes when the grain diameter is less than 500 nm. Concerning the C-349 compound, Zhou *et al.* [22] have shown that the optimum power factor in $(Ca_{2.6}Bi_{0.4})Co_4O_9$ thin films is reached for 100 nm grains. R. Z. Zhang and K. Koumoto [23] theoretically investigated the thermoelectric (TE) performance of $SrTiO_3$ 3D superlattice ceramics (STO-3D) with gas grain boundaries (GBs). The grain size dependence of the power factor, lattice thermal conductivity, and figure of merit value are calculated by using Boltzmann transport equations. It is found that nanostructured STO ceramics with smaller grain size have larger ZT value. This is because the energy filtering effect and interfacial phonon scattering at GBs become stronger with decreasing grain size, resulting in lower lattice thermal conductivity.

The followings are the derived equations of the model:

$$\sigma_{total} = \frac{[(d_{GB}+d_{GI})^2 - d_{GI}^2]\sigma_{2DEG} + d_{GI}^2\sigma_{GI}}{(d_{GB}+d_{GI})^2} \tag{2.2}$$

$$S_{total} = \frac{[(d_{GB}+d_{GI})^2 - d_{GI}^2]\sigma_{2DEG}S_{2DEG} + d_{GI}^2\sigma_{GI}S_{GI}}{[(d_{GB}+d_{GI})^2 - d_{GI}^2]\sigma_{2DEG} + d_{GI}^2\sigma_{GI}} \tag{2.3}$$

where d_{GB}, d_{GI}, σ, and S are the GB thickness, grain size, electrical conductivity, and Seebeck coefficient, respectively. S_{2DEG} and σ_{2DEG} are experimentally investigated.

Boltzmann transport equations based on the relaxation time approximation is applied in order to obtain thermal conductivity equation;

$$\tau_e = \begin{cases} (1-p)\tau_e(E < E_{GB}) \\ \tau_e(E < E_{GB}) \end{cases}, \quad p = \frac{I}{d_{GI}} \tag{2.4}$$

where τ_e, p, E, E_{GB}, I, and d_{GI} are the carrier relaxation time, probability of an electron being scattered by the GB, electronic energy, GB potential barrier height, electronic mean free path and grain size, respectively. Another variable is the GB potential barrier height, E_{GB}. Electrons with energy less than E_{GB} cannot transport across the GB potential barrier, which is well known as the *energy filtering effect*. Equation 2.4 indicates that electrons with energy higher than E_{GB} will not be scattered by GBs, while electrons with energy lower than E_{GB} have a probability p of being scattered by GBs, which is determined by the ratio of carrier mean free path to grain size. According to the model given above, as the grain size increases and becomes much larger than the carrier mean free path, not all the electrons can be scattered by the GB. Therefore, higher power factor must be observed as it is seen from the figure 2.6 (a). This trend can be attributed to two reasons. First of all, the contribution of the GI to the power factor of STO-3D becomes larger with increasing grain size according to eqs. 2.2 and 2.3. Due to the quantum confinement effect at GBs, the power factor of GBs is much larger than that of the GI. Therefore, as the grain size increases, the volume ratio of the GI increases, resulting in a decreasing power factor. Even increasing the volume ratio of GB by increasing the GB thickness is not effective. This is because when the GB thickness increases, the quantum confinement effect becomes weaker. Therefore, STO-3D with one-unit-cell GBs and the smallest grain size has the largest power factor. Secondly, the distance between GB potential barriers becomes larger with increasing grain size. This means that fewer electrons are filtered by the GB potential barrier, resulting in a weaker energy filtering effect and hence a lower power factor. In other words, the energy filtering effect in ceramics with larger grain size is not as effective as that in ceramics with smaller grains. According to these simulation results, it is concluded that for the power factor to be clearly increased to be more than 10 %, grain size should be smaller than 15 nm, which corresponds to a distance five times larger than the electronic mean free path for STO [23].

The lattice thermal conductivity can be determined by using the following equation [24]

$$\kappa_{ph} = \frac{\kappa_0}{1+\frac{\kappa_0 R}{d_{GI}}} \tag{2.5}$$

where κ_{ph} and d_{GI} are the phonon thermal conductivity and the grain size of STO-3D, respectively. κ_0 is the lattice thermal conductivity of bulk single crystal, and R is the interfacial thermal resistance that are obtained experimentally. Figure 2.6 (b) shows the calculated lattice thermal conductivity κ_{ph} of STO-3D as a function of grain size using equation 2.5. The obtained lattice thermal conductivity of STO-3D is much smaller than that of single crystal [25]. This is because the interface phonon scattering effect occurring at GBs that reduces the phonon and lattice mean free path.

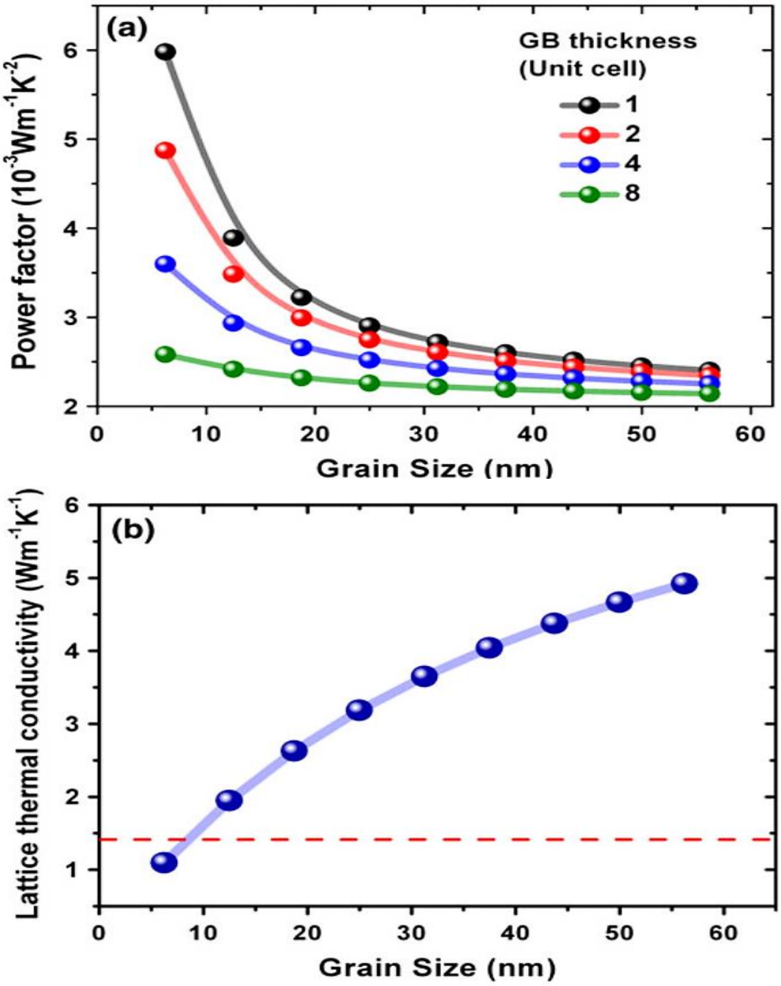

Figure 2.6 (a) Power factor, **(b)** lattice thermal conductivity as a function of grain size [23].

2.4 Elemental Substitution Approach

Substitution could be a way for decreasing thermal conductivity by introducing the increase amount of optical phonon modes. Similarly, structures with weakly bound or out-of-site atoms can create rattling modes, which interfere with the heat conduction. The approach is so called '*phonon glass-electronic crystals*' (PGEC) in which it is proposed that crystal structures containing weakly bound atoms or molecules that "rattle" within an atomic cage that produce low frequency anharmonic modes that strongly scatter the heat carrying acoustic modes of the material. Therefore, crystal-like electricity conduction; however, glass-like heat conduction could be achieved [26]. The PGEC material has an open semiconducting or semi-metallic framework (electron crystal) containing loosely bound guest atoms (phonon glass). Substitution with large atoms could be helpful in order to decrease the magnitude of thermal conductivity without reducing electrical conductivity to improve the thermoelectric performance of materials [27].

Partial substitution of heavier elements for constituent elements generally results in a reduction of κ_{ph} due to reduction of phonon group velocity enhancement in umklapp scattering of phonons [28] and scattering probability enhancement [29,30]. Nevertheless, the introduced disordering by such element substitution mostly leads to an increase in electrical resistivity. Therefore, the selection of the substitution element is highly significant in order to gain a large enhancement in dimensionless figure of merit [31].

Another way to enhance the *ZT* is actually increasing the Seebeck coefficient using a substituting element. Many recent works suggested that the spin entropy plays a highly significant role in enhancing the Seebeck coefficient [32–35]. Particularly, Wang *et al.* [36] discovered a suppression of the Seebeck coefficient under a longitudinal magnetic field in $NaCo_2O_4$ metal oxide thermoelectric material at low temperatures. In his research, it is investigated that the spin entropy is the main source for the observed high Seebeck coefficient. Indeed, G. Tang *et al.* [37] provided an evidence for significant spin entropy contribution to Seebeck coefficient as a function of temperature for cobalt oxides.

2.5 Conclusion

In this chapter, several *ZT* enhancing paths, like nanostructuring, providing porosity and elemental substitution are introduced. Structural modifications can lead not only to the decrease of thermal conductivity, but also to the enhance power factor at the same time. In order to reach this goal, an attempt to introduce nano-grained bulk materials with porosity contribution for reducing phonon contribution to total thermal conductivity by phonon-scattering at grain boundaries and interfaces leading to reduction in thermal conductivity without severely degrading electrical conductivity or suppressing Seebeck coefficient could be highly efficient. Because the thermal conductivity of a thermoelectric material can be decreased by increasing boundary scattering, thermoelectric device is expected to maintain a large temperature difference across its two sides leading to an improvement in its performance. On the other hand, Seebeck coefficient and electrical resistivity could be enhanced via elemental substitution to Ca-site of C-349 thermoelectric materials. The most effective way could be Ca-site substitution because the Ca-site is mainly used to change the charge carrier concentration or mobility. Therefore, elemental substitution to this site may lead to a great change in electrical conductivity. Also, the spin-entropy contribution to the Seebeck coefficient is related with the spin-entropy current and the population of free spins, which depends largely on the Co^{4+} concentration and the degeneracy of the Co ions.

REFERENCES

[1] H. Zeng, Y. Wu, J. Zhang, C. Kuang, M. Yue, S. Zhou, Grain size-dependent electrical resistivity of bulk nanocrystalline Gd metals, Prog. Nat. Sci.: Mater. Int. 23 (2013) pp 18-22

[2] G. S. Nolas, J. W. Sharp, H. J. Goldsmid, Thermoelectrics: Basic principles and new materials developments (2001) Berlin / Heidelberg: Springer

[3] G. Chen, M. Y. Tang, R. G. Yang, H. Lee, D. Z. Wang, Z. F. Ren, J. P. Fleurial, P. Gogna, New directions for low-dimensional thermoelectric materials. Adv. Mater. 19 (2007) pp 1043-1053

[4] A. J. Minnich, M. S. Dresselhaus, Z. F. Ren, G. Chen, Bulk nanostructured thermoelectric materials: current research and future prospects, Energ. Environ. Sci. 5 (2009) pp 466-479

[5] M.G. Kanatzidis, Nanostructured Thermoelectrics: The new paradigm? Chem. Mater. 22 (2009) pp 648-659

[6] S. K. Bux, R. G. Blair, P. K. Gogna, H. Lee, G. Chen, M. S. Dresselhaus, R. B. Kaner, J. P. Fleurial, Nanostructured bulk silicon as an effective thermoelectric material. Adv. Func. Mater. (15) 2009 pp 2445-2452

[7] J. F. Li, W. S. Liu, L. D. Zhao and M. Zhou, High-performance nanostructured thermoelectric materials, NPG Asia Mater. 4 (2010) pp 152–158

[8] D. Li, Y. Wu, R. Fan, P. Yang, A. Majumdar, Thermal conductivity of Si/SiGe superlattice nanowires, Appl. Phys. Lett. 83 (2003) pp 3186-3188

[9] Y. Lan, A. J. Minnich, G. Chen, Z. Ren, Enhancement of thermoelectric figure-of-merit by a bulk nanostructuring approach. Adv. Funct. Mater. 20 (2010) pp 357-376

[10] K. Koumoto, Y. Wang, R. Zhang, A. Kosuga, R. Funahashi, Oxide thermoelectric materials: A nanostructuring approach. Ann. Rev. Maters. Res. 40 (2010) pp 363-394

[11] B. Poudel, Q. Hao, Y. Ma, Y. Lan, A. Minnich, B. Yu, Z. Ren, High-thermoelectric performance of nanostructured bismuth antimony telluride bulk alloys, Science 320 (2008) pp 634-638

[12] J. F. Li, W. S. Liu, L. D. Zhao, M. Zhou, High-performance nanostructured thermoelectric materials. NPG Asia Mater. 4 (2010) pp 152-158

[13] A. Shakouri, Recent developments in semiconductor thermoelectric physics and materials, in Ann. Rev. Mater. Res. 41 (2011) pp 399-431

[14] D.M. Rowe, V. S. Shukla, N. Savvides, Phonon scattering at grain boundaries in heavily doped finegrained silicon-germanium alloys, Nature 290 (1981) pp 765–66

[15] A.M. Limarga, D.R. Clarke, The grain size and temperature dependence of the thermal conductivity of polycrystalline, tetragonal yttria-stabilized zirconia, Appl. Phys. Lett. 98 (2011) pp 211906-3

[16] S. Ohta, T. Nomura, H. Ohta, K. Koumoto, High-temperature carrier transport and thermoelectric properties of heavily La-or Nb-doped $SrTiO_3$ single crystals, J. Appl.Phys. 97 (2005) pp 034106

[17] T. Okuda, K. Nakanishi, S. Miyasaka, Y. Tokura, Large thermoelectric response of metallic perovskites: $Sr_{1-x}La_xTiO_3$ ($0 <= x <= 0.1$). Phys. Rev. B, 63 (2001)

[18] S. Raghavan, H. Wang, R.B. Dinwiddie, W.D. Porter, M.J. Mayo, The effect of grain size, porosity and yttria content on the thermal conductivity of nanocrystalline zirconia, Scr. Mater. 39 (1998) pp 1119–1125

[19] E. Ya. Litovsky, M. Shapiro, Gas pressure and temperature dependences of thermal conductivity of porous ceramic materials: Part 1, Refractories and ceramics with porosity below 30%, J. Am. Ceram. Soc. 75 (1990) pp 3425

[20] T. M. Tritt, B. Zhang, N. Gothard, J. He, X. Ji, D. Thompson and J. Kolis, New directions in bulk thermoelectric materials research: synthesis of nanoscale precursors for “bulk-composite” thermoelectric materials, MRS Proceedings, 886 (2005) doi: http://dx.doi.org/10.1557/PROC-0886-F02-01

[21] X. J. Zheng, L. Zhu, Y. H. Zhou, Q. Zhang, Impact of grain sizes on phonon thermal conductivity of bulk thermoelectric materials, Appl. Phys. Lett. 87 (2005) pp 242101-3

[22] Y. Zhou, I. Matsubara, W. Shin, N. Izu, and N. Murayama. Effect of grain size on electric resistivity and thermopower of $(Ca_{2.6}Bi_{0.4})Co_4O_9$ thin films, J. Appl. Phys. 95 (2004) pp 625-628

[23] R. Z. Zhang and K. Koumoto , Grain-size-dependent thermoelectric properties of $SrTiO_3$ 3D superlattice ceramics, J. Electron. Mater. 42 (2013)

[24] M.S. Toprak, C. Stiewe, D. Platzek, S. Williams, L. Bertini, E.C.Muller, C.Gatti, Y.Zhang, M.Rowe, and M.Muhammed, Adv. Funct. Mater. 14 (2004) pp 1189

[25] H. Muta, K. Kurosaki, and S. Yamanaka, Thermoelectric properties of reduced and La-doped single-crystalline $SrTiO_3$, J. Alloy. Compd. 392 (2005) pp 306

[26] M.A. Hayward, R. J. Cava, The effect of elemental substitution on the electronic properties of Ru_2Ge_3, J. Phys.: Condens. Matter 14 (2002) pp 6543–6552

[27] J.W. Fergus, Oxide materials for high temperature thermoelectric energy conversion, J. Eur. Ceram. Soc. 32 (2012) pp 525–540

[28] T. Takeuchi, N. Nagasako, R. Asahi, and U. Mizutani, Extremely small thermal conductivity of the Al-based Mackay-type 1/1-cubic approximants, Phys. Rev. B 74 (2006) pp 054206

[29] Y. Nishino, S. Deguchi, and U. Mizutani, Thermal and transport properties of the Heusler-type $Fe_2VA_{l1-x}Ge_x$ $(0 \leq x \leq 0.20)$ alloys: Effect of doping on lattice thermal conductivity, electrical resistivity and Seebeck coefficient, Phys. Rev. B 74 (2006) pp 115115

[30] P.G. Klemens, The Scattering of Low-Frequency Lattice Waves by Static Imperfections, Proc. Phys. Soc. Lond. A 68 (1955) pp 1113

[31] Y. Terazawa, M. Mikami, T. Itoh and S. Takeuchi, Effects of heavy element substitution on electronic structure and lattice thermal conductivity of Fe_2VAI thermoelectric material, J. Electron. Mater. 41 (2012) pp 1348-1353

[32] P. Limelette, S. He´ bert, V. Hardy, R. Fre´ sard, Ch. Simon, A. Maignan, Scaling Behavior in Thermoelectric Misfit Cobalt Oxides, Phys. Rev. Lett. 97 (2006) pp 046601

[33] C.J. Liu, P.K. Nayak, G.V.M. Williams, Magnetothermopower and magnetoresistivity of $RuSr_2Gd_{2-x}Ce_xCu_2O_{10+\delta}$ (x= 0.6, 1.0) Appl. Phys. Lett. 91 (2007) pp 123110

[34] G.D. Tang, X.N. Xu, C.P. Tang, Z.H Wang, Y. He, L. Qiu, L.Y. Lv, L. Xing, Y.W. Du, The spin-entropy enhancement induced by Ce doping in $Ca_3Co_4O_{9+\delta}$, Europhysics Lett. 91 (2010) pp 17002

[35] G.D. Tang, T. Yang, X.N. Xu, C.P. Tang, L. Qiu, Z.D. Zhang, L.Y. Lv, Z.H. Wang, Y.W. Du, Enhancement of the spin entropy in $Na_xCo_2O_4$ by Ni doping, Appl. Phys. Lett. 97 (2010) pp 032108

[36] Y. Wang, S. Nyrissa, R. J. Rogado, R.J. Cava, N.P. Ong, Spin entropy as the likely source of enhanced thermopower in $Na_xCo_2O_4$, Nature 423 pp (2003) 425

[37] G. Tang, F. Xu, D. Zhang, Z. Wang, Improving the spin entropy by suppressing Co^{4+} concentration in thermoelectric $Ca_3Co_4O_{9+\delta}$, Ceram. Int. 39 (2013) pp 1341–1344

CHAPTER 3

EXPERIMENTAL PROCEDURES

In this chapter, chemical synthesis of oxide powders and sintering of solid pellet samples will be described in detail. This will be followed by the structural characterization methods and techniques which are employed in this Ph.D. research study, including differential thermal analysis (DTA), thermal gravimetric analysis (TG) X-ray diffraction (XRD), true density measurements, BET analysis, particle size analysis, field emission scanning electron microscopy (FE-SEM) with Energy-dispersive X-ray Spectrometer (EDS), and X-ray photoemission spectroscopy (XPS). In order to obtain the figure of merit, the measurements of Seebeck coefficient, electrical resistivity and thermal conductivity as a function of temperature are necessary. For this reason thermal conductivity measurements will be also described in detail in this chapter. The detailed description of Seebeck coefficient and resistivity measurements are provided in chapter 4.

3.1 Chemical Synthesis of C-349 Oxide Powders

As a start, stoichiometric mixtures of high-purity commercial nitrate salts having the chemical formula $Ca(NO_3)_2.4H_2O$ and $Co(NO_3)_2.6H_2O$ are dissolved in an aqueous solution of citric acid in the range of 0.01 molar ratio and stirred uniformly. The stages of the synthesis are illustrated in figure 3.1. A few organic fuels are added into the following mixed solutions; PEG 400 and citric acid. These chemicals are used as a dispersant and a complexion agent in the nitrate solution during the formation of sol precursor and eventually converted the mixed solution liquid into gel in which different species of ions are kept to the designated ratios. Indeed, strong aggregation of the particles is supposed to be prevented in the colloidal solution by this way. The resulting solution is heated up and held at 353 K with continuous stirring. During this process, reflux is applied for 2 h in order to prevent evaporation before the completion of the dissolution. After that, the reflux is removed in order to obtain the gel. Then, the gel of violet color is dried initially in the low temperature drying furnace at 393 K for 12 h. The dried gel is crushed and ground into small particles using agate mortar or ball. It is further calcined in air at a ramp rate of 10 °C/min in a programmable box furnace (Protherm) for 2 h at temperature of 823 K, for residual carbon and organic compounds to be removed and self-assisted chemical reactions occur. As a result, pure C-349 phase powder is formed. This wet chemistry technique is applied in order to provide uniform mixture of added dissimilar ions in the atomic or molecular level. Moreover, this method provides a good adjustment of chemical composition. Table 3.1 provides the properties of chemicals used in synthesis procedures.

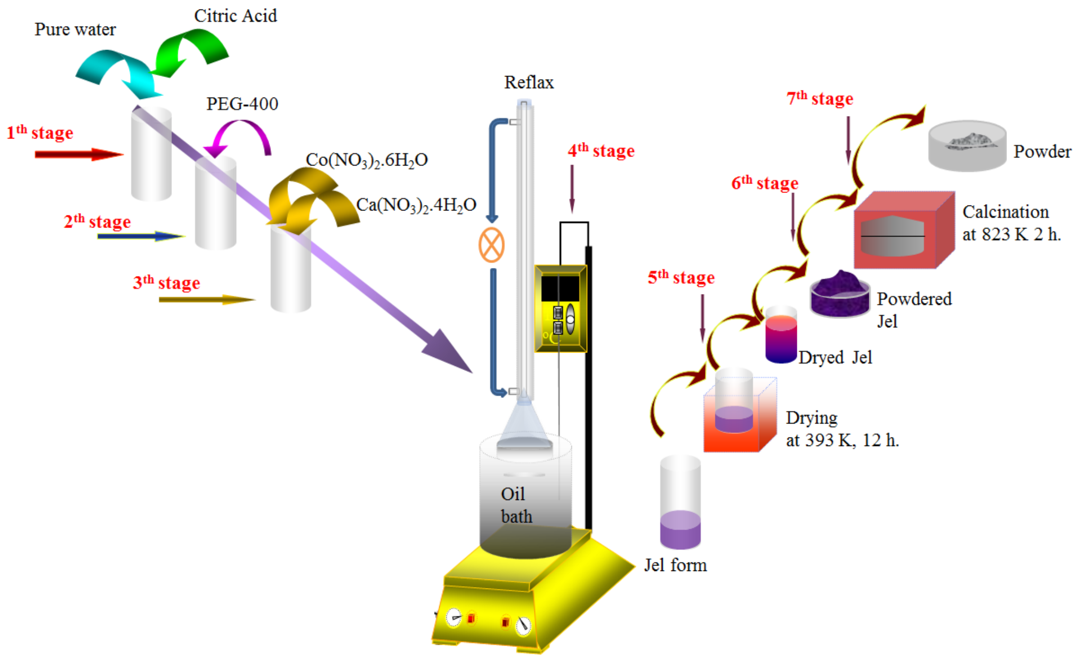

Figure 3.1 Synthesis stages of C-349 metal oxide powders.

Table 3.1 Description of chemicals used in synthesis procedure.

	Calcium Nitrate	**Cobalt Nitrate**	**Citric Acid**	**PEG-400**	**Pure Water**
Chemical Formula	$Ca(NO_3)_2.4H_2O$	$Co(NO_3)_2.6H_2O$	$C_6H_8O_7.H_2O$	$HO(C_2H_4O)_nH$	H_2O
Molecular Weight (g/mole)	236.15	291.03	210.14	-	18

3.2 Sintering Treatments

Finally, synthesized powder is grinded in agate mortar and this fine powder is cold pressed into a pellet of 16 x 20 x 20 mm size and then conventional annealing is applied at 1123 K for 2 h again to obtain pure C-349 phase. The sintering and compressing parameters are illustrated in figure 3.2. The applied pressure is 120 MPa for 10 min following 60 MPa for 5 min. As a result, the materials have been consolidated into bulk pellets by cold compaction and sintering. This pellet is cut into a disk in 15.84 mm radius for thermal conductivity measurements. In order to carry out Seebeck coefficient and electrical resistivity measurements, the pellet is again cut into a bar in 3 x 3 x 12 mm size in order to specify the heat flow direction and to make thermoelectric measurements to be in the same direction.

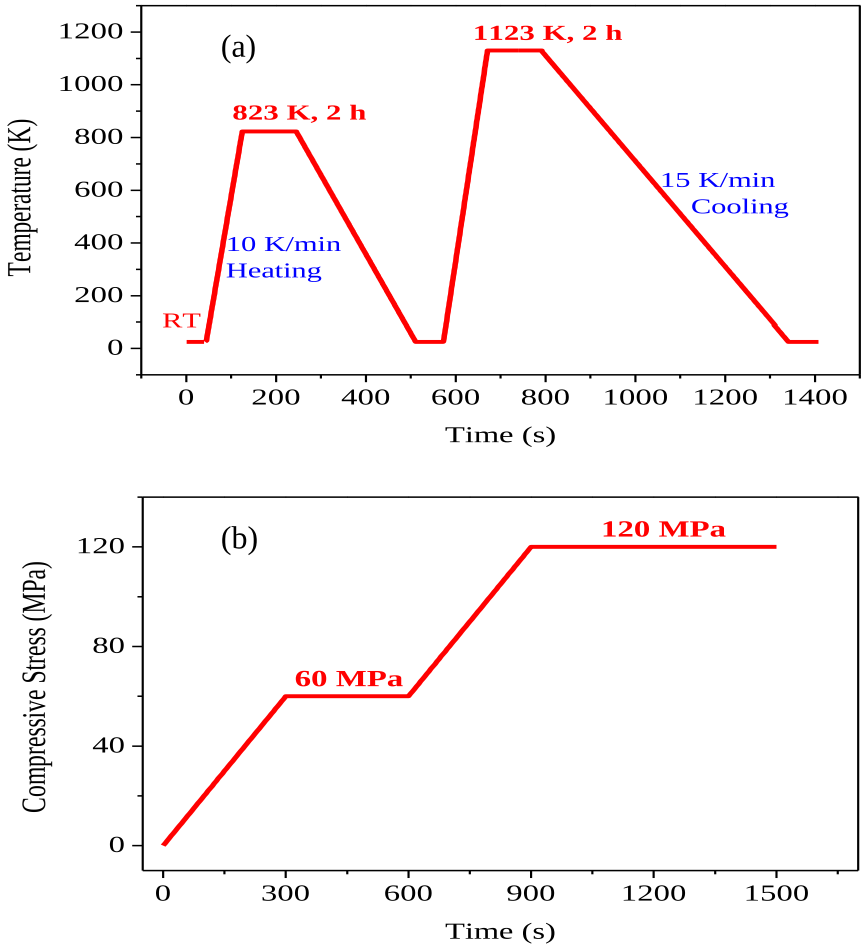

Figure 3.2 Illustration of **(a)** sintering and **(b)** pressure profiles.

Whereas the holding parameter is kept the same for all the sample preparation procedures, the sintering parameters such as target temperature are changed up to the different material that is going to be produced. Table 3.2 provides the general steps and properties for synthesis of C-349 samples. Also, figure 3.3 shows pictures of furnace, oven and ball mill that are used during the synthesis processes in our laboratory.

Table 3.2 General description of the synthesis procedures step by step.

	Ca-Nitrate Solution	**Co-Nitrate Solution**	**PEG-400**	**Citric Acid**
Mixing Proportion	15 ml.	20 ml.	% 1 - % 10 of total volume	2 % of total volume
Synthesis	6 – 8 h at 353 K on hot plate			
Drying	12 h at 393 K in furnace			
Calcination	1 – 2 h at 823 K in oven			
Sintering	2 h at 1023 K / 1123 K in oven			
Grinding	1 – 6 h in agate mortar / 10 – 30 min 300 cycle in ball mill			
Pellet Feature	16 x 20 x 20 mm size 120 MPa for 10 min 60 MPa for 5 min			
Measurement sample	3 x 3 x 12 mm rectangular in shape			

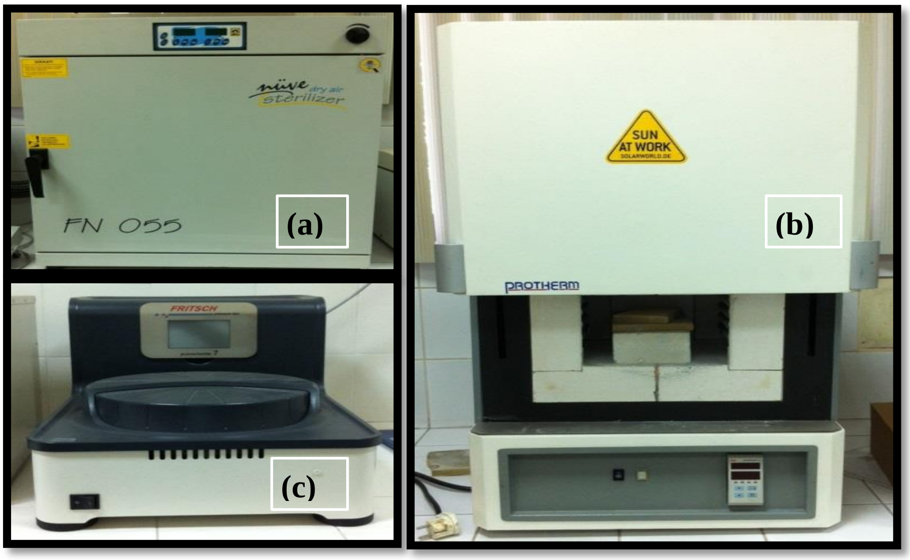

Figure 3.3 Pictures of **(a)** furnace, **(b)** oven and **(c)** ball mil.

3.3 Structural Characterization

In order to reach pure phase for C-349 materials, the annealing temperature is selected based on the Setaram Labsys TG-DTA differential thermal analyzer at METU Central Laboratory. These measurements are done under room temperature to 1100 K in the air.

X-ray diffraction analysis is performed using Rigaku Ultima-IV powder diffractometer. X-ray diffractograms are recorded at room temperature using CuKα radiation source in order to get information about the structure and phase composition. The phases are analyzed and identified using Rigaku Qual Analysis software including ICDD PDF database [1] at METU METE X-ray Laboratory.

Gravimetric method of porosity measurement is used to determine the density of the specimens. True density of the samples is investigated by Quantachrome Ultrapycnometer 1000 Helium Pycnometer based on Archimedes' principle and Boyle law with the error less than 0.03 % at METU Central Laboratory.

Surface area and pore size distribution characterizations or so called BET analysis, is carried out using Quantachrome Corporation Autosorb-6 under nitrogen gas atmosphere at METU Central Laboratory.

Malvern Mastersizer 2000 following the Mie scattering principles is used for particle size analysis. The measurements are obtained after sonicating for at least three hours prior to analysis and results are compared and acquired via different methods at METU Central Laboratory.

Quanta 400F field emission scanning electron microscope system attached to a JXA-8230 detector is used for micro and nano structural analysis at METU METE SEM Laboratory. Microstructures of sintered oxide pellets are examined under Field Emission. The cross-sections of samples are prepared and ground and polished down to 0.5 μm. Variable pressure mode and gold coatings are applied in some cases when conducting is a matter.

Bruker S8 TIGER ECO X-ray fluorescence X-ray is used for supporting elemental analysis. X-ray photoemission spectroscopy (XPS) experiments are carried out on a PHI 5000 VersaProbe spectrometer equipped with a monochromatized Al Ka X-ray source. The overall energy resolution is 0.6 eV. Before each measurement an Ar etching ion gun is used to clean the sample surfaces at METU Central Laboratory.

3.4 The Measurement of Thermoelectric Properties

The thermal conductivity of samples is measured by Flash Laser method at Istanbul Technical University Corrosion Laboratory. A reference sample such as pyroceramic material with ~1 W/mK thermal conductivity value at room temperature thermal conductivity of which is very close to C-349 material is chosen for reliable measurement. The thermal conductivity of samples is calculated by following the standard relation

$$\kappa = \alpha C_p d \tag{4.1}$$

where α, C_p and d are thermal diffusivity, specific heat capacity and density, respectively. The heat flow direction of the thermal conductivity is equal to the direction that is chosen for Seebeck coefficient and electrical resistivity.

The Seebeck coefficient and resistivity measurement are conducted using a system which is set up in our laboratory and its description in detail is introduced in chapter 4.

REFERENCES

[1] ICDD (2003). PDF-2+ 2003 (Database), International Centre for Diffraction Data: Newtown Square, PA, USA.

CHAPTER 4

THERMOELECTRIC PROPERTIES MEASUREMENT SYSTEM

In this chapter, the relevant measurement techniques and apparatus designs required to effectively manage uncertainty, while also providing a reference resource of some previous advances in high temperature thermoelectric metrology are summarized and compared. Labview 8.0 software is used for measurements. Software for measurements is provided in Appendix A and Appendix B. In this work, many progressive and unique contributions to the metrology science are demonstrated. The aim of the work, which are not presented in the other reports in literature, is to show

i. how the measurement accuracy of thermoelectric materials can be enhanced by beadless thermocouple,

ii. how the external magnetic field is eliminated by extraordinarily designed micro heaters,

iii. how the differential temperature measurement option could be applied,

iv. how Seebeck coefficient and resistivity measurements can be performed with a reference sample,

v. how to perform axial 4-point probe resistivity measurement,

vi. how to disuse main heater or furnace.

The answers for above questions are introduced and explained in next sections.

Thermoelectric materials in the form of bulk and thin film with high efficiency are necessary for practical applications such as power generation and cooling. The efficiency of thermoelectric materials is evaluated by dimensionless figure of merit ZT, which is introduced in chapter 1,

$$ZT = \frac{S^2 T}{\rho \kappa} \tag{4.1}$$

where S is the Seebeck coefficient, ρ is the electrical resistivity, and κ is the total thermal conductivity. Measurements of Seebeck coefficient, electrical conductivity / resistivity and thermal conductivity are unavoidable for evaluation of *ZT*. Besides, due to significant improvements in thermoelectric area for renewable energy applications, great attention has been given to the measurements of high temperature Seebeck coefficient and resistivity for power factor calculations [1, 2]. For the practical application of thermoelectric materials, reliable, accurate and consistent measurements of these two are necessary. In the literature, along with many earlier reports [1-21], there are recently published research [22-27] concerning Seebeck coefficient and/or resistivity measurements of bulk materials providing their capabilities and limitations of measurement systems. A recent detailed overview of the challenges and influence of thermoelectric metrology on bulk materials for high temperature range has been given by Martin *et al.* [26].

There are several possible sources of errors that negatively affect measurement of Seebeck coefficient at high temperature. One of the frequent sources of error is related with a poor thermal contact between a sample surface and thermocouples, leading to systematic errors as reported in the studies [6, 24, 29, 30]. Another source of error might be the distance between the measurement points of the temperature gradient and thermoelectric voltage, so called "*cold-finger effect*". The third error contribution could be unexpected external magnetic field created by current carrying resistive wires in the furnace where the sample probe is inserted for Seebeck coefficient and electrical resistivity measurements. Thermoelectric properties are rather sensitive to the applied magnetic field for some kind of materials such as bismuth - antimony alloys [28] and this effect can be eliminated by some simple modifications (detail description is given in section 4.5.1). In addition, resistivity and thermoelectric power measurements should be performed on the same sample in order to avoid potential inconsistencies which could be due to unintentional and inhomogeneous doping [6]. Therefore, a non-destructive type of contacts for the measurements will be substantial for proper characterizations of samples.

Usually, scientists prefer thermocouples to measure both potential difference and temperature on the sample. Therefore, thermocouples should be chosen specifically to prevent any interaction between the sample and the temperature sensors especially at high temperature [26, 29]. For different types of thermoelectric materials, different kinds of temperature sensors are recommended considering chemical reaction and oxygen resistance sensitivity [31].

In the present study, we designed and implemented a device to measure Seebeck coefficient, differential temperature and resistivity of one and/or two bulk samples simultaneously in the range of 300 to 1000 K in any desired inert atmosphere or vacuum. Our system is constructed to address problems mentioned above with : ***i)*** a new kind of sample probe, ***ii)*** the beadless thermocouples placed side by side, ***iii)*** the magnetic field eliminated micro heater and ***iv)*** axial force contacts in a water cooled vacuum chamber.

In order to minimize the cold-finger effect, the beadless thermocouple design is performed, and the design allows user to replace the thermocouples without dispatching the whole sample probe and/or the system itself because it has modular structure. Besides, undesired mechanical forces caused by the bead of the thermocouple are also eliminated by this design. Non-destructive good electrical and thermal contacts are provided between the sample and the thermocouples by mechanical force that is applied in axial direction. Moreover, the proposed type of connection configuration also gives the user the advantage of making two Seebeck coefficient measurements at different points on the same face of the sample. Micro heaters are specifically designed and placed in order to eliminate the magnetic field that surrounds the sample. On the other hand, differential temperature gradient measurement is proposed in order to reduce the error contribution that comes from the number of thermocouples and the uncertainties of the temperature measurement [32]. Providing axial contact configuration, the resistivity of the bulk samples can be measured by applying four-point probe method. Finally, the thermoelectric properties of two samples as well as one sample can be analyzed at the same time with this system.

4.1 General Requirements for Seebeck Coefficient Measurement

The spatial arrangement of the probes may affect the result if the Seebeck coefficient is not geometry dependent (for isotropic materials), the two primary arrangements developed in part from early thermal conductivity measurements [33], as both quantities S and κ require the measurement of ΔT under an applied axial heat flux. By measuring the electric potential, the Seebeck coefficient can be calculated. There are two contact techniques for measurements:

i. *Axial-flow technique (two-probe):* In the axial-flow technique, the temperature difference and the electric potential are measured on the probes which are in direct contact with the ends of the specimen. This is the arrangement preferred by Goldsmid and Tritt for improved thermal and electrical contact [34-36]. However, many Seebeck coefficient apparatus also concurrently measure resistivity, requiring additional voltage contacts away from the ends of the sample.

ii. *Potentiometric arrangement (four-probe):* In the potentiometric arrangement, the temperature difference and the voltage difference are measured at two points on the sample (or inserted within the sample) equidistant from the hot and cold sinks and on the axis parallel to the thermal gradient.

To maintain accuracy, the diameter of each temperature/voltage probe must be much smaller than the effective distance between them. There is some debate as to which method provides the most accurate determination of temperature and voltage difference at the same points. Wood [3] compared the results of thermocouples pressed at the ends of a sample with those obtained by inserting them in holes drilled in the sample. For the temperature and the material evaluated, the results are consistent within the measurement uncertainty.

It would be useful to evaluate these arrangements over a broad temperature range and for a variety of materials. Considering the diversity of research materials in both geometry and contact resistance, the potentiometric arrangement may benefit longer, lower cross-sectional area specimens, while the axial-flow arrangement may benefit shorter or disk-shaped specimens, provided the thermal resistance of the sample is larger than the thermal resistance of the contact interface. Thus, a versatile and flexible apparatus would not only enable comparative measurements on materials with different contact resistances, thermal conductivities, and heat capacities, but also expand the practical range of sample geometries.

The primary requirements for “good” Seebeck coefficient measurements are:

1. the spatially synchronous measurement of voltage and temperature, that is, the voltage and temperature must be measured at the same location and at the same time;
2. very good thermal and electrical contact between the probe and the specimen;
3. the acquisition of low voltages (microvoltages) with minimal extraneous contributions.

Since at high temperature thermocouples are used to determine the temperature difference, where one pair of identical wires can used to measure the thermoelectric voltage, measurement of the Seebeck coefficient is essentially a practice in low voltage measurements. The various methods are defined to measure Seebeck coefficient: integral and differential methods. These methods will be explained in the next section.

4.1 Methods for Measuring Seebeck Coefficient

There are two primary techniques used to measure the relative Seebeck coefficient: the integral and the differential methods (see figure 4.1). In the integral mode, the temperature gradient between the two ends of the sample could exceed to 40 - 50 K, whereas this gradient should be less than 10 K. The information about these two measurement methods are explained in detail with some mathematical formulas.

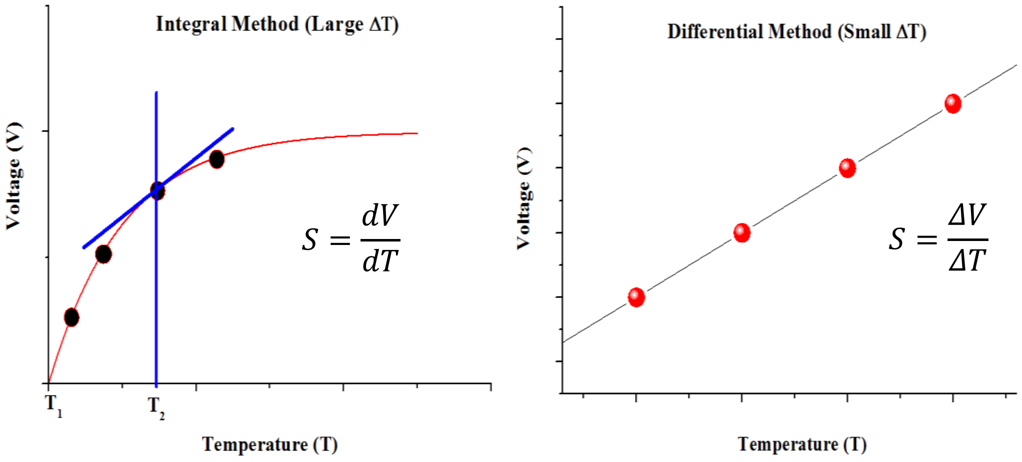

Figure 4.1 The illustration of integral (left) and differential (right) methods comparison chart [26].

4.2.1 The Integral Method

- In the integral method (or large ΔT), one end of the specimen is maintained at a fixed temperature T_C while the opposite end is varied through $T_H=T_C+\Delta T$, the temperature range of interest [4, 37-39]. Integral method is used normally for long metal wire specimens.

- For material *a* whose junctions are Ohmic and isothermal with material *b*, both of which are chemically and physically homogeneous and isotropic, the electric potential is defined as [37],

$$V_{AB}(T_C, T_H) = \int_{T_C}^{T_H} S_{AB}(T)dT = \int_{T_C}^{T_H} [S_B(T) - S_A(T)]\, dT \tag{4.2}$$

  An appropriate analytic approximation is selected and applied to the entire data set $V_{AB}(\,T_H, T_C\,)$, (A and B are two metals that are introduced in previous section 1.1.1) then differentiated with respect to T_H, where Eq. (4.2) becomes

$$S_{AB}(T_H) = S_B(T_H) - S_A(T_C) = \frac{dV_{AB}(T_C, T_H)}{dT} \tag{4.3}$$

In order to evaluate the Seebeck coefficient value reliable curve fitting is necessary. The fitting method must comprise the data set with minimal oscillations, as small random and biased errors will be amplified in the derivative.

Moreover, various curve fitting techniques have been explored. One common analytical representation is to continuously approximate the data by a series of orthogonal coefficients with the order selected by an F-test [4].

Other curve fitting approaches such as

a. Walking polynomial
b. Spline fit
c. Global least-squares fits of varying order
d. Orthogonal coefficient decrease

Powell *et al.* [40] warn that F-test can sometimes give misleading results "if some particular coefficient happens to be accidentally low." Since this problem has not been encountered in many applications, and the methods generally produce the best results of all, this method is selected by many scientists who use integral measurement method.

However, it is difficult to maintain T_C isothermal throughout the large ΔT at high temperatures, requiring additional corrections, and even more difficult to obtain a satisfactory fit for complex S_{AB} (T), where the Seebeck coefficient may have many more components than simple carrier diffusion. Furthermore, there are no objective criteria to evaluate the accuracy of the obtained derivative.

4.2.2 The Differential Method

For the reasons described above, the differential method (or small ΔT) comprises the majority of high temperature Seebeck coefficient characterizations. In this technique, a small thermal gradient ΔT is applied across a specimen maintained at the mean temperature of interest $T_o = (T_C+T_H)/2$, where $T_C = T_o-\Delta T/2$ and $T_H = T_o+\Delta T/2$ [37, 38]. By expanding the Seebeck coefficient $S_{AB}(T)$ in a Taylor series with center T_o and integrating, Eq. (4.2) becomes,

$$\frac{\Delta V_{AB}}{\Delta T} = S_{AB}(T_o) + \sum_{n=1}^{\infty} \frac{1}{(2n+1)!} \frac{d^{2n} S_{AB}(T)}{dT_o^{(2n)}} \left(\frac{\Delta T}{2}\right)^{2n} \tag{4.4}$$

$$= S_{AB}(T_o) + \Delta S_{AB}(T_o) \tag{4.5}$$

Therefore, in the differential technique, the Seebeck coefficient is given exclusively by the ratio of the electric potential and the temperature difference, provided $\Delta T / T_o \ll 1$ and $\Delta S_{AB} / S_{AB} \ll 1$, when $V_{AB} \propto T_o$ and the latter term in Eq. (4.4) can be neglected. In addition, the linearity in $S_{AB}(T)$ observed for typical metals cannot be expected in semiconductors, where larger thermal gradients would effectively average the structure in $S_{AB}(T)$ and reduce measurement resolution in T. Here, observation time is defined as the interval required to acquire one voltage measurement (assuming T_C, T_H, and V_{AB} are measured simultaneously) and is therefore instrumentation dependent.

Differential methods can be categorized into three conditions: steady-state (dc), quasi-steady-state (qdc), and transient (ac), assuming the observation time scale.

4.2.2.1 The steady state condition

Under steady-state conditions, differential methods often calculate the Seebeck coefficient from the linear fit of multiple electric potential/temperature difference data points rather than one. This practice avoids the assumption that the curves intersect the ordinate ($V_{AB} = 0,\ \Delta T = 0$), effectively eliminating the offset voltages arising from thermocouple inhomogeneity and non-equilibrium contact interfaces (the entire series of interfaces between thermocouple wires and the voltmeter). However, the selected temperature differences must be acutely incremental, such that the total range satisfies the assumption of linearity in $S_{AB}(T)$. In addition, the temperature for $S_{AB}(T_{\text{avg}})$ must represent the average for the collection of steady-state T_o. Depending on temperature, and sample length, thermal gradients between 5 and 20 K and the measurement range can be arranged between 100 and 1300 K for this method. The resulting slope of each line can be used to calculate the Seebeck coefficient, and the estimated accuracy could be in ± 5 μV/K.

4.2.2.2 The quasi-steady-state condition

Although the steady-state condition succeeds in reducing the contribution of offset voltages, the time burden to properly stabilize each increment of ΔT may be impractical and inefficient. To enable rapid measurements of the Seebeck coefficient the quasi-steady-state condition is introduced [41-43]. This condition simultaneously measures multiple electric potential/temperature difference data points but employs a continuously increasing heat flux rather than multiple static, steady-state ΔT's. However, to proper implementation these dynamic (or gradient sweep) techniques requires multiple high impedance nano-voltmeters (voltage meters with uncertainty < 100 nV). There is also a question of how to select the appropriate time rate of change in ΔT. Unfortunately, this is rarely stated in the literature making comparison of data quality a challenge. One modern embodiment of the differential technique under the quasi steady-state condition is given by Wood [3]. The base temperature is also increasing at a steady rate rather than stabilized at each temperature of interest. In our study, 5 K/min. ramp rate is preferred.

4.3 The Methods for Measuring Electrical Resistivity

Among other resistivity measurement methods, a configured axial four-point probe method is applied in our measurement system. Generally, four–point probe method is an electrical resistivity measuring technique that uses separate pairs of current-carrying and voltage sensing electrodes in order to make more highly accurate measurements than traditional two-point probe method. Typically, a constant current is applied to two probes and the voltage drop on the other two probes is measured with a sensitive voltmeter. The advantage of four- point probe method is that the separation of current and voltage leads eliminates the impedance contribution of the contact resistances and wiring. In two-point probe method, the measured voltage is at its terminals and not across the component. Therefore, the voltage drop across the connection leads is also included in the resistivity calculation.

4.3.1 Developed Van der Pauw Technique

On the other hand, the Van der Pauw technique is one of widely used in the semiconductor industry to determine the resistivity of uniform samples [44, 45]. In this technique, four very small ohmic contacts placed preferably in the corners of the sample and resistivity is derived from these four points using specific configurations. Volume resistivity is a measurement of the resistivity of a material perpendicular to the plane. It is also called bulk resistivity because it is a measure of the resistivity across a defined thickness.

In our study, Van der Pauw method as a configuration for axial four-point probe resistivity measurements is used. Since both methods are combined in one configuration, wide range of sample with different sizes and properties can be measured with the high accuracy. Detailed description of the measurement setup has been explained in the section 4.5.

4.4 The Measurement Error Estimation

When the measurement is repeated with a sensitive instrument, slightly different results can be obtained. The measurement error is the deviation of the outcome of a measurement from the true value. It is the difference between a measured value of quantity and its true value [46]. It is well known that an error is not a mistake. There are two types of errors; ***i)*** *systematic error* which always occurs with the same value, when the instrument is used in the same way and in the same case. ***ii)*** *random error* which may vary from observation to observation and cannot be controlled due to some unknown factors or conditions. There are two different kinds of error contribution which are coming from both instruments and wires in our system. These contributions for Seebeck coefficient and resistivity measurements separately need to be considered carefully.

All the uncertainties are estimated based on the uncertainties of each instrument in our study. Since each instrument has its own measurement uncertainty, each contribution is evaluated for both Seebeck coefficient and resistivity measurements and showed below. In the part below, we summarized our uncertainty estimation procedure for the measurement system.

4.4.1 Error Estimation of the System

There are two different kinds of error contribution which come from both instruments and wires in our system. These contributions for Seebeck coefficient and resistivity measurements separately need to be considered carefully.

4.4.1.1 Error Estimation for Seebeck Coefficient Measurements

First of all, error contribution of instruments can easily be estimated considering device itself. Each device has their own measurement conditions those changes depending on the environment and signal level. For instance, in Seebeck coefficient measurement, errors are coming from the Keithley 2182 (K2182) nanovoltmeter and thermocouple itself.

a.) Error Estimation of K2182 Nanovoltmeter

For K2182 Nanovoltmeter, error estimation can be explained as given below.

For instance, for **10 mV** range, **50 ppm** of reading and **4 ppm** of range will be obtained. Generally, for a measurement of a «**5 mV** signal», the uncertainty is; 50.10^{-6} x 5.10^{-3} V + 4.10^{-6} x 10^{-2}V= **290 nanovolts (0.29 µV**).

i. An instrumental uncertainty of **± 0.29 µV** for each point that is measured.

ii. *dV* vs. *dT* can be plotted including this error ($S = dV/dT \pm 0.29$ µV).

b.) Error Contribution of Thermocouple Wires

The temperature error of thermocouples is larger (typically 1 or 2 K) but that will not change the Seebeck coefficient because the slope (dV / dT) is being calculated.

4.4.1.2 Error Estimation for Resistivity Measurements

There are three basic error sources in resistivity measurement which are K2182 nanovoltmeter, Keithley 238 (K238) current source and thermocouple itself.

Source I (current) Mode, Manual Ohms: Total uncertainty = *I* source accuracy + *V* measure accuracy (4-wire remote sense).

i. Thermocouple error, which can be expressed as lead wire contribution to the resistivity measurement, is eliminated by current reversal and 4-point probe method.

4.4.2 Standard Deviation Calculations

According to the statistics and probability theory, the *standard deviation (SD)* demonstrated how much variation or dispersion from the average exists [47]. It is represented by the Greek letter sigma, σ. A low standard deviation indicates that the data points tend to be very close to the mean that is called expected value whereas a high standard deviation indicates that the data points are spread out over a large range of values.

In order to obtain standard deviation, 33 measurements are performed and a part of it is shown in figure 4.2. A mean of 133.4 μV/K with a standard deviation 1.47 μV/K are obtained. A measurement error of ± 0.29 μV/K is measured. Multiplying this standard deviation with the number of 3 and adding the measurement error, the sampling error of the measurements as ± 4.70 μV/K is calculated. Adding and subtracting the sampling error to the mean value, we obtained the specification limits as the interval within 128.70 μV/K to 138.10 μV/K. Then, we need to know how many of the observations the obtained interval should include. According to statistical theory, Chebyschew asserts that 89% of the observations should lie within this interval. However, if measured data follows a Gaussian distribution, it could infer that 99.7 % of the observations must be within this interval. Therefore, Anderson Darling normality test is performed to data, and obtained a p_value of 0.773. As a result, it can be inferred that data follows a normal distribution with high confidence, and corresponding normality test that cannot be rejected at any acceptable significance level. Mean calculation for the standard deviation is as follows.

Mean= Average ±3*standard deviation (±*calculated error of the system)

- **i.** Data strongly supports normal data at any acceptable significance level.
- **ii.** According to the statistical theory, it can be safely asserted that 99.7% of the measurements are within lower and upper limits.

Measured Seebeck coefficient at room temperature for a C-349 sample : 133.00 ± 0.29 μV/K, 131.60 ± 0.29 μV/K, 132.80 ± 0.29 μV/K, …. , 135.50 ± 0.29 μV/K. These 33 data points have the mean (average) of Seebeck coefficient: 133.40 μV/K.

The normality test for the data is as follows:

H_0: Data follows Normal Distribution
H_A: Data does not follow Normal distribution
p_value=0,773

The summary and result of standard deviation calculations for sample C-349 is demonstrated in table 4.1. RT represents room temperature.

The Anderson-Darling Normality test [48] is used to test the evaluation a sample of data came which came from a population with a specific distribution. Since the data obtained follow the Normal Distribution, the Anderson-Darling test could be applied. The result of this test is presented in the figure 4.2 providing the information that data has a specific distribution.

Table 4.1 Standard deviation calculations for sample C-349.

Calculations	**Results at RT (µV/K)**
1. Measurement	133.0
2. Measurement	131.6
3. Measurement	132.8
....	...
33. Measurement	135,5
Mean	**133.4**
Std_dev	1.47
3*Std_dev	**4.41**
Measurement Error	± 0.29
Total Error	**4.70**
Lower	128.70
Upper	138.10

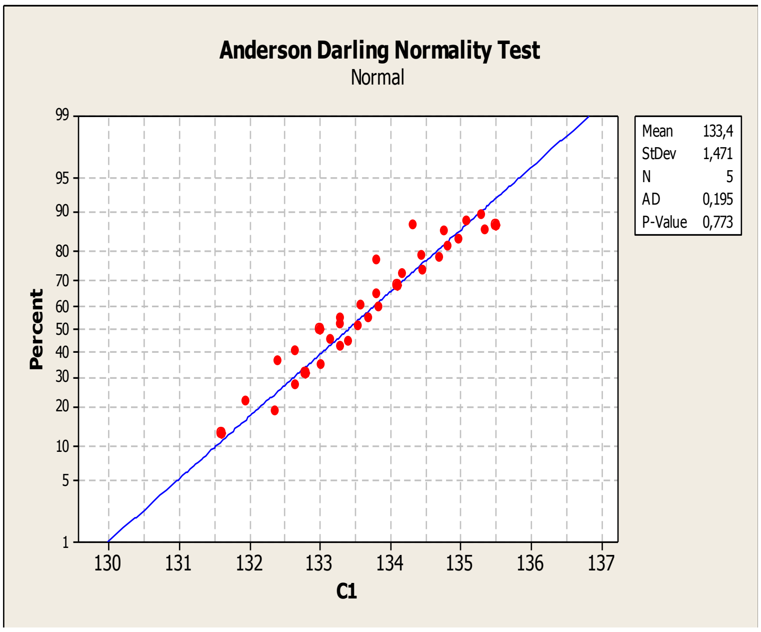

Figure 4.2 Normality test of Seebeck coefficient values of C-349 for 33 data points.

4.5 Description of the Measurement Set-up

The system basically consists of a vacuum chamber (VC), a vacuum pump, a sample probe (SP), two micro heaters (Mhs) and electronics (see figure 4.3). VC is built in order to eliminate the environmental effects and to provide good temperature control under any desired inert atmosphere and/or vacuum while measuring the TE properties of materials. VC has four standard KF 25 gates which provide wide range of connections from electronics to the SP via vacuum tight connectors. These connectors are for thermocouples and power cables of the heaters. Indeed, with a water-cooled wall, an independent temperature control from outside environment is provided. Vacuum pump is connected to the VC via vacuum hose and pressure inside the VC is controlled by a vacuum gauge.

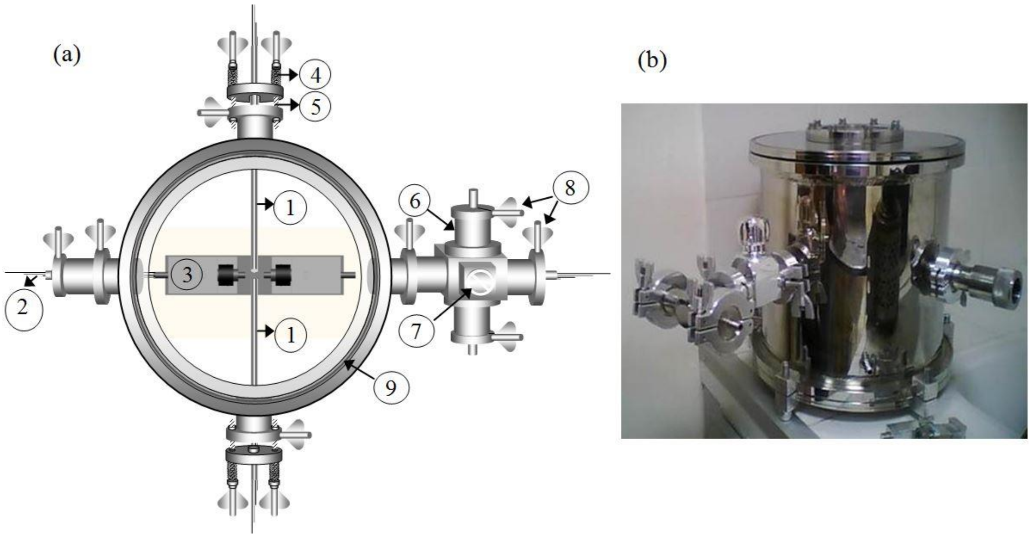

Figure 4.3 (a) The layout of the vacuum chamber; 1) thermocouples placed for two samples option, 2) thermocouples, 3) sample probe, 4) spring, 5) screw, 6) KF25 standard ports for gas inlet / outlet tube, 7) valve, 8) clamp, 9) gasket. **(b)** Real image of the vacuum chamber.

The image and enumerated components of the sample probe are illustrated in figure 4.4. The SP consists of two sample holders (SHs) (12) and two sample probe blocks (SPBs) (7). Sample (1) is mounted between the SHs. Each SHs has been achieved by introducing 7-bore alumina isolator (7AI) (3) into a stainless steel tube (SST) (5) tightly in order not to allow 7AI to move on undesired axis. They are placed mutually and are centered by SPBs. 7AI tubing is used for isolating each thermocouple wire (2) and for their stable mounting. The thickness and length of SSTs have been designed small enough to prevent heat loss away from the sample by conduction. The sample holder screws (9) which are placed in order to keep 7AI and SST together have the advantages of replacing the thermocouples and of maintenance purposes without ordering-off the whole system. These two SPBs are perfectly oriented along the horizontal axis of the sample probe to provide a homogeneous pressure on the sample, made of a brass material. They are mounted using down-sample probe block screws (10) that are on the brass support (11) and they can be moved forward and backward with the help of a sled when the sample is large enough to fit. There are also two top-sample probe block screws (8) on top of the SPBs for the purpose of adjusting sample holders at a specific distance for the mounting and removal of the sample before and after the measurements. Two springs (6) are located inside the SPBs, where axial force is applied by these springs on both ends of the sample through the SPs. The material of the spring does not lose its strength and the spring applies gradually the same force on the specimen from room temperature to 1200 K; therefore, poor mechanical and electrical contact leading to significant errors are avoided [2, 6]. Sample heating is provided by mutually placed Mhs (4). Each Mh is attached firmly on the each 7AI. Detail description about Mhs is given in section 4.5.1.

7. Sample probe blocks (SPBs)
8. Top sample probe block screws
9. Sample holder screws
10. Down sample probe block screws
11. Brass support
12. Sample holders

1. Sample
2. Triple Beadless thermocouple
3. 7-bore alumina isolator (7AI)
4. Micro Heaters (Mhs)
5. Stainless steel tube (SST)
6. Springs

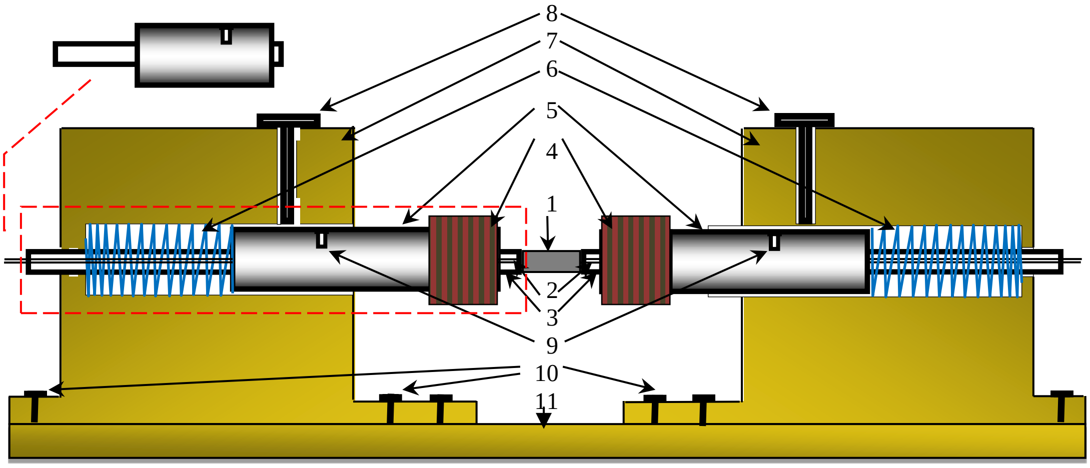

Figure 4.4 General cross-sectional view of the sample probe.

The electronic part, which is shown in figure 4.5 (a), consists of the Lakeshore 336 (LS336) temperature controller unit for controlling and monitoring the temperature and micro heaters. K2182 digital nanovoltmeter is used to measure the voltage. Current is provided by K238 current source unit for resistivity measurement and switcher is used to switch the wires to adjust the wire configurations. In order to provide inert atmosphere (see figure 4.5 (b)) in the camber nitrogen, helium or any other desired gas may be attached to the vacuum chamber. Thermocouple wires are directly connected to the LS336, whereas electrical connections are made using the switcher as it is shown in figure 4.5 (c).

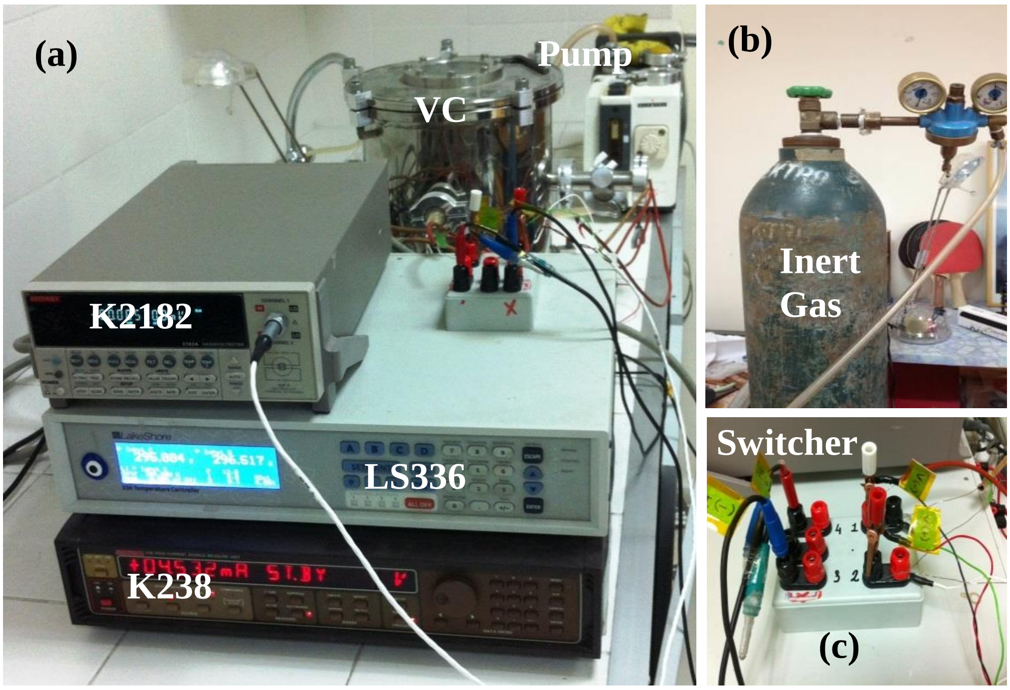

Figure 4.5 Devices that are used in high temperature Seebeck coefficient and resistivity measurement system.

4.5.1 Elimination of Magnetic Field by Micro Heater Design

Two micro heaters are designed in order to eliminate the magnetic field created generally by heaters itself (figure 4.6). There are two micro heaters (Mhs) controlled by LS336 that have two independent proportional-integral-derivative (PID) controllers. Both micro heaters fit over the sample holders completely so that temperature convection across the sample is minimized to obtain higher temperature measurement accuracy.

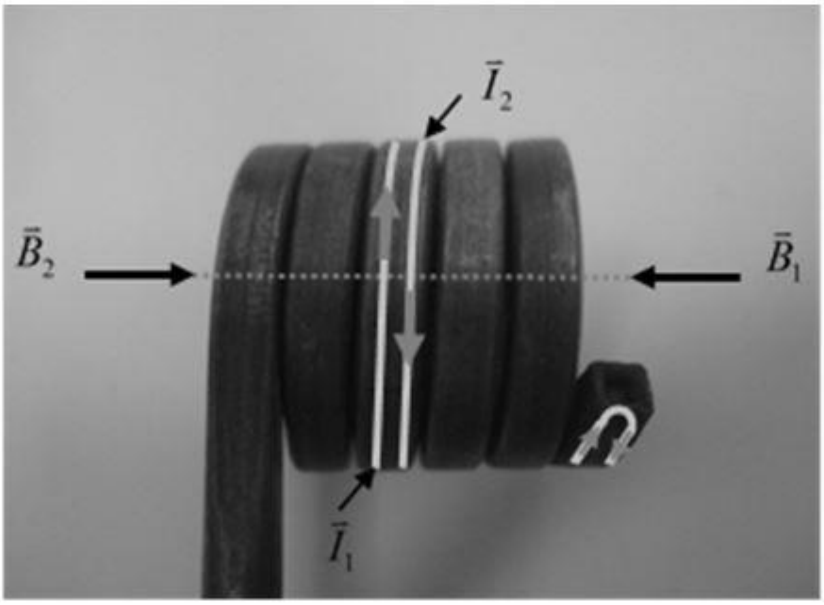

Figure 4.6 The image of a micro heater with applied current follow direction.

Figure 4.6 shows the micro heater, where $\vec{I}_1$ and $\vec{I}_2$ show the directions of the applied current on the resistive wire, and $\vec{B}_1$ and $\vec{B}_2$ are directions of the magnetic field created by the currents $\vec{I}_1$ and $\vec{I}_2$, respectively. In order to eliminate the effect of magnetic field, micro heaters are given a spiral form. A two-layer spiral is formed to eliminate this magnetic field by twisting a 15 mm long wire leftwards and moving counter clockwise, then rightwards and moving clockwise, resulting in a micro heater of 11 mm in radius.

Since the resistive wire is twisted and bended backwards, the magnitudes of currents become equal, $\left|\vec{I}_1\right| = \left|\vec{I}_2\right|$; however, it is directed in the opposite direction, $\vec{I}_1 = -\vec{I}_2$. Therefore, even if the magnitude of the magnetic fields are equal, $\left|\vec{B}_1\right| = \left|\vec{B}_2\right|$, the directions of them will be opposite $\vec{B}_1 = -\vec{B}_2$, cancel each other, $\left|\vec{B}_1\right| - \left|\vec{B}_2\right| = 0$. By this way, magnetic field around the sample is eliminated.

4.5.2 Triple Beadless Thermocouple Design

Some source of errors during the TEP measurements are studied and reported elsewhere [26]. Among them, contact issue which is one of the most problematic one, should be considered while setting up a device. Basic contact types with their advantages and disadvantages are summarized in a recent research by Iwanaga *et al.* [24]. In this study, along with various features of device, Crossed Wire Junction (CWJ) design offered in order to minimize so called “cold - finger effect” that is one of the problematic issues in Seebeck coefficient measurements. Moreover, unwanted mechanical forces occurring due to the ball shaped bead of the thermocouples can also be eliminated by this way. However, since the thermal expansion coefficients of thermocouple legs are different, there might be a contact problem between the thermocouple wires themselves at the junction point at high temperature. Furthermore, with this configuration only two-point probe resistivity measurement is possible and some additional modifications might be necessary for the four-point probe resistivity measurement to eliminate lead resistance. However, this can be proposed for this configuration only by inserting wires into the sample by drilling or by un-axial mechanical forces if the sample is not fragile to withstand the force that is applied. Considering these issues, we offer newly designed beadless thermocouple in our system. Mostly, thermocouples are formed in a way that the wires are arranged and welded side by side (figure 4.7 (a)) leading to a big bead junction. These big beads cause some measurement errors such as unwanted mechanical force [26]. Reducing the size of the bead that is built using this technique will lead to poor mechanical strength [24]. The specialty of beadless thermocouple is that mutually placed wire ends of the thermocouple wires (figure 4.7 (b)) are welded in a different way in which the radius of the bead of the thermocouples is reduced to the radius of the wires of thermocouples (figure 4.7 (c)). One of the advantages of this design is that when the size of the bead is reduced Seebeck coefficient and temperature can be measured almost at the same point limiting this distance to several micrometers (figure 4.7 (d)); thus, “*cold-finger effect*” is minimized. Indeed, due to the junction of the thermocouple is flattened to a smooth surface instead of bead, non-destructive homogeneous mechanical force and thus, good thermal and electrical contact between the thermocouples and the sample is provided.

The second advantage of the design is that each thermocouple fills only two holes on an AI in our design. Therefore, three thermocouples can be inserted into 7AI in order to provide two more contact points at the same end of the sample. Four-point probe resistivity and differential temperature difference can be measured at once along with Seebeck coefficient measurement without drilling the sample or wrapping the thermocouple wires on the sample using this configuration (described in section 4.5.3). Therefore, 3-beadless thermocouples can be inserted adjusting the junction point of thermocouples to be in the middle (figure 4.7 (e)) into the 7AI.

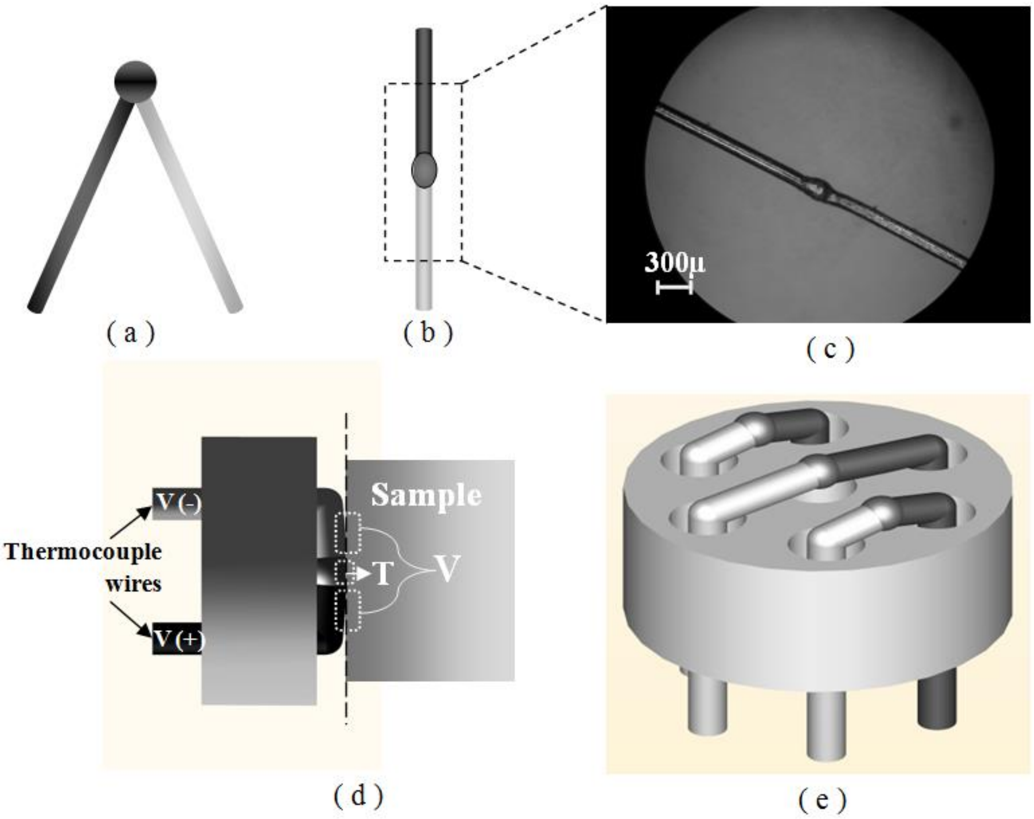

Figure 4.7 (a) The form of common thermocouple welding. **(b)** The form of mutually placed thermocouple welding. **(c)** A picture of a beadless thermocouple. **(d)** Contact diagram showing the measurement points for voltages and temperature on the sample where$T$; Temperature, V; Voltage corresponding to temperature ($V(+)$ and $V(-)$ correspond to positive $(+)$ and negative $(-)$ thermocouple wires, respectively). **(e)** 3-beadless thermocouple design.

The third advantage of this design is that Seebeck coefficient and resistivity of two samples with the same size can be measured simultaneously. The benefit of this configuration is that it gives the opportunity to use one of the samples as reference sample for environmentally sensitive materials to obtain more accurate results.

4.5.3 Contact Design and Measurement Configuration

Seebeck coefficient, differential temperature and four-point probe resistivity measurements of the samples can easily be done with the given contact configuration shown in figure 4.8. Wood *et al.* [6] pointed out that there is no significant difference between soldering a wire to the sample and direct contact to the sample. In our system, instead of damaging the sample by drilling, the non-destructive direct contact type is preferred to make measurements.

The system has two measurement options according to the number of samples to be measured. First one is the single sample configuration option (SSC); that is; only the Seebeck coefficient and resistivity of one sample can be measured. The possible types of contacts between the thermocouples and sample in order to measure Seebeck coefficient, resistivity and differential temperature in SSC is given in figure 4.8 (a) and 4.8 (b). In this figure, each number represents the junction point of a beadless thermocouple.

In SSC configuration, both contacts of 1 and 4, or 2 and 3 for Seebeck coefficient and contacts of 1, 2, 3 and 4 for resistivity measurements can be used (see figure 4.8 (a)). The connection points of the Seebeck voltage measurement should be also the points where the temperature is going to be measured. This configuration gives the user an advantage during the Seebeck coefficient measurements. That is, the user can make two Seebeck coefficient measurements from two different points on the sample at the same time. By comparing these two measurement results, the user can study local properties (i.e. structural). Differential temperature difference can be measured only by using contacts of 5 and 6 (figure 4.8 (b)). A thin mica sheet as an insulator is placed between the mutually placed beadless thermocouples and the sample in order to prevent electrical contact during the differential temperature measurement. The sample size of 3 up to 30 mm in length, and from 3 up to 8 mm in radius can be measured by 1SC.

Accuracy in Seebeck coefficient measurement relies on determining the temperatures of hot side; T_H and cold side; T_C, precisely at the location of the voltage probes, V_H and V_C, respectively. Thus, beadless thermocouple contacts of 1 and 4 are used as current source; contacts of 2 and 3 are used to measure thermal-emf (ΔV) for Seebeck coefficient and voltage (V_{IR}) for resistivity calculations or vice versa. Temperature difference (ΔT_2) is calculated by subtracting the temperatures read from hot side (T_H) and cold side (T_C) of the sample; $\Delta T_2 = T_H - T_C$ (figure 4.8 (b)). As seen in figure 4.8 (a), three pairs of thermocouples, which are enumerated from 1 to 6 according to the type of measurement, are mutually connected to the sample. Negative (-) legs of thermocouples (enumerated as 5 and 6) are shorted; thus, positive (+) wires of thermocouples are used for direct measurement of differential temperature; $\Delta T_1 = dT_1$.

Second measurement option is double sample configurations (DSC). Seebeck coefficient and electrical resistivity measurements for DSC are given in figure 4.8 (c, d). Unlike SSC, in DSC, voltage created by applied current (V_{IR}) and Seebeck voltage (ΔV) are measured by beadless thermocouples that are inserted into an additionally placed 4-bore alumina isolator (4AI) (figure 4.3 and figure 4.8 (d)). Springs are placed externally to the VC in order to maintain the contacting pressure of 4AI (see also figure 4.3 (4)). Seebeck coefficient of each sample can be measured by contacts of 1 and 4. In this configuration, the physical properties of the sample can be measured sensitively when the other sample position is replaced with a known reference material. In this case, two-point probe method for measuring resistivity can be applied using only those contacts of 1 and 4. However, four-point probe resistivity measurement of two samples is possible using additionally placed 4AI (figure 4.8 (c, d)). Here, beadless thermocouple contacts of 1 and 4 are used as current source; contacts of 2 and 3 are used to measure thermal-emf (ΔV) for Seebeck coefficient and voltage (V_{IR}) for resistivity calculations, respectively.

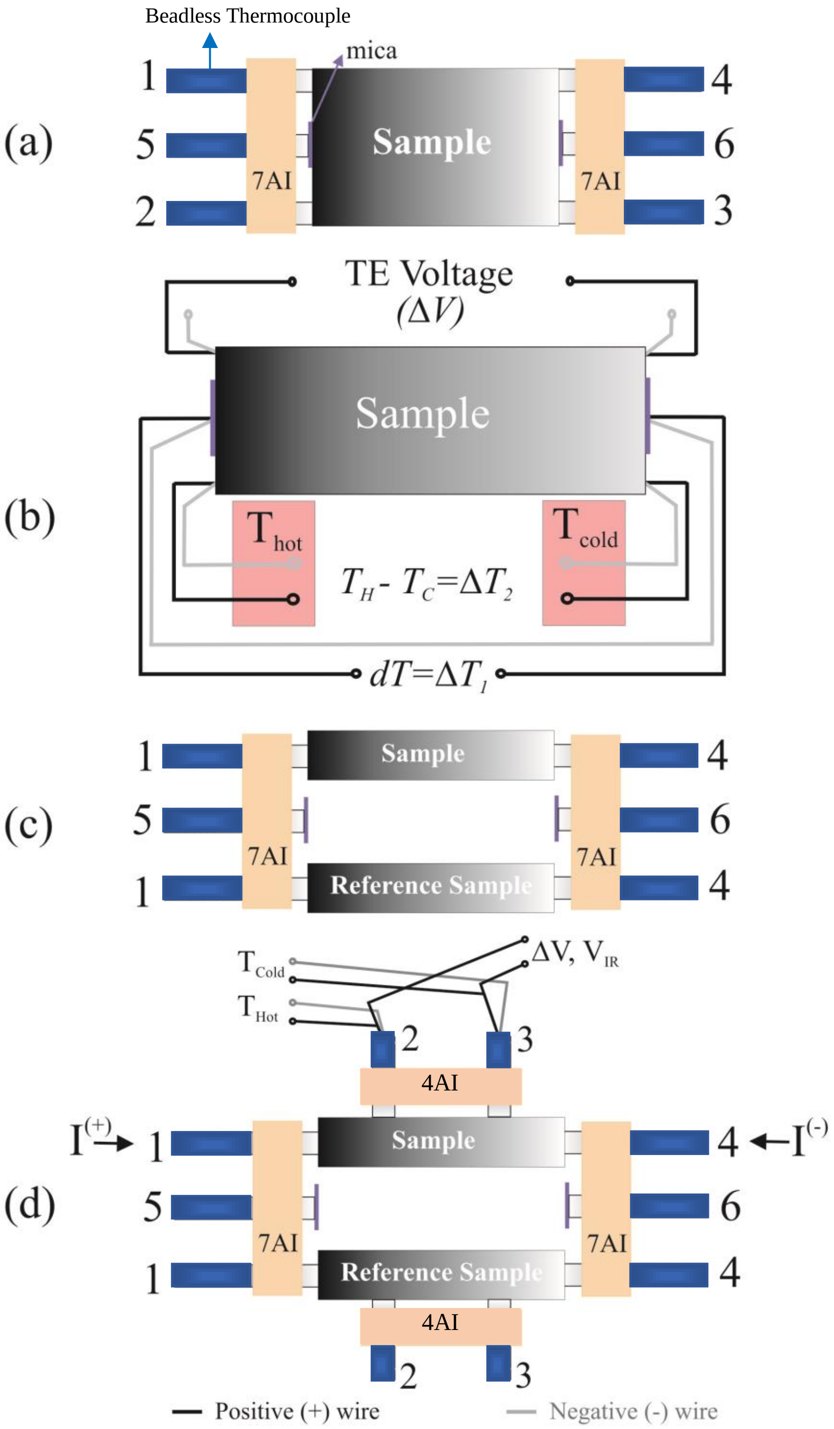

Figure 4.8 **(a)** and **(b)** the type of contacts and configurations for Seebeck coefficient and differential temperature measurements for SSC, respectively. **(c)** and **(d)** the type of contacts and configurations for Seebeck coefficient and four-point probe resistivity measurements for DSC, respectively.

The measurement of resistivity in thermoelectric materials presents unique difficulties [26]. One of them is thermal-emf presented in the circuit that can be cancelled out by current reversing and averaging of the measured resistances [6]. In order to conduct a resistivity measurement, current flowing along one edge of the sample (e.g. I_{12}) and the voltage across the opposite edge (in this case, V_{34}) is measured (see figure 4.8 (a) and 4.8 (d)). The measured potential drop V_{34} consists of the resistive voltage V_{IR} at current I_{12} and V_{EMF} that is the contribution of thermal-emf resulting in an equation of $V_{34} = V_{IR} + V_{EMF}$. A further improvement in the accuracy of the resistance values can be obtained by repeating the resistance measurements after switching polarity of the current source I_{12}' (negative) immediately to measure $V_{34}' = -V_{IR} + V_{EMF}$. This provides the elimination of the offset voltages, such as thermoelectric potentials due to the Seebeck effect, will be cancelled out. From these two values, average resistance (for this example, $R_{12,34}$) can be calculated [50] using the expression;

$$R_{12,34} = \frac{V_{34} - V_{34}'}{2I_{av}} = \frac{(V_{IR} + V_{EMF}) - (-V_{IR} + V_{EMF})}{I_{12} - I_{12}'} = \frac{V_{IR}}{I_{av}} \tag{4.6}$$

Van der Pauw showed that the resistance of samples can be determined from two of these resistances - one measured along a vertical edge $R_{12,34}$, and a corresponding one measured along a horizontal edge, $R_{23,41}$.The total resistance of the sample can be calculated by averaging these measured resistance data as given below;

$$R = \frac{R_{12,34} + R_{23,41} + R_{34,12} + R_{41,23}}{4} \tag{4.7}$$

The proposed four-point probe system will also be very beneficial for investigation the effect of structural changes in the resistivity of composites such as carbon fibre epoxy laminates [49]. In this study, for instance, the resistivity behavior would depend on whether the composite between the electrodes is unidirectional or multidirectional and if unidirectional whether it is oriented perpendicular or parallel to the direction of largest conductivity in a carbon fibre composite. Indeed, if the structure is unidirectionally oriented to the low resistivity direction, this system would permit exploration of the changes in potential difference at different locations around two points where current is being introduced. The measurement error is estimated by using uncertainties of each instrument for Seebeck coefficient and resistivity measurements [50].

4.6 Thermocouple Tests and Temperature Calibration of the System

Relative Seebeck coefficient is calculated using the slope in which the voltage difference vs. temperature difference is plotted. In order to avoid miscalculation, these two factors should be measured correctly. If there is any miscorrelation between them, the Seebeck coefficient will be measured wrongly. For instance, if the user measures the temperature wrongly, the voltage difference will also be wrong. As it is illustrated in figure 4.9, even if the temperature differences are the same in both Test-1 and Test-2 measurements, the voltage differences are different on the same sample. As a result of the Seebeck coefficient calculations, there is a distinct difference between both measurements. This is due to wrong calibration of thermocouples or bad contact. It is also highly significant for resistivity measurements. During the resistivity measurements, the temperature between the two ends of the sample should exactly be the same in order to have accurate measurement. The temperature difference will cause thermal –emf and this will contribute to the voltage negatively. For this reason, the best way for testing the accuracy of the device is to do temperature calibration of both thermocouples and to do temperature measurements of both side of the sample vs. time.

Thermocouple calibration for our system is done using the calibrator at high temperature. Ice bath or other low temperature calibration methods are not suitable for this setup because of the high temperature measurements. Temperature calibration needs to be made at a temperature range where the measurements are conducted. After the calibration, thermocouples are connected to the LS366 and both heaters on it are set to 500 and 1000 K. As it is clearly seen from the figure 4.10, there is highly good correlation between the thermocouples. The difference between both measurements is less than 2 and 30 mK at 500 and 1000 K, respectively.

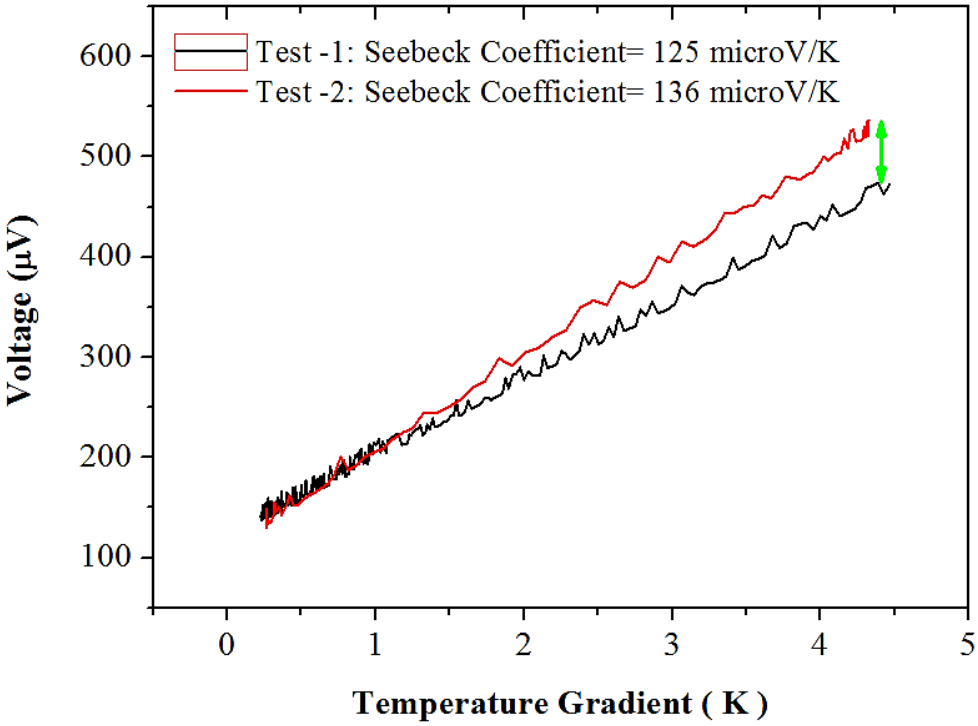

Figure 4.9 The different Seebeck coefficient measurements results on the same sample.

Figure 4.10 Temperature measurement results of thermocouples The Input C and Input D represent thermocouples that are attached to the sample.

In addition to this, linear voltage measurements need to be observed while the pulsing at a set temperature and during heating and cooling. Figure 4.11 shows the short (1th pulse) and long (2th pulse) pulsing. In highly sensitive measurement devices, the response of the sample is correlated with the pulsing. Therefore, as soon as the temperature gradient is created, the voltage difference should occur. During this treatment, the voltage difference (ΔV) is measured and data plotted vs. real time in order to investigate the accuracy of the calibration (figure 4.12). It can be seen that voltage difference is recorded as cycle. These cycles are correlated with the temperature gradient. When the temperature gradient increases, the voltage difference increases and vice versa as it is expected. The quick response of the sample demonstrates the high-quality contact between the sample and the thermocouples.

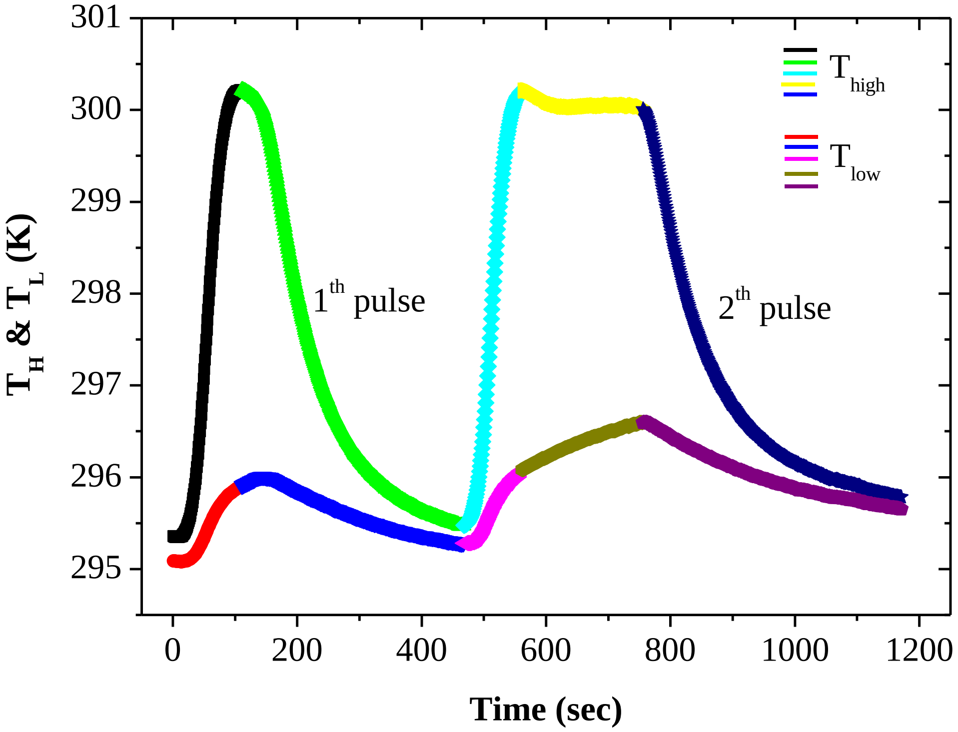

Figure 4.11 Temperature gradient created by pulsing one of the micro heaters.

It is obvious that there is expected correlation as can be seen below in figure 4.13. In this figure, it is illustrated that the time to create temperature gradient is 55 s and 57 s during heating and cooling at 400 K, respectively. Actually, the time difference is rather low and 2 s difference occur due to heat absorbed by the alumina ceramics. In order to decrease this time, the length of the alumina ceramic is shortened.

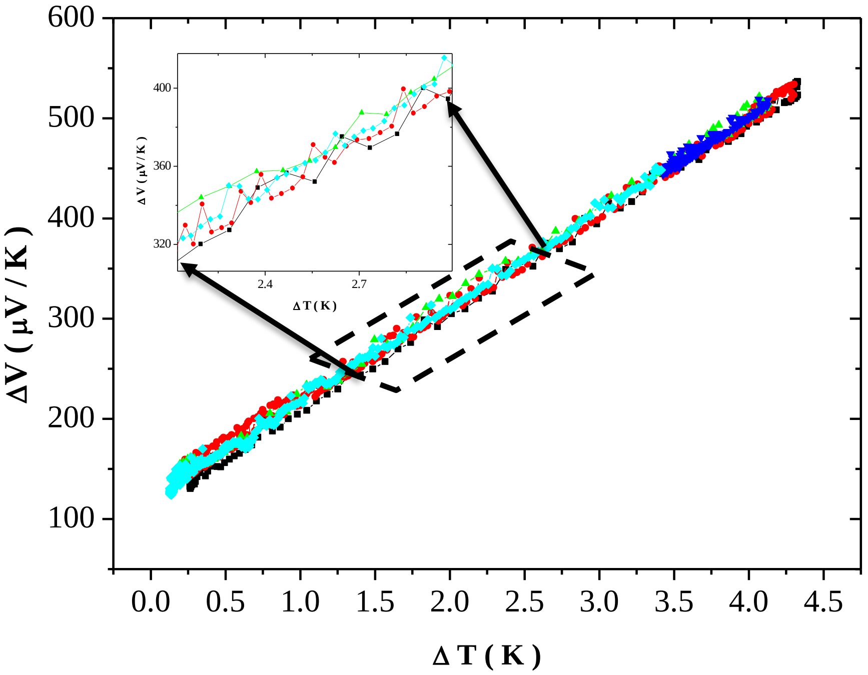

Figure 4.12 Differential voltage drop vs. differential thermal gradient is plotted as multiple measurements to calculate Sc. Inset shows the closer view of the graph.

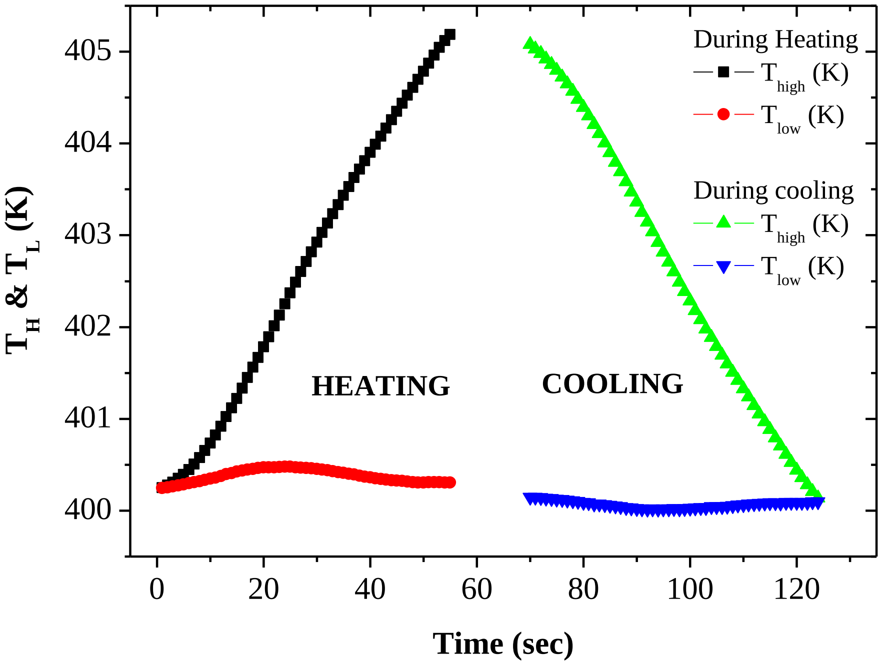

Figure 4.13 Temperature gradient created by pulsing the micro heater during heating and cooling.

4.7 Temperature Profile Options for Measurements

Temperature profile of the sample as a function of time during heating and cooling cycles at room temperature is shown in figure 4.14 (a). A temperature gradient of 5 to 10 K is applied [24], (figure 4.14 (b)). Because the sample space is quite small, the heating and cooling rates are almost equal during the Seebeck coefficient measurements. After stabilization of the temperature at the set point temperature, temperature gradient is created between two ends of the sample by heating one of the Mhs. Alternatively, since the Mhs give fast response, one of the Mhs can be heated up and the other one can be cooled down in order to create desired temperature gradient to obtain voltage difference [24].

4.7.1 Differential Temperature Measurement

The measurement of a temperature gradient by using the differential thermocouple arrangement is more accurate than direct subtraction of temperatures measured between two ends of the sample because each thermocouple has its own error and relative error in two temperature measurements is more pronounced as compared to the differential temperature measurements. Using one of the mutual thermocouple wires (preferably the middle one) differential temperature can be measured (contacts of 5 and 6 as shown in figure 4.8 (d)). The points where thermoelectric voltage and temperature difference measurements are taken on the edge of the sample should be as adjacent as possible [1, 24, 26]. In 3-beadless thermocouple configuration, differential temperature measurement might not be a good idea for Seebeck coefficient calculations due to the distance between two thermocouples on AI that is about 0.5 mm. However, this option might be used for other beneficial information such as homogeneity of a sample. For instance, temperature gradient can be measured either by direct subtraction of hot side and cold side temperatures or by differential method using 3-beadless thermocouples configuration. User can use both measurement data for Seebeck coefficient calculations. These two temperature gradient data (direct subtraction and differential) are taken at the same axial direction; however, from different lateral points on the edge of the sample. Thus, if the sample is structurally not homogenous at this direction, the measurements of these two temperature gradients might be slightly different depending upon the degree of homogeneity that might slightly effect the Seebeck coefficient calculations.

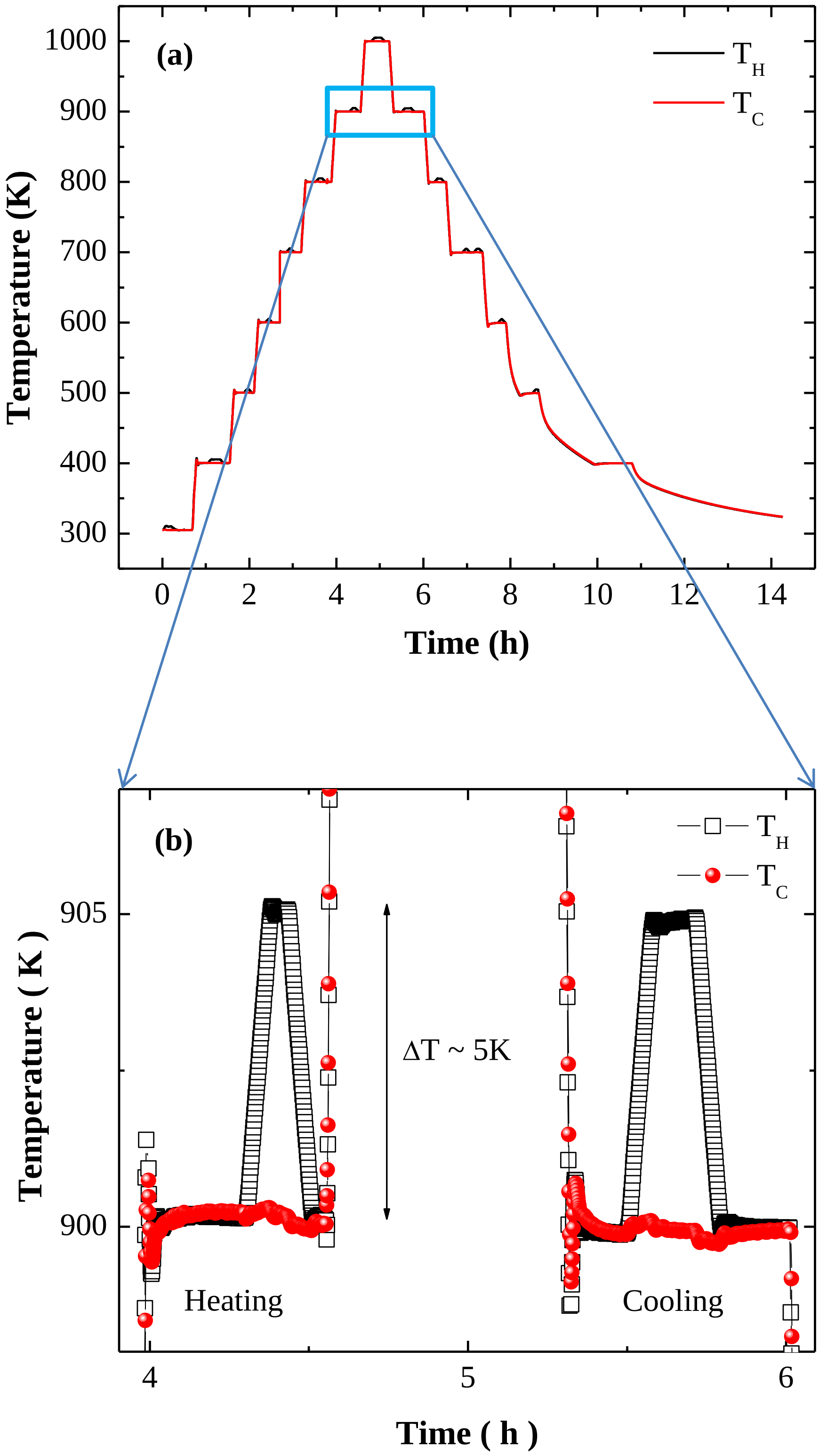

Figure 4.14 (a) Temperature profile of a sample during Seebeck coefficient and resistivity measurements during heating and cooling cycles as a function of time. **(b)** the closer view of figure 6.a, 5K temperature gradient during heating and cooling.

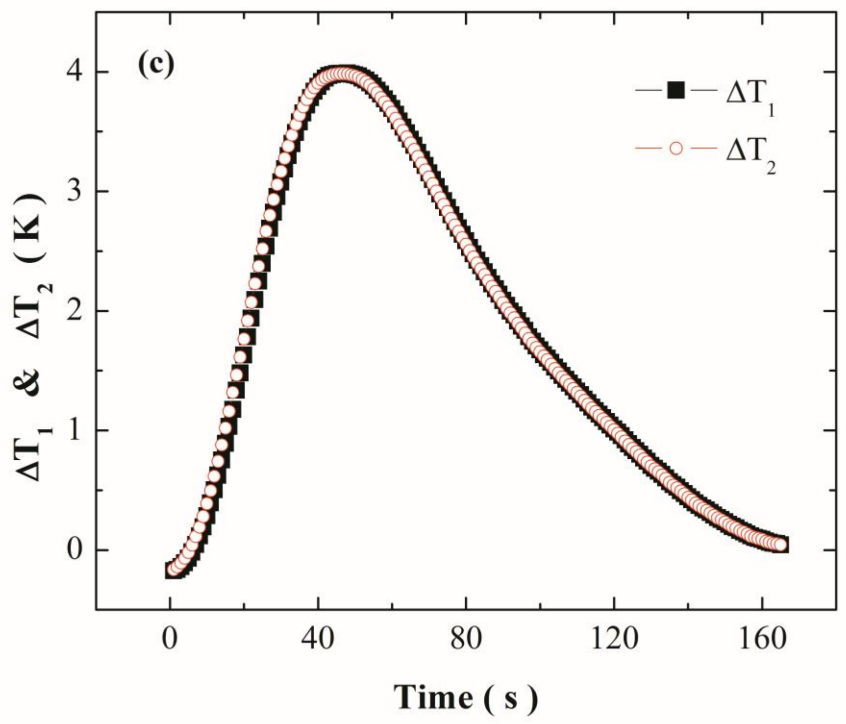

Figure 4.15 The comparison of temperature gradient data measured via differential method (ΔT_1) and the subtraction of hot and cold side temperatures (ΔT_2).

4.8 Reference Measurement Results

The accuracy and the reliability of the system has been tested using pure Pt and Nb reference samples. Seebeck coefficient and resistivity measurements of these reference samples are conducted from 300 K to 1000 K under vacuum. The obtained results are compared with theoretical values from the literature.

4.8.1 Seebeck Coefficient Measurements

Two measurement techniques which are differential and integral methods [29] that differ in the magnitude of the temperature gradient are mainly used in order to measure the Seebeck coefficient of the materials. Since there are some drawbacks of integral method [26], in which the reason is detailed in the section 4.2.1, steady-state differential method is preferred for our system. The description of the apparatus and instrumentation for high temperature implementation of the differential steady-state method has already been provided in detail [1, 2, 26]. The measurements result carried out by using the improvements as explained in section 4.5 will be given here. Type-K thermocouples (chromel-alumel) 0.125 mm thick are used for Seebeck voltage and temperature measurements. In our system, platinum wire (0.8 mm radius and 12 mm long) and niobium rod (3 mm radius and 12 mm long) are chosen as reference materials. In order to check the reliability and the accuracy of the system and to understand any structural and/or electrical changes in the sample, the Seebeck coefficient measurements during heating and cooling cycles are significant. If the accuracy of the system is good, a significant difference in Seebeck coefficient and resistivity measurements from heating and cooling modes would indicate a change in the sample. The reason can be a change in the oxidation state of the sample during the measurement [30]. Obtained Seebeck coefficient data points for reference samples are different by about ± 0.10 and ± 0.15 μV/K than the results of the theoretical for Pt [2, 30] and for Nb data [51], respectively. Such differences are quite small when compared within the experimental uncertainty and with other reported results [52].

Thermoelectric voltage was measured from the positive (chromel) legs of the thermocouples that were mutually placed at the both ends of the sample. Time dependent temperature gradient (dT/dt) and thermoelectric voltage (dV/dt) were recorded synchronously during the measurement, during heating and cooling cycles using a software written in our laboratory. Typical measurements of the thermoelectric voltage plotted against temperature gradient and linear fitting of these data took place at room temperature in relative Seebeck coefficient for platinum wire and niobium rod shown in figure 4.16 (a) and figure 4.16 (b), respectively. The intercept should ideally be null but usually it is not because of various voltage offsets [30]. Both error bars for voltage and temperature are indicated with red color.

The absolute value was calculated by adding the Seebeck coefficient of the chromel leg of Type-K (Table 4.2) thermocouple at each temperature interval from the relative one considering the measurement uncertainties in the intercept at $\Delta T = 0K$.

Table 4.2 Seebeck coefficient values of chromel leg of Type-K thermocouple at each 100 K temperature interval.

Temperature (K)	**Seebeck coefficient of chromel leg (µV/K)**
300	29.25
400	27.46
500	25.69
600	23.85
700	21.98
800	20.07
900	18.12
1000	16.13
1100	14.11

Seebeck coefficient measurements were repeated at least 3 times at each temperature level. Seebeck coefficient of platinum wire and niobium rod were measured at every interval of 100 and 50 K, respectively from 300 to 1000 K as seen in figure 4.17. The results of the Seebeck coefficient measurements conducted in this study are in very good agreement with the reference data [2] over the whole temperature range. The total error in the Seebeck coefficient measurements for any given temperature is estimated to be less than 2.6 % for both platinum and niobium samples.

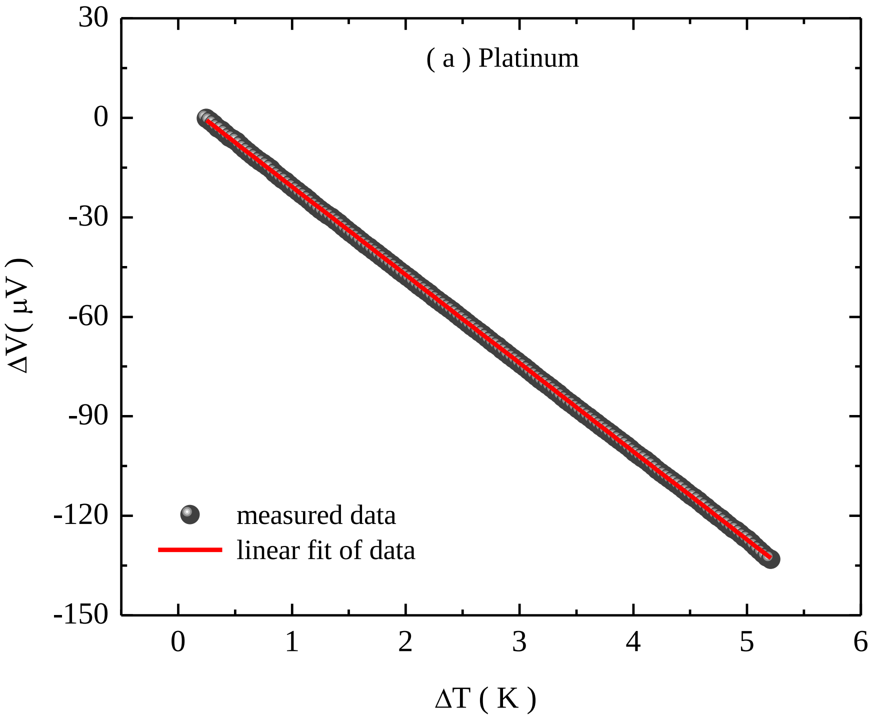

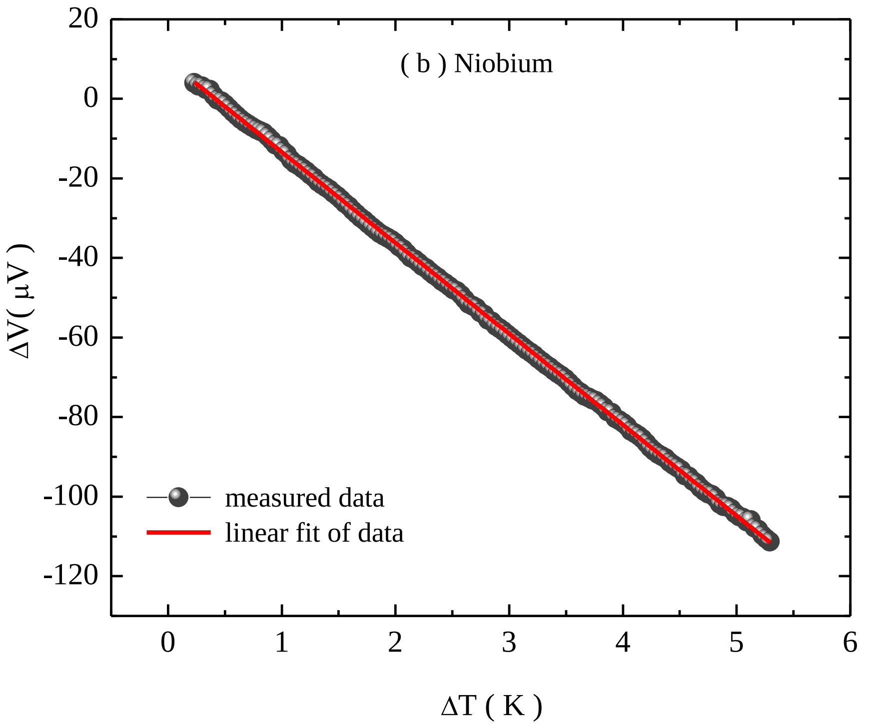

Figure 4.16 Data and linear fit graphs for ΔV versus ΔT for platinum wire **(a)** and niobium rod **(b)** at room temperature. The estimated measurement error is less than 2.6 % for both Pt wire and Nb rod.

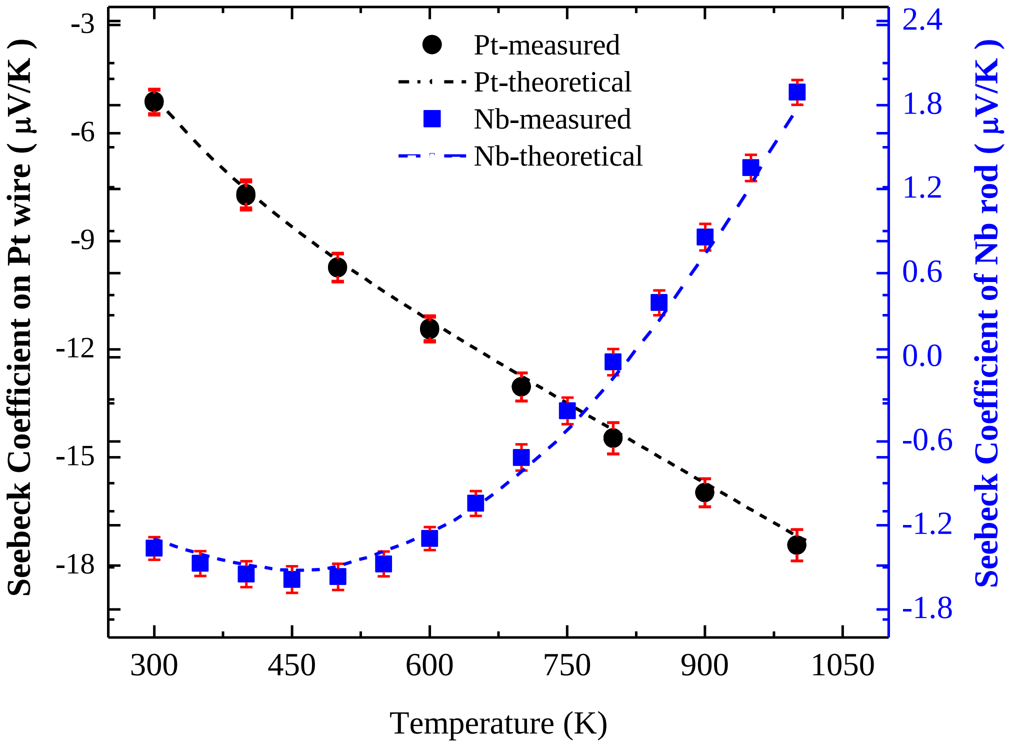

Figure 4.17 Temperature dependent absolute Seebeck coefficient values of platinum wire (black solid circle) and niobium rod (blue solid square) with respect to theoretical reference data [2, 30, 51]. Error bars for both samples are indicated with red color.

4.8.2 Resistivity Measurements

A four-point probe technique was used for resistivity measurements under the conditions given in section 4.3. In our design, the temperature gradient between two ends of the sample is less than 0.05 K for each temperature range. I_{src}, the applied current is typically from 1 to 100 mA depending on the electrical conductivity of the sample. A direct current for short time (0.1 sec) was applied in order to avoid the Peltier effect [26]. Wires were twisted to avoid magnetic field coupling [50]. The resistivity measurement is, in general, less prone to errors than thermopower measurement. Resistance measurements were repeated at least 3-times at each temperature interval to ensure the reliability of the measurements. The measurement uncertainty is estimated for resistivity measurement is less than 1 %.

Table 4.3 Resistivity values of platinum wire. Percentage difference of measurements is calculated based on each earlier report and represented by their reference numbers.

T(K)	**Burkov [2]**	**Powell [53]**	**Martin [54]**	**Our Result**	***Ref.* [2]**	***Ref.* [53]**	***Ref.* [54]**
	ρ ($\mu\Omega$.cm)				**(%) Difference**		
273	-	9.9	9.76	-	-	-	-
300	10.96	10.95	10.8	11.02	0.54	0.63	1.99
400	14.75	14.78	14.6	14.82	0.47	0.26	1.48
500	18.45	18.37	18.28	18.52	0.37	0.80	1.29
600	22.04	21.95	21.84	22.09	0.22	0.63	1.13
700	25.52	25.42	25.3	25.61	0.35	0.74	1.21
800	28.85	28.76	28.64	28.96	0.37	0.69	1.10
900	32.05	31.96	31.87	32.11	0.18	0.46	0.74
1000	35.12	35.44	34.98	35.23	0.31	0.59	0.70

The result of the resistivity measurement of platinum wire that is conducted in our laboratory is in good agreement with the reference data performed independently by Burkov *et al.* [2], Powell *et al.* [53], and Martin *et al.* [54] over the same temperature range with less than 2 % difference as given in table 4.3. The resistivity measurement result of niobium rod is demonstrated in table 4.4. This result shows that the measurement result of niobium is in good agreement among individual measurements presented in literature [55, 56] with less than 0.7 % difference.

Table 4.4 Resistivity values of niobium rod. Percentage difference of measurements was calculated based on the earlier report and represented by its reference number.

T(K)	**K.D. Maglić [55] ρ ($\mu\Omega$.cm)**	**Our Result ρ ($\mu\Omega$.cm)**	**(%) Difference**
300	15.08	15.06	0.13
350	--	17.57	--
400	19.75	19.64	0.56
450	--	21.76	--
500	23.95	23.83	0.50
550	--	25.83	--
600	27.92	27.75	0.61
650	--	29.69	--
700	31.69	31.65	0.12
750	--	33.33	--
800	35.28	35.11	0.48
850	--	36.90	--
900	38.72	38.57	0.38
950	--	40.24	--
1000	42.02	41.99	0.07

4.9 Conclusion

A detailed description of a system that was designed to measure the thermoelectric properties of one and/or two samples at high temperature with good accuracy is presented. Seebeck coefficient, four-point probe resistivity and differential temperature gradient can be measured under controlled vacuum and/or any inert atmosphere. The main features of the system are accuracy and precision with the help of the beadless thermocouple design and improved contact configurations. Moreover, external magnetic field around the sample is eliminated by micro heaters that response quickly and effectively for good temperature control. The device is easy to operate and suitable for bulk samples with a broad range of physical types and shapes. Since the system is modular, design allows user to replace the temperature sensors without dispatching the whole sample probe and/or the system itself. The evaluation of the results is presented in detail in chapter 7.

REFERENCES

[1] Z. H. Zhou and C. Uher, Apparatus for Seebeck coefficient and electrical resistivity measurements of bulk thermoelectric materials at high temperature, Rev. Sci. Instrum. 76 (2005) pp 023901

[2] A. T. Burkov, A. Heinrich, P. P. Konstantinov, T. Nakama and K. Yagasaki, Experimental set-up for thermopower and resistivity measurements at 100–1300 K Meas. Sci. Technol. 12 (2001) pp 264–72

[3] D. Zoltan and G. Stapfer, Measurement of Seebeck coefficient using a light-pulse Rev. Sci. Instrum. 56 (1985) pp 719–22

[4] C. Wood, A. Chmielewski, D. Zoltan, Measurement of Seebeck coefficient using a large thermal-gradient, Rev. Sci. Instrum. 59 (1988) pp 951–4

[5] J. L. Short, J. D'Angelo, A. D. Downey, M. A. Pajor, E. Timm, H. Schock, M. G. Kanatzidis and T. P. Hogan, Characterization of thermoelectric power generation modules made from new materials Mater. Res. Soc. Symp. P. 866 (2006) pp 309–15

[6] V. Ponnambalam, S. Lindsey, N. S. Hickman and T. M. Tritt, Sample probe to measure resistivity and thermopower in the temperature range of 300–1000 K, Rev. Sci. Instrum. 77 (2006) pp 073904

[7] T. P. Hogan, S. Y. Loo and F. Guo, Thermoelectric measurements low temperature electronics and low temperature cofired ceramic based electronic devices, Electrochem. Soc. Series 27 (2004) pp 231–46

[8] S. Y. Loo, K. F. Hsu, M. G. Kanatzidis and T. P. Hogan, High temperature power factor measurement system for thermoelectric materials, Proc. Electrochem. Soc. 27 (2004) pp 247–56

[9] G. T. Kim, J. G. Park, J. Y. Lee, H. Y. Yu, E. S. Choi, D. S. Suh, Y. S. Ha and Y. W. Park, Simple technique for the simultaneous measurements of the four-probe resistivity and the thermoelectric power, Rev. Sci. Instrum. 69 (1998) pp 3705–6

[10] S. R. S. Kumar and S. Kasiviswanathan, A hot probe setup for the measurement of Seebeck coefficient of thin wires and thin films using integral method, Rev. Sci. Instrum. 79 (2008) pp 024302

[11] S. Loo, J. Short, K. F. Hsu, M. Kanatzidis and T. Hogan, High temperature measurement system design for thermoelectric materials in power generation application, Thermoelectric Materials 2003 Research Applications 793 (2004) pp 375–83

[12] S. Fujimoto, H. Kaibe, S. Sano and T. Kajitani, Development of transient measurement method for investigating thermoelectric properties in high temperature region, Japan. J. Appl. Phys. 45 (2006) pp 8805–9

[13] T. Hogan, S. Loo, F. Guo and J. Short, Measurement techniques for thermoelectric materials and modules, Thermoelectric Materials 2003 Research and Applications 793 2004 pp 405–11

[14] M. Kawai, T. Miyakawa, T. Tako, Ac measurement of Seebeck coefficient in disk-shaped semiconductors using CW-lasers, Japan. J. Appl. Phys. 23 (1984) pp 1202–8

[15] G. Min and D. M. Rowe, A novel principle allowing rapid and accurate measurement of a dimensionless thermoelectric figure of merit, Meas. Sci. Technol. 12 (2001) pp 1261–2

[16] T. Dasgupta and A. M. Umarji, Apparatus to measure high-temperature thermal conductivity and thermoelectric power of small specimens, Rev. Sci. Instrum. 76 (2005) pp 094901

[17] S. S. Lee and M. Kimura Short-circuit measurement by Seebeck current detection of a single thermocouple and its application, Sensors Actuators A 139 (2007) pp 104–10

[18] B. Poumellec, F. Marcelet, F. Lagnel and J. F. Marucco, Computer-controlled simultaneous measurements of the thermopower and conductivity of thin-films, J. Phys. E: Sci. Instrum. 21 (1988) pp 159–63

[19] A. Trestmanmatts, S. E. Dorris and T. O. Mason, Measurement and interpretation of thermopower in oxides, J. Am. Ceram. Soc. 66 **(**1983) pp 589–92

[20] I. A. Nishida, Measurements of electrical properties In CRC handbook of thermoelectrics, Rowe D M, ed. (1994) CRC Press Boca Raton FL US

[21] H. C. Montgomery, Method for measuring electrical resistivity of anisotropic materials, J. Appl. Phys. 42 (1971) pp 2971 - 5

[22] J. D’Angelo, A. Downey, T. Hogan, Temperature dependent thermoelectric material power factor measurement system, Rev. Sci. Instrum. 81 (2010) pp 075107

[23] J. D’Angelo, E. D. Case, N. Matchanov, C. I. Wu, T. P. Hogan, J. Barnard, C. Cauchy, T. Hendricks and M. G. Kanatzidis, Electrical, thermal, and mechanical characterization of novel segmented-leg thermoelectric modules, J. Electron. Mater. 40 (2011) pp 2051–62

[24] S. Iwanaga, E. S. Toberer, A. LaLonde and G. J. Snyder, A high temperature apparatus for measurement of the Seebeck coefficient, Rev. Sci. Instrum. 82 (2011) pp 063905

[25] P. H. M. Böttger, E. L. Flage, O. B. Karlsen, and T. G. Finstad, High temperature Seebeck coefficient and resistance measurement system for thermoelectric materials in the thin disk geometry, Rev. Sci. Instrum. 83 (2012) pp 025101

[26] J. Martin, T. Tritt and C. Uher, High temperature Seebeck coefficient metrology, J. Appl.Phys. 108 (2010) pp 121101

[27] J. Ravichandran, J. T. Kardel, M. L. Scullin, J. H. Bahk, H. Heijimerikx, J. E. Bowers, and A. Majumdar, An apparatus for simultaneous measurement of electrical conductivity and thermopower of thin films in the temperature range of 300–750 K, Rev. Sci. Instrum. 82 (2011) pp 015108

[28] R. Wolfe and G. E. Smith, Effects of a magnetic field on the thermoelectric properties of a bismuth-antimony alloy, Appl. Phys. Lett. 1 (1962) pp 5

[29] A. T. Burkov, Thermoelectric Handbook: Macro to Nano, D. M. Rowe ed. (2006), CRC Press Boca Raton FL US

[30] C. Byl, D. Bérardan and N. Dragoe, Experimental setup for measurements of transport properties at high temperature and under controlled atmosphere, Meas. Sci. Technol. 23 (2012) pp 035603

[31] O. P. Astakhov, V. V. Lobankov and B. M. Surkov, Apparatus for Measuring Thermoelectric Power and Electrical Conductivity of Semiconductors Up to 1000 °C Meas. Tech+ 15 (1972) pp 889-890

[32] R. B. Crawford, Industrial applications of temperature difference measurements temperature, its measurement and control in science and industry, Remhold Publishing Corporation New York, Part 2, 3 (1962) pp 913-925

[33] J. D. Nobel, Heat conductivity of steels and a few other metals at low temperatures, Physica, 17 (1951) pp 551-562

[34] T. M. Tritt and V. Browning, Overview of measurement and characterization techniques for thermoelectric materials, Sem. Semimet. 69 (2001) pp 25-49

[35] A. L. Pope, R. T. Littleton IV, and T. M. Tritt, Apparatus for the rapid measurement of electrical transport properties for both "needle-like" and bulk materials, Rev. Sci. Instrum. 72 (2001) pp 3129 -3131

[36] J. Kopp and G. A. Slack, Thermal contact problems in low temperature thermocouple thermometry, Cryogenics, 11 (1971) pp 22-25

[37] T. Heikes and R. W. Ure, Thermoelectricity: Science and Engineering Interscience, New York USA (1961) pp 311

[38] A. T. Burkov, Thermoelectrics Handbook: Macro to Nano (CRC, Boca Raton, FL (2005) pp 22

[39] R. M. White, Sandia Laboratories Report No. SC-RR-68-636 (1968)

[40] R. L. Powell, W. J. Hall, and J. G. Hust, Temperature, Its Measurement and Control in Science and Industry (Instrument Society of America, Pittsburgh, PA, 4 (1972) pp 1423

[41] L. R. Testardi and G. K. McConnell, Measurement of the Seebeck coefficient with small temperature differences, Rev. Sci. Instrum. 32 (1961) pp 1067

[42] J. E. Ivory, Rapid method for measuring Seebeck coefficient as ΔT approaches zero, Rev. Sci. Instrum. 33 (1962) pp 992

[43] C. N. Berglund and R. C. Beairsto, An automatic technique for accurate measurements of Seebeck coefficient, Rev. Sci. Instrum. 38 (1967) pp 66

[44] L. J. Van der Pauw, A method of measuring specific resistivity and hall effect of discs of arbitrary shapes, Philips Res. Repts. 13 (1958) pp 1-9

[45] L. J. Van der Pauw, A method of measuring the resistivity and hall coefficient on lamellae of arbitrary shape, Philips Tech. Rev. 20 (1958) pp 220-224

[46] Y. Dodge, The Oxford Dictionary of Statistical Terms, OUP. ISBN 0-19-920613-9 (2003)

[47] Hazewinkel, Michiel, ed. "Quadratic deviation", Encyclopedia of Mathematics, Springer, ISBN 978-1-55608-010-4 (2001)

[48] M. A. Stephens, EDF statistics for goodness of fit and some comparisons, *J. Am. Stat. Assoc.* 69 (1974) pp 730-737

[49] N. Angelidis, C. Y. Wei and P. E. Irving, The electrical resistance response of continuous carbon fibre composite laminates to mechanical strain, Composites: Part A 35 (2004) pp 1135-1147

[50] Keithley 2004 Low Level Measurements Handbook – Precision DC Current, Voltage, and Resistance Measurements 6th edition Keithley Instruments 28775 Cleveland Ohio U S A

[51] H. Brodowsky, Q. Chen, Z. Xiao and Z. Yin, Calculation of the thermoelectric power of vanadium, niobium, and tantalum, J. Electron. Mater. 40 (2011) pp 1984

[52] N. D. Lowhorn, W. Wong-Ng, W. Zhang, Z. Q. Lu, M. Otani, E. Thomas, M. Green, T. N. Tran, N. Dilley, S. Ghamaty, N. Elsner, T. Hogan, A. D. Downey, Q. Jie, Q. Li, H. Obara, J. Sharp, C. Caylor, R. Venkatasubramanian, R. Willigan, J. Yang, J. Martin, G. Nolas, B. Edwards, T. Tritt, Round-robin measurements of two candidate materials for a Seebeck coefficient Standard Reference Material, Appl. Phys. A 94 (2009) pp 231–234

[53] R. W. Powell, R. P. Tye, The promise of platinum as a high temperature thermal conductivity reference material, Br. J. Appl. Phys. 14 (1963) pp 662

[54] J. J. Martin, P. H. Sidles, G. C. Danielson, Thermal diffusivity of platinum from 300K to 1200K, J. Appl. Phys. 35 (1967) pp 3075

[55] K. D. Maglić, N. L. Perović, G. S. Vuković, L. P. Zeković, Specific heat and electrical resistivity of niobium measured by subsecond calorimetric technique, International Journal of Thermophysics 15 (1994) pp 963-972

[56] J. M. Abraham, B. J. Devoit, Resistivite d'un niobium de haute purete de 20 °k a la temperature de fusion, Less-Common Met. 29 (1972) pp 311

CHAPTER 5

THE EFFECT OF NANOSTRUCTURING AND POROSITY ON $Ca_3Co_4O_9$ METAL OXIDE

In this part of the thesis, the variation of *Seebeck coefficient, electrical resistivity and thermal conductivity* values individually via low dimensional systems on cobalt oxide thermoelectric material is presented. The size and porosity effect have been proven to enhance figure of merit of cobalt oxide material. Nano-grained structure helps to reduce phonon contribution to the thermal conductivity by phonon-scattering at grain boundaries and interfaces leading to reduce the total thermal conductivity without severely degrading electrical conductivity or suppressing Seebeck coefficient.

A significant amount of research has been performed on thermoelectrics to improve their efficiency for industrial and automobile applications [1]. Interest has grown in this area due to increasing awareness of the deleterious effect of fossil fuels, which are supposedly the major sources of CO_2 emissions and lead to global warming [2]. Over the last decade, the demand for renewable energy sources, such as TEs, has increased for long-life electrical power sources [3]. Thermoelectric materials, which exhibit high conversion efficiencies and contain non-toxic and abundantly available elements with high chemical stability in air even at temperatures of 800 - 1000 K, must be used effectively for the efficient conversion of heat into electricity [4, 5].

The performance of a thermoelectric material is characterized by the dimensionless figure of merit $ZT = S^2T / \rho\kappa$, where S , T , ρ and κ represent Seebeck coefficient, absolute temperature, electrical resistivity and thermal conductivity, respectively. A good thermoelectric material should exhibit a large thermopower, low electrical resistivity, and low thermal conductivity [6, 7]. However, in most materials, high electrical conductivity is generally accompanied by high thermal conductivity according to the Wiedemann-Franz law. Hence, Dresselhaus *et al.* [8] proposed that it is possible to vary the values of S, ρ, and κ individually using low-dimensional systems by introducing interfaces, which scatter phonons more effectively than electrons or serve to scatter out the low energy electrons. The structural modifications may lead not only to a decrease of the thermal conductivity but also to an enhanced power factor. To achieve this goal, an attempt was made to introduce nano-grained bulk materials to reduce the phonon contribution to the thermal conductivity through phonon-scattering at grain boundaries and interfaces, leading to a reduction of the thermal conductivity without severely degrading the electrical conductivity or suppressing the thermopower ($S^2\sigma$) [9]. Because the thermal conductivity of a thermoelectric material can be decreased by increasing boundary scattering, a thermoelectric device is expected to maintain a large temperature difference across its two sides, leading to an improvement in its performance.

Several reviews have provided insight into the properties of nanocrystalline [10] and nanostructured regions [11] and interfaces [12] in bulk thermoelectric materials. A recent study performed by Nong *et al.* demonstrated that metallic nano-sized inclusions are promising for enhancing the Seebeck coefficient and reducing the electrical resistivity [13]. As an example of the numerous theoretical studies related to the size effect of the properties of thermoelectric materials [14-16], a recent study [17] illustrated that these thermoelectric properties are size dependent. Although a ceramic with a grain size of 6.4 nm exhibited a ZT of approximately 1.13 at 300 K [18], it is very difficult to synthesize ceramics with such small grain sizes [19]. Therefore, the thermoelectric performance of ceramics as a function of grain size should be evaluated to better understand the effect of the grain size on thermoelectric performance.

Another possible approach to reduce the thermal conductivity involves the porosity. The porosity can be proportional to the thermal conductivity; that is, a porous structure can contribute to the reduction of the thermal conductivity as a thermal barrier (resistance). It is investigated that when the density of a nanocomposite changes by only a few percent, the effect of porosity on the electrical conductivity of the material changes by orders of magnitude [8]. However, porosity may produce different effects for different materials; for example, experimental results on nanograined SiGe have revealed that porosity causes a significant increase in the resistivity, which results in a lower *ZT* [20]. The positive contribution of porosity to decreasing the thermal conductivity has also been observed. For instance, nanoporous [21-25] and mesoporous [26] structures were introduced as new approaches to further contribute to enhance *ZT*. The results were attributed to the reduction of the phonon mean free path and, thus, the lattice thermal conductivity. Furthermore, it was also asserted that a possible increase in *ZT* can be achieved due to the 30 % increase in the ratio of electrical conductivity to thermal conductivity obtained using a micro-sized porous structure [27]. Similar results have been observed in thin films [28-30]. Therefore, electrical and structural optimization of electron and phonon transports must be very effective to improve their conversion efficiencies using the aforementioned techniques (nanostructuring and porosity).

Cobalt oxides ($Na_xCo_2O_4$), which were first considered as thermoelectric materials by Terasaki et al. [31], exhibit extraordinary thermoelectric properties as metal oxides. These metal oxides are thermodynamically stable at elevated temperatures, nontoxic, abundant, easy to fabricate and economical [32, 33]. $Ca_3Co_4O_9$ (C-349) is a promising material among these oxides due to its high Seebeck coefficient, low thermal conductivity and low electrical resistivity values at high temperatures. This compound belongs to the family of misfit cobalt oxides, and the structure of the crystal can be described as an alternate stacking along [001] of distorted rock-salt-type slabs [Ca_2CoO_3] and [CoO_2] layers, resulting in a distorted CdI2-type structure [34]. In these layers, the CoO_2 nanosheets contain a strongly correlated electron system and a Ca_2CoO_3 misfit layer, which serves as an electronic transport layer acting as a potential phonon scattering region [35-38].

Further developments require a better understanding of the mechanism of the aforementioned unique behaviors. However, no detailed reports are available on the C-349 thermoelectric metal oxide concerning the combined nanostructure and porosity. In this work, the effect of nanostructuring and porosity on the thermal and electrical properties of C-349 ceramics is reported. Our goal is to optimize these two features to decrease the total thermal conductivity without significantly degrading the Seebeck coefficient or electrical conductivity. To attain this objective, C-349 metal oxide thermoelectric materials with average grain sizes ranging from 68 to 18 nm were synthesized via the citrate sol-gel method and their thermoelectric and structural properties were compared with those of their bulk counterparts with 2 μm average grain sizes. A great enhancement in *ZT* was achieved in the nanostructured materials.

5.1 Experimental Procedure

The $Ca_3Co_4O_9$ composition can be obtained by solid-state [39-42] coprecipitation of oxalates [43] or various sol-gel methods [44-46]. The sol-gel method is one of the best synthesis methods that yield homogeneous nanoparticles [47, 48]. In this study, the citrate sol-gel process [49] was applied to synthesize C-349 thermoelectric materials with particle sizes ranging from the nanoscale to the microscale. First, stoichiometric mixtures of high-purity calcium nitrate and cobalt nitrate salts with the chemical formulas $Ca(NO_3)_2.4H_2O$ and $Co(NO_3)_2.6H_2O$, respectively, were dissolved in an aqueous solution of ~0.01M citric acid. PEG 400 and citric acid were used as a dispersant and complexion agent, respectively, in the nitrate solution during the formation of the sol precursor; strong aggregation of the particles is supposed to be prevented in the colloidal solution. Then, 3, 5 and 7 % PEG 400 was added to the C-349 solutions to produce particles with different sizes. Another sample with a 2-μm average grain size was synthesized using the same method without the PEG 400 addition. A reflux was applied for 2 h to prevent evaporation before the completion of the dissolution. Then, the resulting solution was heated at 353 K with continuous stirring, removing the reflux for gelation. Then, the violet-colored gel was dried initially at 393 K for 12 h before being further calcined in air at a ramp rate of 10 °C/min in a programmable box furnace (Protherm) at 1023 K for 2 h to remove any organic compounds and to yield pure C-349 phase powder samples. Finally, the synthesized powders were ground in an agate mortar. These fine powders were cold pressed into a pellet shape of 16 x 20 x 20 mm^3 size, and then, conventional annealing was applied at 1123 K for 2 h to obtain a pure C-349 phase. The samples were consolidated into bulk pellets by cold compaction and sintering. These pellets were cut into disks with diameter of 15.84 mm for the thermal conductivity measurements. To perform the Seebeck coefficient and electrical resistivity measurements, the pellets were again cut into bars with dimensions of 3 x 3 x 12 mm^3 to specify the heat flow direction and to conduct the thermoelectric properties measurements in the same direction. Finally, four samples with average grain sizes of 18, 30 and 68 nm and 2 μm were successfully synthesized and labeled as S7, S5 and S3 and S0, respectively. The sizes were measured for the powder after the first annealing. Table 5.1 shows the amount of chemical used for the synthesis of C-349 materials.

Table 5.1 The amount of chemical used for the synthesis of C-349 materials.

Sample	Molarity	Ca-Nitrate Solution	Co-Nitrate Solution	PEG-400	Citric Acid
S0	0.01 M	15 ml	20 ml	% 0 of volume	1.4709 g
S3	0.01 M	15 ml	20 ml	%3 of volume 1.05 ml	1.4709 g
S5	0.01 M	15 ml	20 ml	%5 of volume 1.75 ml	1.4709 g
S7	0.01 M	15 ml	20 ml	%7 of volume 2.45 ml	1.4709 g

For continuous reading and for better understanding the achievements and conclusion are introduced with the obtained results. This section is divided in two parts: structural characterization and thermoelectric analyses.

5.2 Structural Characterizations

To obtain a pure phase for the C-349 materials, the annealing temperature was selected based on the TG-DTA analysis. The results of the TG and DTA analysis of the dried gel are presented in figure 5.1. The C-349 phase can be seen at 1040 K, according to the analysis of the TG and DTA curves. The wide endothermic peaks at 533 and 560 K accompanied by the weight loss of 12.3 % originate from the decomposition of excess citric acid and nitrate salts. Two successive exothermic peaks are observed near 633 and 684 K and are accompanied by a two-step weight loss of 16.1 %; these peaks are assigned to the decomposition of the citrate complex into Co_3O_4 and $CaCO_3$. The endothermic peak over the range of 1009 - 1040 K is associated with the decomposition of $CaCo_3$ to CaO - CaO reaction with Co_3O_4. Therefore, a sintering temperature of 1123 K was selected, which enables us to obtain pure C-349 powders.

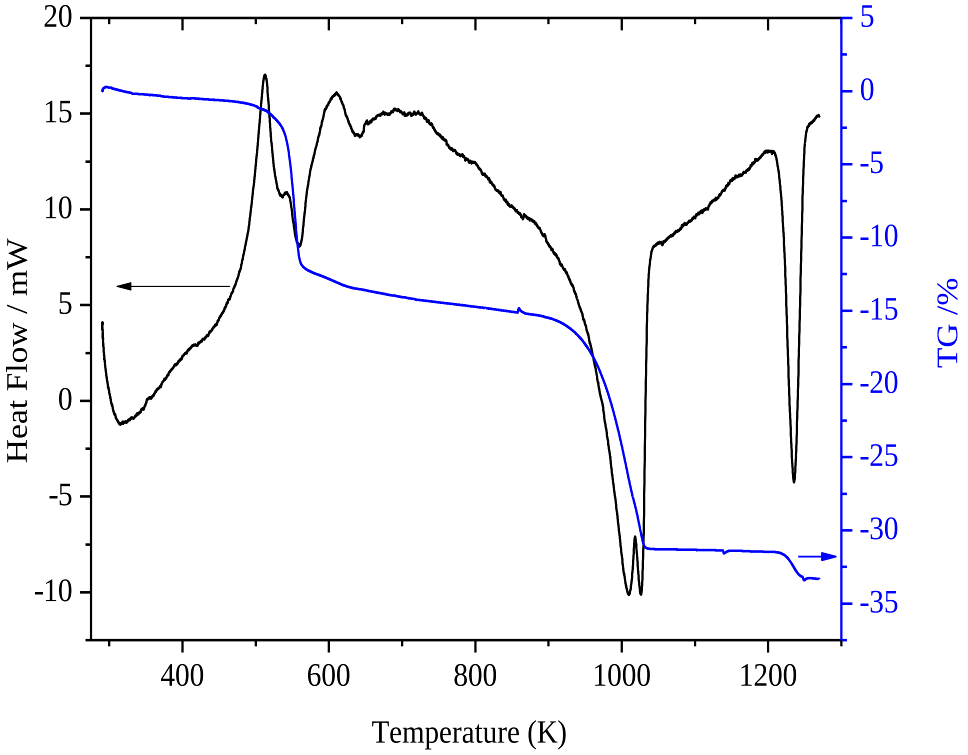

Figure 5.1 The results of TG and DTA analyses.

X-ray diffractograms show that all of the peaks can be indexed as the $Ca_3Co_4O_9$ phase with monoclinic symmetry [56], which indicates that C-349 materials were prepared successfully using the citrate sol-gel method (see figure 5.2). No observable traces of extraneous phases or impurities were detected. Due to the particle sizes falling in the nano-range for the S3, S5 and S7 samples, broader diffraction peaks are observed compared with the micro-structured S0 sample.

The particles in this figure have spherical shapes. In figure 5.3, the particle size of the samples is plotted as a function of the quantity of PEG 400, which was measured from the FE-SEM images. Sample S0 has an average particle size of approximately 2 μm with a density of 80 % without the PEG 400 addition, while the addition of 3, 5 and 7 % PEG 400 resulted in decreases in the density and average particle size to 74.2 %/~55-70 nm, 72.5 %/~35-45 nm, and 66 %/~18-25 nm, respectively, as observed in figures 5.4(b), 5.4(c) and 5.4(d), respectively. The particle size of the C-349 samples was observed to decrease significantly with increasing quantities of PEG 400. Interestingly, except for the coarse-grained S0 sample, the other samples exhibit similar structures.

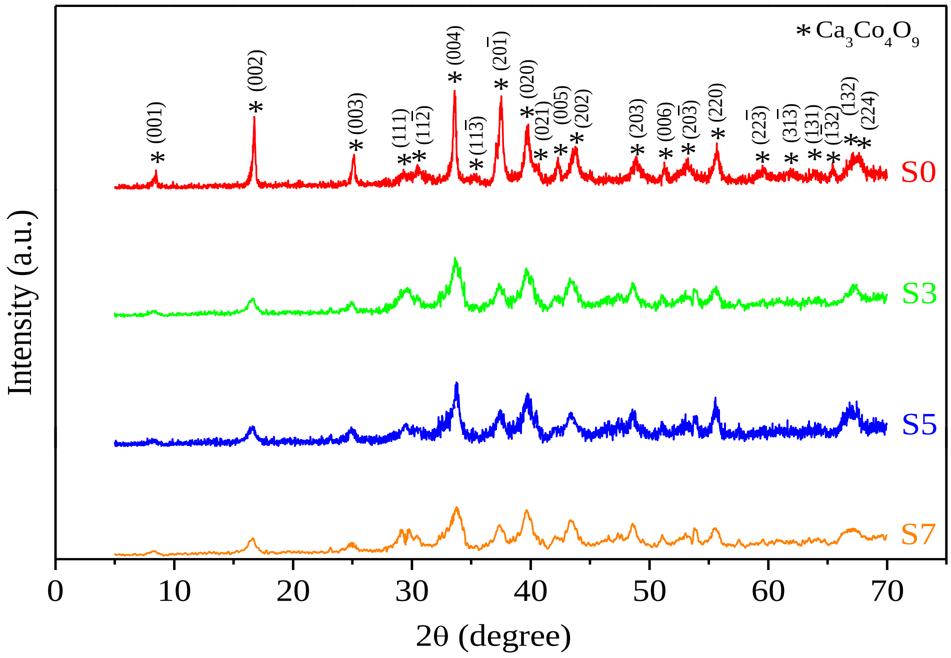

Figure 5.2 XRD patterns of C-349 compounds.

When the particle size measurements and calculations (BET and Scherrer formula) are compared with FE-SEM images, the sizes of the particles are not different. It is difficult to distinguish such small particles due to charging during the analysis. Pt or Au coatings are also not helpful because these coatings cover these strongly aggregated particles, and therefore, the particles cannot be observed using this approach. Strong aggregation is observed, which is due to the formation of covalent or metallic bonds that cannot be easily disrupted on the nanoscale [57]. Therefore, the particle size observed from FE-SEM images is compared with the techniques discussed later to confirm the results.

The Mie scattering principles is used for particle size analysis and results are given in table 5.2. The results, which were obtained after sonicating for at least 3 h before analysis, are more accurate and also consistent with other results acquired using different methods. For instance, the average particle size of the powders calculated using the Scherrer formula is ~ 17 nm, whereas the Mie scattering principle result indicates an average particle size of ~ 18 nm for sample S7.

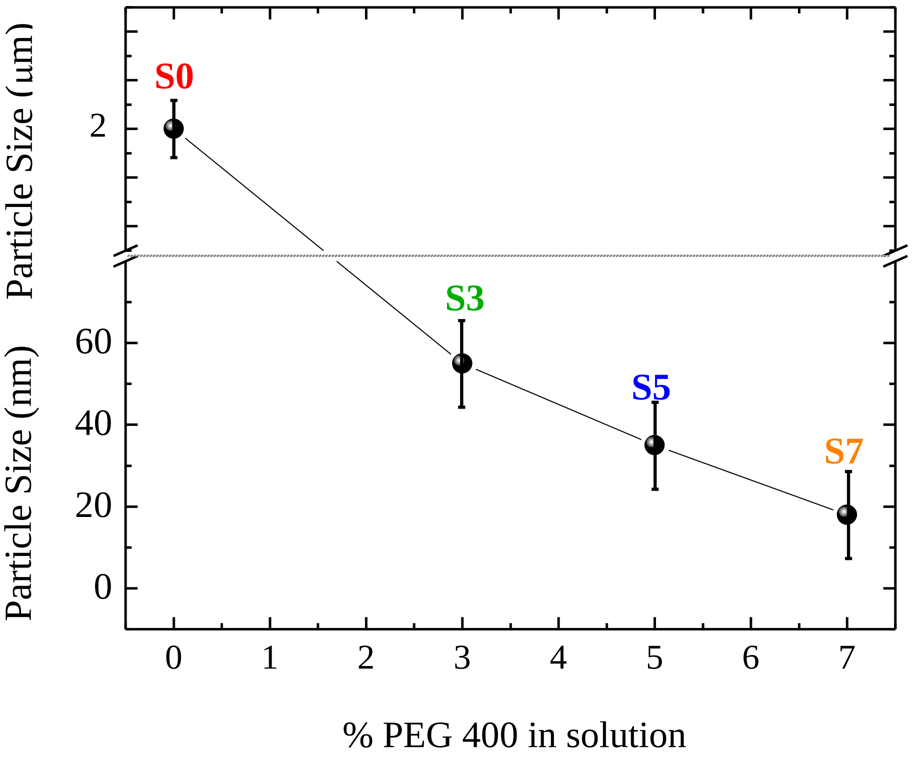

Figure 5.3 The particle size of the samples calculated using FE-SEM images vs % PEG 400 in solution.

The particle size results for all the samples obtained using the Mie scattering principle and Scherrer formula are listed in table 5.2. If nanoparticles exist in a dry powder in an aggregated form, such as the materials used in this research, a reasonable primary particle size may be obtained by calculating the average particle diameter using a measured BET surface area. Powder surface areas varying from 3.98 to 66.08 m^2 g^{-1} were determined using BET analysis. An average particle diameter was calculated assuming porous spherical particles and the theoretical density of the individual materials. Without presenting the entire derivation, the equation for calculating the average particle diameter in nanometers is 6000/(BET surface area in m^2/g) x (density in g/cm^3). The calculated particle sizes from the BET analysis are in good agreement with other results obtained using other experimental methods, as shown in table 5.2. The slightly larger particle sizes observed using the BET analysis are due to the low surface area, which indicates strong aggregation and high porosity. Although PEG 400 is useful in reducing the material dimensions of the particles, its inclusion did not sufficiently prevent the aggregation of particles. It is rather challenging to obtain such small particles in ceramic materials. However, particle sizes in these ranges can be obtained using a very low molar ratio (0.01 M), enough PEG and citric acid, and an optimized sintering time and temperature. These results indicate that various quantities of PEG 400 in aqueous solution yield various nano-sized particles using the citrate sol-gel method. As demonstrated in table 5.2, all the results are in good agreement with the results of the particle size analysis and most of the FE-SEM images.

Table 5.2 The result of measured and calculated particle size and density values of all samples. Samples are entitled as S0, S3, S5 and S7 that corresponds to the percentage of PEG 400 addition.

	S0	**S3**	**S5**	**S7**
PEG-400 (%)	0	3	5	7
Density (g/cc)	3.72	3.47	3.39	3.08
BET (m^2/g) surface area	3.98	25.23	50.27	66.08
Calculated Avg. Particle Size from BET	2.3 µm	69 nm	36 nm	30 nm
Particle Size Analysis	1.98 µm	68 nm	30 nm	18 nm
Scherrer formula	-	67 nm	29 nm	17 nm

In order to investigate the atomic percentage (at. %) of each atom corresponds to the stoichiometry of the nominal composition of C-349, the quantitative EDS analyses with and without oxygen for all the samples are investigated and shown in figure 5.5 and 5.6, respectively. The results of the EDS analysis were consistent with the stoichiometry of C-349. During EDS analyses, elemental composition is obtained in atomic % concentration. The atomic percentage of Ca to Co is 0.75. According to the table 5.3, measured atomic ratio of all the samples are very close to the label ratio of C-349. These experimental results coincide with the stoichiometry of C-349.

Table 5.3 Atomic percentage values of Ca to Co for C-349 composition from EDS analysis.

Samples	**S0**	**S3**	**S5**	**S7**
Atomic % of Ca/Co	0.71	0.77	0.73	0.73

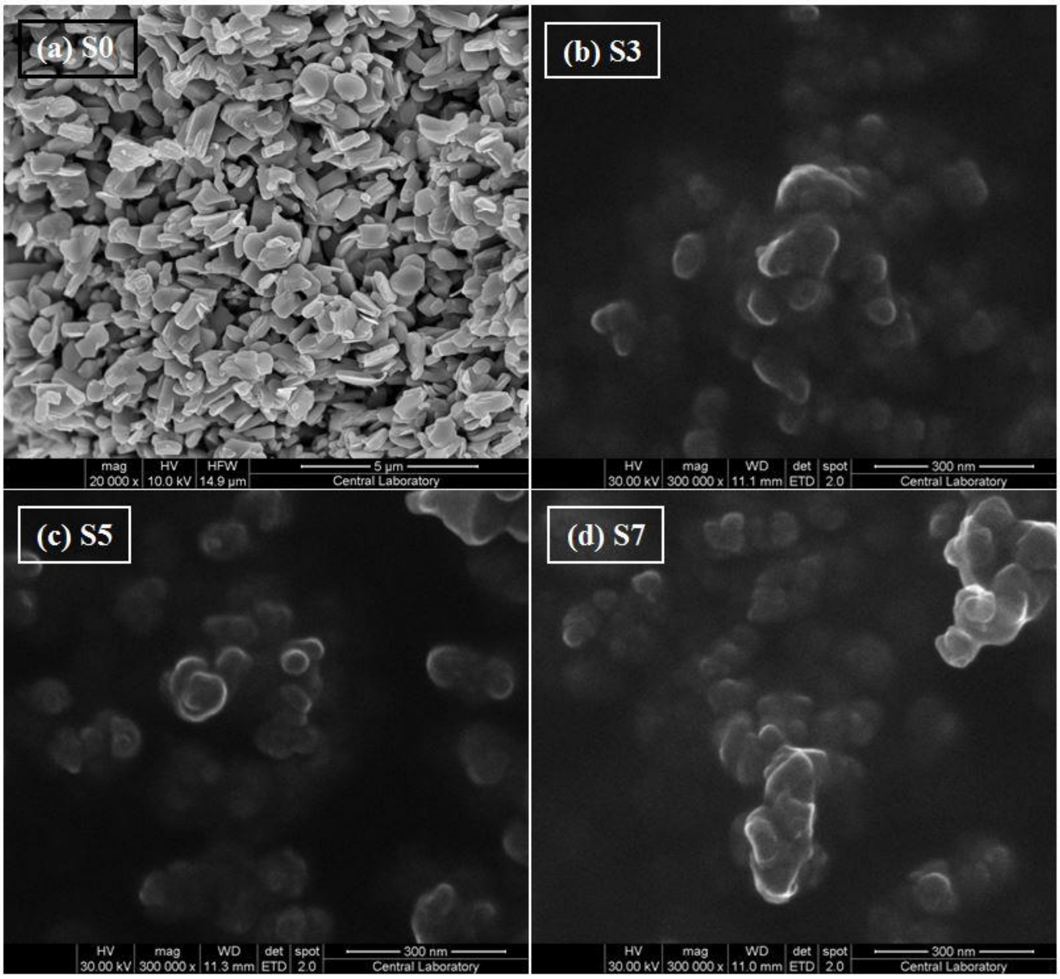

Figure 5.4 FE-SEM images of C-349 compounds of S0, S3, S5 and S7 samples.

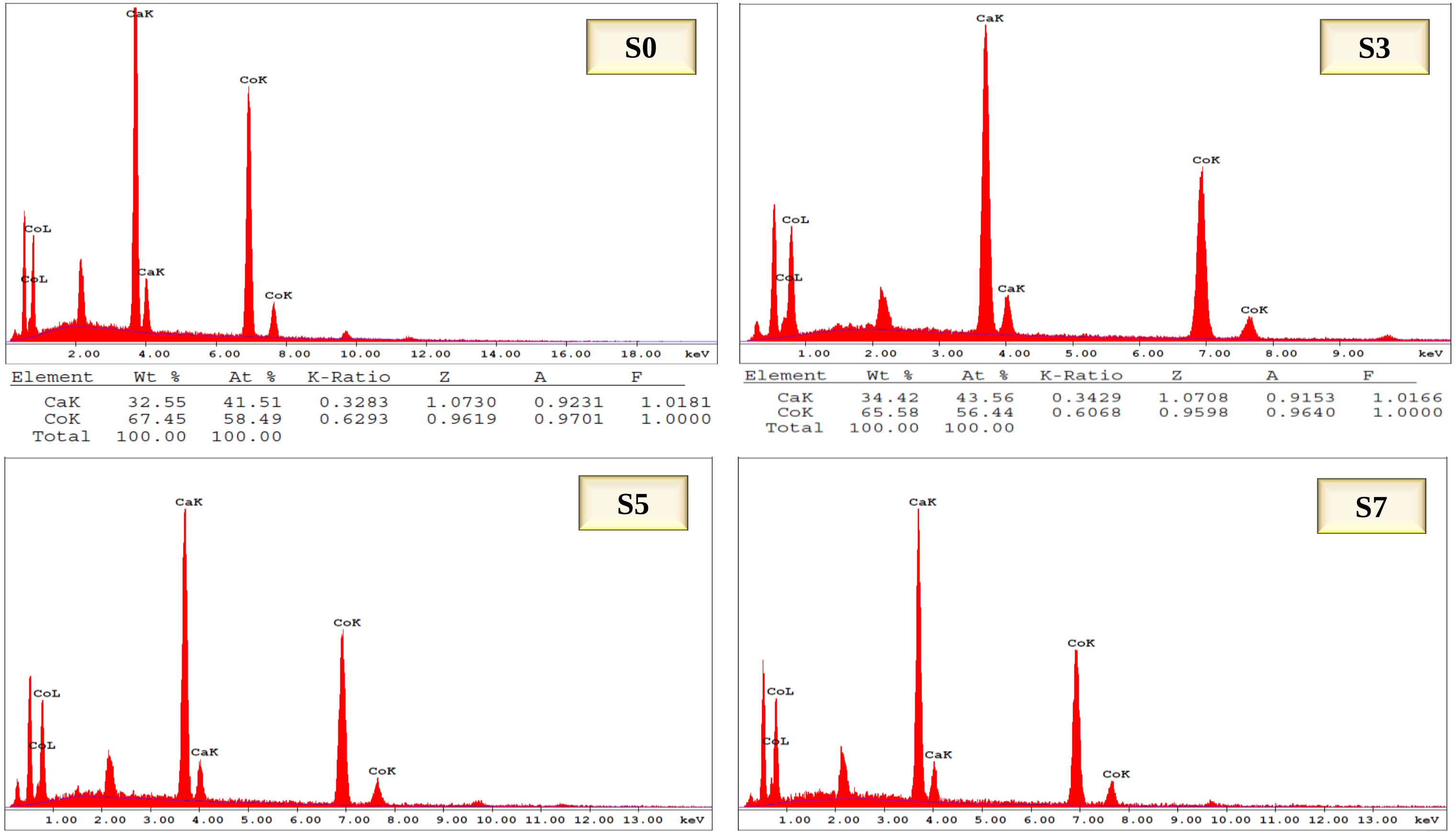

S0

Element	Wt %	At %	K-Ratio	Z	A	F
CaK	32.55	41.51	0.3283	1.0730	0.9231	1.0181
CoK	67.45	58.49	0.6293	0.9619	0.9701	1.0000
Total	100.00	100.00				

S3

Element	Wt %	At %	K-Ratio	Z	A	F
CaK	34.42	43.56	0.3429	1.0708	0.9153	1.0166
CoK	65.58	56.44	0.6068	0.9598	0.9640	1.0000
Total	100.00	100.00				

S5

Element	Wt %	At %	K-Ratio	Z	A	F
CaK	33.22	42.25	0.3313	1.0722	0.9144	1.0170
CoK	66.78	57.75	0.6196	0.9611	0.9655	1.0000
Total	100.00	100.00				

S7

Element	Wt %	At %	K-Ratio	Z	A	F
CaK	33.21	42.24	0.3307	1.0722	0.9133	1.0169
CoK	66.79	57.76	0.6195	0.9611	0.9650	1.0000
Total	100.00	100.00				

Figure 5.5 EDS spectrum and element analysis result for S0 and S3, S5, and S7 samples (without oxygen).

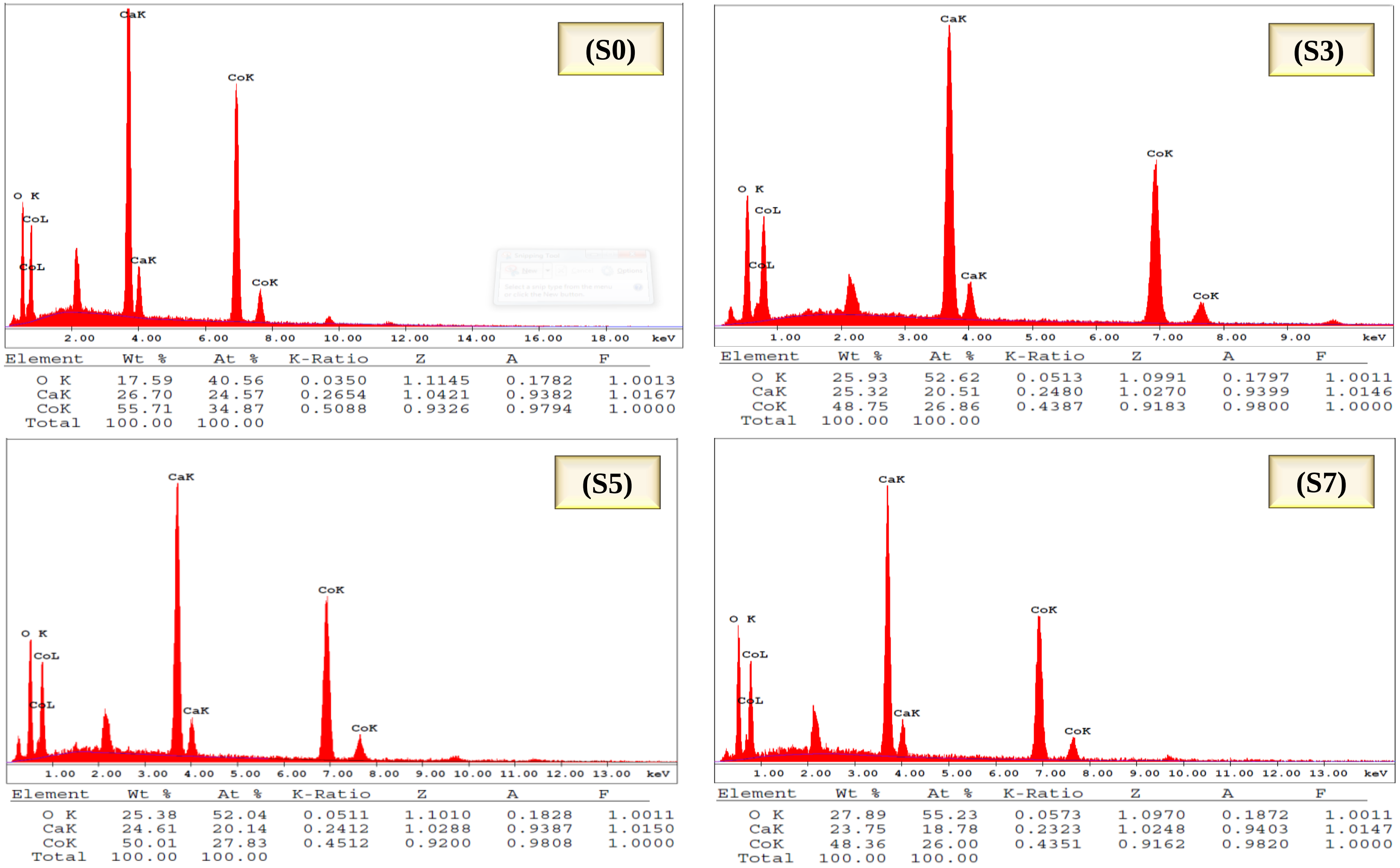

(S0)

```
Element   Wt %    At %   K-Ratio    Z       A       F
  O K    17.59   40.56   0.0350  1.1145  0.1782  1.0013
  CaK    26.70   24.57   0.2654  1.0421  0.9382  1.0167
  CoK    55.71   34.87   0.5088  0.9326  0.9794  1.0000
  Total 100.00  100.00
```

(S3)

```
Element   Wt %    At %   K-Ratio    Z       A       F
  O K    25.93   52.62   0.0513  1.0991  0.1797  1.0011
  CaK    25.32   20.51   0.2480  1.0270  0.9399  1.0146
  CoK    48.75   26.86   0.4387  0.9183  0.9800  1.0000
  Total 100.00  100.00
```

(S5)

```
Element   Wt %    At %   K-Ratio    Z       A       F
  O K    25.38   52.04   0.0511  1.1010  0.1828  1.0011
  CaK    24.61   20.14   0.2412  1.0288  0.9387  1.0150
  CoK    50.01   27.83   0.4512  0.9200  0.9808  1.0000
  Total 100.00  100.00
```

(S7)

```
Element   Wt %    At %   K-Ratio    Z       A       F
  O K    27.89   55.23   0.0573  1.0970  0.1872  1.0011
  CaK    23.75   18.78   0.2323  1.0248  0.9403  1.0147
  CoK    48.36   26.00   0.4351  0.9162  0.9820  1.0000
  Total 100.00  100.00
```

Figure 5.6 EDS spectrum and element analysis result for S0, S3, S5, and S7 samples (with oxygen).

5.3 Electrical and Thermal Transport Properties

In this part, the thermoelectric properties that are Seebeck coefficient, electrical resistivity, and thermal conductivity of C-349 thermoelectric materials have been studied to investigate the thermoelectric efficiency. The result of these measurements and their effect on C-349 are follow. Seebeck coefficient and electrical resistivity measurements are performed with a device build in our laboratory of which introduced in chapter 4.

The thermoelectric properties, including the Seebeck coefficient, electrical resistivity, and thermal conductivity, of the C-349 materials were examined to determine their thermoelectric efficiencies. The typical temperature-dependent Seebeck coefficient values of the C-349 material, which exhibits p-type conduction, are presented in figure 5.7. The microstructured S0 and nanostructured S3, S5, and S7 samples exhibit the same trend for the Seebeck coefficient values, which slightly increase with the temperature. The Seebeck coefficients of all the samples only differ by 6-11 μW/K. The highest Seebeck coefficient value of 143.2 μW/K was obtained for the micro-sized sample (S0) at 1000 K. The absolute values of the Seebeck coefficient starting from the lowest value 106.2 μW/K for sample S7 increase with temperature and reach a maximum of 132.4 μW/K at 1000 K. The measurement results match with those presented in the literature [58] and imply that the nanostructuring combined with porosity does not have a considerable effect on the Seebeck coefficient. As previously reported, when the size of the grain decreases, the Seebeck coefficient should increase due to the energy filtering effect [17]. However, in our study, the Seebeck coefficient decreased due to the effect of porosity being dominant, which leads to an increase in the density of the scattering region. It can be concluded that while nanostructuring has a positive contribution on the Seebeck coefficient, the effect of porosity is negative. Therefore, it is observed that the Seebeck coefficient does not degrade as much as intended. While the Seebeck coefficient is rather low for the nano-sized material with porosity, it is possibly higher than that of the macro-sized material with porosity.

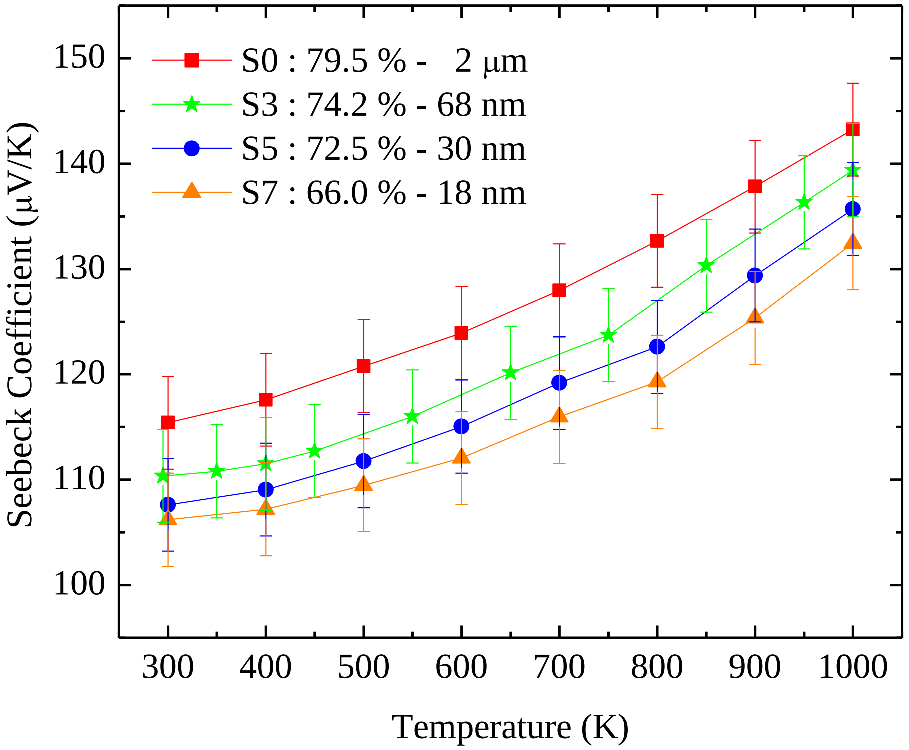

Figure 5.7 The results of Seebeck coefficient measurements as a function of temperature. Error bars are indicated with each representing color for each sample.

The heat flow direction of the thermal conductivity is the direction that was selected for the Seebeck coefficient and electrical resistivity. The total thermal conductivity values of all the samples are presented in figure 5.8(a). The thermal conductivity curves exhibit similar behavior with the temperature; however, these values exhibit weak temperature dependence. It is of interest that as the grain size of the samples decreases, the values of the thermal conductivities decrease significantly. In the present study, the total thermal conductivity values of 0.91, 0.66, 0.43 and 0.32 W/mK were obtained at 300 K for samples S0, S3, S5 and S7, respectively. The thermal conductivity value of 0.41 W/mK for the S7 material measured at 1000 K is 34 % lower than the value of 1.2 W/mK reported in the literature [59]. The nano-sized S3, S5 and S7 samples clearly exhibit much lower thermal conductivity values than the micro-sized S0 sample due to the increasing amount of interface phonon scattering occurring at the grain boundaries, which reduces the phonon mean free path [60]. The lattice thermal conductivity increases with increasing grain size, because a larger grain size means fewer grain boundaries in C-349 and weaker phonon interface scattering at the grain boundaries. Moreover, it is expected that porosity additionally limits the mean free path of some of the phonon modes and thus contributes to a further decrease in the thermal conductivity in nanocrystalline C-349, as observed in figure 5.8(a).

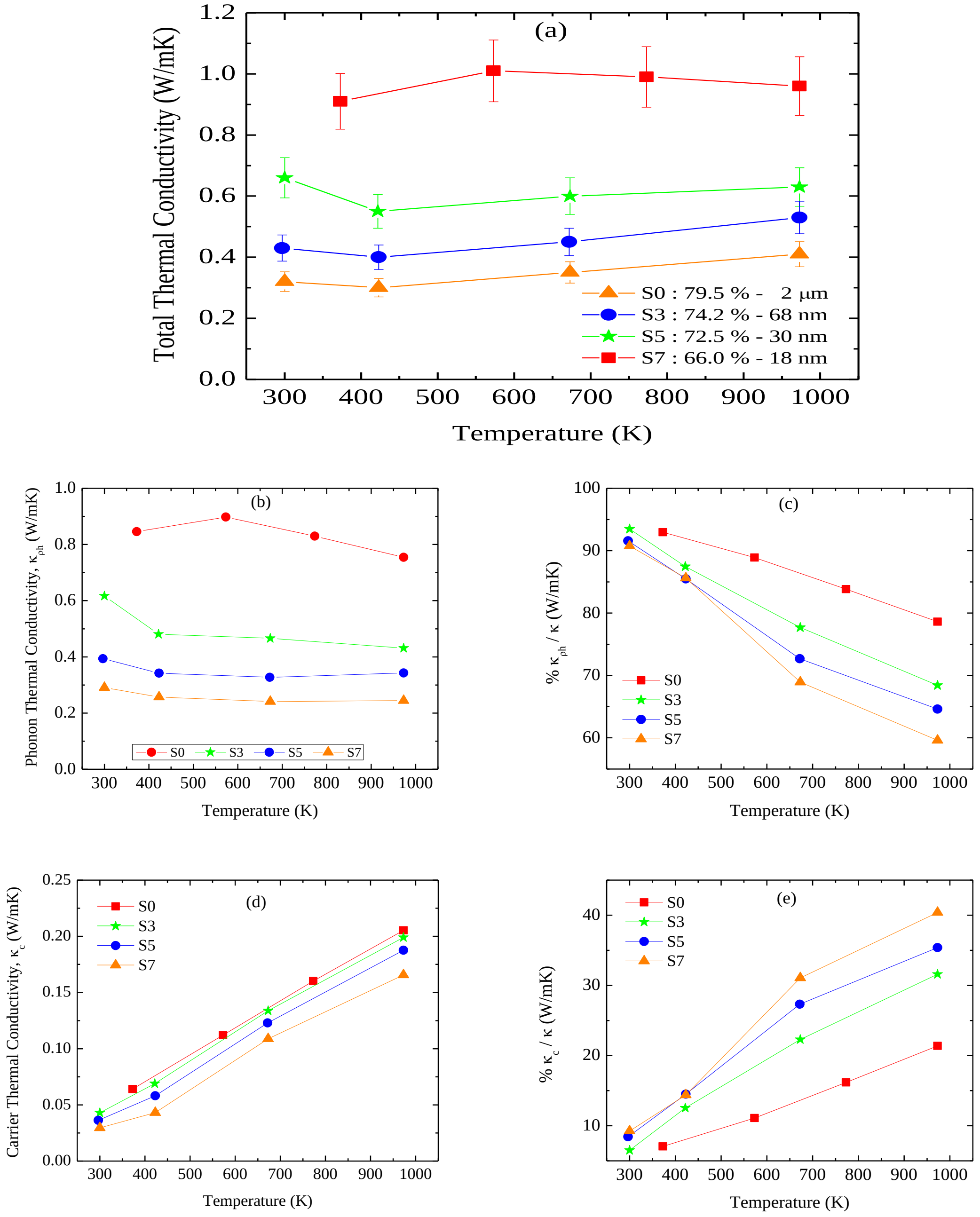

Figure 5.8 Temperature dependence of **(a)** the thermal conductivity; κ, **(b)** the phonon thermal conductivity; $\kappa_{\rho h}$, **(c)** the ratio of $\kappa_{\rho h}/\kappa$ (%), **(d)** the carrier thermal conductivity; κ_c and **(e)** the ratio of κ_c/κ (%), of all the C-349 samples.

The carrier thermal conductivity κ_c and the phonon thermal conductivity κ_{ph} contribute to the total thermal conductivity of the materials, $\kappa = \kappa_c + \kappa_{ph}$, which allows us to consider each component of the thermal conductivity independently. To explain the decrease of the total thermal conductivity of the materials due to the phonon scattering at grain boundaries, the main contribution to the thermal conductivity must be the phonon thermal conductivity. By implementing the Wiedemann-Franz law, $\kappa_c = L_0\sigma T$, where L_0 is the Lorenz number, ($2.45\times10^{-8} W\Omega K^{-2}$) and σ is the electrical conductivity, the carrier contribution can be calculated. The phonon contribution (κ_{ph}) can be determined by subtracting the carrier contribution (κ_c) from the total thermal conductivity (κ), and then, the temperature dependences of κ_{ph} and κ_{ph}/κ (%) can be plotted, as shown in figure 5.8(b) and figure 5.8(c), respectively. In addition, the temperature dependences of κ_c and κ_c/κ (%) can be plotted as shown in figure 5.8 (d) and figure 5.8 (e), respectively. κ_{ph} (%) is approximately 92 %, whereas the ratio of κ_c (%) is approximately 8 % for all the samples at 300 K. Based on these results, it can be inferred that phonons dominate the thermal conduction processes for all samples at 300 K. Nevertheless, the κ_{ph} (%) values decrease to 68.4 % for S3, 64.6 % for S5 and 59.6 % for S7, whereas this value is 78.6 % for sample S0 at 1000 K. This finding could be due to the decreased phonon contribution to the total thermal conductivity because of phonon scattering at boundaries leading to a significant decrease in the total thermal conductivity at 1000 K. This result also implies that nanostructured samples exhibit significant enhancement in phonon scattering at the grain boundary regions, resulting in a lower total thermal conductivity for the C-349 system. However, this substantial decrease in the lattice thermal conductivity cannot be explained based only on nanostructuring models when these data are compared with the values in the literature [3, 61, 62].

In addition to the results provided above, the contribution of the porosity to further decreasing the thermal conductivity cannot be ignored. Therefore, it is beneficial to investigate the degree of the effect of porosity on the lattice thermal conductivity. Among the most popular analytical models that are available to predict the bulk thermal conductivity, κ_{eff} of a two-phase material, the Maxwell-Eucken equation is one of the most powerful methods if the pores are spherical and dispersed in the ceramics [63, 64]. Therefore, the matrix can be defined as a two-component composite medium of C-349 solid grains and pores [65]. The effect of porosity on the total thermal conductivity can be estimated by solving this well-known equation, which was derived in a similar analysis by Mi *et al.* [66] and Adachi *et al.* [67], given as $\kappa = \kappa_0 v/(1+\beta(1-v))$, where v is the volume fraction (i.e., the relative density) of the material, κ is the measured total thermal conductivity with porosity, κ_0 is the bulk thermal conductivity and β is the pore shape factor. Among several possibilities for this factor, $\beta = 2/3$ indicates randomly dispersed cylindrical pores and this selection fits our condition. Densities of 79.5, 74.2, 72.5 and 66.0 % were derived based on the true densities of the S0, S3, S5 and S7 samples (table 5.2), respectively, using the theoretical density (4.677 g/cc).

The bulk thermal conductivities of all the samples are listed with respect to volume fraction in table 5.4. The bulk thermal conductivity values for the S0, S3, S5 and S7 samples are calculated as 1.3, 1.0, 0.7 and 0.5 W/mK at 300 K and are higher than the measured values as presented earlier. This result indicates that the degree of porosity plays a substantial role in the reduction of thermal conductivity.

Table 5.4 The bulk thermal conductivity values with respect to volume fraction.

Sample	β	*v(1-%g/cc)*	*v (%g/cc)*	κ *(W/mK)*	κ_{eff} *(W/mK)*	κ / κ_{eff} *(%)*
S0	2/3	0.205	0.795	0.91	1.3	30.1
S3	2/3	0.258	0.742	0.66	1.0	36.7
S5	2/3	0.275	0.725	0.43	0.7	38.7
S7	2/3	0.34	0.66	0.32	0.59	46.2

To clarify the reason for this thermal transport behavior, the effective κ values are plotted as a function of reciprocal temperature in figure 5.9. The sample size of lattice thermal conductivity was extrapolated to obtain better results. Figure 5.9

demonstrates that the κ value for the C-349 sample exhibits a strong linear dependency on 1000/T in a specific temperature range. This finding means that characteristic phonon-phonon scattering, the Umklapp process [60], is predominant in the C-349 bulk polycrystalline samples. This process effect is predominant until approximately 600 K for the C-349 sample with a grain size of ~2 μm. It can be inferred that certain phonon-phonon scattering processes can drastically affect the thermal conductivity. Umklapp processes, for which the total momentum of the interacting phonons is not conserved, are capable of affecting the conduction of heat [68]. In contrast, a nonlinear region exists from approximately 400 K to an elevated temperature above which the temperature dependency is linear. This finding signifies an additional effect on phonon scattering in addition to phonon-phonon interactions. This effect is grain boundary scattering due to the smaller grain size and higher porosity which increase the density of the scattering medium [69]. Moreover, as the grain size decreases, the nonlinear range widens, which means that grain boundary scattering remains effective in restricting phonon propagation at higher temperatures, where the phonon mean free path is even shorter due to enhanced phonon-phonon scattering.

Figure 5.10 illustrates the temperature dependence of the electrical resistivity values of all the samples. According to the graph, all the samples exhibit similar behavior. A slight reduction of the resistivity starts at 300 K and ends at approximately 420 K for samples S5 and S7 representing semiconductor-like behavior. Within this temperature range, the system exhibits metal-like transport up to 475 K. However, the curve shifts toward higher temperature by 75 K for the nanostructured S3 sample. In these regions, the transport behavior changes again with a decrease in the resistivity with increasing temperature up to 1000 K. The resistivity of the micro-sized S0 sample is higher than that in earlier reported works [36, 62, 70] due to the increased porosity.

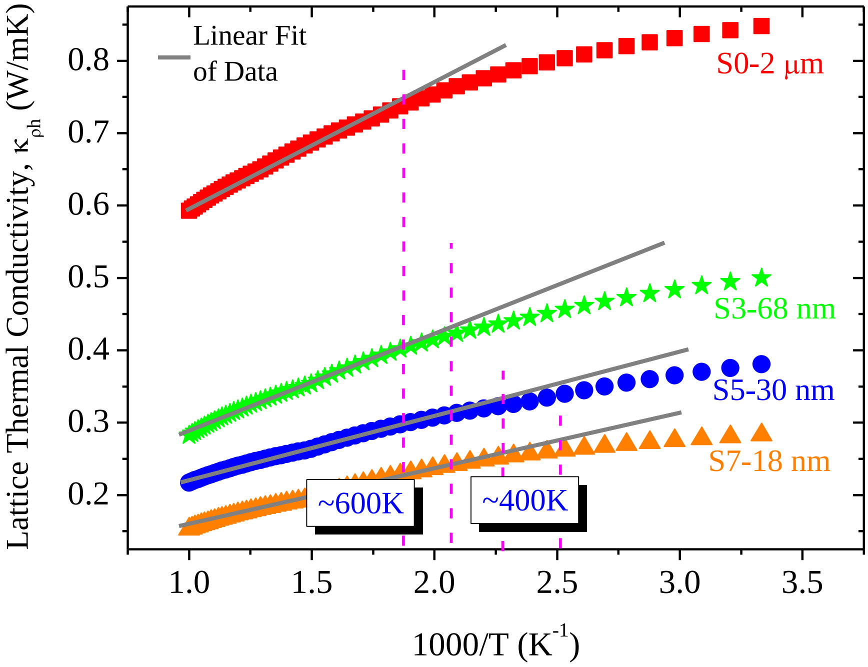

Figure 5.9 Lattice thermal conductivity vs 1000/T for all C-349 samples with micro- and nano-sized samples.

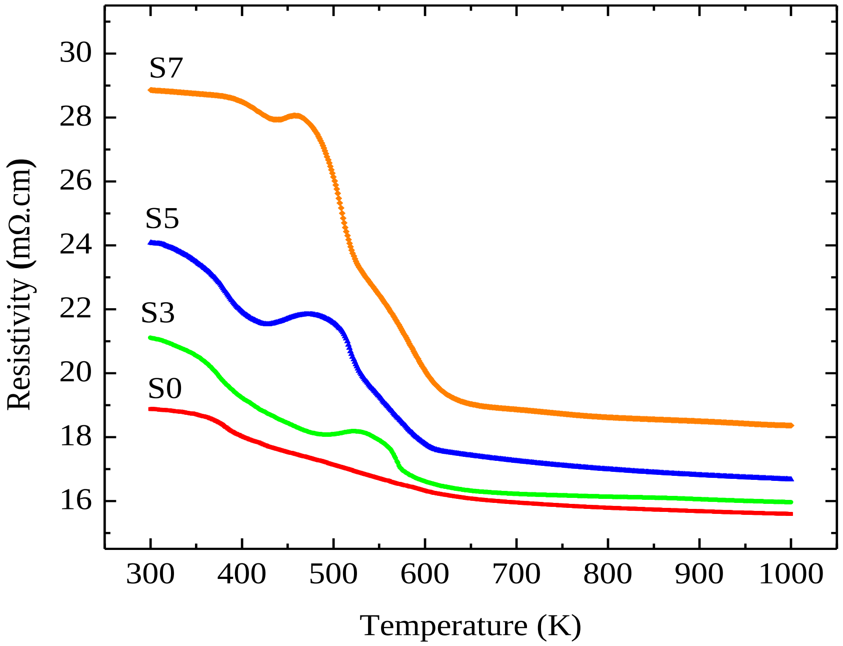

Figure 5.10 The variation of electrical resistivity with temperature for S0, S3, S5 and S7 samples.

Figure 5.10 also indicates that the nano-sized S3, S5 and S7 samples exhibit higher resistivities than the micro-sized S0 sample. There are considerable gaps between the resistivities of the samples at 300 K, whereas at high temperature, a distinct difference is not observed. According to the measurement results, the 2-μm-sized sample (S0) exhibited the lowest resistivity, 15.6 mΩ.cm at 1000 K, whereas that of the 18-nm-sized sample (S7) was 18.4 mΩ.cm. The resistivities for samples S3 and S5, 16 and 16.7 mΩ.cm at 1000 K, respectively, fall in the middle range. The decreasing resistivity and transformation from metallic to semiconducting behavior associated with the first-order phase transition, which lead to the enhancement of the thermoelectric properties at high temperatures [70, 71], are due to the decrease in the density and the random orientation distribution of the grains in the ceramics. Moreover, the charge carriers are scattered more severely in the nano-sized porous materials than in the macroscale porous materials due to the higher density of scattering sites.

The power factors $(PF = S^2 / \rho)$ of the C-349 samples are presented in figure 5.11. All of the samples exhibit the same PF value characteristics, with the values increasing with increasing temperature. The PF values obtained for the nano-sized samples are lower than the values for the micro-sized one. The calculated PF value of S0 is 0.09 mW/mK^2 at 300 K and reaches 0.18 mW/mK^2 at 1000 K. The PF values are 0.16, 0.14 and 0.12 mW/mK^2 for samples S3, S5 and S7 at 1000 K, respectively.

Figure 5.12 presents the temperature-dependent *ZT* for the nanostructured and micro-structured C-349 samples. The *ZT* values tend to increase with increasing temperature, as clearly observed in figure 5.12. The graph reveals that the nano-sized S3, S5 and S7 samples exhibit higher *ZT* values than the micro-sized S0 sample. The *ZT* value reaches 0.29 for the S7 sample and 0.18 for the S0 sample at 1000 K. The increase in *ZT* at high temperature is due to several factors. First, the thermal conductivity is already low and remains constant. Second, the Seebeck coefficient increases with temperature; however, the electrical transport behavior change and resistivity decrease near 420 K, which substantially contributes to the enhancement of *ZT* at high temperature [61, 72, 73].

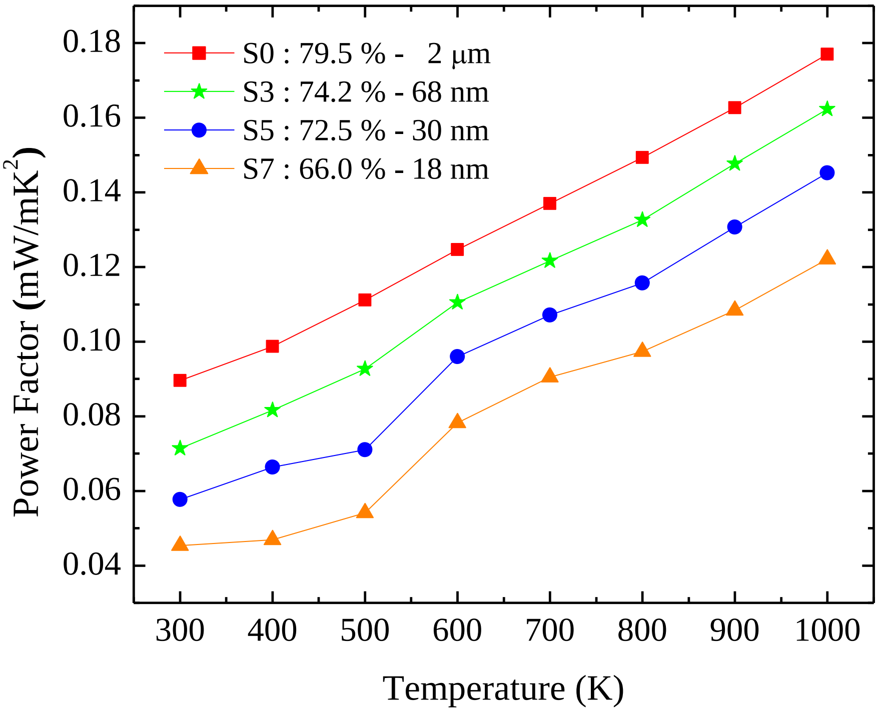

Figure 5.11 Temperature dependence of power factor values from 300 to 1000 K.

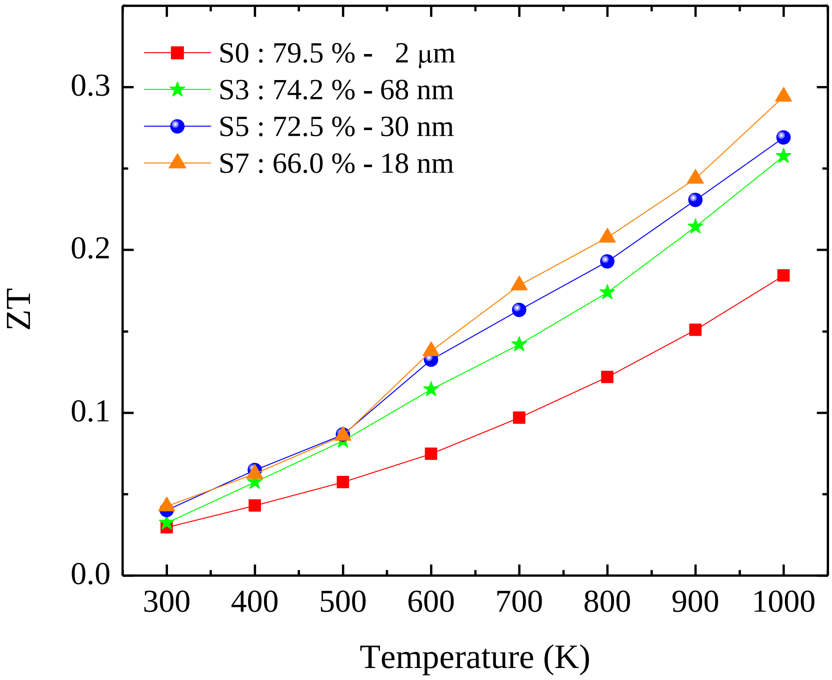

Figure 5.12 *ZT* values as a function of temperature for all the samples.

Although the *ZT* values are not sufficiently high for practical applications, this study demonstrates that the nanostructuring approach combined with high porosity is fairly effective for improving the *ZT* of the C-349 system. The results indicate that for high temperature applications of C-349 metal oxide materials, nanostructuring could be a significant starting point. It would be beneficial to investigate the mechanical properties of this conventionally sintered high-efficiency but low-density material to determine its applicability [74].

5.4 Conclusion

In this research, C-349 metal oxide thermoelectric materials with various grain sizes ranging from 18 nm to 2 μm were synthesized using the citrate sol-gel method and their thermoelectric properties were compared at high temperatures ranging from 300 K to 1000 K. Particle size measurements were conducted using different techniques, and the results corresponded well with each other. The synthesized nano-sized samples exhibited higher electrical resistivity due to the quantity of pores, which increased the carrier scattering at boundaries, and the lower thermal conductivity due to phonon boundary scattering at the increased number of interfaces. *ZT* was enhanced due to the substantial decrease in the thermal conductivity despite the great increase in resistivity. The total thermal conductivity reduction was experimentally observed to be larger for smaller grain sizes and higher porosities. Because the size and morphology of materials strongly affect *ZT* values, the growth of grains on the nano-scale can therefore be achieved by adjusting the quantity of PEG 400. Nano-sized C-349 may be a promising thermoelectric material for high temperature practical applications. The evaluation of the results is presented in detail in chapter 7.

REFERENCES

[1] F. Delorme, D. Ovono Ovono, P. Marudhachalam, C. Fernandez Martin, O. Fraboulet, Mater. Res. Bull. 47 (2012) 1169–1175

[2] D. M. Rowe, CRC Handbook of thermoelectrics, CRC Press. FL (2006) 1-2

[3] Y. Tongfang, L. Dawei, O. Yun, M. Feiyue, X. Shuhong, L. J. Feng, L. Jiangyu, J.Phys. Chem. C. 114 (2010) 10061–10065

[4] R. J. Mehta, Y. Zhang, H. Zhu, D. S. Parker, M. Belley, D. J. Singh, R. Ramprasad, T. Borca-Tasciuc, G. Ramanath, Nano Lett. 12 (2012) 4523–4529

[5] A. J. Minnich, M. S. Dresselhaus, Z. F. Ren, G. Chen, Energy Environ. Sci. 2 (2009) 466-479

[6] F. J. DiSalvo, F. J. Science, 285 (1999) 703

[7] T. M. Tritt, M. A. Subramanian, MRS Bulletin 31 (2006) 188-194

[8] M. S. Dresselhaus, G. Chen, M. Y. Tang, R. G. Yang, H. Lee, D. Z. Wang, Z.F. Ren, J. P. Fleurial, P. W. Gogna, Adv, Mater. 19 (2007) 1043–1053

[9] J. Nowotny, T. Bak, T. Burg, M. K. Nowotny, L. R. Sheppard, J. Phys. Chem. C. 111 (2007) 9769-9778

[10] H. Gleiter, Prog. Mater. Sci. 33 (1989) 223-315

[11] P. Pichanusakorn, P. Bandaru, Mater. Sci. Eng. R 67 (2010) 19-63

[12] D. L. Medlin, G. J. Snyder, Curr. Opin. Colloid & In. 14 (2009) 226-235

[13] N. V. Nong, N. Pryds, S. Linderoth, M. Ohtaki, Advanced Materials 23 (2011) 2484-2490

[14] X. J. Zheng, L. L. Zhu, Y. H. Zhou, Q. Zang, Appl. Phys. Lett. 87 (2005) 242101-242104

[15] L. L. Zhu, K. Jin, X. J. Zheng, Appl. Phys. Lett. 91 (2007) 103108-3

[16] B. L. Yu, Q. Qi, X. F. Tang, Acta. Phys. Sin. 54 (2005) 5763− 5768

[17] R. Z. Zhang and K. Koumoto, J. Electron. Mater. 42 (2013) 1568-1572

[18] R. Zhang, C. Wang, J. Li, and K. Koumoto, J. Am. Ceram. Soc. 93 (2010) 1677

[19] Y.F. Wang, K. Fujinami, R.Z. Zhang, C.L. Wan, N. Wang, Y.S. Ba, and K. Koumoto, Appl. Phys. Express 3 (2010) 031101

[20] H. Lee, D. Z. Wang, M. Y. Tang, Z. F. Ren, P. Gogna, J. P. Fleurial, M. S. Dresselhaus, and G. Chen, The 24th International Conference on Thermoelectrics (IEEE) 2005 Clemson SC

[21] J. Tang, H. Wang, D. H. Lee, M. Fardy, Z. Huo, T. P. Russell, and P. Yang, Nano Lett. 10 (2010) 4279-4283

[22] M. Kashiwagi, S. Hirata, K. Harada, Y. Zheng, M. Yahiro, C. Adachi, and K. Miyazaki, Appl. Phys. Lett. 98 (2011) 023114-3

[23] Z. Yanliang, J. M. Rutvik, B. Matthew, H. Liang, R. Ganpati, B. T. Theodorian, Appl. Phys. Lett. 100 (2012) 1193113-4

[24] G. D. Mahan, J. Appl. Phys. 76 (1994) 4362-4366

[25] A. Shakouri and J. E. Bowers, Appl. Phys. Lett. 71 (1997) 1234-1236

[26] N. Wang, L. Han, H. He, Y. Ba, K. Koumoto, J. Alloys Compd. J. Alloys Compd. 497 (2010) 308–311

[27] N. S. Lidorenko, O. M. Narva, L. D. Dudkin, and R. S. Erofeev, Inorg. Mater. 6 (1970) 1853

[28] D. W. Song, W. N. Shen, B. Dunn, C. D. Moore, M. S. Goorsky, T. Radetic, R. Gronsky, and G. Chen, Appl. Phys. Lett. 84 (2004) 1883-1885

[29] D. Song and G. Chen, Appl. Phys. Lett. 84 (2004) 687-689

[30] R. G. Yang, G. Chen, and M. S. Dresselhaus, Nano Lett. 5 (2005) 1111-1115

[31] I. Terasaki, Y. Sasago, K. Uchinokura, Phys. Rev. B 56 (1997) 12685–12687

[32] K. Koumoto, I. Terasaki, R. Funahashi, MRS Bull. 31 (2006) 206-210

[33] L. Zhang, X. F. Tang, W. B. Gao, J. Phys. Chem. C 113 (2009) 7930-7934

[34] S. Lambert, H. Leligny, D. Grebille, J. Solid State Chem. 160 (2001) 322–331

[35] R. Funahashi, I. Matsubara, H. Ikuta, T. Takeuchi, U. Mizutani, S. Sodeoka, Jpn. J. Appl. Phys. Part 2 39 (2000) 1127-1129

[36] A. C. Masset, C. Michel, A. Maignan, M. Hervieu, O. Toulemonde, F. Studer, B. Raveau, J. Hejtmanek, J. Phys. ReV. B 62 (2000) 166-175

[37] T. Takeuchi, T. Kondo, K. Soda, U. Mizutani, R. Funahashi, M. Shikano, S. Tsuda, T. Yokoya, S. Shin, T. Muro, J. Electron Spectrosc. Relat. Phenom. 137 (2004) 595-599

[38] S. Bhattacharya, S. Rayaprol, A. Singh, A. Dogra, C. Thinaharan, D. K. Aswa, S. K. Gupta, J. V. Yakhmi, R. N. Kulkarni, S. M. Yusuf, S. N. Bhatia, J. Phys. D: Appl. Phys. 41 (2008) 085414-5

[39] Y. Miyazaki, K. Kudo, M. Akoshima, Y. Ono, Y. Koike, T. Kajitani, Jpn. J. Appl. Phys. 39 (2000) 531–533

[40] S. Horii, I. Matsubara, M. Sano, K. Fujie, M. Suzuki, R. Funahashi, M. Shikano, W. Shin, N. Murayama, J.-I. Shimoyama, K. Kishio, Jpn. J. Appl. Phys. 42 (2003) 7018–7022

[41] Y. Zhou, I. Matsubara, S. Horii, T. Takeuchi, R. Funahashi, M. Shikano, J.-I. Shimoyama, K. Kishio, W. Shin, N. Izu, N. Muroyama, J. Appl. Phys. 93 (2003) 2653–2658

[42] C.D. Ling, K. Aivazian, S. Schmid, P. Jensen, J. Solid State Chem. 180 (2007) 1446–1455

[43] Y. Zhang, J. Zhang, J. Mater. Process. Technol. 208 (2008) 70–74

[44] H. Hu, Y. Deng, J. Li, G. Wang, Key Eng. Mater. 68 (2008) 559–561

[45] Y.-H. Lin, C.-W. Nan, Y. Liu, J. Li, T. Mizokawa, Z. Shen, J. Am. Ceram. Soc. 90 (2007) 132–136

[46] N. Wu, T. C. Holgate, N. V. Nong, N. Pryds, S. Linderoth, J. Eur. Ceram. Soc. 34 (2014) 925-931

[47] Y. Zhang, R. Li, Y. Jiang, B. Z, H. Duan, J. Li, Z. Feng, J. Solid State Chem. 184 (2011) 2047–2052

[48] M. Gunes, H. Gencer, V.S. Kolat, S. Vural, H.I. Mutlu, T. Seckin, S. Atalay, Mater. Sci. Eng., B 136 (2007) 41–45

[49] Y. F. Zhang, J. X. Zhang, Q. M. Lu, Q. Y. Zhang, Mater. Lett. 60 (2006) 2443–2446

[50] M. Gunes, M. Parlak, M. Ozenbas, Meas. Sci. Technol. 25 (2014) 055901 (10pp)

[51] S. Iwanaga, E. S. Toberer, A. LaLonde, G. J. Snyder, Rev. Sci. Instrum. 82 (2011) 063905-6

[52] A. T. Burkov, A. Heinrich, P. P. Konstantinov, T. Nakama, K. Yagasaki, Meas. Sci. Technol. 12 (2001) 264–272

[53] Z. H. Zhou and C. Uher, Rev. Sci. Instrum. 76 (2005) 023901-5

[54] J. Martin, T. Tritt, C. Uher, J. Appl. Phys. 108 (2010) 121101-12

[55] C. Byl, D. Bérardan and N. Dragoe, Meas. Sci. Technol. 23 (2012) 035603

[56] W.S.N. Murayama, J. Mater. Res. 15 (2000) 382-386

[57] I. Gosens , J. A. Post, L. JJ de la Fonteyne, E. HJM Jansen, J. W Geus, F. R Cassee, W. H de Jong, Part. Fibre Toxicol. 37 (2010) pp. 1-11

[58] L. Yuheng, L. Yuanhua, S. Zhan, N. Ce-Wen, J. Am. Ceram. Soc. 88 (2005) 1337–1340

[59] N. Prasoetsopha, S. Pinitsoontorn, V. Amornkitbamrung, Electronic Materials Letters, 8 (2012) 305-308

[60] S. Raghavan, H. Wang, R.B. Dinwiddie, W.D. Porter, M.J. Mayo, Scr. Mater. 39 (1998) 1119–1125

[61] G. J. Xu, R. Funahashi, M. Shikano, I. Matsubara and Y. Q. Zhou, Appl. Phys. Lett. 80 (2002) 3760-3762

[62] Y. H. Lin, J. Lan, Z. J. Shen, Y. H. Liu, C. W. Nan, J. F. Li, Appl. Phys. Lett. 94 (2009) 072107-3

[63] J. Wang, J.K. Carson, M.F. North, D.J. Cleland. Int. J. Heat Mass Transfer 49 (2006) 3075

[64] C. Vincent, J. F. Silvain, J. M. Heintz, N. Chandra, J. Phys. Chem. Solids 73 (2012) 499–504

[65] J. K. Carson, S. J. Lovatt, D. J. Tanner, A. C. Cleland, Int. J. Heat Mass Transfer 48 (2005) 2150–2158

[66] J. L. Mi, T. J. Zhu, X. B. Zhao, J. Ma, J. Appl. Phys. 101 (2007) 054314-6

[67] J. Adachi, K. Kurosaki, M. Uno, S. Yamanaka, J. Alloys Compd. 432 (2007) 7-10

[68] N. W. Ashcroft, N. D. Mermin, Solid State Physics, HRW International Editions, CBS Publishing Asia Ltd 1976

[69] H. Lee, D. Vashaee, D. Z. Wang, M. S. Dresselhaus, Z. F. Ren, G. Chen, J. Appl. Phys. 107 2010 094308-7

[70] J. Cheng, Y. Sui, Y. Wang, X. Wang, W. Su, Appl. Phys. A 94 (2009) 911–916

[71] T. Wu, T. A. Tyson, H. Chen, J. B., H. Wang, C. Jaye, J. Phys.: Condens. Matter 24 (2012) 455602-7

[72] M. Shikano, R. Funahashi, Appl. Phys. Lett., 82 (2003) pp. 1851–1853

[73] S. Li, R. Funahashi, I. Matsubara, K. Ueno, S. Sodeoka and H. Yamada, Chem. Mater. 12 (2000) 2424-2427

[74] D. Kenfaui, D. Chateigner, M. Gomina, J. G. Noudem, J. Alloys Compd. 490 (2010) 472–479

CHAPTER 6

THERMOELECTRIC PROPERTIES OF Cr SUBSTITUTED $Ca_3Co_4O_9$ METAL OXIDE

In this part of the thesis, polycrystalline Cr substituted $Ca_{3-x}Cr_xCo_4O_9$ (x = 0.01, 0.03, 0.05 and 0.07) thermoelectric samples and unsubstituted one (C-349) are prepared by citrate sol-gel process and their thermoelectric properties are carefully studied at temperatures from 300 up to 1100 K. The improvement of thermoelectric performance is the most significant in x = 0.03 Cr substituted sample with *ZT* value of 0.26 at 1100 K.

For any real practical use of thermoelectric materials in power generator, *ZT* needs to be higher than 1 [1]. At present, widely studied conventional materials with the highest thermoelectric performance are intermetallic compounds, such as Bi_2Te_3, $CoSb_3$. However, they are easily decomposed or oxidized at high temperatures in air, which limits their industrial applications [2].

Not only some early discovered oxides such as Na_xCoO_2 [3], but also newly discovered promising thermoelectric materials such as $Bi_{1-x}Sr_xCuSeO$ [4] have shown extraordinary high thermoelectric properties that makes oxides potential candidates for thermoelectric applications. Due to their good stability at elevated temperatures, being nontoxic, well-supplied, easy to fabricate and cheap, they can be used as thermo-elements in oxidizing conditions up to 1073 K [5, 6]. C-349 is one of the most promising materials among all other oxides with its high thermo-power, low thermal conductivity and electrical resistivity values at high temperatures since it is composed of CoO_2 nanosheets possessing a strongly correlated electron system and calcium cobalt oxide misfit layers which serve as electronic transport layers, potential phonon scattering regions [7–10]. One of the ways for optimizing both these layers by doping and substitutions must be very effective to improve their conversion efficiencies [11–14]. Partial substitution that can take place either at Ca-site or at Co-site of some elements into C-349 in order to improve Seebeck coefficient and to reduce electrical resistivity and thermal conductivity simultaneously can also be useful. Excellent review demonstrates different types of oxides and their thermoelectric properties through both transition and rare earth elemental doping and substitution [15]. There have been some experimental studies on partial substitution at Ca-site [16–24], but very few studies reported Seebeck coefficient, resistivity and thermal conductivity measurements together at high temperature [17, 18, 22]. The effect of partial substitution at Ca-site is mainly to change the charge carrier concentration or mobility. Therefore, elemental substitution to this site may lead to a great change in electrical conductivity [25, 26]. Also, the spin-entropy contribution to the Seebeck coefficient is related with the spin-entropy current and the population of free spins [27], which depends largely on the Co^{4+} concentration and the degeneracy of the Co ions [28]. For instance, a theoretical model gives strong evidence that the enhanced Seebeck coefficient mainly originates from enhancement of the spin entropy [29]. Experimental findings show that the substitution of Ca sites can suppress the Co^{4+} concentration leading to enhancement of Seebeck coefficient [30, 31]. In addition, it has been reported that porosity is one of the ways for lowering the total thermal conductivity which positively affect the figure of merit [16]. In this respect, understanding the microscopic mechanisms by which substitution affects the spin entropy can pave an effective way to improve the Seebeck coefficient for thermoelectric materials. Moreover, due to the difference between the substitution and substitute elements (i.e. ionic radii), some structural changes are also cause significant changes on electrical and thermal properties of materials [15].

The goal of this research is to study the effect of Cr substitution for Ca on the microstructure and high temperature thermoelectric properties of $Ca_{3-x}Cr_xCo_4O_9$ prepared by the citrate sol-gel method. In this study, we investigated a set of thermoelectric properties (Seebeck coefficient, resistivity and thermal conductivity) at high temperature in order to disclose the effect of Cr substitution on the spin entropy and over all thermoelectric properties. Therefore, the concentrations of the substituted Cr metal vary as x = 0.01, 0.03, 0.05 and 0.07 and they are compared with unsubstituted one.

6.1 Experimental Procedure

In this study, citrate sol-gel process [32] is applied to synthesize C-349 samples. Cr substituted $Ca_{3-x}Cr_xCo_4O_9$ (x = 0.01, 0.03, 0.05 and 0.07) by Ca and one unsubstituted C-349 particle are prepared by mixing appropriate amounts of $Ca(NO_3)_2$, $Co(NO_3)_2$, $Cr(NO_3)_3$ in the range of 0.2 M and 5% PEG-400 (99%) added to the aqueous solution of citric acid, which is then heated to the desired reaction temperature in a oil bath (see figure 6.1). In most cases the temperature is raised to 353 K and held there for 4 h with continuous stirring in order to obtain the gel. As a further advantage, the polyol medium is complexing the surface of the particles efficiently. Consequently, the particle growth is limited. Furthermore, agglomeration of the particles is prevented in the colloidal solution. The obtained gel is dried initially at 393 K for 12 h and further heat treated in air at a ramp rate of 10 °C/min in a programmable box furnace (Protherm), at temperatures 1023 K for 2 h and cooled down naturally in order to remove organic compounds and to form powder samples with pure C-349 phase. As a result, pure C-349 particles with the size range of ~ 30 - 50 nm powders are produced. Obtained powders are ball milled to prevent possible agglomeration, and then pressed into a disk shape with a diameter of 16 mm and a thickness of ~ 2.5 mm. Since Ca-based oxide is easy to disintegrate at high temperature over 1193 K, obtained samples are subsequently annealed at 1123 K for 2 h in air to eliminate oxygen deficiency. In this process, PEG 400 and citric acid as dispersant and complexing agent are used, respectively.

Table 6.1 Stoichiometric amounts of ingredients of $Ca_{3-x}Cr_xCo_4O_9$ samples.

	Molarity (M)	**Nitrates (g)**			**PEG-400 % / volume**	**Citric Acid (g)**
$Ca_{3-x}Cr_xCo_4O_9$		Ca	Co	Cr		
x = 0.00	0.2	3.036	4.989	-	0.5	2.94196
x = 0.01	0.2	3.026	4.989	0.017	0.5	2.94196
x = 0.03	0.2	3.005	4.989	0.051	0.5	2.94196
x = 0.05	0.2	2.985	4.989	0.085	0.5	2.94196
x = 0.07	0.2	2.965	4.989	0.120	0.5	2.94196

6.2 Structural Characterizations

Microstructural characterizations have demonstrated that all the Cr has been incorporated into C-349 structure and no secondary phases have been investigated. XRD patterns illustrate that unsubstituted and Cr substituted samples are pure and identical (see figure 6.1) and of match with the standard JCPDS card of C-349 [8]. This result indicates that all of the samples are prepared successfully using citrate sol-gel method. In order to determine the chemical composition of the prepared specimens, x-ray fluorescence spectroscopy is used. The results show that the ratio of Ca, Cr, Co and O for x = 0.07 Cr and unsubstituted samples are 2.94:0.06:3.99:9.2 and 2.99:3.99:9.3, respectively, which matches the nominal composition 3:4:9 well. The oxygen nonstoichiometric is caused by the oxygen-rich atmosphere in the air.

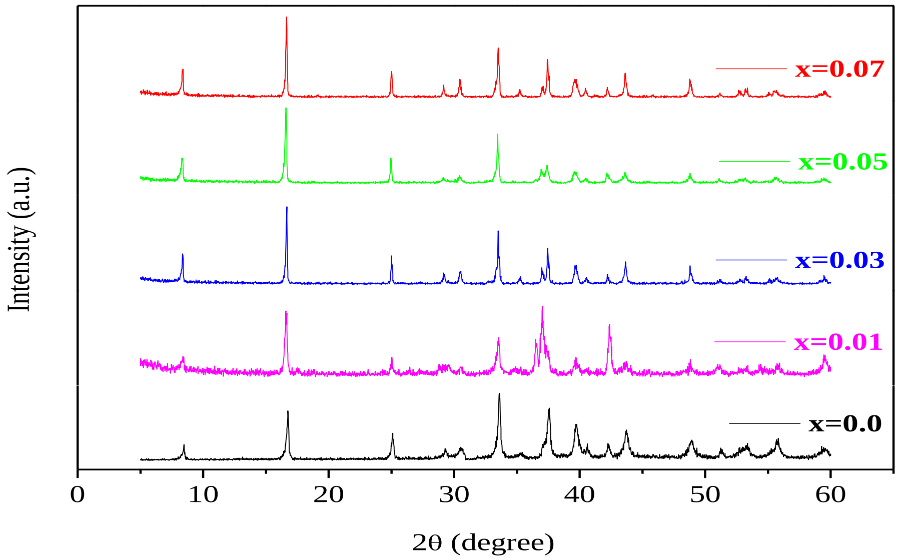

Figure 6.1 XRD patterns of Cr-substituted samples and unsubstituted one. No observable traces of extraneous phases and impurities are detected.

Figure 6.2 demonstrates the bulk densities of the annealed samples as a function of Cr substitution content, x. Apparent density measurements have shown that as the amount of Cr increases, the relative density values increases from 69 to 77 % of the theoretical one indicating that Cr addition does affect the densification. This observation has shown that all samples possess relatively high degree of porosity, where a general representative view of the x = 0.07 Cr sample is displayed, which cause lover thermal conductivity [16]. It is claimed that the reason of a relatively high degree of porosity is the highly big gradient between low temperature stability of C-349 phase and the liquid phase temperatures that results in a very slow densification process at the sintering temperatures [29] and also less pressure while pellet is made.

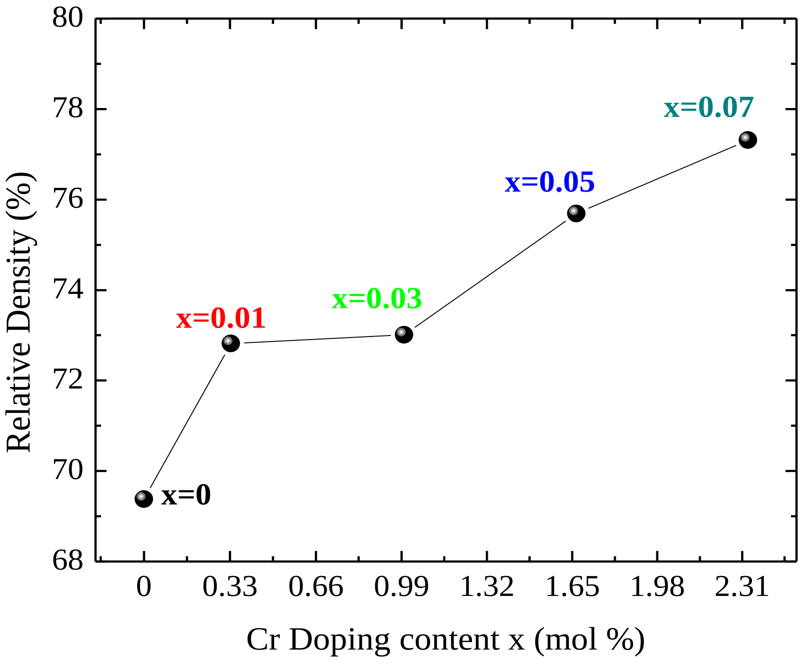

Figure 6.2 Relative densities of the C-349 samples as a function of Cr substitution content - x.

The FE-SEM images and EDS analysis results of each sample are given in difference figures. For instance, figure 6.3 demonstrates the FE-SEM images and EDS analyses of x = 0.01 and x = 0.03 of Cr substituted C-349 samples. In this figure, general surface morphologies are represented in figure 6.3 (a) and (b). EDS analyses are presented for x = 0.01 and x = 0.03 in figure 6.3 (a.1) and (b.1), respectively. It can be inferred that there is no clear grain orientation of both samples. This low substitution does not seem to affect grain sizes. Figure 6.4 demonstrates the FE-SEM images and EDS analyses of x = 0.05 and x = 0.07 Cr substituted C-349 samples. In this figure, general surface morphologies are represented in figure 6.4 (a) and (b). EDS analyses are presented for x = 0.05 and x = 0.07 in figure 6.4 (a.1) and (b.1), respectively. It can be inferred that there is clear grain alignment of both samples. Indeed, grains in x = 0.07 sample are much bigger than ones in x = 0.05 sample.

Because both samples are prepared in the same condition, it can be concluded that Cr substitution causes grain growth.

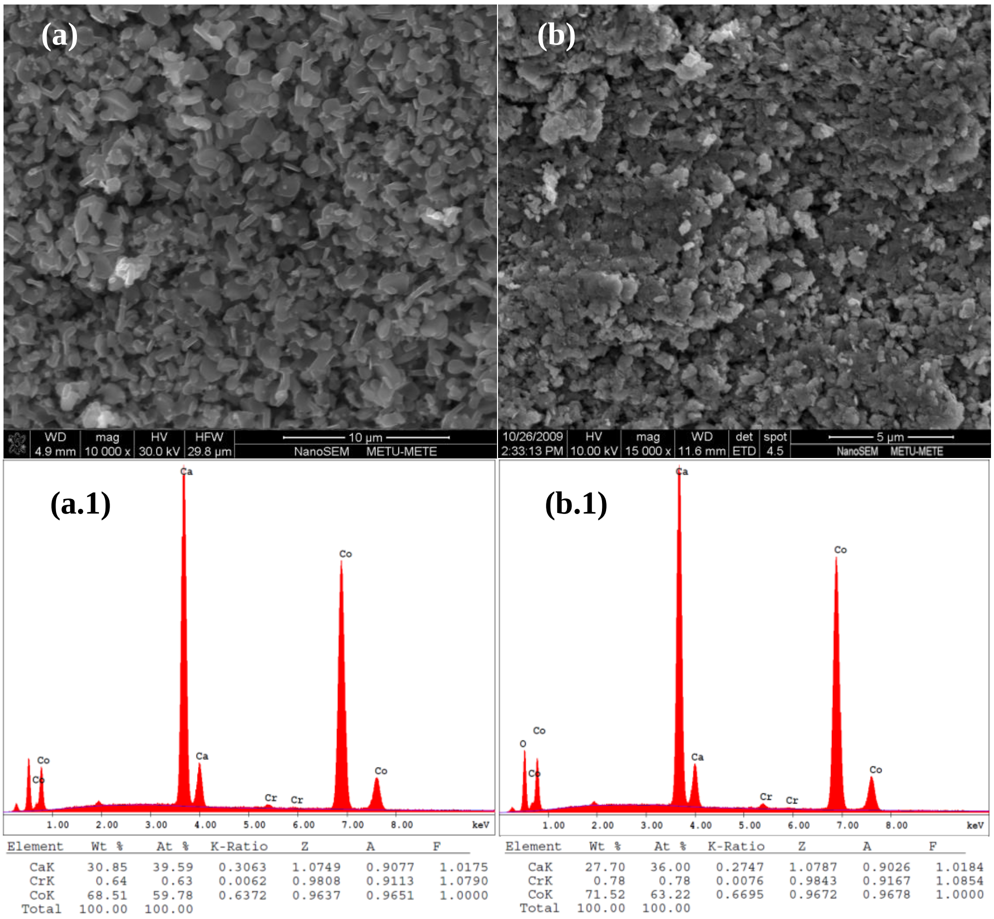

Element	Wt %	At %	K-Ratio	Z	A	F
CaK	30.85	39.59	0.3063	1.0749	0.9077	1.0175
CrK	0.64	0.63	0.0062	0.9808	0.9113	1.0790
CoK	68.51	59.78	0.6372	0.9637	0.9651	1.0000
Total	100.00	100.00				

Element	Wt %	At %	K-Ratio	Z	A	F
CaK	27.70	36.00	0.2747	1.0787	0.9026	1.0184
CrK	0.78	0.78	0.0076	0.9843	0.9167	1.0854
CoK	71.52	63.22	0.6695	0.9672	0.9678	1.0000
Total	100.00	100.00				

Figure 6.3 (a) and **(b)** are the FE-SEM images and **(a.1)** and **(b.1)** are the EDS analyses results of the x = 0.01 and x = 0.03 Cr substituted samples, respectively.

Weight percentage of each element of $Ca_{3-x}Cr_xCo_4O_9$ samples obtained from EDS analyses results in table 6.2. It is well known that EDS analysis is not a very good method for weight percentage analysis, but it is good enough to give a general idea. For this reason, EDS analyses result are gathered in one table to show the amount of Cr in the structures. It can be seen that the values are quite different than the substitutions. However, it is relatively increasing as the Cr content increases from x = 0.01 to x = 0.07. Additionally,

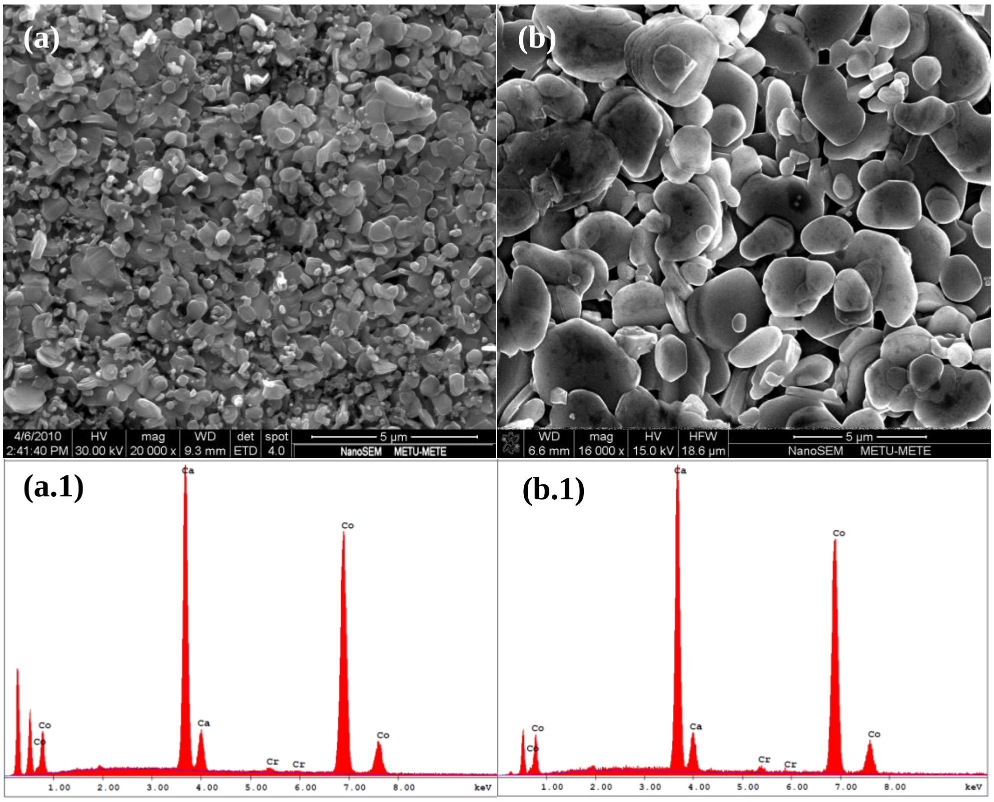

Element	Wt %	At %	K-Ratio	Z	A	F
CaK	29.70	38.27	0.2944	1.0763	0.9051	1.0178
CrK	0.86	0.86	0.0083	0.9820	0.9126	1.0807
CoK	69.44	60.87	0.6470	0.9649	0.9655	1.0000
Total	100.00	100.00				

Element	Wt %	At %	K-Ratio	Z	A	F
CaK	29.83	38.43	0.2958	1.0761	0.9054	1.0178
CrK	0.97	0.97	0.0094	0.9819	0.9123	1.0802
CoK	69.19	60.61	0.6443	0.9647	0.9652	1.0000
Total	100.00	100.00				

Figure 6.4 (a) and (b) are the FE-SEM images and (a.1) and (b.1) are the EDS analyses results of the x = 0.05 and x = 0.07 Cr substituted samples, respectively.

Table 6.2 Weight percentage of elements of $Ca_{3-x}Cr_xCo_4O_9$ samples obtained from EDS analyses results.

	Weight (%)		
$Ca_{3-x}Cr_xCo_4O_9$	**Ca**	**Co**	**Cr**
x = 0.01	30.85	68.51	0.64
x = 0.03	27.70	71.52	0.78
x = 0.05	29.70	69.44	0.86
x = 0.07	29.83	69.19	0.97

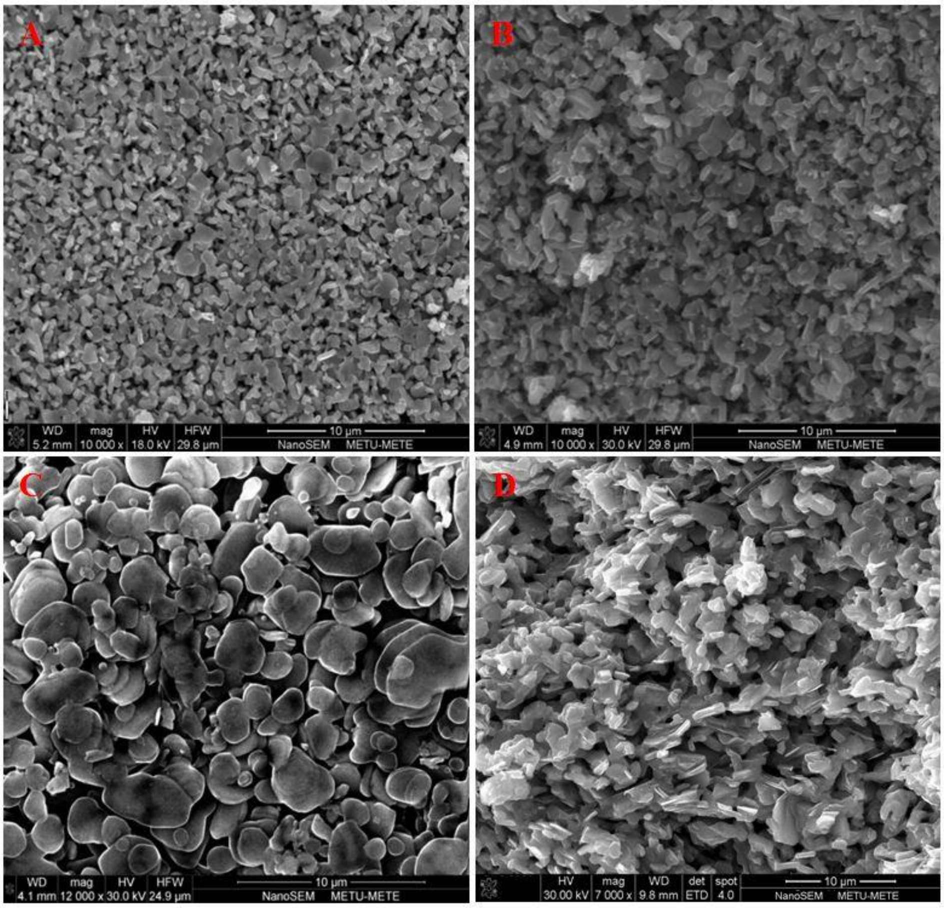

Figure 6.5 FE-SEM images of the surface **(A)** and cross sectional view **(B)** of unsubstituted (x = 0.0) and the surface **(C)** and cross sectional view **(D)** of 0.07 Cr- substituted pellet sample.

Figure 6.5 (A) and (D) are the surface images (parallel to pressure axis), whereas, (B) and (C) are the cross sectional images of unsubstituted and x = 0.07 Cr substituted bulk samples, respectively. As illustrated in figure 6.5 (C), Cr-substituted sample possesses large micro-sized structure (~5 µm) and plate- or sheet-like grains with relatively higher orientation, which are not observed in every substituted sample, whereas unsubstituted sample shows smaller grain size (~1 µm) with lower grain orientation. In addition, the grains in x = 0.07 Cr substituted sample (D) aligned relatively better than unsubstituted (B) one. The result reveals that substitution of Cr for Ca in C-349 sample has substantial effect on the grain growth.

An attempt has also been made to reveal the chemical composition of the microstructural features of substituted $Ca_{2.93}Cr_{0.07}Co_4O_9$ sample using energy dispersive spectrometer (EDS) that is attached to FE-SEM. Figure 6.6 illustrates quantitative maps of main constituents of the sample. In this figure, the pictures show the distribution of each element in the structure: the dark area shows that the element does not exist or is present only in trace amounts. In color mapping, Ca is represented by green, Co by yellow and Cr by white color. This figure proves that Cr is substituted to C-349 material with no accumulation. Considering this discussion and XRD patterns, XRF results, it can be concluded that all the elements exist in one phase with homogeneous distribution as observed in EDS maps.

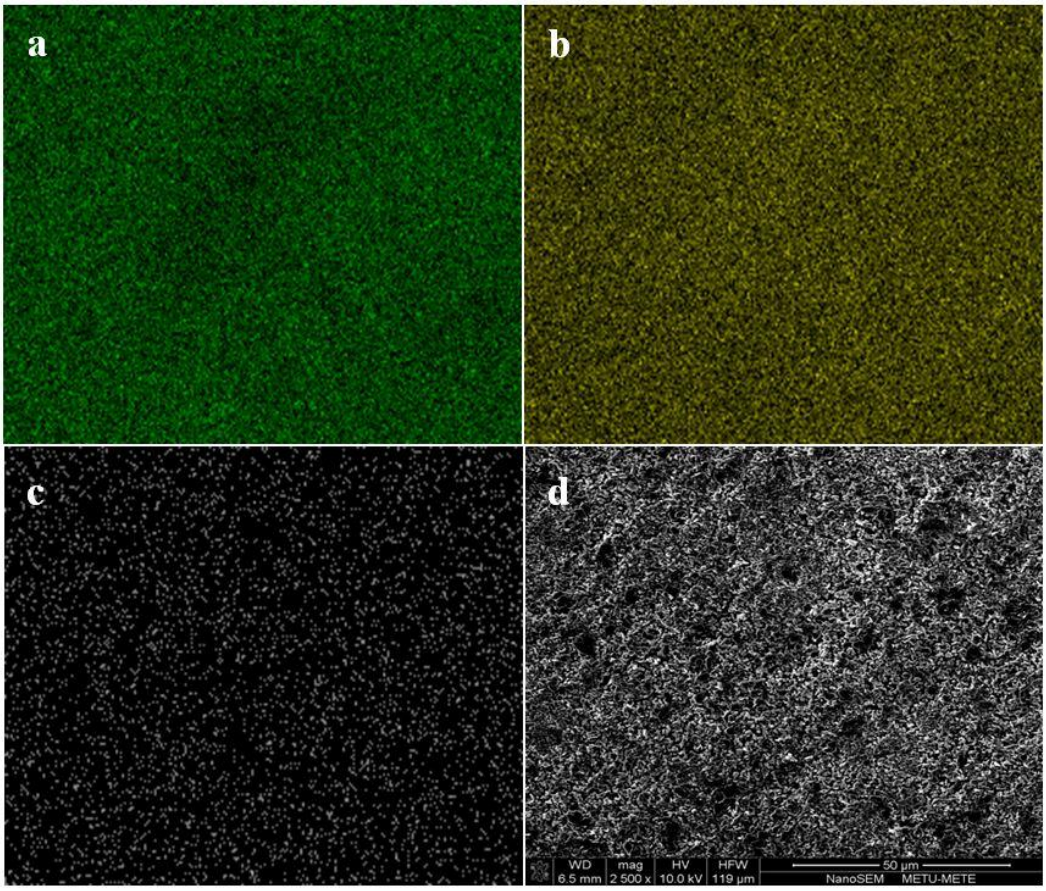

Figure 6.6 Quantitative maps of main constituents calcium **(a)**, cobalt **(b)**, chromium **(c)** and FE-SEM image **(d)** of x = 0.07 Cr sample. Major phases are identifiable by comparing concentrations in the individual maps.

The full XPS spectrums of all the samples are presented in figure 6.7. The Co 2p XPS spectrum for $Ca_{3-x}Cr_xCo_4O_9$ where x = 0.01, 0.03, 0.05, 0.07 and unsubstituted one are presented in the figure 6.8. In order to understand the spin-entropy mechanism and to determine the variation of Co^{4+} concentration induced by Cr substitution, Co 2p spectra are computer-fitted that is performed after Shirley back-ground subtraction by a non-linear least-square fitting method using a Gaussian–Lorentzian product function.

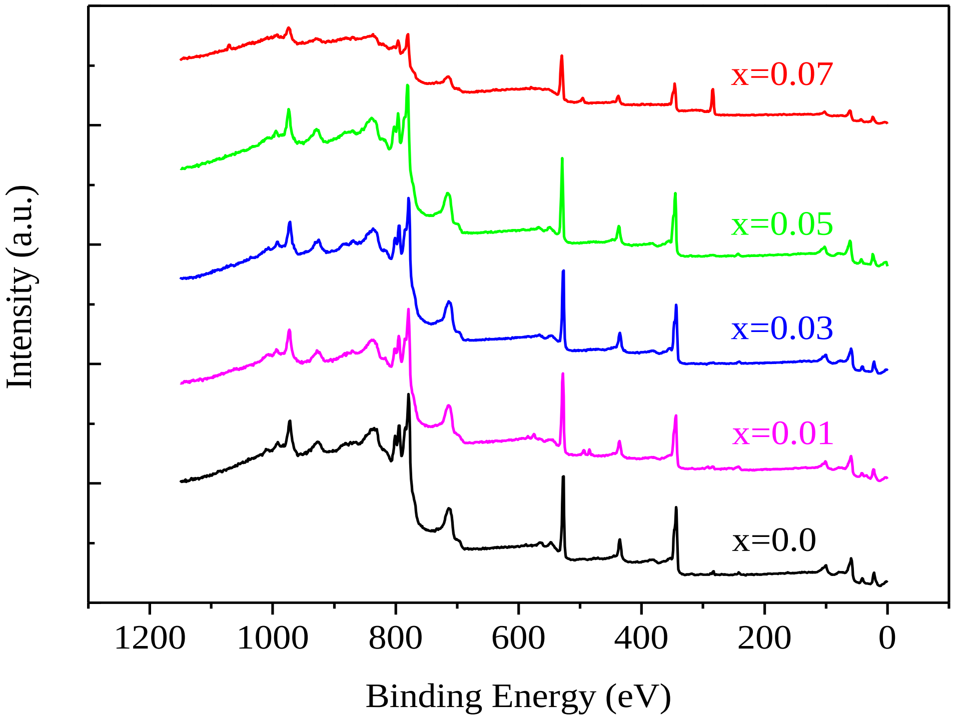

Figure 6.7 Full XPS spectra of $Ca_{3-x}Cr_xCo_4O_9$ samples (x = 0.0, 0.01, 0.03, 0.05, 0.07)

Peaks around 778.32 eV and 780.22 eV are observed, which reveals that Cr^{3+} and Cr^{4+} ions do coexist in this composition series, respectively. This indicates that the Co–O rock-salt layers in the CCO structure have similar Co^{3+} and Co^{4+} low spin configuration as that of the Co–O triangular layers [34].

It can be seen from the figure 6.8 that ratios of fitting peak areas of Co^{4+} to the total Co sites for each composition decreases through Cr substitution as it is illustrated in table 6.3. This implies that Cr substitution makes the Co^{4+} concentration decrease. It can be understood that Co^{4+} concentration decreases with increasing Cr^{3+} content to balance the total valence from the standpoint of charge balance as it is investigated for Gd substitution to Ca-site by G. Tang *et. al.* [35]. The XPS spectra of Cr for $Ca_{3-x}Cr_xCo_4O_9$ are presented in figure 6.9. Peaks of Cr^{3+} present in the substituted samples and are in good agreement with those reported by Biesinger [36].

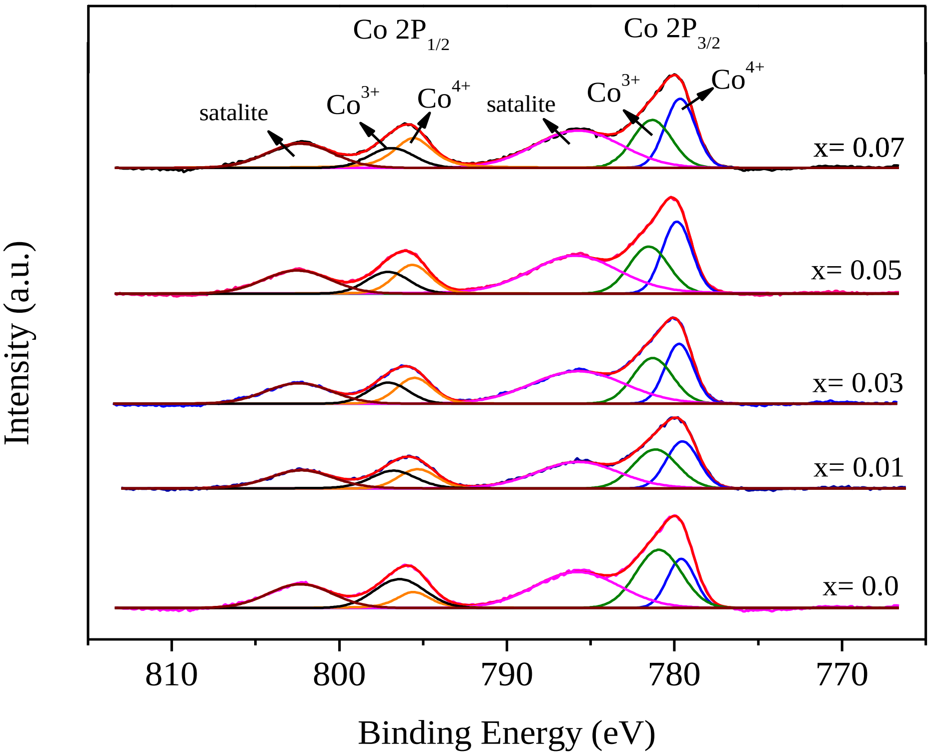

Figure 6.8 Co 2p XPS spectra of $Ca_{3-x}Cr_xCo_4O_9$ samples (x = 0.0, 0.01, 0.03, 0.05, 0.07)

Table 6.3 Ratio of Co^{4+} and Co^{3+} in $Ca_{3-x}Cr_xCo_4O_9$ calculated from XPS spectra.

Samples	**Co^{4+}**	**Co^{3+}**
	Amount (%)	
x = 0.0	49.89	50.11
x = 0.01	46.44	53.56
x = 0.03	45.89	54.11
x = 0.05	44.72	55.28
x = 0.07	42.52	57.48

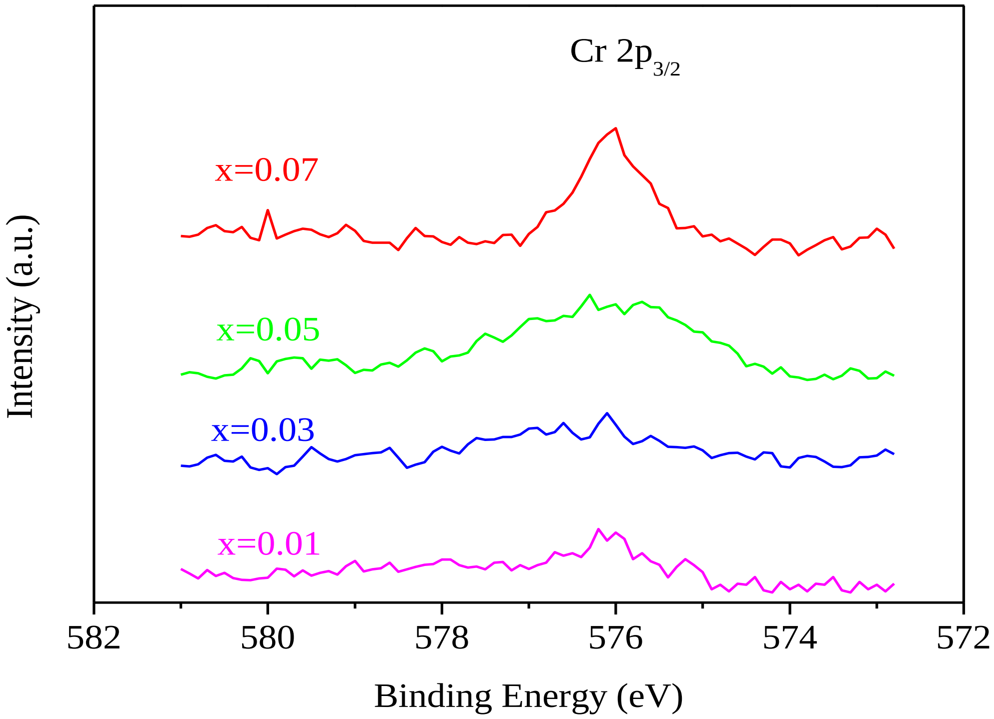

Figure 6.9 XPS spectrum of Cr region for $Ca_{3-x}Cr_xCo_4O_9$ samples (x = 0.01, 0.03, 0.05, 0.07)

The powder diffraction data were refined by a profile analysis using the GSAS program package with all the capabilities and notations to show the changes in lattice parameters. Results are proposed according to a Rietveld refinement associating X-ray diffraction data of the main phase. Before refinement of Cr substituted C-349 samples, instrument parameters are concerned. In order to investigate the instrument parameters, Si standard crystal is refined. Cell parameters are taken from ICSD No: 01-073-2534. After refinement, instrument parameters demonstrated in figure 6.10. Moreover, to show the accuracy of refinement CHI^2 value and corresponding graphs are shown in figure 6.11 and figure 6.12, respectively.

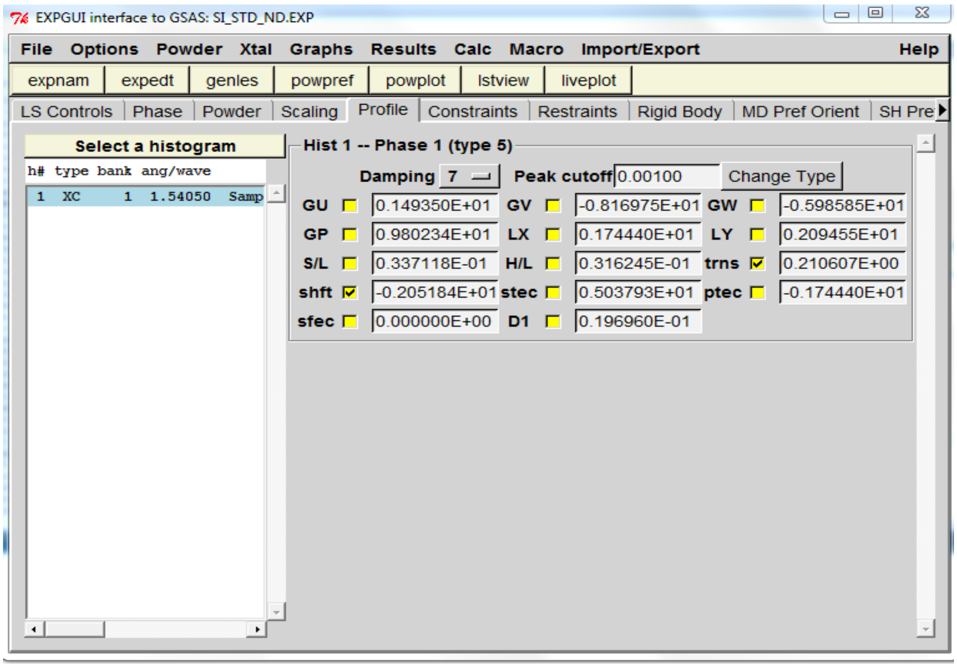

```
h# type bank ang/wave
1   XC    1  1.54050  Samp
```

Hist 1 -- Phase 1 (type 5)

Damping 7
Peak cutoff 0.00100

GU ☐ 0.149350E+01 GV ☐ -0.816975E+01 GW ☐ -0.598585E+01
GP ☐ 0.980234E+01 LX ☐ 0.174440E+01 LY ☐ 0.209455E+01
S/L ☐ 0.337118E-01 H/L ☐ 0.316245E-01 trns ☑ 0.210607E+00
shft ☑ -0.205184E+01 stec ☐ 0.503793E+01 ptec ☐ -0.174440E+01
sfec ☐ 0.000000E+00 D1 ☐ 0.196960E-01

Figure 6.10 Instrument parameters for Si-crystal standard sample.

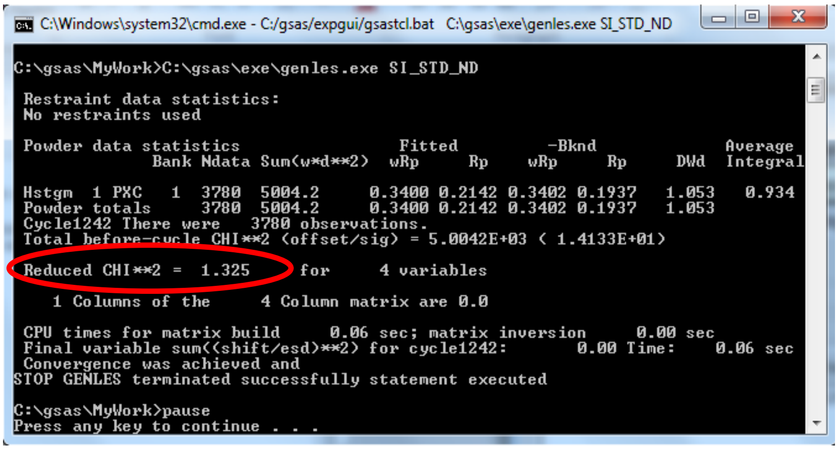

```
C:\gsas\MyWork>C:\gsas\exe\genles.exe SI_STD_ND

 Restraint data statistics:
 No restraints used

 Powder data statistics                 Fitted          -Bknd             Average
             Bank Ndata Sum(w*d**2)  wRp      Rp     wRp      Rp     DWd  Integral

 Hstgm  1 PXC   1  3780  5004.2     0.3400 0.2142 0.3402 0.1937   1.053   0.934
 Powder totals     3780  5004.2     0.3400 0.2142 0.3402 0.1937   1.053
 Cycle1242 There were   3780 observations.
 Total before-cycle CHI**2 (offset/sig) = 5.0042E+03 ( 1.4133E+01)

 Reduced CHI**2 =  1.325      for     4 variables

    1 Columns of the      4 Column matrix are 0.0

 CPU times for matrix build     0.06 sec; matrix inversion     0.00 sec
 Final variable sum((shift/esd)**2) for cycle1242:       0.00 Time:    0.06 sec
 Convergence was achieved and
STOP GENLES terminated successfully statement executed

C:\gsas\MyWork>pause
Press any key to continue . . .
```

Figure 6.11 CHI^2 value for Si-crystal standard sample.

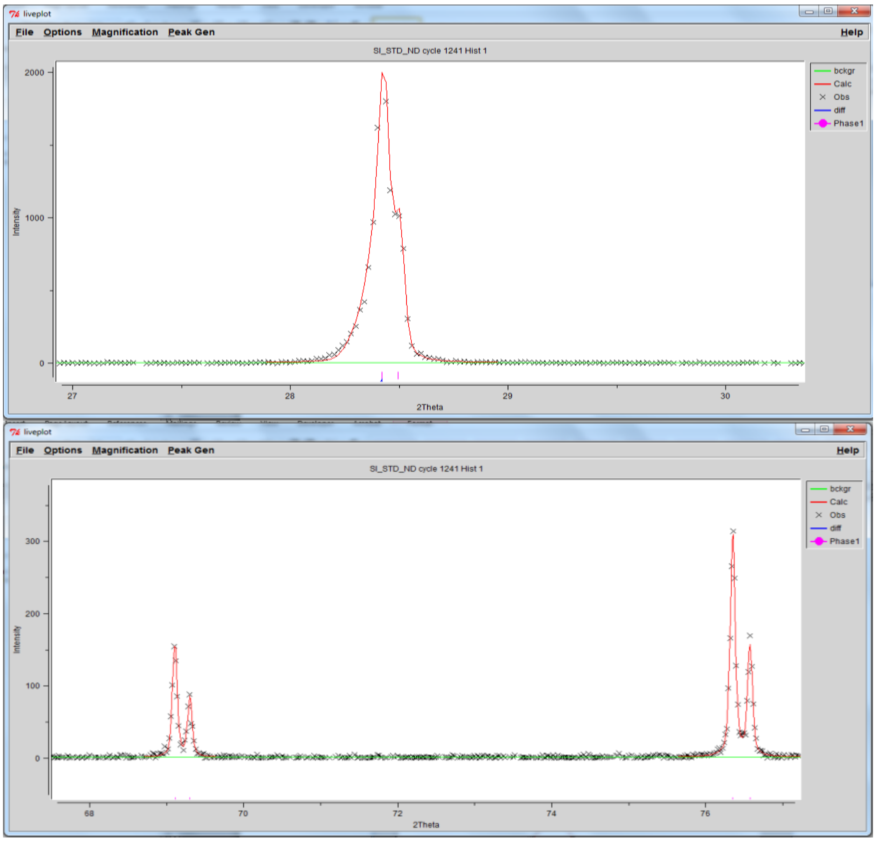

Figure 6.12 Original and calculated plots for Si-crystal standard sample.

After that, X-ray diffraction patterns for un-substituted and Cr-substituted C-349 samples are indexed using two subsystems with cell parameters $a \simeq 4.83, b_1 \simeq 4.56, c_1 \simeq 10.83$ Å, $\beta = 98.11, \delta = b_1/b_2 \simeq 1.618$. The [$Ca_2CoO_3$] system was chosen as a reference. The superspace group was supposed to be *C2/m(1,* δ *,0)s0*. Refined structural parameters are given in table 6.4. The corresponding calculated and observed diffraction patterns are shown in figure 6.13. The excellent agreement between the observed and calculated data is obtained. CHI^2 value for each refinement is less than 1.5. It could be inferred from the table 6.4 that there is no clear structural modifications in Cr substituted samples. It appears that the Cr substitution does not change the lattice parameters in a great extent. A possible reason is because of their close ionic radii.

Table 6.4 Refined cell parameters (Å) from X-ray diffraction data.

Sample	***a* (nm)**	***b_1* (nm)**	***c* (nm)**	α	β (°)	γ
Reference	4.8376	4.5565	10.8330	90.00	98.06	90.00
C-349	4.8390	4.5530	10.8579	90.00	98.11	90.00
x = 0.01	4.8365	4.5666	10.8531	90.00	98.10	90.00
x = 0.03	4.8358	4.5659	10.8498	90.00	98.09	90.00
x = 0.05	4.8335	4.5646	10.8420	90.00	98.09	90.00
x = 0.07	4.8327	4.5578	10.8076	90.00	98.06	90.00

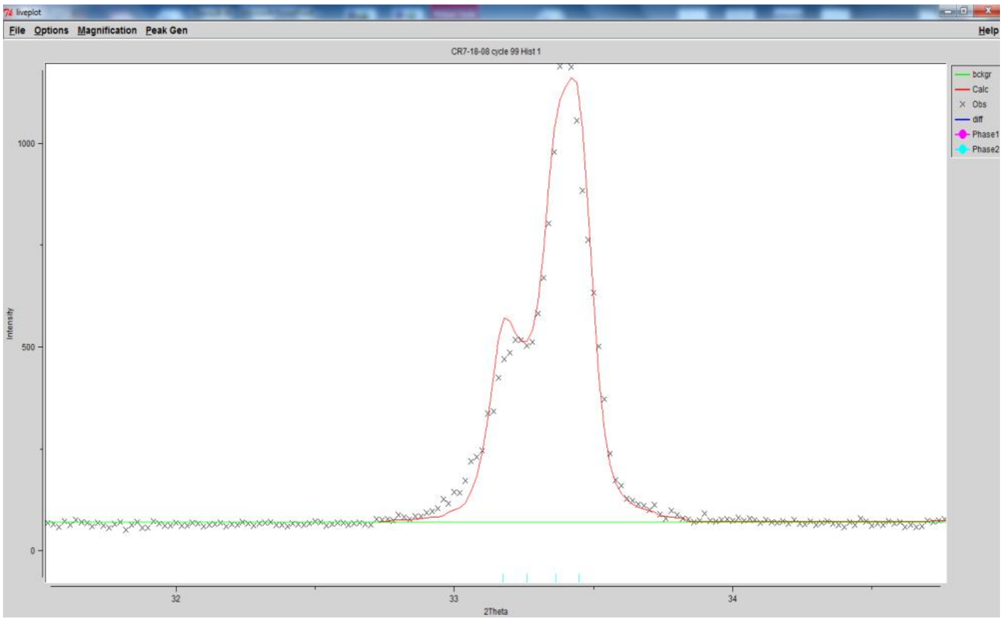

Figure 6.13 Original and calculated plots for unsubstituted C-349 sample.

6.3 Electrical and Thermal Transport Properties

The temperature dependence of Seebeck coefficient and electrical resistivity are measured using a home-made system set up in our laboratory in the temperature interval from 300 K to 1100 K [37]. The detail of the set-up has been described in chapter 4.

The typical temperature dependence Seebeck coefficient values of C-349 material which indicate hole (p-type) conduction are presented in figure 6.14. The values of the Seebeck coefficient exhibit the same trends which slightly increase with the temperature for all the samples.

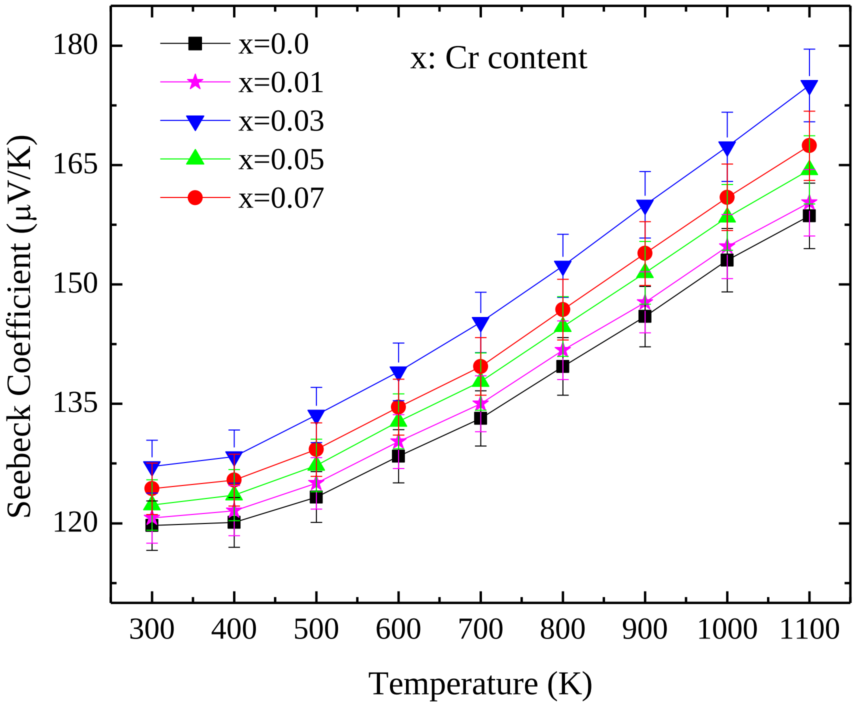

Figure 6.14 Seebeck coefficient vs temperature of Cr substituted $Ca_{3-x}Cr_xCo_4O_9$ (x = 0.01, 0.03, 0.05, 0.07) samples and unsubstituted (x = 0.0) one.

The absolute value of Seebeck coefficient of unsubstituted sample is measured as 119.7 μW/K at 300 K that increases with the temperature and reaches the maximum value of 158.6 μW/K at a 1100 K. Sample with x = 0.01 and x = 0.05 Cr substituted samples show Seebeck coefficient value of 160 and 164.4 μW/K at 1100 K. However, the maximum Seebeck coefficient value of ~175 μV/K measured for x = 0.03 Cr substituted sample is higher than the value of ~167 μV/K obtained for the x = 0.07 Cr substituted sample at 1100 K. The increase in Seebeck coefficient could be attributed to the spin-entropy enhancement [30]. Nevertheless, the decrease in the value of Seebeck coefficient over x = 0.03 might be due to the larger grains.

The temperature dependence electrical resistivity values of all the samples are illustrated in figure 6.15. According to the result of measurements, the resistivity of every sample does vary significantly throughout the measurement temperature from 300 to 700 K. A slight increase of resistivity starts at 300 K and ends at about 400 K for all the samples representing metal-like behavior. After these temperatures the system exhibits semiconductor-like transport up to 900 K where the resistivity decreases with temperature. Over these regions, the transport behavior changes again to very slight increase in resistivity with increasing temperature up to 1100 K. The resistivity value of unsubstituted sample (15.3 mΩ.cm at 300 K) is consistent with the earlier reported works [8, 44, 45].

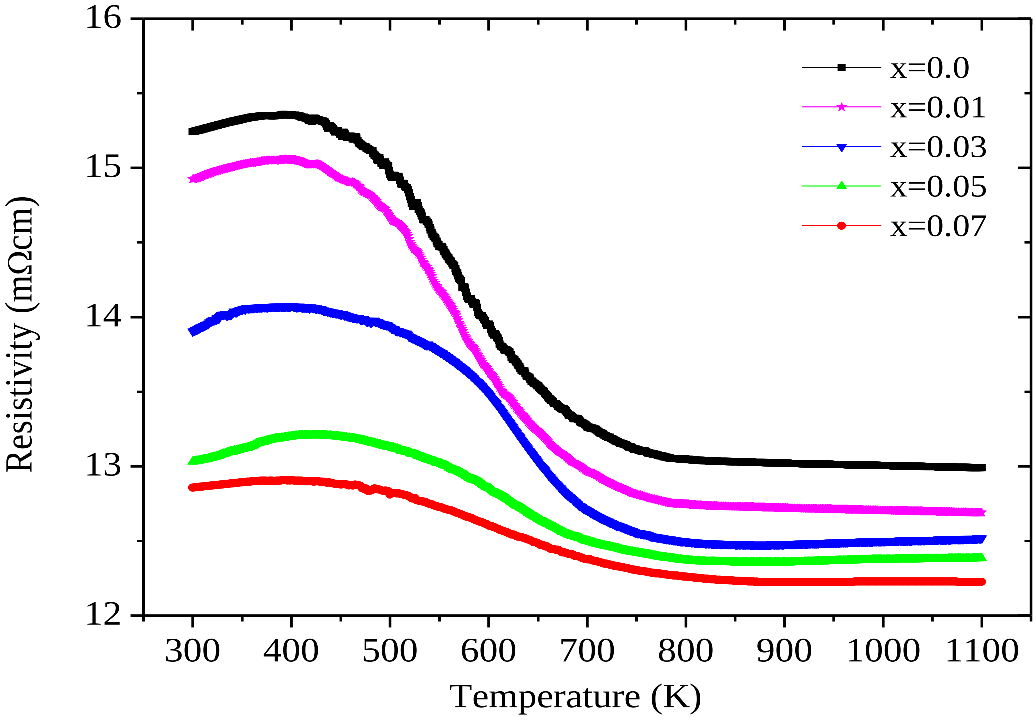

Figure 6.15 Resistivity measurements of Cr-substituted and unsubstituted samples from 300 K to 1100 K.

The result of resistivity measurements indicate that the Cr substituted samples show lower resistivity values than unsubstituted sample. Indeed, as the Cr content increases, the resistivity decreases drastically. The x = 0.07 Cr sample shows the lowest resistivity value of 12.2 mΩ.cm whereas unsubstituted sample shows the highest resistivity value of 13 mΩ.cm at 1100 K. Cr samples with x = 0.03 and x = 0.05 stays in the middle range with the values of 12.5 and 12.3 mΩ.cm at 1100 K, respectively. Total chance in resistivity is around ~6.1 %. The reason can be explained in the following way. If the Ca^{2+} are replaces by dominant valence state of Cr^{+3} ion, it would result in a reduction in the concentration of holes, and higher resistivity [26]. Our experimental results imply that there exists another factor which affects the electrical resistivity. In this case, two possible explanations might be very helpful to understand this phenomenon. First possible interpretation can be the improvement of the carrier mobility by Cr^{3+} substitution [46, 47]. It has been indicated that the increase in conductivity is attributed to an increase in carrier mobility rather than carrier concentration, because an increase in carrier concentration tends to lead to a decrease in the Seebeck coefficient [48, 49]. However, in our results Seebeck coefficient values increased together with Cr substitution to the level of x = 0.03. Therefore, we can imply that the Cr substitution leads to an increase in carrier mobility to a definite level when it is substituted to Ca-site. Secondly, it has been indicated that improvements in the electrical conductivity have also been attributed to differences in the microstructures [15, 50]. This idea matches our result since Cr substitution leads to the higher degree of grain alignment along with larger grains and higher densities than unsubstituted one as it is demonstrated in figure 6.5. Therefore, we can assume that Cr substitution to Ca site not only highly influential on the microstructural properties but also affects electronic properties.

The elementary charge-transport process mechanism of the C-349 system is the hopping of a hole from Co^{4+} to Co^{3+} in these layered misfit oxide compounds [51]. According to the polaron theory [52], the electrical conductivity of small polaron hopping conduction mechanism can be written as

$$\sigma = nea^2(A/T)\exp(-E_g/k_BT) \tag{6.1}$$

where n, e, a, E_g, and A are the carrier concentration, the electron charge of carrier, the intersite distance of hopping, the activation energy, and a pre-exponential term related to the scattering mechanism, respectively. k_B is the Boltzmann constant, and T is the absolute temperature.

As shown in figure 6.16 (a), linear relationships between ln(σT) and 1000/T are obtained in the temperature range above 500 K, indicating a small polaron-hopping conduction mechanism in this system. The activation energy can be obtained from a plot of log(σT) vs 1000/T, as shown in figure 6.16 (b). The activation energies for various Cr substitution levels are noted to be almost independent of substitution. The differences in the activation energies are slightly larger than 0.02 eV, indicating that the transport properties did change slightly with the amount of Cr substitution [51].

As it is introduced in section 1.4, C-349 is made up of a single CdI2-type CoO_2 layer and an alternating stack along the c-axis of triple rock-salt-type Ca_2CoO_3 layers. Whereas this edge-shared CoO_2 layers are responsible for the electrical conduction, the rock-salt-type Ca_2CoO_3 layers are considered to be charge reservoirs to supply charge carriers to the CoO_2 layers [51]. Therefore, if the Cr substitutes for the Co-site in the CoO_2 layer, the defect might be brought into the conduction path leading to a significant influence on the activation energy. Nevertheless, due to a very slight influence on the activation energy, Cr substitution is in the Ca_2CoO_3 layers and therefore the conduction path might slightly be disturbed because the ionic radii of Cr (63 Å) are smaller than the radii of Ca (0.99 Å).

Thermal conductivity measurement results are presented in figure 6.17. The heat flow direction of the thermal conductivity is equal to the direction that is chosen for Seebeck coefficient and electrical resistivity. Thermal conductivity measurements of substituted (for x = 0.07: 1.2 W/mK at 1100 K) and unsubstituted (for x = 0.0: 0.91 W/mK at 1100 K) samples show no significant difference in value and nearly steady trend as a function of temperature is observed. Thermal conductivity results are in a good agreement with recently reported research [26]. The increase in these results is due to larger grains which reduce grain boundary scattering at interfaces [50, 51].

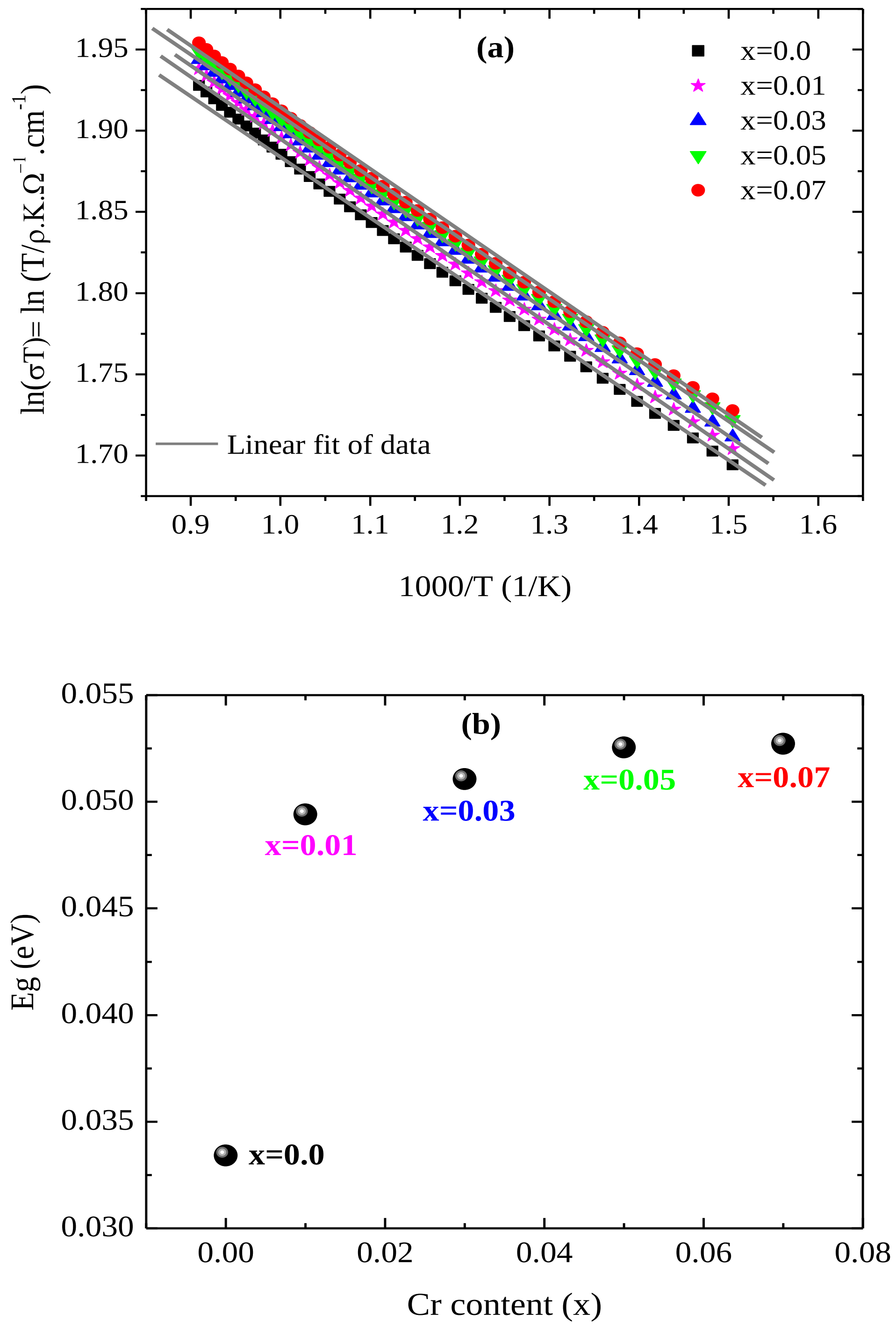

Figure 6.16 **(a)** Linear fit for ln (T/ρ) versus 1000/T and **(b)** The activation energy, Eg of $Ca_{3-x}Cr_xCo_4O_9$ (x = 0.0, 0.01, 0.03, 0.05, 0.07) bulk materials.

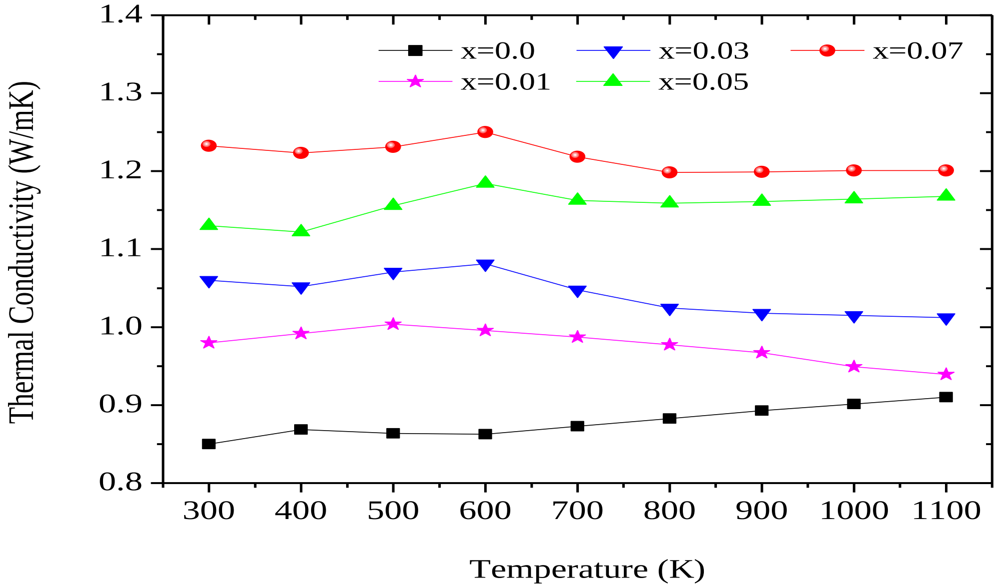

Figure 6.17 Thermal conductivity of Cr substituted $Ca_{3-x}Cr_xCo_4O_9$ (x = 0.01, 0.03, 0.05, 0.07) samples and unsubstituted (x = 0.0) one.

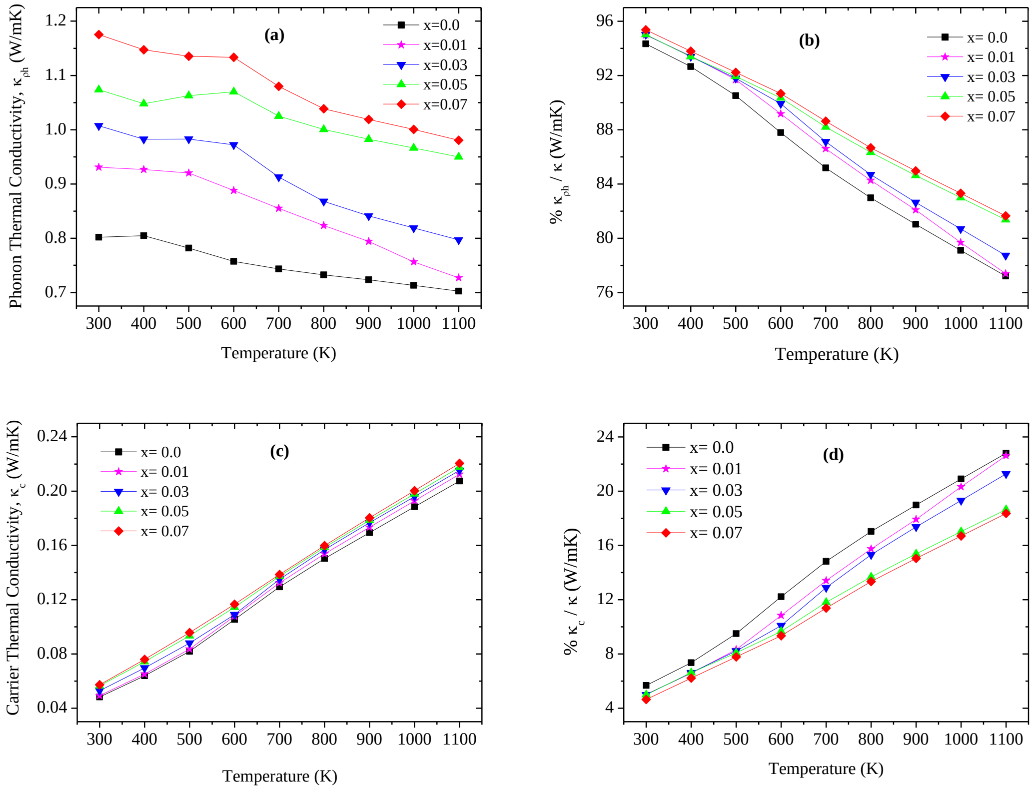

Figure 6.18 Temperature dependence of **(a)** the phonon thermal conductivity; κ_{ph}, **(b)** the ratio of κ_{ph} / κ (%), **(c)** the carrier thermal conductivity; κ_c and **(d)** the ratio of κ_c / κ (%), of all samples.

The phonon contribution (κ_{ph}), the carrier contribution (κ_c), the temperature dependences of κ_{ph} and κ_{ph}/κ (%) can be calculated with the same method used in section 5.3 and plotted, as shown in figure 6.18. Based on these results, it can be inferred that phonons dominate the thermal conduction processes for all samples at 300 K.

The power factor of Cr substituted and unsubstituted samples are shown in figure 6.19. It can be seen that all of the samples exhibit the same characteristics of *PF* values which increase with the temperature. *PF* values of samples are increasing with the Cr-substitute. *PF* values of unsubstituted and x = 0.01 Cr samples are almost same in the measured temperature range.

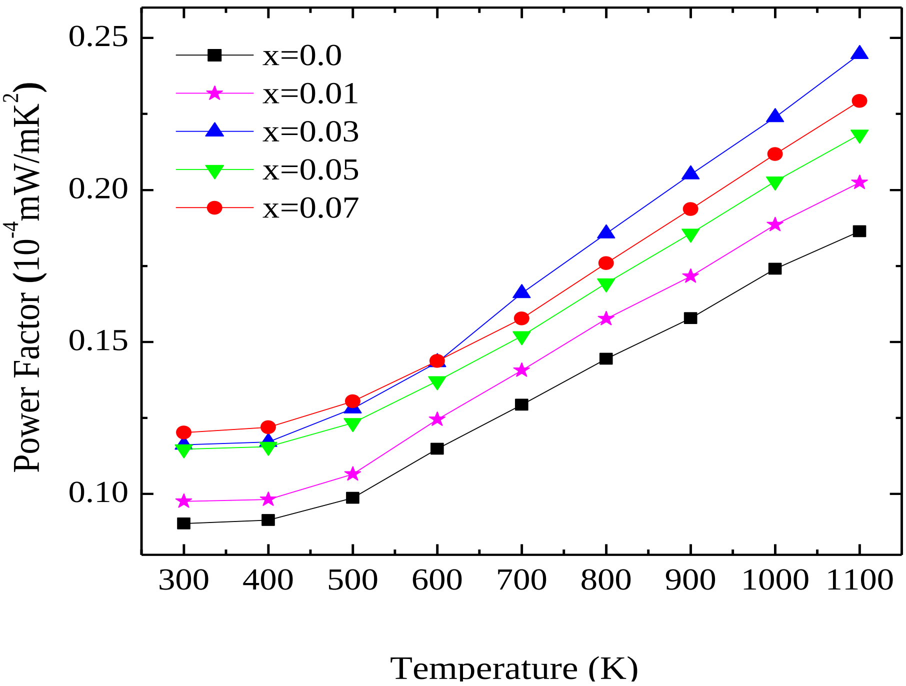

Figure 6.19 Power Factor of Cr substituted $Ca_{3-x}Cr_xCo_4O_9$ (x = 0.01, 0.03, 0.05, 0.07) and unsubstituted (x = 0.0) samples.

The calculated *PF* value of unsubstituted sample reached 0.19 mW/mK^2, and x = 0.01 Cr sample has the *PF* values of 0.20 mW/mK^2 at 1100K. However, the *PF* values of x = 0.05 and x = 0.07 samples show similar trend but slightly larger than those of unsubstituted and x = 0.01 samples with the value of 0.22 and 0.23

mW/mK^2 that occurs mainly because of their higher conductivities. The *PF* value obtained for sample x=0.03 Cr is the highest with the values of 0.25 mW/mK^2 at 1100 K due to its higher Seebeck coefficient value.

Figure 6.20 demonstrates the temperature dependent *ZT* for unsubstituted and substituted samples from 300 K to 1100 K. The figure of merit values tend to increase with increasing temperature. The graph shows that all Cr substituted samples show higher *ZT* values than that of unsubstituted sample. *ZT* value reaches 0.24 and 0.20 for x = 0.01 and x = 0.05 Cr samples at 1100 K, respectively. The highest *ZT* calculated as 0.26 for x = 0.03 Cr samples indicate that Cr does affect, to a great extent, the C-349 conduction band. The improvement of thermoelectric performance is most significant in x = 0.03 Cr substituted sample due to no considerable change in thermal conductivity values. The most attractive aspect of Cr substituted samples is their considerably low resistivity and thermal conductivity. This study indicated that elemental substitution is fairly effective for improving *ZT* of C-349 system.

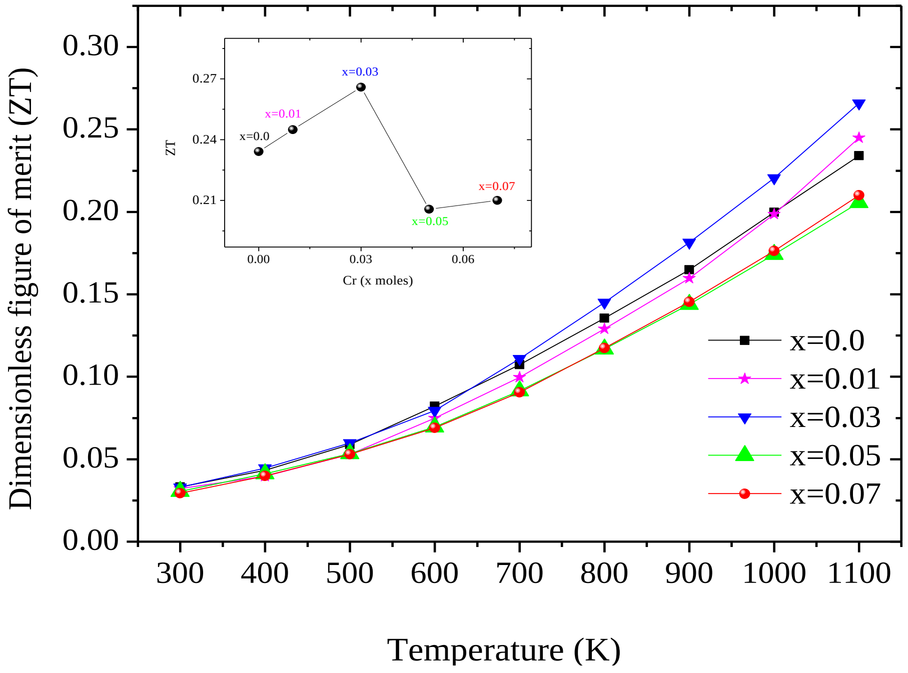

Figure 6.20 *ZT* of Cr substituted $Ca_{3-x}Cr_xCo_4O_9$ (x = 0.01, 0.03, 0.05, 0.07) samples and unsubstituted (x = 0.0) one. The inset presents *ZT* values at different Cr content.

6.4 Conclusion

The effects of Cr substitution on structural, electrical and thermal properties in C-349 have been studied. The grain size of x = 0.07 Cr substituted sample is much larger than that of unsubstituted sample, indicating that Cr substitution promotes the growth of grains which results in lower resistivity and higher thermal conductivity. The increase of total thermal conductivity takes place because of the increase in density and grain growth that reduces the grain boundary scatterings at boundaries. XPS results confirm that Cr substitution improves the spin entropy in C-349 that results in higher Seebeck coefficient values to a definite point (x = 0.03) because of dominance effect on the grain growth. The higher figure of merit is observed for x = 0.03 Cr substitution sample revealing the limit of amount of Cr-substitution. The evaluation of the results is presented in detail in chapter 7.

REFERENCES

[1] T. M. Tritt and M. A. Subramanian, MRS Bulletin 31(2006) pp 188-229

[2] G. Chen, M. S. Dresselhaus, G. Dresselhaus, J.-P. Fleurial and T. Caillat, Int. Mater. Rev. 48 (2003) pp 45–66

[3] I. Terasaki, Y. Sasago, and K. Uchinokura, APS 56 (1996) pp 685–687

[4] L. D. Zhao, D. Berardan, Y. L. Pei, C. Byl, L. P-Gaudart, and N. Dragoe, Appl. Phys. Lett. 97 (2010) pp 092118

[5] K. Koumoto and I. Terasaki, MRS Bulletin 31(2006) pp 206–210

[6] L. Zhang, X. Tang, and W. Gao, J. Phys. Chem. C 113 (2009) pp 7930–7934

[7] R. F. Funahashi, I. M. Atsubara, H. I. Kuta and T. T. Akeuchi, Jpn. J. Appl. Phys. 39 (2000) pp L1127–L1129

[8] A. C. Masset, C. Michel, A. Maignan, M. Hervieu, O. Toulemonde, F. Studer, B. Raveau, and J. Hejtmanek, Phys. Rev. B 62 (2000) pp 166–175

[9] T. Takeuchi, T. Kondo, K. Soda, U. Mizutani, R. Funahashi, M. Shikano, S. Tsuda, T. Yokoya, S. Shin, and T. Muro, J. Electron Spectros. Relat. Phenomena 137–140 (2005) pp 595–599

[10] S. Bhattacharya, S. Rayaprol, A. Singh, A. Dogra, C. Thinaharan, D. K. Aswal, S. K. Gupta, J. V Yakhmi, R. N. Kulkarni, S. M. Yusuf, and S. N. Bhatia, J. Phys. D. Appl. Phys. 41 (2008) pp 085414

[11] V. A. M. Brabers, H. Meuter, Z. Šimša, Solid State Commun. 45 (1983) pp 807–809

[12] T. Tsubota, M. Ohtaki, K. Eguchi, and H. Arai, J. Mater. Chem. 7 (1997) pp 85–90

[13] W. Shin and N. Murayama, Japanese J. Appl. Physics, Part 2 Lett. 38 (1999) pp 19

[14] J. W. Moon, W. S. Seo, H. Okabe, T. Okawa, and K. Koumoto, J. Mater. Chem. 10 (2000) pp 2007–2009

[15] J. W. Fergus, J. Eur. Ceram. Soc. 32 (2012) pp 525–540

[16] Y. Wang, Y. Sui, P. Ren, L. Wang, X. Wang, W. Su, H. Fan, Chem. Mater. 22 (2010) pp 1155–1163

[17] N. V. Nong, C.J. Liu and M. Ohtaki, J. Alloys Compd. 491 (2010) pp 53

[18] Y. Wang, L. Xu, Y. Sui, X. Wang, J. Cheng and W. Su, Appl. Phys. Lett. 97 (2010) pp 062114

[19] J. L. Chen, Y. S. Liu, C. J. Liu, L. C. Huang, C. L. Dong, S. S. Chen and C. L. Chang, J. Phys. D. Appl. Phys. 42 (2009) pp 135418

[20] C. J. Liu, J. L. Chen, L. C. Huang, Z. R. Lin, and C. L. Chang, J. Appl. Phys. 102 (2007) pp 014908

[21] C. J. Liu, L. C. Huang and J. S. Wang, Appl. Phys. Lett. 89 (2006) pp 204102

[22] L. Xu, F. Li, and Y. Wang, J. Alloys Compd. 501 (2010) pp 115–119

[23] Q. Yao, D. L. Wang, L. D. Chen, X. Shi, and M. Zhou, J. Appl. Phys. 97 (2005) pp 103905

[24] Y. Miyazaki, Y. Suzuki, M. Onoda, Y. Ishii, Y. Morii, and T. Kajitani, Jpn. J. Appl. Phys. 43 (2004) pp 6252–6258

[25] J. C. Diez, M. A. Torres, S. Rasekh, G. Constantinescu, M. A. Madre and A. Sotelo, Ceram. Int. 39 (2013) pp 6051–6056

[26] S. Pinitsoontorn, N. Lerssongkram, N. Keawprak, and V. Amornkitbamrung, J. Mater. Sci. Mater. Electron. 23 (2011) pp 1050–1056

[27] Y. Wang, N. Rogado, R. Cava, and N. Ong, Nature 423 (2003) pp 425–428

[28] W. Koshibae, K. Tsutsui, and S. Maekawa, Phys. Rev. B 62 (2000) pp 6869–6872

[29] G. D. Tang, X. N. Xu, C. P. Tang, Z. H. Wang, Y. He, L. Qiu, L. Y. Lv, L. Xing, and Y. W. Du, Europhysics Lett. 91 (2010) pp 17002

[30] R. Asahi, J. Sugiyama, and T. Tani, Phys. Rev. B 66 (2002) pp 155103

[31] H. Q. Liu, X. B. Zhao, F. Liu, Y. Song, Q. Sun, T. J. Zhu and F. P. Wang, J. Mater. Res. 43 (2008) pp 4933

[32] Y. F. Zhang, J. X. Zhang, Q. M. Lu and Q. Y. Zhang, Mater. Lett. 60 (2006) pp 2443–2446

[33] A. Sotelo, G. Constantinescu, S. Rasekh, M. A. Torres, J. C. Diez, and M. A. Madre, J. Eur. Ceram. Soc. 32 (2012) pp 2415–2422

[34] Y. Song and C.W. Nan, Phys. B Condens. Matter. 406 (2011) pp 2919–2923

[35] G. Tang, F. Xu, D. Zhang, and Z. Wang, Ceram. Int. 39 (2013) pp 1341–1344

[36] M. C. Biesinger, B. P. Payne, A. P. Grosvenor, L. W. M. Lau, A. R. Gerson, and R. St. C. Smart, Appl. Surf. Sci. 257 (2011) pp 2717–2730

[37] M. Gunes, M. Parlak, M. Ozenbas, Meas. Sci. Technol. 25 (2014) pp 055901-10

[38] Z. Zhou and C. Uher, Rev. Sci. Instrum. 76 (2005) pp 023901

[39] A. T. Burkov, A. Heinrich, P. P. Konstantinov, T. Nakama, K. Yagasaki, Meas. Sci. Technol. 12 (2001) pp 264–272

[40] J. Martin, T. Tritt, C. Uher, J. Appl. Phys. 108 (2010) pp 121101-12

[41] S. Iwanaga, E. S. Toberer, A. LaLonde, G. J. Snyder, Rev. Sci. Instrum. 82 (2011) pp 063905-6

[42] C. Byl, D. Bérardan and N. Dragoe, Meas. Sci. Technol. 23 (2012) pp 035603

[43] V. Ponnambalam, S. Lindsey, N. S. Hickman and T. M. Tritt, Rev. Sci. Instrum. 77 (2006) pp 073904

[44] G. Xu, R. Funahashi, M. Shikano, I. Matsubara and Y. Zhou, Appl. Phys. Lett. 80 (2002) pp 3760

[45] T. Wu, T. A. Tyson, H. Chen, J. Bai, H. Wang and C. Jaye, J. Phys. Condens. Matter 24 (2012) pp 455602

[46] Y. Liu, Y. Lin, L. Jiang and C. Nan, J Electroceram 21 (2008) pp 748–751

[47] B. Fisher, L. Patlagan, G. M. Reisner and A. Knizhnik 61 (2000) pp 470–475

[48] Y. Song, Q. Sun, L. Zhao, F. Wang and Z. Jiang, Mater. Chem. Phys. 113 (2009) pp 645–649

[49] T. Sun, H. H. Hng, Q. Y. Yan and J. Ma, J. Appl. Phys. 108 (2010) pp 083709

[50] H. Hao, L. Zhao and X. Hu, J. Mater. Sci. Technol. 25 (2009) pp 105-108

[51] Y.H. Lin, C.W. Nan, Y. Liu, J. Li, T. Mizokawa and Z. Shen, J. Am. Ceram. Soc. 90 (2007) pp 132–136

[52] A. J. Bosman and H. J. Van Daal, Adv. Phys. 19 (1970) pp 1-117

[53] H. Lee, D. Vashaee, D. Z. Wang, M. S. Dresselhaus, Z. F. Ren, and G. Chen, J. Appl. Phys. 107 (2010) pp 094308

[54] D. L. Medlin and G. J. Snyder, Curr. Opin. Colloid Interface Sci. 14 (2009) pp 226–235

CHAPTER 7

SUMMARY, CONCLUSION AND FURTHER SUGGESTIONS

As a final chapter, the significance of the improvements on electrical measurement system, structural and thermoelectric findings of C-349 based thermoelectric materials will be summarized and concluded. Future work in this subject will be suggested.

7.1 The Properties of Electrical Measurement System

The improvements in thermoelectric property measurement systems are the followings.

1. Beadless thermocouple:

   a. The unstable thermocouple junction would cause electrical noise. However, beadless thermocouple is a unique thermocouple with its featured properties. Such as, beadless structure and its stable junction point decreases the measurement uncertainties by shorting the contact distance between the sample and the probes.

   b. Estimated measurement uncertainty for Seebeck coefficient measurement is 2.6 % which is lower than the other studies reported in literature.

   c. User cannot make differential temperature and four-point probe resistivity measurements using any other measurement systems.

2. Micro heaters:

   a. Undesired magnetic fields due to the heater wires, which can cause incorrect measurement results, are eliminated by our micro heaters. Due to the fact that micro heaters response fast and can reach up to 1100 K,

  - **b.** There is no need to have a main heater and this reduces the size of the system.

  - **c.** There is no need to have one more temperature controller which decreases the cost.

  - **d.** The measurements conducted using micro heaters demonstrated significant accuracy so that temperature convection across the sample is minimized.

  - **e.** Micro heaters are located in the nearest place to the thermocouples for the possibility of fast response. Thermal anchoring, similar to the one used for the sensor leads, is included so that any heat transfer does not warm the load when the heater is not running.

  - **f.** The lead wires are twisted to minimize noise coupling between the heaters and the other leads in the system.

3. Differential temperature measurement:

  - **a.** Differential temperature measurement which many devices do not provide in their measurement systems along with Seebeck coefficient and resistivity measurements.

  - **b.** It is the most accurate way for the measurement of temperature that is possible with the help of additional beadless thermocouple occupying two holes at the middle of the alumina isolator.

4. Axial four-point probe resistivity measurements:

  - **a.** There are many well designed devices developed for resistivity measurements of the thermoelectric materials providing two- or four-point probe resistivity measurements. However, none of them provide nondestructive “axial” four-point probe resistivity measurements.

  - **b.** This design satisfies some other necessities during thermoelectric measurements such as good electrical and thermal contact with the sample, non-destructive technique and good temperature control.

c. The installed Seebeck coefficient and resistivity device is very small, compact and modular as it is compared to other homemade and commercial devices.

In most commercial thermoelectric properties measurement systems (e.g. Linseis LSR, ZEM3) there are top and bottom contacts in order to apply electrical current to create temperature gradient. Furthermore, there will be two thermocouples located on one side of the sample that measures voltage drop and temperature to calculate Seebeck coefficient at each temperature interval. However, these thermocouples are a possible heat connection to the environment. For instance, if these thermocouples are connected thermally to the outside of the measurement system, they will serve as a heat sink called cold finger. This leads to miscalculation of Seebeck coefficient. The reason why scientists create heated environment around the sample in order to thermalize the thermocouples and other connections. Because we do use both beadless thermocouples and micro heaters and no side contacts, there is no need to use furnace for external heating. As a result, better electrical and thermal conduct and high measurement accuracy is achieved. Indeed, the whole measurement system is much smaller than the commercial or other measurement systems.

Therefore, the work presented in this dissertation provides better conditions for the Seebeck coefficient and resistivity measurements for bulk thermoelectric samples. The summary of improvements on high temperature Seebeck coefficient and resistivity measurement device is listed in the table 7.1.

Table 7.1 The summary of improvements on high temperature Seebeck coefficient and resistivity measurement device

		High Temperature Seebeck Coefficient & Resistivity Measurement Device
System Properties		**Achievements**
Measurements	Seebeck Coefficient	✓
	Electrical Resistivity	✓
	Differential Temperature	✓
Temperature Range	High	• 300 K to 1100 K
	Low	• 77 K with some modifications
Error	Minimization	• Cold-finger effect is limited to the thickness of the contact wire
	Elimination	• External magnetic field • Thermal & electrical contact
Atmosphere	Vacuum	✓
	Inert gas	✓
Differences & Achievements		• Reference Sample measurement • Simultaneously 2-sample measurement option • 2- and 4-point probe resistivity measurement • Large contact area • Axial contact for good thermal &electrical contact • Modular • Software control • Easy to use
Thermocouple Design	Triple Beadless thermocouple design	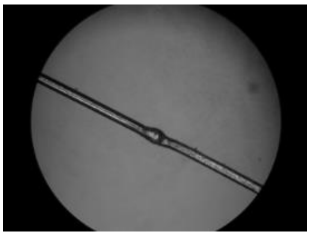 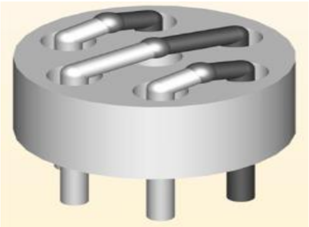

7.2 Phonon Scattering Enhancement by Porosity and Nanostructure Engineering

1. It is investigated that as the amount of PEG-400 increases in the chemical solution, the size of the particles decreases and reaches several tens of nano meters.

2. The nano-sized samples show higher electrical resistivity due to quantity of pores which increase carrier scattering at boundaries.

3. Reduction in lattice thermal conductivity due to phonon boundary scattering at increased number of interfaces.

4. Due to the increasing in carrier scattering, electronic contribution to total thermal conductivity is also reduced and this results in further thermal conductivity reduction.

5. Due to more substantial fall in thermal conductivity than electrical resistivity. *ZT* is enhanced by 61 %.

6. In figure 7.1, it is observed that nanosized (18, 30, 68 nm) C-349 samples show lower Seebeck coefficient, higher electrical resistivity and thus, lower power factor as it is compared with their 2 μm grain size counterpart. It is due to the higher porosity which is observed in nanosized samples.

7. Additionally, the energy filtering effect can be effective only in nanostructured ceramics with very small grains.

8. According to the result shown in figure 7.2, *ZT* increases as the size decreases because of the effect of grain size. It is due to the thermal conductivity that is getting lower as the size decreases along with increase in porosity, thermoelectric parameters are optimized and therefore *ZT* value is increased.

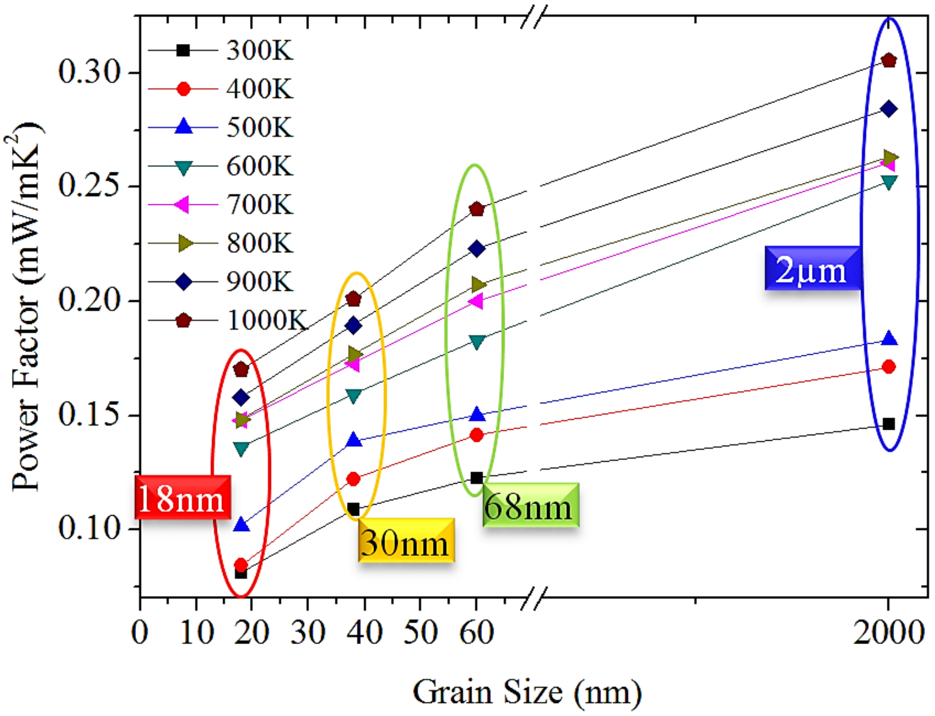

Figure 7.1 Power factor values as functions of grain size for C-349 samples.

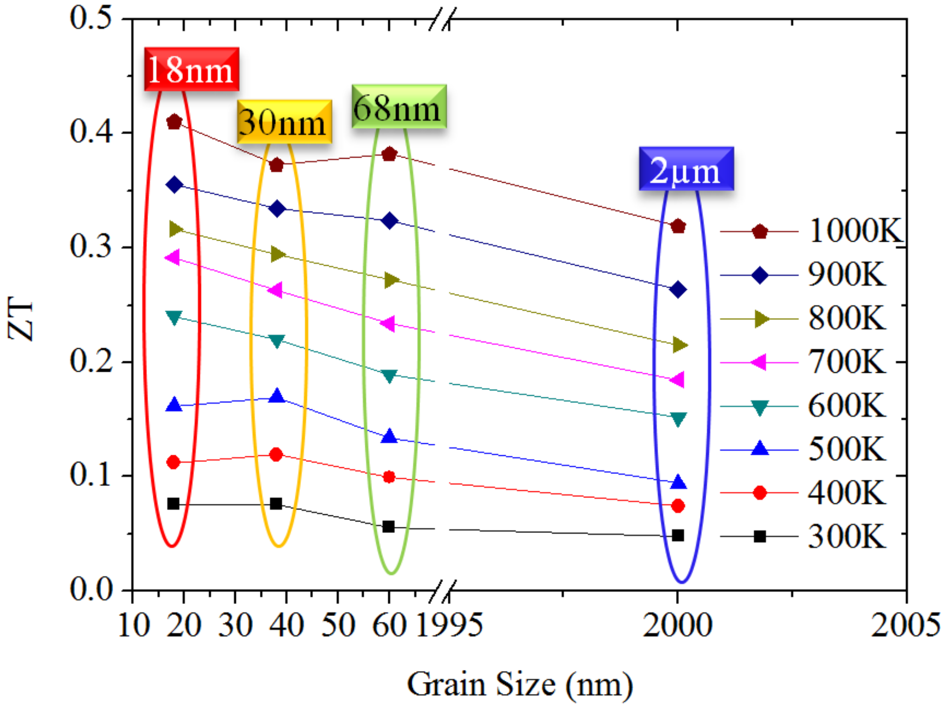

Figure 7.2 *ZT* values as functions of grain size for C-349 samples.

Structural characterizations and thermoelectric measurements are summarized in table 7.2.

Table 7.2 Summarize of sol-gel derived nano-structuring effect.

Material	**C-349**			
Samples	**S0**	**S3**	**S5**	**S7**
Method	**Citrate Sol-Gel**			
PEG-400(%)	-	3 %	5 %	7 %
Average grain size	~2 µm	~68 nm	~30 nm	~18 nm
FE-SEM	✓	✓	✓	✓
XRD	✓	✓	✓	✓
TG / DTA	✓	✓	✓	✓
Density	✓	✓	✓	✓
$\boldsymbol{S_{1000\,K}}$ **(µV/K)**	**143.2**	139.1	134.5	132.4
$\boldsymbol{\rho_{1000\,K}}$ **(mΩ.cm)**	**15.6**	16	16.7	18.4
$\boldsymbol{\kappa_{1000\,K}}$ **(W/mK)**	0.93	0.6	0.45	**0.41**
$\boldsymbol{PF_{1000\,K}}$ **(mW/mK^2)**	**0.18**	0.16	0.14	0.12
$\boldsymbol{ZT_{1000\,K}}$	0.18	0.26	0.27	**0.29**

7.3 Spin-Entropy Enhancement by Cr substitution to Ca-site of C-349 Metal Oxide

1. Cr substituted $Ca_{3-x}Cr_xCo_4O_9$ (x = 0.01, 0.03, 0.05 and 0.07) samples have been prepared successfully.

2. Larger grains are observed as the amount of Cr increases in the composition.

3. Cr substitution to Ca-site leads to the spin-entropy enhancement and this results in increase in the Seebeck coefficient up to the range of x = 0.03 Cr substitution.

4. Over x = 0.03 value, Seebeck coefficient tends to decrease due to the dominance effect of the larger grains, which caused the resistivity reduction about 6.1 %, over spin-entropy effect on Seebeck coefficient.

5. A slight increase in the magnitude of the thermal conductivity values from 0.9 to1.2 W/mK is measured at 1100 K for unsubstituted and x = 0.07 Cr sample, respectively.
6. The improvement of thermoelectric performance is the most significant in x = 0.03 Cr substituted sample with *ZT* value of 0.26 at 1100 K.

Table 7.3 lists the obtained thermoelectric measurement results for all the samples at 300 and 1000 K for better comparison.

Table 7.3 The list of thermoelectrics measurements including Seebeck coefficient, electrical resistivity, thermal conductivity, power factor and figure of merit values for all the samples.

		$Ca_{3-x}Cr_xCo_4O_9$			
	C-349	**x = 0.01**	**x = 0.03**	**x = 0.05**	**x= 0.07**
$S_{300\,K}$ **(μV/K)**	119.7	120.6	**127.1**	122.3	124.3
$S_{1100\,K}$ **(μV/K)**	158.6	160.0	**175.0**	167.4	167.0
$\rho_{300\,K}$ **(mΩ.cm)**	15.3	15.0	13.9	13.0	**12.8**
$\rho_{1100\,K}$ **(mΩ.cm)**	13.0	12.7	12.5	12.4	**12.2**
$\kappa_{300\,K}$ **(W/mK)**	**0.85**	0.98	1.06	1.13	1.23
$\kappa_{1100\,K}$ **(W/mK)**	**0.91**	0.94	1.01	1.17	1.2
$PF_{300\,K}$ **(mW/mK^2)**	0.09	0.1	0.11	0.11	**0.12**
$PF_{1100\,K}$ **(mW/mK^2)**	0.19	0.20	**0.25**	0.22	0.23
$ZT_{300\,K}$	**0.033**	0.032	**0.033**	0.031	0.029
$ZT_{1100\,K}$	0.24	0.25	**0.26**	0.20	0.21

7.4 Outlook for the Future Work

7.4.1 Nano-doping

- Nanostructuring and elemental doping offer us great opportunity for altering the thermoelectric properties.

- On one hand, the thermal conductivity can significantly be reduced by introducing increased amount of interfaces and/or grain boundaries using nano-sized structures.

- On the other hand, enough amount of dopant to the appropriate site in the structure is also helpful to tune the electronic structure by creating donor states close to the conduction band edge.

- Accordingly, these two parameters; nanostructuring and doping, could be helpful when they are applied simultaneously in one system.

- With proper tuning of structure and composition, not only thermal conductivity reduction, but also Seebeck coefficient enhancement could be possible in order to enhance *ZT* for practical application even at room temperature.

- Due to good thermoelectric and environmental properties, C-349 based oxides could be one of the best candidates.

7.4.2 Nano-texturing

- It is well known that microstructural properties, such as grain size and porosity, affect electrical and heat transport. The orientation affects the thermoelectric performance of the material if the structure of the material is layered [1].

- As it is introduced, the micro structure of C-349 metal oxides is layered and therefore properties are anisotropic. Therefore, texturing the lamellar structure could highly be advantageous for thermoelectric performance because the thermoelectric properties of these kinds of metal oxides are highly anisotropic [1].

- If the material were synthesized in nano-scale with textured structure, both Seebeck coefficient and electrical conductivity would be enhanced and thermal conductivity would be lowered.

- These kinds of materials could be prepared by pressing [2-4], rolling [5] or by means of controlled deposition [6]. Using spark plasma sintering technique (SPS), the size of the particles could also be controlled and kept at nano-scale.

- Nevertheless, SPS is expensive and not suitable for mass production. Accordingly; a new synthesis technique could be offered which is effective, economic and good for fabrication.

7.4.3 Micro-Nano Composite

Although lattice thermal conductivity could be reduced by introducing several scattering mechanisms, electrical conductivity is also affected at these scattering regions. Accordingly, if these regions were selected by carriers using new scattering mechanisms, electronic transport could not be affected while thermal conductivity would be reduced. The mechanism of micro-nano mixed composite structure is demonstrated as it is theoretically modeled in figure 7.3 (a) [7]. In this work, micro particles network are used for electron transport whereas nanoparticles are dispersed to scatter the phonons. Figure 7.3 (b) demonstrates *ZT* as a function of weight fraction of fine particles (%). As a result, as the volume fraction of fine particles is about 60 %, *ZT* value reaches the maximum value of about 0.66 for Bi_2Te_3 thermoelectric material [7]. That means, *ZT* would be tuned by optimizing the volume percentage of fine particles.

From this point of view, C-349 samples could also be prepared as micro-nano mixed composite and *ZT* would be enhanced by this way.

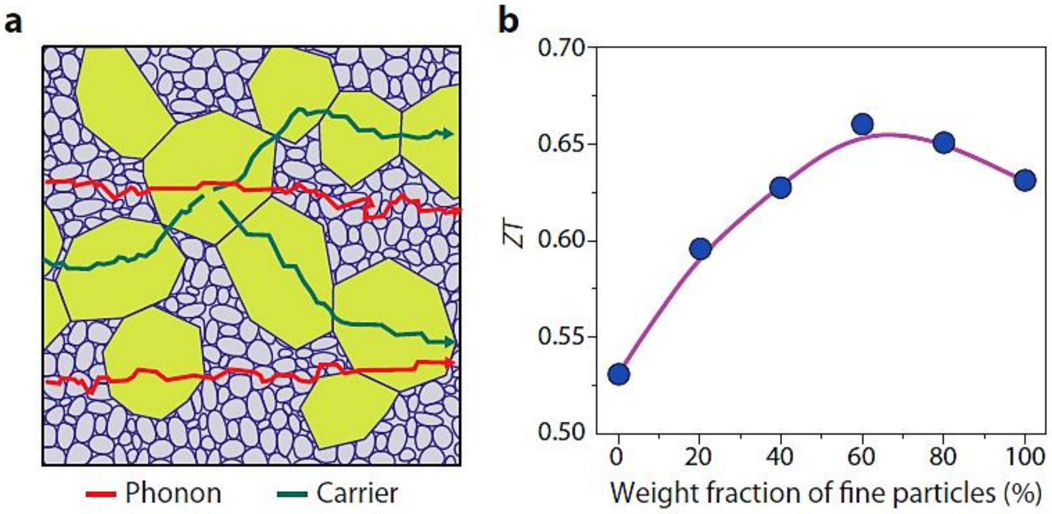

Figure 7.3 (a) Illustration of micro-nano mixed composite structure and *ZT* as a function of weight fraction of fine particles (%) [7].

7.4.4 Elemental Substitutions of Bi and K for Ca-site of C-349

One dopant commonly used with C-349 is bismuth, which has been shown to increase both the electrical conductivity and Seebeck coefficient as well as decrease the thermal conductivity. The increase in conductivity is attributed to an increase in carrier mobility rather than carrier concentration, which is generally desired in thermoelectric materials, since an increase in carrier concentration tends to lead to a decrease in the Seebeck coefficient. However, improvements in the conductivity have also been attributed to differences in the microstructure. The decrease in thermal conductivity has been attributed to the larger size and mass of bismuth as compared to calcium. The thermoelectric measurement results of C-349 doped with bismuth and potassium that are taken from the literature are shown in figure 7.4. The $Ca_{2.7}Bi_{0.3}Co_4O_9$ material illustrates the highest *ZT* as ~ 0.4 at around 1000K [8]. On the other hand, potassium substitution with calcium demonstrates the lowest thermal conductivity value. The substitution at the Ca^{2+} site of K^+ could also cause the site to act as a phonon scattering point to reduce the thermal conductivity of doped C-349, because of the large ionic radius of K^+ (1.38 Å). Therefore, since bismuth shows higher Seebeck coefficient and electrical conductivity but also high thermal conductivity, it would be very beneficial to combine these two elements and dope them together in an appropriate amounts. As a result, we take the advances of these two element properties in one material [8]. Expected compositions are to be synthesized as $Ca_{3-x-y}Bi_xK_yCo_4O_9$. The x and y values and four different compositions are presented in table 7.4.

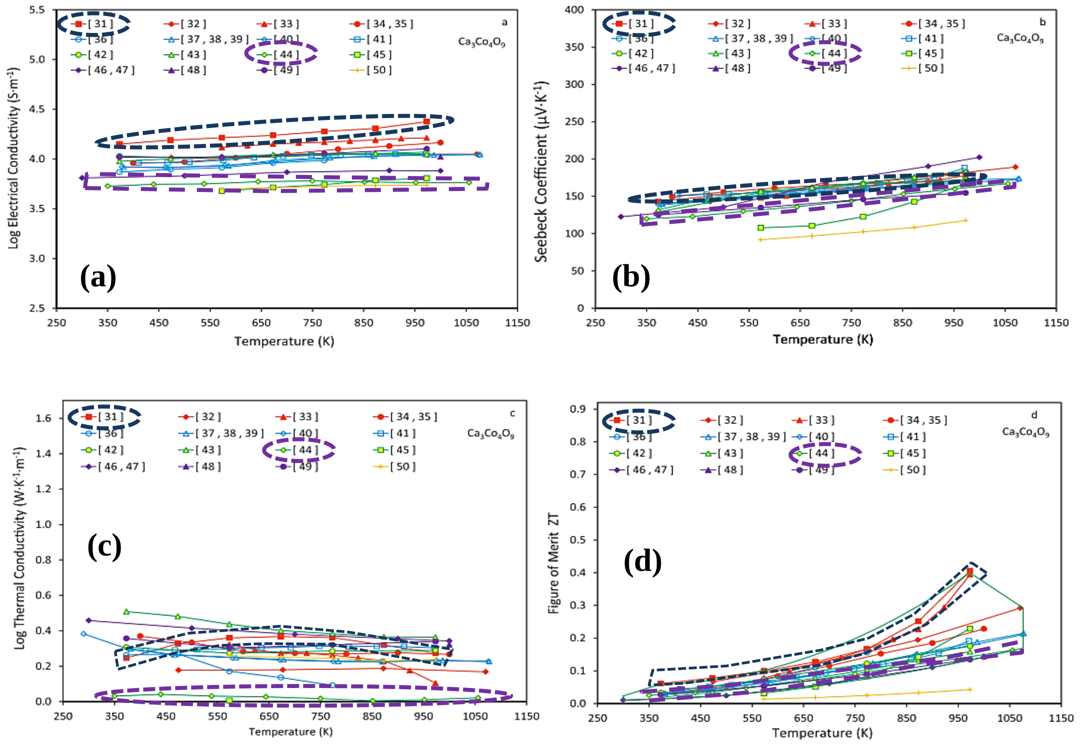

Figure 7.4 (a) Electrical conductivity, **(b)** Seebeck coefficient, **(c)** thermal conductivity and (d) *ZT* for C-349 [8].

Table 7.4 The amount of substitution of Bi and K in the composition of $Ca_{3-x-y}Bi_xK_yCo_4O_9$

	Compositions			
	1	**2**	**3**	**4**
x	0.2	0.2	0.3	0.3
y	0.1	0.2	0.1	0.2

REFERENCES

[1] T. Yin, D. Liu, Y. Ou, F. Ma, S. Xie, J.-F. Li, J. Li, Nanocrystalline Thermoelectric $Ca_3Co_4O_9$ Ceramics by Sol-Gel Based Electrospinning and Spark Plasma Sintering, J. Phys. Chem. C 114 (2010) pp 10061–10065

[2] X.Y. Huang, Y. Miyazaki, K. Yubuta, Y. Oide, T. Kajitani, The thermoelectric properties of $[Ca_2CoO_3]_{0.62}[CoO_2]$ textured ceramics. In: Proc. 2006 Int. Conf. Thermoelectrics, IEEE. (2006) pp 81–91

[3] Y. Zhang, J. Zhang, Q. Lu, Synthesis of highly textured $Ca_3Co_4O_9$ ceramics by spark plasma sintering Ceram. Int. 33 (2007) pp 1305–8

[4] J. G. Noudem, A new process for lamellar texturing of thermoelectric $Ca_3Co_4O_9$ oxides by spark plasma sintering, J. Eur. Ceram. Soc. 29 (2009) pp 2659–62

[5] J. W Park, D. H Kwak, S. H. Yoon, S. C. Choi, Thermoelectric properties of highly oriented $Ca_{2.7}Bi_{0.3}Co_4O_9$ fabricated by rolling processes, J. Ceram. Soc. Jpn. 117 (2009) pp 643–6

[6] W. -H. Yoon, J. Ryu, J. J. Choi, B. -D. Hahn, J. H. Choi, B. -K. Lee, Enhanced thermoelectric properties of textured $Ca_3Co_4O_9$ thick film by aerosol deposition, J. Am. Ceram. Soc. 93 (2010) pp 2125–7

[7] J. F. Li, W. S. Liu, L. D. Zhao and M. Zhou, High-performance nanostructured thermoelectric materials, NPG Asia Mater. 4 (2010) pp 152–158

[8] J.W. Fergus, Oxide materials for high temperature thermoelectric energy conversion, J. Eur. Ceram. Soc. 32 (2012) pp 525–540

APPENDIX A

LABVIEW CODE FOR SEEBECK COEFFICIENT MEASUREMENT

Front Panel of Software

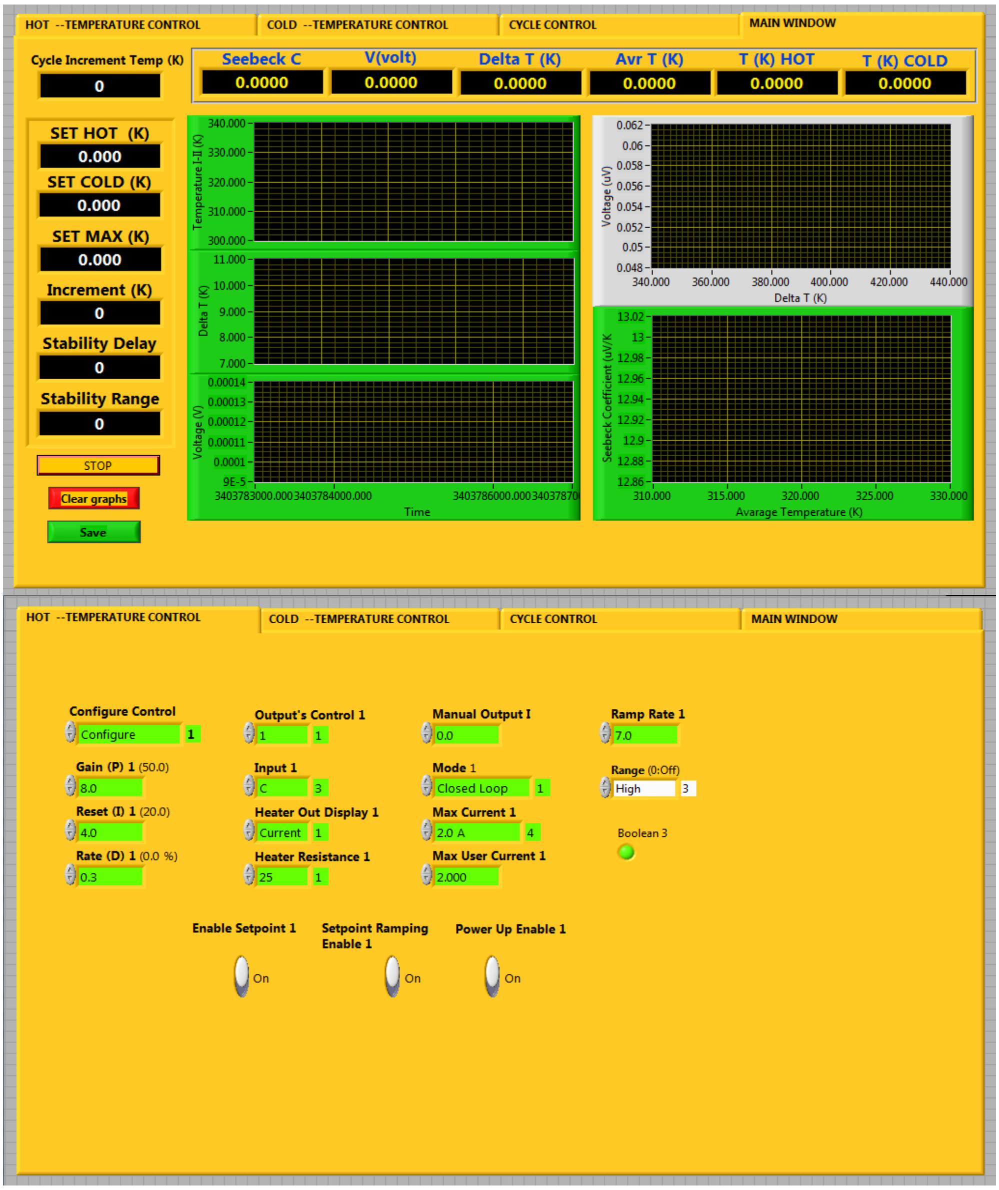

Cycle Increment Temp (K) 0

Seebeck C 0.0000
V(volt) 0.0000
Delta T (K) 0.0000
Avr T (K) 0.0000
T (K) HOT 0.0000
T (K) COLD 0.0000

SET HOT (K) 0.000
SET COLD (K) 0.000
SET MAX (K) 0.000
Increment (K) 0
Stability Delay 0
Stability Range 0

Configure Control: Configure 1
Gain (P) 1 (50.0): 8.0
Reset (I) 1 (20.0): 4.0
Rate (D) 1 (0.0 %): 0.3
Output's Control 1: 1 1
Input 1: C 3
Heater Out Display 1: Current 1
Heater Resistance 1: 25 1
Manual Output I: 0.0
Mode 1: Closed Loop 1
Max Current 1: 2.0 A 4
Max User Current 1: 2.000
Ramp Rate 1: 7.0
Range (0:Off): High 3
Enable Setpoint 1: On
Setpoint Ramping Enable 1: On
Power Up Enable 1: On

Figure A.1 Front panels of Seebeck coefficient measurement software.

Block Diagram of Software: Part-1

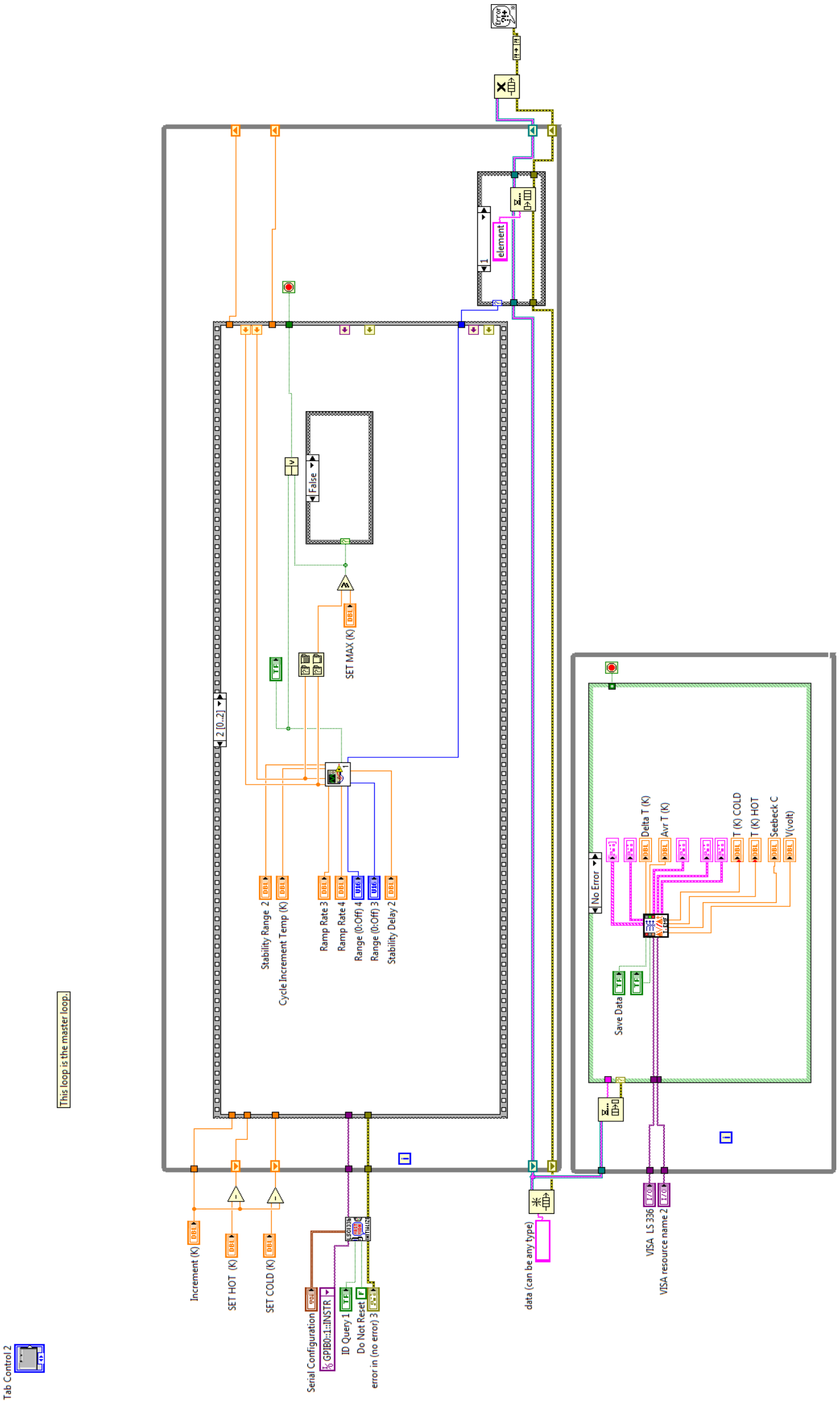

Figure A.2 First part of block diagram of Seebeck coefficient measurement software.

Block Diagram of Software: Part-2

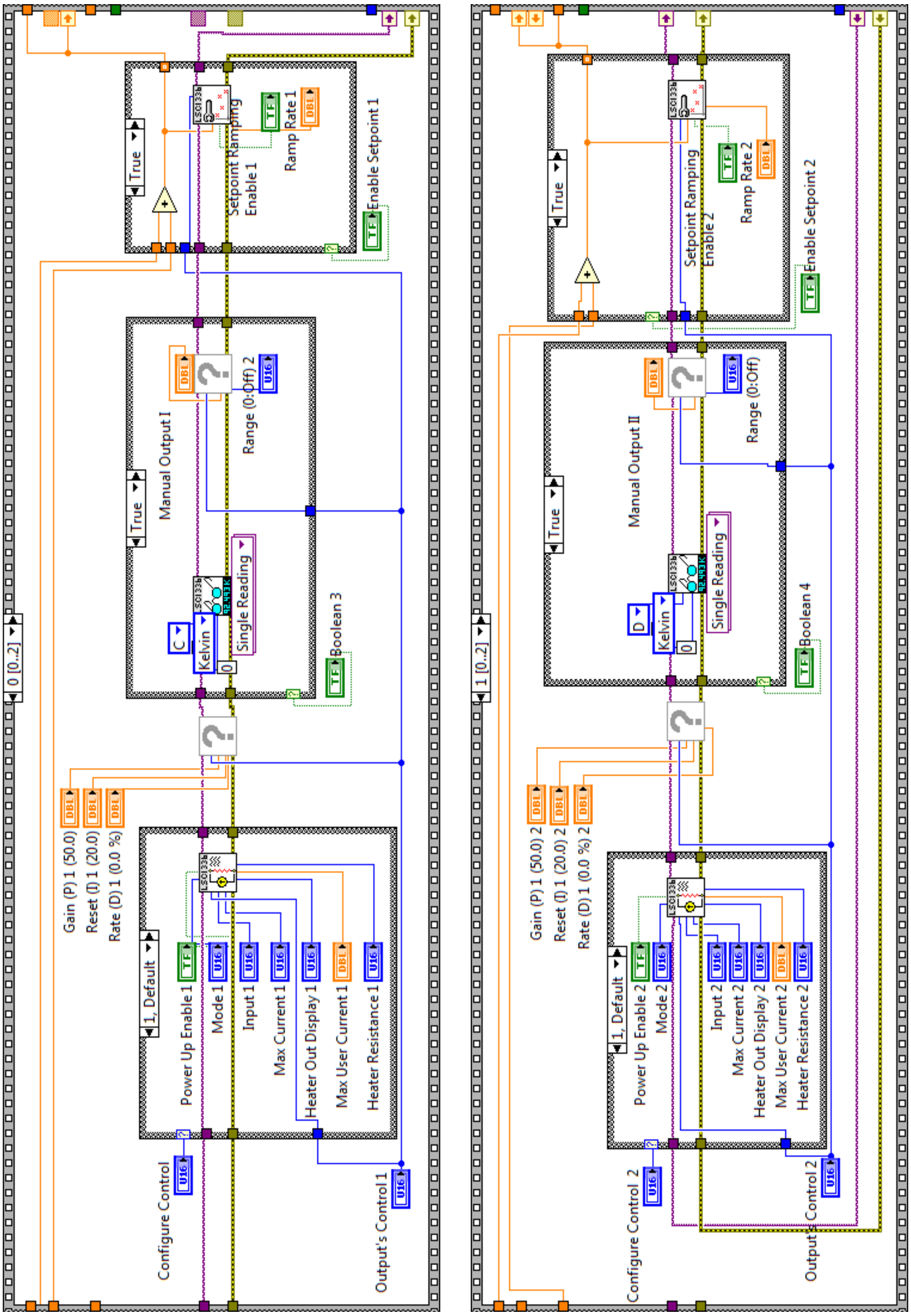

Figure A.3 Second part of block diagram of Seebeck coefficient measurement software.

APPENDIX B

LABVIEW CODE FOR ELECTRICAL RESISTIVITY MEASUREMENT

Front Panel of Software

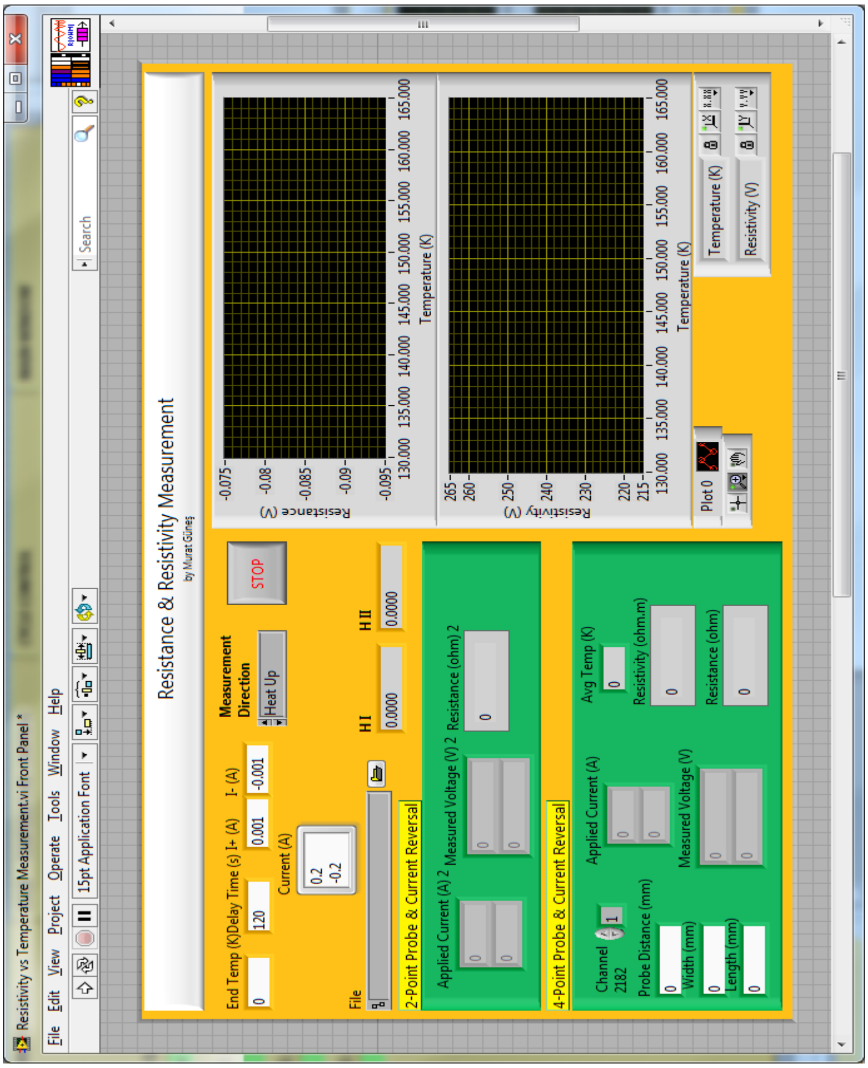

Figure B.1 Front panel of electrical resistivity measurement software.

Block Diagram of Software: Part-1

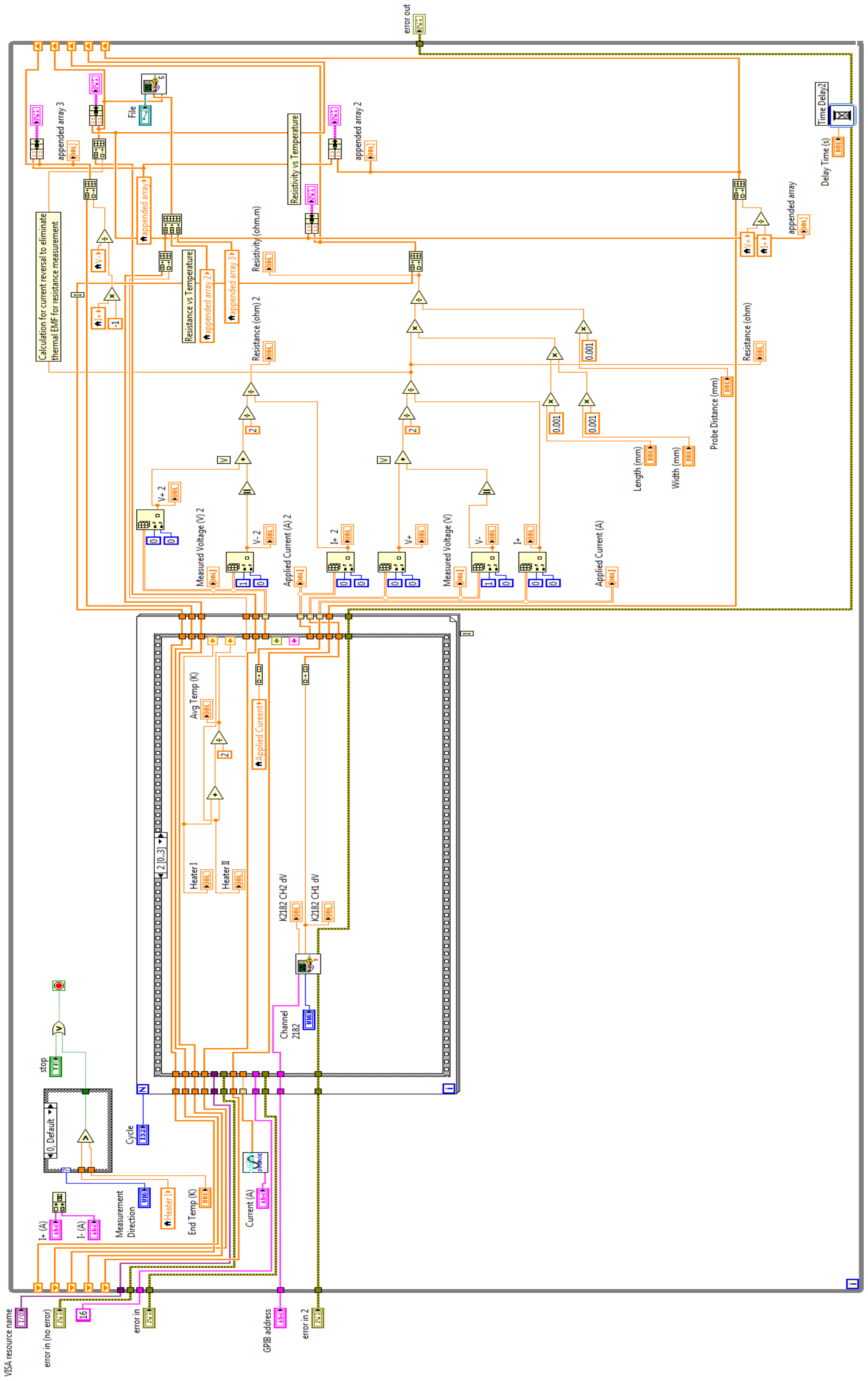

Figure B.2 First part of block diagram of electrical resistivity measurement software.

Block Diagram of Software: Part-2

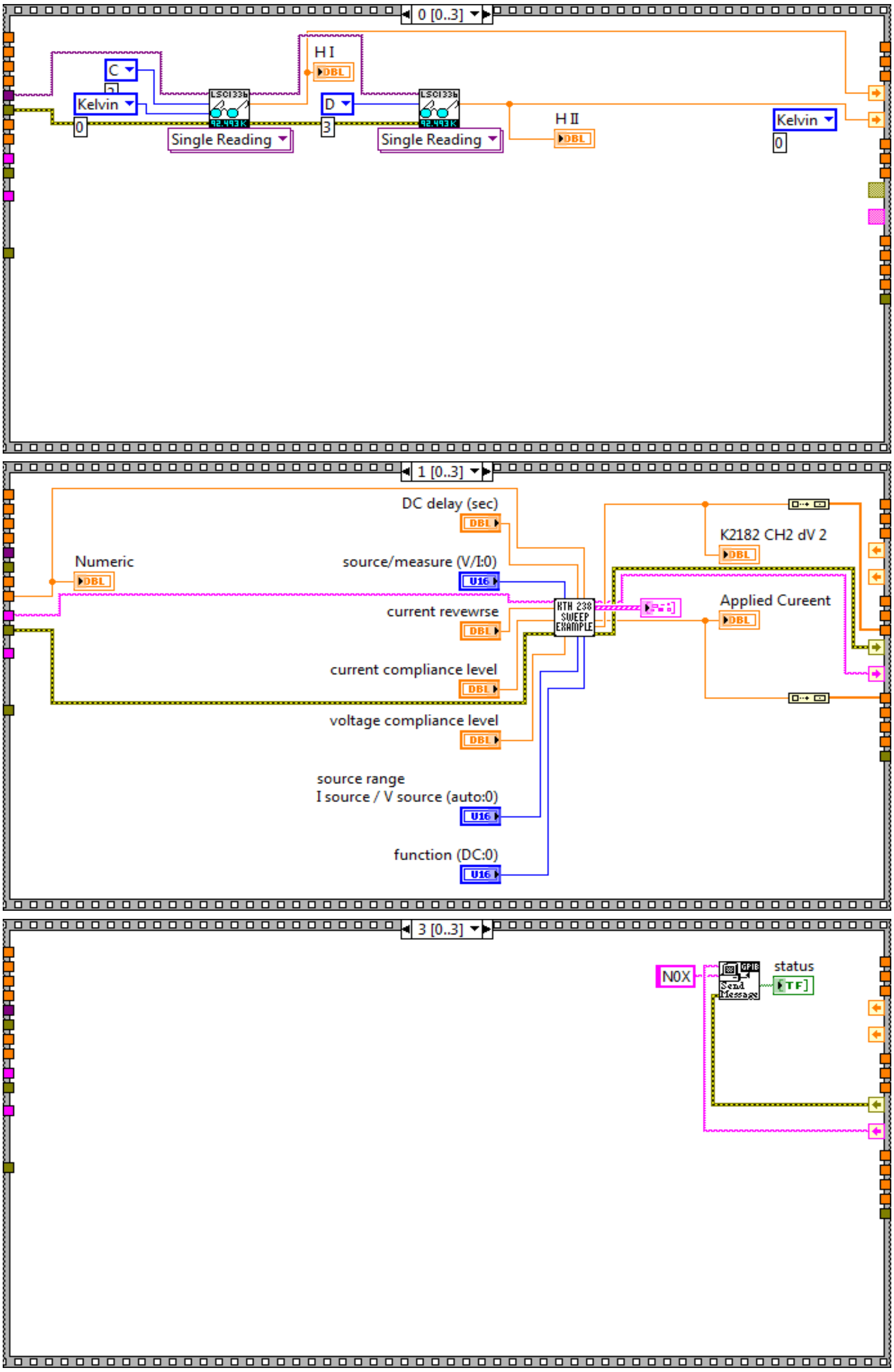

Figure B.3 Second part of block diagram of electrical resistivity measurement software.

CURRICULUM VITAE

PERSONAL INFORMATION

Surname, Name: Güneş, Murat
Nationality: Turkish (TC)
Date and Place of Birth: 17 March 1980, Malatya
Marital Status: Married
Phone: +90 312 210 59 17
Fax: +90 312 210 25 18
email: gunesm@metu.edu.tr

EDUCATION

Degree	**Institution**	**Year of Graduation**
Ph.D.	METU, Micro & Nano Technology	2014
M.Sc.	İnönü University, Department of Physics	2007
B.Sc.	İnönü University, Department of Physics	2003
High School	Sümer High School, Ankara	1997

WORK EXPERIENCE

Year	**Place**	**Enrollment**
2008 - Present	METU Micro & Nanotechnology Program	Research Assistant
2003 - 2007	İnönü University	Expert (PPMS)

FOREIGN LANGUAGES

English

PUBLICATIONS

A. Thesis

1. Murat Güneş, Ph. D. Thesis, METU, August 2014.
   Effect of Transition Metal Substitution on High-Temperature Properties of Thermoelectric Materials

2. Murat Güneş, M. Sc. Thesis, İnönü University, May 2007.
   Synthesis and Properties of $NiFe_2O_4$ Magnetic Nanoparticles

B. Journal Articles

1. M. Gunes, M. Parlak, M. Ozenbas, An instrument for the high temperature measurement of Seebeck coefficient and electrical resistivity, Meas. Sci. Technol 25 (2014) pp 055901

2. M. Gunes, H. Gencer, S. Atalay, V.S. Kolat, T. Izgi, Size-induced effects on nanostructured $NiFe_2O_4$, International J. Mod. Phys. B 24 (2010) pp 5973-5985

3. N. Bayri, T. Izgi, H. Gencer, P. Sovak, M. Gunes, S. Atalay, Crystallization kinetics of $Fe_{73.5-x}Mn_xCu_1Nb_3Si_{13.5}B_9$ (x =0, 1, 3, 5, 7) amorphous alloys J. Non-Cryst. Solids 355 (2009) pp 12-1

4. H. Gencer, A. Goktas, M.Gunes, H.I. Mutlu and S. Atalay, Electrical Transport and Magnetoresistance of $La_{0.67}Ca_{0.33}MnO_3$ film coated on pyrex glass substrate, Int. J. Mod. Phys. B**,** 22 (2008) pp 497-506

5. H. Gencer, M. Gunes, A. Goktas, Y. Babur, H.I. Mutlu and S. Atalay, LaBaMnO films produced by dip-coating on a quartz substrate J. Alloys Compd. 465 (2008) pp 20-23

6. H. Gencer, N. Kervan, A. Gencer, M. Gunes and S. Atalay, Magnetocaloric effect in $CeCo_4B$ compound, J. Alloys Compd. 466 (2008) pp 1-4

7. V.S. Kolat, H. Gencer, M. Gunes and S. Atalay, Effect of B-doping on the structural, magnetotransport and magnetocaloric properties of $La_{0.67}Ca_{0.33}MnO_3$ compounds, Mater. Sci. Eng., B 140 (2007) pp 212-21

8. M. Gunes, H. Gencer, V.S. Kolat, S. Vural, H.I. Mutlu, T. Seckin and S. Atalay, Microstructure and Magnetoresistance of a $La_{0.67}Ca_{0.33}MnO_3$ Film Produced Using The Dip-Coating Method, Mater. Sci. Eng., B 136 (2007) pp 41-45

C. Conference and Meeting Presentations

1. M. Gunes, M. Ozenbas, Thermoelectric efficiency enhancement by Cr doping at Ca-site of $Ca_{3-x}Cr_xCo_4O_9$ (x=0.01, 0.03, 0.05 and 0.07) material synthesized by citrate sol-gel, MRS Fall-2013, Dec. 1-6, Boston/U.S.A.

2. M. Gunes, M. Ozenbas, Design and implementation of modular high temperature Seebeck coefficient and resistivity measurement system for bulk and film samples, MRS Fall-2012, Nov. 25-Nov. 30, Boston / U.S.A.

3. M. Gunes, M. Parlak, M. Ozenbas, Design and implementation of complete thermoelectric properties measurement system: thermopower, electrical conductivity/resistivity and thermal conductivity, MRS Fall-2011, Nov. 28-Dec. 2, Boston / U.S.A.
4. M. Gunes, M. Parlak, M. Ozenbas, True measurements of Seebeck coefficient and resistivity, NiPS Summer School and Workshop 2011, Aug. 01-05, 2011, Perugia / Italy
5. M. Gunes, M. Parlak, M. Ozenbas, Effect of synthesis methods on thermoelectric properties of metal oxides, INTEN-C (M.E.T.U. & T.U.D. Research and Educational Network on Nanomaterials and Nanotechnology for Renewables Ankara Workshop), Apr. 09-12, 2010, Darmstadt / Germany
6. M. Gunes, M. Parlak, M. Ozenbas, A novel method to produce thermoelectric materials, INTEN-C (M.E.T.U. & T.U.D. Research and Educational Network on Nanomaterials and Nanotechnology for Renewables Ankara Workshop), Dec. 15-17, 2009, Ankara / Turkey
7. M. Gunes, M. Ozenbas, Improving thermoelectric efficiency of $Ca_3Co_4O_9$ by manipulating size and density, MRS Fall-2012, Nov. 25-Nov. 30, Boston / U.S.A.
8. M. Gunes, M. Parlak, M. Ozenbas, Effect of citrate sol-gel and autoclave processing methods on thermoelectric properties of $Ca_3Co_4O_9$ nanopowders, MRS Fall 2010, 26th Nov. – 4th Dec., Boston MA / U.S.A.
9. M. Gunes, S. Vural, T. Seckin and S. Atalay, Production of $NiFe_2O_4$ nanoparticles and effect of sintering temperature on the magnetic properties, ICNM (International Conference on Nanoscale Magnetism), Jun. 25-29, 2007, Istanbul / Turkey
10. A. Goktas, H. Gencer, M. Gunes, Y. Babur, F. Aslan, H.I. Mutlu and S. Atalay, Magnetoresistance effect in of $La_{0.67}Ca_{0.33}MnO_3$ and $La_{0.67}Sr_{0.33}MnO_3$ films produced using the dip-coating method, ICNM (International Conference on Nanoscale Magnetism), Jun. 25-29, 2007, Istanbul / Turkey
11. S**.** Atalay, H. Gencer, M. Gunes, A. Goktas and H.I. Mutlu, LaBaMnO films produced by dip-coating on a pyrex substrate, Enhanced Imaging of Magnetic Structures in Micropatterned Arrays of Crystals Conference, Wolfson Centre for Magnetics, Nov. 2-5, 2007, Cardiff University / U.K.
12. S. Köytepe, T. Seçin, M. Gunes ,S. Atalay, Synthesis of polyimide- Fe_3O_4 magnetic nanoparticles, Nano Tr-III, Nano Science and Technology Conference, 11-14 Jun. 2007, Bilkent University, Ankara / Turkey

RESEARCH ACTIVITIES

1. NiPs Summer School and Workshop 2011, Energy Harvesting at Micro and Nanoscale, The Noise in Physical System Laboratory, Università di Perugia, Perugia-Italy, August 2011

2. Visitor Researcher, The Department of Metal Physics, Ivan Franko National University of Lviv-Ukraine, August 2010

3. Visitor Researcher, International Thermoelectric Academy, L. I. Anatychuk Chernovtsy-Ukraine, August 2010

HOBBIES

2004-present : Aikido, Professional

1999-2001 : Basketball Player, Professional

1992-present : Playing Baglama

1992-present : Painting, Swimming, Traveling.